Mathematical modelling of *in vitro* microfluidic systems for drug development



Barnum Swannell
Worcester College
University of Oxford

A thesis submitted for the degree of
Doctor of Philosophy

Michaelmas 2025

Acknowledgements

I would like to first thank my academic supervisors, Professor Sarah Waters and Professor James Oliver, for their tireless guidance, support, patience, encouragement, and enthusiasm throughout my DPhil; I learned a lot from working with you both and thoroughly enjoyed the experience.

I would also like to thank my industrial supervisor, Dr Daniela Ortiz Franyuti, as well as collaborators Dr Olivier Frey and Dr Michal Rudnik, for their continuous support and valuable insights throughout this research.

In addition, I would like to thank my friends in Oxford and beyond who supported me throughout my time here, making the whole experience significantly happier and more enjoyable. I am grateful to everyone from the SABS Doctoral Training Programme, OCIAM, WCMB, the wider Mathematical Institute, and Worcester College who made such a positive difference to my studies.

Finally, I would like to thank my family and my partner for all that they have done for me.

Abstract

This thesis will focus on characterising fluid flow and solute transport in a novel microfluidic device in the context of its use for pharmaceutical drug discovery. Advanced microfluidic systems are increasingly important in preclinical studies, and detailed mathematical modelling supports both the design and operation of these systems and contributes to improved understanding of the drug and tissue interactions that occur within them. Our analysis centres on a microfluidic device designed by InSphero and trialled by Roche for preclinical toxicology studies, who are both collaborators in this work. The flow in the system is primarily gravity driven; however, due to the small device length scale, capillary effects can significantly modify the flow, which in turn affects solute transport and biological reactions. In this thesis, we develop mathematical models of the key physical processes within the system, exploiting where possible disparate length scales and timescales to obtain reduced asymptotic models. Insights from our analysis of these models can be used to support the use of the system in typical pharmacological experiments.

Contents

1 Introduction **1**

1.1 Microfluidic systems 1

1.2 Applications in drug discovery 3

1.3 Mathematical modelling 6

1.3.1 Fluid dynamics 7

1.3.2 hydraulic electric circuit analogy 8

1.3.3 Capillary surfaces and moving contact lines 9

1.3.4 Solute transport and reactions 11

1.3.5 Compartmental modelling 12

1.3.6 Model reduction 13

1.4 Thesis summary and overview 13

2 The twin-well microfluidic system **17**

2.1 Introduction 17

2.2 Overview of the twin-well system 18

2.3 System geometry and typical operation 20

2.4 Governing equations for fluid flow 24

2.4.1 The elevation angle 28

2.5 Governing equations for solute transport and reactions 29

2.5.1 Solute reaction terms 30

2.6 Physical and geometrical parameter values 30

2.7 Scaling and non-dimensionalisation 33

2.7.1 Dimensionless equations for fluid flow 33

2.7.2 Dimensionless transport equations 35
2.7.3 Dimensionless parameters 36
2.8 Contact-line dynamics and the Cox-Voinov contact-line law 37
2.8.1 Asymptotic Structure 38
2.8.2 Outer region 39
2.8.3 Inner region 42
2.8.4 Cox-Voinov contact-line law 43
2.8.5 Summary of the reduced model 45
2.9 Twin-well dynamics 45
2.9.1 Region I: the wells 47
2.9.2 Region II and III 48
2.9.3 Summary of twin-well dynamics 50

3 Single-well analysis **51**
3.1 Introduction 51
3.2 The single-well system 52
3.2.1 Reduced model equations 54
3.2.2 Model variables and parameters 55
3.2.3 Properties of the Young-Laplace problem 56
3.3 Numerical methods and Surface Evolver 57
3.3.1 Finite difference scheme for contact-line height 58
3.3.2 Surface Evolver 59
3.3.3 Implementation of the Surface Evolver scheme 60
3.4 Horizontal circular well 62
3.4.1 Spherical cap solutions to the Young-Laplace problem 64
3.4.2 Contact-line dynamics 66
3.4.3 Small relaxation parameter dynamics 69
3.4.4 Contact angle hysteresis 73
3.4.5 Gravitational effects: the Young-Laplace problem 78

3.4.6 Gravitational effects: the moving contact line 81
3.4.7 Pressure variation 83
3.4.8 Summary 86
3.5 Tilted circular well 87
3.5.1 Parameters and variables 88
3.5.2 Tilting without flow 89
3.5.3 Variations in pressure 91
3.5.4 Oscillating contact line 94
3.5.5 Flow and tilting 96
3.5.5.1 Simultaneous flow 97
3.5.5.2 Sequential flow 99
3.5.6 Summary 99
3.6 Discussion 101

4 Fluid flow in a twin-well system **104**
4.1 Introduction 104
4.2 Two-dimensional system 105
4.2.1 Reduced model equations 106
4.2.2 Model structure, variables, and properties 109
4.2.3 Numerical solutions 110
4.3 Surface tension free dynamics 111
4.3.1 Physical mechanisms 111
4.3.2 Flow in a static system 113
4.3.3 Flow in an oscillating system 114
4.3.4 General low frequency oscillations 117
4.3.5 Paused oscillations 118
4.4 Capillary effects in a static system 122
4.4.1 Horizontal system dynamics 123
4.4.2 Equilibrium volume 126
4.4.3 Sensitivity to initial conditions 129

4.4.4 Critical initial volume difference 131
4.4.5 Discussion of system parameters 133
4.4.6 Discussion 135
4.5 Capillary effects in an oscillating system 136
4.5.1 Oscillatory dynamics 136
4.5.2 Sensitivity to initial conditions 138
4.5.3 Critical elevation angle 139
4.5.4 Transfer volume 142
4.6 Discussion 145

5 Solute transport and reactions in two dimensions 149
5.1 Introduction 149
5.2 Overview of solute transport and reactions 150
5.3 Problem setup 152
5.3.1 System geometry 153
5.3.2 Transport equations 154
5.3.3 Numerical scheme 155
5.4 Measures of mixing 158
5.5 Fluid velocity profile 160
5.5.1 Discussion 163
5.6 Dispersal of initial solute profile 165
5.6.1 Diffusive transport and scaling arguments 165
5.6.2 Large Péclet regime 166
5.6.3 Advection and diffusion in a single cycle 169
5.6.4 Multiple oscillation cycles and sequential mixing 171
5.6.5 Oscillation frequency 172
5.6.6 Oscillation amplitude 173
5.7 Solute production 175
5.7.1 Intra-well mixing 177
5.8 Discussion 179

6 Conclusions and future work **181**

6.1 Conclusion 181

6.2 Future work 184

A Derivation of the contact-line law **186**

Bibliography **191**

Chapter 1

Introduction

1.1 Microfluidic systems

Microfluidics refers to the science and technology of systems designed to manipulate small volumes of fluid, which are typically on the order of nanolitres or below [1]. The modern field of microfluidics traces its origin to microfabrication techniques developed for the semiconductor industry and early lab-on-chip technology, which emerged in the 1980s and 1990s and envisioned integrating one or more laboratory functions on a single miniaturised chip [2, 3]. Microfluidic technology has developed rapidly over the last two decades, driven both by advances in materials and fabrication techniques [4] and a growing number of applications in many areas of chemistry, biology, and medicine [1, 5]. Examples include systems tailored for use in chemical synthesis, genome sequencing, *in vitro* modelling, and rapid diagnostic testing, which incorporates microfluidic paper-based analytical devices such as home pregnancy tests or Covid-19 lateral flow tests [1, 5, 6, 7].

The advantages of microfluidic technology stem from the ability to precisely control very small volumes of fluid. This reduces the quantity and costs of reagents while typically increasing the speed of analysis. Microfluidic systems are also well suited for high-throughput analysis, since many individual systems can be incorporated into a single chip, allowing multiple experiments to run in parallel. Furthermore, precise control of the system design and operation allows for the development of highly customised devices well suited for a particular application, while also improving reli-

ability and reproducibility of experimental studies [1, 5].

Microfluidic systems also offer enhanced functionality due to the physics of microflows [8]. For instance, the typical length and fluid velocity scales associated with microfluidic systems correspond to low Reynolds number regimes where the flow is laminar. The regularity of these flows enables precise control of the environment within the system. In addition, the effects of surface tension become increasingly important at small length scales, which enables flows to be driven passively by capillary pressure differences without the need for active pumping [9].

However, these features can also pose challenges for the design and operation of microfluidic systems. Laminar flow is not conducive to the rapid mixing between solutes and reagents, which is desired in many applications, as mixing across adjacent fluid layers by molecular diffusion is typically slow [10]. This has motivated the development of a variety of novel techniques to enhance mixing at low Reynolds number, including chaotic mixing, which involves engineering complex and time-varying flow profiles to increase the contact area between solutes and reduce the distance over which diffusion must act [11]. This can be achieved through active stirring techniques or passively through the use of herringbone or serpentine channels [12, 13]. Other active techniques to promote mixing include acoustic, electrokinetic or magnetic mixing [10].

Many microfluidic systems feature open-air interfaces, which can present further difficulties. For instance, enhanced surface tension effects are not always desirable, particularly for systems designed for flows driven by other mechanisms. In these scenarios, surface tension effects may need to be accounted for to achieve the desired behaviour [14]. The potential negative impact of surface tension is further compounded by the high variability of the capillary pressure, which is sensitive to the shape of the fluid-air interface and contamination due to surfactants. Open-air interfaces also result in fluid loss to evaporation, which is magnified by smaller volume to surface area ratios, although in some cases evaporation can be exploited to drive the flow [15].

Designs of microfluidic devices vary substantially depending on the field and particular use case, and novel systems are often developed for specific applications [1]. Conceptually, however, most consist of a series of chambers, where for instance cell cultures are located or reactions take place, connected by thin microfluidic channels. Originally manufactured using glass or silicon, today the polymer polydimethylsiloxane (PDMS) is widely adopted as a material of choice for many systems, due to favourable properties such as optical transparency and biocompatibility as well as its suitability for soft lithography fabrication techniques [4, 16]. Alternative materials include silicon, thermoplastics, or even paper-based systems [5].

Flow can be driven by a variety of active or passive mechanisms. Active mechanisms include the use of an external pump to drive fluid via inlets and outlets, while most passive mechanisms involve establishing pressure gradients across the channels. These can be achieved by varying the volume of fluid in each well or continuously rocking the system to establish hydrostatic pressure differences, or by exploiting differences in capillary pressure. In many applications, passively driven systems are preferred, as these are simpler to fabricate and use while also requiring fewer resources and less expertise than actively driven systems [9].

This thesis studies a novel microfluidic system designed for use in pharmaceutical drug discovery. This field has benefited significantly from the development of microfluidic technology through the adoption of advanced *in vitro* cell cultures and organ-on-a-chip technology, which have the potential to overcome some of the key challenges facing the industry and the drug development process [17, 18, 19]. We provide some relevant background on pharmaceutical drug discovery and the use of microfluidic systems in the following section.

1.2 Applications in drug discovery

The drug discovery process is notoriously lengthy, expensive, and challenging, with the total development time 'from bench to bedside' for a novel therapeutic compound averaging between ten and fifteen years and typical costs estimated to exceed $1bn

[20]. One major reason for this is the high compound attrition rate, with many promising drug candidates ultimately failing at some point along the development pipeline, often following substantial investment of time and resources.

This high failure rate is due in part to the difficulty in translating preclinical experiments, where drugs are tested using *in vitro* cell cultures or in animal studies, to a clinical setting, where drugs are tested in human subjects [21]. Indeed, only around one in ten drug compounds entering clinical trials are ever approved for release, with previously undetected toxicity responsible for approximately one third of failures [22]. Thus, a key challenge for the pharmaceutical industry is to refine preclinical efficacy and toxicity studies to better predict drug effects in a clinical setting.

One avenue for improving the reliability of preclinical testing is the development of more advanced *in vitro* systems to overcome the limitations of traditional cell cultures, which often do not faithfully recapitulate the environments found *in vivo* [23]. For instance, traditional cell culture systems, which include culture flasks and petri dishes as simple examples, are characterised by a monolayer of a single cell type grown on a flat surface in culture medium and under static conditions. However, *in vivo* cells grow in a three-dimensional arrangement within a complex and dynamic extracellular environment, which allows for interactions between cells of multiple types. Furthermore, cells also experience mechanical stimuli from the vascular network and interstitial flows.

It is therefore unsurprising that many differences are observed between cell behaviour in two-dimensional cell culture and in a physiological environment, including differences in cell morphology and function. For example, hepatocytes (liver cells) in two-dimensional cultures are found to rapidly dedifferentiate and lose function when not exposed to fluid shear forces found *in vivo* [24]. Static cell cultures are also not effective for studying drug effects over a longer time period, since the culture cannot remain viable without a mechanism for replenishing nutrients and removing waste products.

Consequently, advanced systems have been designed to better mimic *in vivo* conditions and thereby more accurately capture the cellular response to drugs. This can

be achieved through the use of three-dimensional cell cultures, where cells are seeded on a scaffold acting as an extracellular matrix or grown to produce self-aggregating three-dimensional spheroids or organoids [25]. Microfluidic technology can further be incorporated into the design of such systems to mimic vascular flow and allow more precise control of the cell environment, providing mechanical stimuli and shear stresses and enhancing nutrient exchange [26].

Furthermore, *in vitro* microfluidic systems often move beyond simply overcoming the limitations of traditional cell cultures by offering fundamentally new functionality. For instance, organ-on-a-chip technology is designed to capture a subset of organ-level function, with cultures of different cell types connected by microfluidic channels to simulate the vascular system. These are increasingly relevant in the field of drug discovery as drugs with more complex mechanisms of action are developed [27]. Examples include systems linking intestine and liver cells to capture their combined function in drug metabolism, systems combining liver cells with another cell type to assess prodrugs, which must be metabolised by the liver to become active, and systems which incorporate immune cells to assess immunotherapy treatments and immune-mediated toxicity [28, 29, 30].

A parallel development in preclinical studies, and in the drug development process more widely, has been the increasing use of *in silico* studies incorporating computer modelling and simulation [31]. Pharmacokinetic studies in particular, which concern the absorption, distribution, metabolism, and excretion (ADME) of drugs in the body, have benefited enormously from the paradigm shift towards computational approaches. Drug failures due to unfavourable pharmacokinetic properties have reduced markedly, while regulators have encouraged modelling to support clinical trials, and even accepted model predictions in lieu of unethical or impractical clinical trials [32]. Pharmacokinetic modelling is also important for designing optimal dosing strategies and will play a key role in the future development of personalised medicine [33].

Pharmacokinetic models involve a large number of parameters corresponding to the ADME processes that occur in the relevant organ systems. These parameters must be determined experimentally and advanced microfluidic systems often provide

more accurate estimates than traditional cell cultures. Thus, microfluidic systems, in tandem with modelling, provide better quantitative and qualitative predictions [34, 35].

In addition to their use in preclinical studies, microfluidic systems find extensive use in other areas of biomedical research, including understanding drug mechanisms [5, 36]. Furthermore, the precise control afforded by microfluidic technology allows concentration gradients to be set up within the system. This enables the study of cells in an inhomogeneous environment or the chemotactic migration of cells along these concentration gradients, which is relevant to immunotherapy treatment [37].

1.3 Mathematical modelling

The complexity of microfluidic systems means that mathematical modelling plays an important role in many aspects of the design and operation of these devices [8, 38]. The benefits of this modelling include efficient prototyping and refinement of systems, since it allows a large number of system geometries and parameters to be investigated quickly and cheaply. Optimal designs and operating conditions can therefore be identified for a desired use case. Furthermore, mathematical models can provide detailed and high-resolution information of the system, providing a more thorough characterisation of the system dynamics and determining quantities which are difficult or impossible to measure directly, such as velocity profiles or concentration values in inaccessible regions. This supports both the design of the system and the experiment methodology and the interpretation of experimental results.

Mathematical modelling also plays a crucial role in understanding the phenomena that the microfluidic system is designed to study. In the context of drug development, this includes modelling drug pharmacokinetics (i.e. drug transport, distribution and absorption) or the biological mechanisms of treatment response. Experiments in microfluidic systems can be used to estimate key parameter values for use in further studies or simulations of drug dosing or response. Modelling can also be used to

improve mechanistic insight into the mechanisms of drug action or toxicity, which is especially relevant for drugs with more complicated reaction mechanisms [39, 40].

Accurately modelling biological processes within a microfluidic system requires a detailed understanding of the behaviour of the system itself. Thus biological models must build on or incorporate models of the system physics. In this section, we provide a brief overview of the established modelling frameworks that are relevant for our analysis. This includes modelling key physical processes affecting fluid flow and solute transport as well as biological reactions. We also discuss the idea of model reduction, which is a key theme throughout this thesis.

1.3.1 Fluid dynamics

Models of flow in microfluidic systems draw on a variety of principles from fluid dynamics. Stokes equations are typically most appropriate to describe flow in microfluidic channels and chambers, which are characterised by low Reynolds numbers. Features of Stokes flow that result in simpler fluid dynamics, including laminar flow profiles and time reversibility, often make mixing more challenging however [8, 38].

For *in vitro* microfluidic systems, it may be necessary to consider the impact of the cell culture on the flow. Where tissue is seeded on a porous scaffold, Darcy's law or the Brinkmann equations may be used to describe flow in the porous media. Larger cell cultures, such as spheroids or organoids, can similarly be modelled as a porous domain or, more simply, as a solid obstacle with rigid boundary conditions. More complex fluid-structure interaction models, accounting for the elastic deformation of the cell culture under the imposed flow, can also be applied. Finally, for cell suspensions, a multiphase modelling approach is often employed, which accounts for the cell culture explicitly as a separate phase [41, 42].

Numerical solutions using computational fluid dynamics (CFD) are often employed to determine the flow in microfluidic systems. However, these methods are computationally expensive, which prohibits exploring large regions of parameter space to optimise device geometry and operating conditions. Furthermore, the disparity of length scales that feature in many devices hampers the implementation of numerical

methods for the full system. This disparity is however advantageous for employing asymptotic techniques to make analytic progress and derive reduced models for which numerical solutions are less computationally intensive.

1.3.2 hydraulic electric circuit analogy

One such reduction is the hydraulic electric circuit analogy modelling framework, which is widely used to analyse the flow in microfluidic systems, as described in [43]. At its core, this uses the generalised Hagen-Poiseuille law to describe the volumetric flow rate Q through a microfluidic channel in terms of the pressure drop ΔP across it. This takes the form of the equation

$$Q = -\frac{\Delta P}{R_h}, \tag{1.1}$$

where R_h is the hydraulic resistance, which depends on the channel geometry and fluid properties. This equation is analogous to Ohm's law for electric current, from where the name of this framework arises.

This framework is extremely useful for the design and analysis of complex microfluidic circuits consisting of a series of interconnected channels and chambers. Chambers act as sources or sinks of pressure, most frequently due to capillary or hydrostatic effects. Each channel has an associated hydraulic resistance, while conservation laws (analogous to Kirchhoff's laws) can be used to determine flow at junctions. In addition to providing a more intuitive understanding of the complex system, this method results in significant computational savings, since it typically reduces the Navier-Stokes equations to a series of algebraic equations or time-dependent ordinary differential equations.

This reduction exploits features such as a low Reynolds number or small channel aspect ratio that are common to many systems. It is chiefly used to understand the macroscopic quantities of a microfluidic system, which include volume flow rates and average pressures. It can also provide estimates for the fluid velocity or shear stresses within the channels, based on the simple flow profiles within these regions that underpin this reduction. However, additional modelling is needed to determine

the full flow profile in the system, particularly in larger chambers or in devices with more complex geometries. This is required to fully characterise transport processes or the shear stress distribution within a system. Nevertheless, an understanding of the volume flow rate in these regions is often useful and can be used as a basis for further modelling at a higher resolution.

1.3.3 Capillary surfaces and moving contact lines

Many microfluidic systems feature open chambers or channels where the fluid is exposed to the surrounding air. Capillary forces are important in these scenarios, with capillary pressure differences often used to drive flows directly or serving to modify flows driven by gravity or other physical mechanisms [9]. The capillary pressure arises as a result of interfacial tension between two fluids and interactions with the solid surface. This depends on properties of the fluid and solid surface, such as wettability. It is therefore important to understand the configuration and evolution of the free surface interface to characterise the capillary pressure.

The starting point for describing the static interface is the Young equation [44]

$$\gamma_{LV} \cos \alpha = \gamma_{SV} - \gamma_{SL}, \tag{1.2}$$

which gives the static contact angle α formed between the interface and the solid surface at the three-point contact line, where γ_{SL}, γ_{SV} and γ_{LV} represent the interfacial tension between the solid-liquid, solid-vapour, and liquid-vapour phases respectively. The shape of the interface itself is described by the Young-Laplace equation, which relates the curvature of the static interface between the liquid and vapour and the capillary pressure difference across the interface [45]. This is a statement of normal stress balance across the interface, with the prescribed contact angle serving as a boundary condition. Alternatively, the static contact angle can be defined by the minimisation of Helmholtz free energy rather than the balance of forces, while the Young-Laplace equation for the free surface shape can also be expressed in variational form as an energy minimisation problem.

Capillary static problems arise in a variety of natural phenomena and have been extensively studied. Particular examples include capillary rise in a tube, determining the shape of sessile and pendant droplets, and determining the shape of the fluid meniscus in containers of various geometries, which can involve the formation of corner rivulets [46, 47, 48, 49, 50]. Solutions to the general Young-Laplace problem with both capillary and gravitational effects must typically be found using a combination of numerical and asymptotic approaches [47], although exact solutions do exist in a limited number of special cases [51].

The above description pertains to the static configuration of the free surface interface. On sufficiently small length scales where capillary effects dominate, a surface will spontaneously evolve towards the corresponding equilibrium configuration, resulting in phenomena such as capillary rise or droplet spreading.

In practice the picture is significantly more complicated than the above idealised scenario. For instance, real surfaces exhibit heterogeneity (due to surface roughness or chemical heterogeneity) which results in a range of meta-stable contact angle states, $\alpha_R \leq \alpha \leq \alpha_A$, as opposed to a unique static contact angle [52, 53]. This results in the phenomenon of contact angle hysteresis, where the static equilibrium configuration depends on the manner in which it is approached. In particular, equilibrium states reached under advancing (respectively receding) motion correspond to the advancing (respectively receding) contact angles denoted by α_A (respectively α_R).

Furthermore, in situations where the contact line is moving, due to spontaneous relaxation to equilibrium or an externally imposed flow, the contact angle is affected by both hydrodynamic and interfacial forces [54, 55]. This results in a deviation between the value of the dynamic contact angle associated with a moving system and the corresponding static or equilibrium contact angle. The dynamic contact angle depends on both the contact-line velocity and whether the contact-line motion is advancing or receding.

Various physical models have been developed to describe the moving contact-line problem, including molecular kinetic models, which focus on molecular activity along the contact line, and the hydrodynamic model, where the dynamic contact angle

arises due to viscous bending near the contact line. A summary of these models is provided in [56]. We adopt the hydrodynamic modelling framework for our analysis which we briefly summarise.

The moving contact line is incompatible with the traditional no-slip boundary condition for the Navier-Stokes equation, resulting in a non-integrable singularity in the stress at the contact line [57]. Regularising this singularity involves replacing this condition with various slip conditions in the vicinity of the contact line [58]. In suitable flow regimes, where the Reynolds number and capillary number are both small, the governing equations can be analysed using the method of matched asymptotics to establish a contact-line law relating the outer (macroscopic) dynamic contact angle and the inner (microscopic) static contact angle [55, 58, 59]. The macroscopic contact angle results from viscous bending and corresponds to the value observed experimentally, while the microscopic contact angle is the true value on a sufficiently small length scale near the contact line.

1.3.4 Solute transport and reactions

Modelling the transport of solutes in a microfluidic system generally follows a continuum mechanics framework, making use of techniques widely applied for studying transport problems more generally, including larger bioreactor systems as described in [42]. Transport of a generic passive solute, representing drug molecules, nutrients, or waste products, can be described by a reaction-advection-diffusion equation. The advection term requires the details of the underlying flow field, while reaction terms allow the incorporation of biological or chemical reactions.

Many transport problems in microfluidic systems are characterised by large Péclet numbers, where advective transport dominates over diffusion. Reliance on advective transport led to the development of chaotic mixing protocols to overcome limited mixing in low Reynolds number flows, which are based on dynamical systems theory [11, 13]. The large Péclet number can be exploited to simplify the equations and resulting numerical simulations by neglecting diffusive effects and using techniques such as Lagrangian particle tracing to provide information on the concentration field.

The reaction-advection-diffusion framework is applicable to dilute cells in suspension and can be extended to incorporate other transport mechanisms. This includes chemotactic transport, where cells move along concentration gradients, which is especially relevant to the movement of immune cells and immunotherapy treatments [60].

In simpler models where the cell cultures are not modelled explicitly, reactions can be represented by source or sink terms in appropriate regions of the system, or by boundary conditions representing a thin layer of cells. These reaction terms can be coupled to additional equations describing intracellular dynamics or reaction pathways as part of a multi-scale model. More sophisticated multiphase modelling approaches can also be taken to include cell culture explicitly, with associated reaction terms [42].

1.3.5 Compartmental modelling

Continuum-based reaction-advection-diffusion models account for the spatial structure of the system. This is important where the system exhibits significant concentration gradients or spatial heterogeneity. However, continuum models are also complex and computationally intensive to solve and thus simpler modelling frameworks are often preferred in practice, particularly in the context of pharmaceutical modelling where the underlying biological reactions are themselves complex.

Compartmental models are one of the simplest and most widely used modelling frameworks. They are used extensively in biomedical applications, including in epidemiological modelling, chemical reaction systems, immune system dynamics and pharmacokinetic modelling [40, 61, 62]. In the context of pharmacokinetic modelling, compartments represent spatial structure such as drug concentrations in particular regions, while transport between compartments is governed by time-dependent ordinary differential equations.

They can be applied to both *in vitro* and *in vivo* systems, with the former often used to estimate parameters for simulating the latter. A key assumption of the compartmental modelling framework is that compartments are homogeneous and well

mixed. Their appropriateness for microfluidic systems therefore hinges on the validity of this assumption. If this is a reasonable approximation then the corresponding compartmental model can typically be obtained as a reduction of the full continuum equations.

1.3.6 Model reduction

Systematic model reduction is a key theme of our analysis, as we aim to exploit the disparate time and length scales associated with the problems considered to derive reduced models. Examples of such reductions, which we have highlighted in the above discussion, include hydraulic electric circuit analogy models as a reduction of a Stokes flow problem and compartmental models as a reduction of a reaction-advection-diffusion system. A further example is advection-only transport models in high Péclet number regimes.

Model reduction has a number of advantages. Complex models comprised of partial differential equations are computationally intensive, which is a particular issue in the context of parameter estimation or design optimisation problems which require many simulations. In addition, simpler reduced models, which nevertheless retain the key physics of the system, are often easier to understand and interpret. They can therefore offer greater physical insight into the underlying mechanisms or the dependence on the system parameters. Simpler models are also easier to parameterise when fitting to experimental data, while also being more accessible to biologists, experimentalists, and other users without a background in mathematical modelling or access to high-performance computing or proprietary simulation software [42].

1.4 Thesis summary and overview

The aim of this thesis is to develop and analyse models for fluid flow and solute transport, incorporating simple reaction mechanisms to capture biological processes, in a novel microfluidic system designed for pharmaceutical drug development. Starting from a continuum-based description, we perform a suite of asymptotic reductions to

derive a series of reduced models for these processes, which we use to characterise the system under a range of representative operating regimes applicable to preclinical studies.

This modelling work draws on many of the established modelling frameworks outlined in the previous section, which have been used extensively to study a variety of microfluidic systems. However, studies of novel systems can present unique modelling challenges involving the synthesis of multiple physical processes leading to new models.

Our analysis seeks to offer new and valuable insight not only by providing a detailed characterisation of the relevant physical processes within the system but also by anchoring our investigation in the context of its intended use for pharmaceutical drug development. Motivated by partners in pharmaceutical drug development at Roche and *in vitro* systems design at InSphero, our theoretical analysis is underpinned by its practical relevance and serves as a foundation for further and more sophisticated *in silico* modelling within the system.

An overview of our analysis and the structure of this thesis is presented below. Particular aspects that we emphasise include a detailed treatment of the moving contact-line problem, which includes contact angle hysteresis and a non-uniform contact line. These capillary effects are often neglected or highly simplified in models for other similar gravity-driven systems [14]. Additionally, we consider the problem of solute transport in the context of typical experiments and discuss comparisons with compartmental models widely used in industry. Finally, asymptotic model reduction plays a key role throughout our analysis, which is motivated by the advantages and practical relevance of these simplified models for users of the system.

In chapter 2, we outline the geometry of the microfluidic device which motivates our work. This is a gravity-driven microfluidic system consisting of two microfluidic chambers or wells connected by a microfluidic channel. We present the equations governing fluid flow and solute transport within the system. These equations describe the key physical processes and are based on classical fluid dynamics. We also derive a reduced model for the evolution of the fluid free surface and contact line, following

hydrodynamic contact-line theory, and a reduced model for the fluid volume flow rate, which is based on the hydraulic electric circuit analogy. These models underpin our analysis in the remainder of the thesis.

In chapter 3, we examine the problem of a moving contact line in detail by restricting attention to a single microfluidic well. This restriction allows us to explore the contact-line problem in isolation from other components of the system and in greater depth. We investigate how the contact line, meniscus, and capillary pressure vary under a range of flow regimes. Here we make use of the *Surface Evolver* software package [63] to determine the free surface shape in more complex conditions.

In chapter 4, we analyse fluid flow in the system in terms of the volume flow rate using a reduced hydraulic electric circuit analogy model. We study how the gravity-driven flow, resulting from volume differences or tilting, depends on the system operating conditions. While the flow is gravity driven, examining surface tension effects is a key theme of our work here. We quantify these capillary effects to ultimately inform and identify practical steps that can be taken to mitigate the variability introduced by surface tension. This builds on our analysis of the contact-line problem and its impact on the flow via the capillary pressure in the previous chapter.

In chapter 5, we consider the problem of solute transport, combined with simple biological reactions, within the system. We implement a particle-based numerical scheme to solve the appropriate reaction-advection-diffusion equation, which requires details of the velocity field obtained from our analysis of the flow problem. This is motivated by the high Péclet regime which we exploit, in conjunction with periodic flow conditions, to develop a simplified iterative scheme. We use this scheme to analyse mixing problems within the system, which are representative of typical experimental scenarios, aiming to inform experimental design and interpretation of results. A further motivation for our analysis here is to understand concentration heterogeneity within the system, which informs whether a simpler compartmental modelling framework is appropriate.

While our analysis in chapters 2 and 3 concerns a three-dimensional system, in chapters 4 and 5 we restrict our attention to a two-dimensional representation of the

microfluidic system to simplify our analysis and computation of numerical solutions. This representation retains the key features of the system geometry, however, and thus we expect our analysis to still provide relevant qualitative insights into the design and operation of the device and its use in experiments. Extension of our modelling to three dimensions is needed to obtain precise quantitative predictions for the three-dimensional system. We provide a summary of our conclusions and discuss potential future work in chapter 6.

Chapter 2

The twin-well microfluidic system

2.1 Introduction

In this chapter, we introduce the specific microfluidic system which forms the basis of our subsequent work. We begin by giving an overview of the system and the typical problems in drug discovery and development that it can be used to study. We then provide a detailed description of the system geometry and typical operating conditions, highlighting the key physical and biological processes that motivate our modelling work. We present the governing equations for both fluid flow and the transport of a general passive solute in the system, which incorporates solute reactions to capture biological processes. We also non-dimensionalise these equations and summarise the key parameters on which they depend.

Starting from the equations for fluid flow, we present the derivation of two key asymptotic reductions of the full continuum model. Specifically, in §2.8 we obtain the equations for the evolution of the fluid free surface and contact line, which is based on the Cox-Voinov contact-line law [55, 59]. We follow the analysis of [58] and [59], with adaptations for our specific problem to account for the system geometry and hysteresis of the microscopic contact angle. In §2.9 we use lubrication theory to derive a hydraulic electric circuit analogy model governing the relationship between the volume flow rate and pressure difference across the channel. These reductions exploit disparities in the system length scales and the timescales of physical processes.

We analyse a suite of reduced models for fluid flow and solute transport in the

system, under a range of settings and parameter regimes representative of typical operating conditions, in subsequent chapters to reveal key mechanisms and provide practical insights into the use of the system. In chapter 3 we analyse the dynamics of the contact line in a single isolated well, in chapter 4 we analyse the flow in the twin-well system, and in chapter 5 we analyse solute transport and simple solute reactions.

2.2 Overview of the twin-well system

The *Akura*^{TM} *Twin Microplate* is a novel microphysiological system developed by InSphero, a company specialising in the development of 3D *in vitro* models for use in drug discovery, as part of its range of 3D spheroidal microplates and organ-on-a-chip technology. The microplate is manufactured from polystyrene, and a hydrophilic coating is used to prevent cell adhesion to the walls of the device. A single microplate is composed of approximately 200 individual twin-well systems, each of which consists of two identical vertical wells which are connected at their base by a thin horizontal channel [64]. This individual 'twin unit', which we typically refer to as the microfluidic or twin-well system, is the focus of our investigation.

Figure 2.1 illustrates the design of the twin-well system as part of the larger Twin Microplate. Each well consists of a cylindrical culture chamber above which sits a larger fluid reservoir. The cell cultures, which can include up to two 3D spheroidal cell cultures as well as additional individual cells such as immune cells, are located in the culture chamber and are shown in the figure.

The system is designed for investigating 3D tissue interactions as the twin-well structure allows for cross-talk between the two spheroidal cultures. This cross-talk is mediated by solutes, such as proteins and other biomolecules, or by individual cells, all of which can travel across the connecting channel. Indeed, the thin channel geometry is purposely designed to allow the transfer of such solutes (typical diameter $\sim 5\,\text{nm}$ for proteins) and individual cells (typical diameter $\sim 5\,\mu\text{m}$ for immune cells) while preventing the movement of the larger spheroidal cell cultures (typical diameter

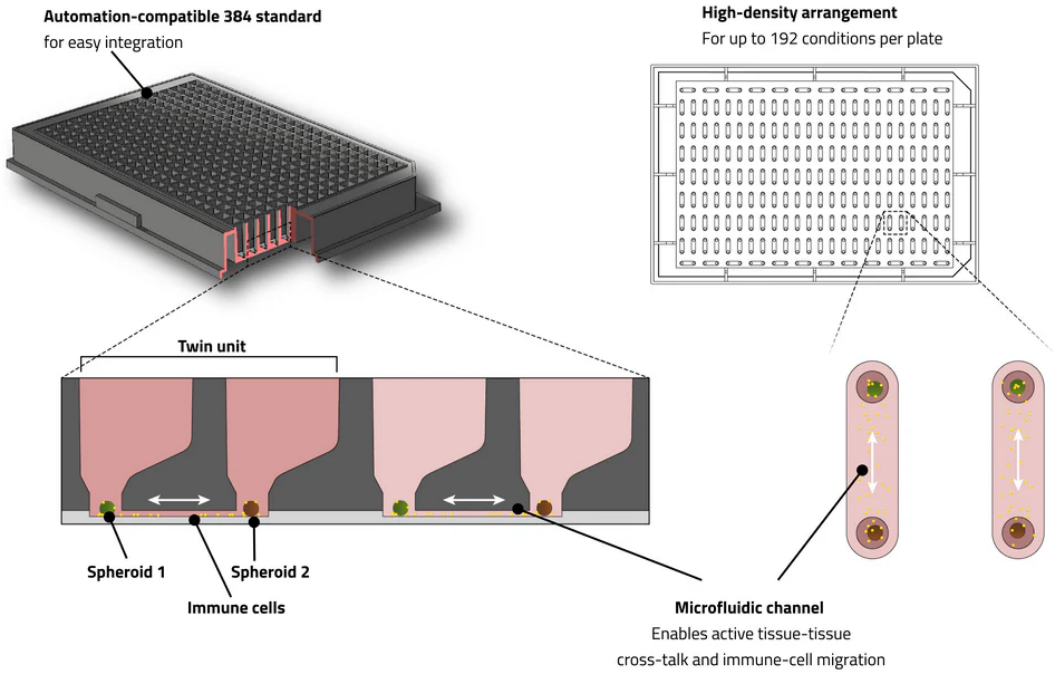

Figure 2.1: The Akura^{TM} Twin Microplate. The two upper diagrams show a side and top-down view of the entire plate, which consists of 192 individual twin-well systems. The two lower inset diagrams show a side and top-down view of the individual twin-well units, showing the location of the spheroidal cell cultures at the base of each well, and the connecting microfluidic channel. Smaller immune cells are also indicated, which are relevant to applications of the system studying immune-mediated toxicity, although these do not feature in our analysis. Image reproduced with permission from InSphero [64].

$\sim 0.4\,\text{mm}$), which can additionally be secured in place in the culture chamber. Cross-channel transport can be enhanced by inducing flow in the culture medium, which is achieved by tilting the system on a rocker.

The novel design of the twin-well system makes it suitable for investigating a variety of problems in the field of drug development, including pharmacokinetic studies, toxicology and safety assessments, and disease modelling. It is especially relevant for studies of drug mechanisms involving interactions between multiple cell types. In our analysis and characterisation of the system, we do not consider a specific biological application and focus instead on the physical problems of fluid flow and solute transport that are common to most use cases, which we illustrate with simple reaction mechanisms where appropriate. Transport problems common to most studies in the

system include controlling the transfer of cells and solutes between the two culture chambers and understanding the typical distribution of solutes in the system.

One motivating example for our work is provided by toxicology and safety assessments of immunotherapy treatments. By placing a tumour spheroid in one well and a healthy organ spheroid in the other, the device can be used to study immune-mediated toxicity where activated immune cells attack healthy tissue. Since this toxicity is mediated by immune cells and immune proteins, which can travel across the channel from the tumour spheroid to the healthy tissue, controlling and understanding the distribution of these cells and solutes is of critical importance.

2.3 System geometry and typical operation

We now describe the system geometry and typical operating conditions in further detail. This includes a discussion of the most relevant physical processes that serve as the foundation for our modelling work.

The twin-well system consists of two vertical wells, which are open at the top to the atmosphere and connected at the base by a thin horizontal channel. Each well is identical and is subdivided into three components. The first component is the fluid reservoir at the top of the well, which has a rectangular cross section of length L_A^* and width W_A^*, and has height H_A^*. The second component is the mid-well region, which connects the reservoir and culture chamber. This connecting region has height H_B^* and a tapering edge, designed to optimise sampling and medium exchange, and approximately forms a trapezoidal prism. The third well component is the cylindrical culture chamber at the well base, which has diameter L_C^* and height H_C^*.

The horizontal channel can be subdivided into two regions. The main connecting channel region has a rectangular cross section with width W_D^*, height H_D^*, and length L_D^*. The channel also includes the small extended regions at each end of the main connecting channel, which surround the opening at the circular base of each culture chamber. The reservoir separation distance L_{sep}^* corresponds to the distance between

the centre line of each reservoir. The system geometry is shown in figure 2.2 and representative values for these geometrical parameters are given in §2.6.

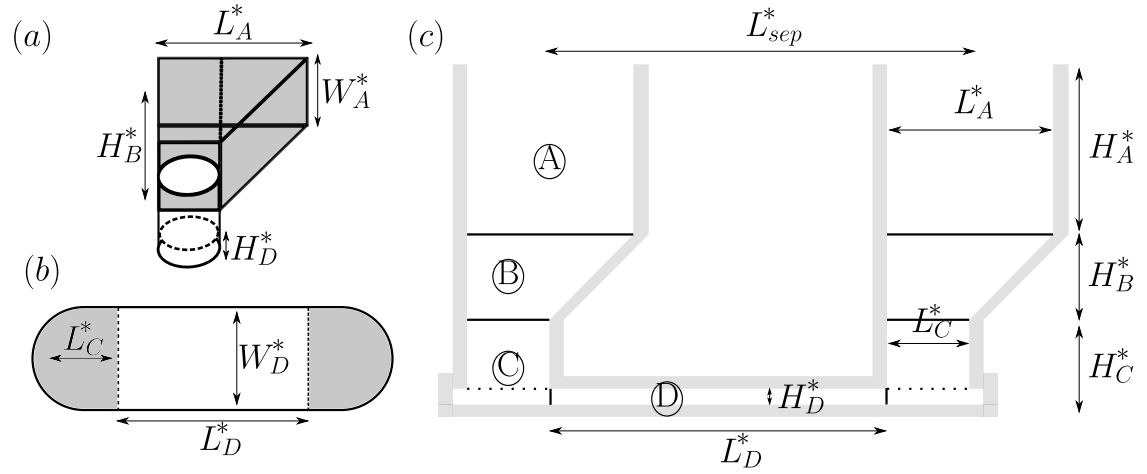

Figure 2.2: Diagram showing views of the twin-well microfluidic system with relevant lengths indicated as described in the main text. (a) View of the mid and lower well regions consisting of the mid-well connecting region and the culture chamber, (b) top-down view of the horizontal channel showing the main connecting channel (unshaded) and the extended channel regions (shaded). (c) Profile view of the full system with components indicated by (A) fluid reservoir, (B) mid-well connecting region, (C) culture chamber, and (D) thin horizontal connecting channel.

At times throughout our analysis, we consider systems with slight modifications to the core twin-well geometry. These modifications include a reservoir of circular rather than rectangular cross-section, a uniform well cross-section without a tapering connecting region, and restricting attention to a two-dimensional representation of the system. These modifications are typically done for computational efficiency while retaining the essence of the twin-well system.

In a typical experimental setup, a 3D spheroidal cell culture is secured at the base of each culture chamber and the device is partially filled with culture medium. We first describe the relevant physics of the fluid flow and solute transport in turn, before discussing biological reactions.

Flow in the system is passively driven and induced by establishing a pressure gradient across the horizontal channel. This pressure gradient and the resulting flow are impacted by both gravitational and capillary effects due to the small system

length scales. A hydrostatic pressure difference across the channel can be established by manually varying the volume of fluid in each well or, more typically, tilting the device in an oscillatory manner to enable continuous flow. This tilting motion also induces flow in each well independently, although in general this flow is less significant than the flow driven by the pressure gradient across the channel.

Capillary effects also contribute to the pressure difference across the channel. Surface tension results in the fluid free surface in each well forming a curved meniscus with an associated capillary pressure jump between the fluid at the surface and the air above. This pressure jump depends on the contact angle(s) formed between the fluid surface and the solid well wall along the contact line, which can be different in each well. The resulting difference between the capillary pressures at each surface gives rise to a pressure difference across the channel.

Furthermore, this capillary pressure difference can vary in time due to the movement of the contact line with the flow. We refer back to §1.3 for a more comprehensive discussion of the relevant contact-line physics and summarise the key points here. We recall that in a moving contact-line problem, the macroscopic or observed contact angle varies with the velocity of the contact line due to hydrodynamic effects [55]. The macroscopic contact angle also depends on the value of the microscopic contact angle, which itself depends on the properties of the fluid and solid surface. Moreover, the microscopic contact angle can also vary with the contact-line velocity and exhibit contact angle hysteresis, where a range of metastable microscopic contact angle states are possible when the contact line is stationary. Typically, the microscopic contact angle takes a maximal advancing value or minimal receding value at points where the contact line advances or recedes, and lies between these two extremal values at points where the contact line is stationary [65].

During an experiment, the spheroidal cell cultures must always remain immersed in the culture medium. This places restrictions on the operation of the device and the tilting regimes which can be considered. We require that the device is operated such that the culture chambers, the thin horizontal channel, and the mid-well connecting region (i.e. components B–D of each well) remain filled with fluid at all times and

that no fluid overspills the reservoir. Under these conditions, the meniscus in each well is located in the fluid reservoir.

The culture medium itself contains a wide variety of dissolved solutes ranging from small molecules, such as nutrients or small molecule drugs, to larger biomolecules, which can include proteins or biotherapeutic drugs. Single cells, such as immune cells, may also be present and suspended in the culture medium, though we restrict attention to passive solutes in our modelling. These solutes may be present in the culture medium from the outset of the experiment or can be added later manually via the well reservoirs. Solutes are also produced and degraded over the course of an experiment by biological reactions that occur either at the spheroid surfaces or in the bulk fluid due to interactions between solute species.

The two key physical processes which affect the transport of solutes within the culture medium are advection and diffusion. In general, solute diffusivity depends on solute shape and size, which can vary over several orders of magnitude for different solute species. However, in general solute diffusivity is small and so advective transport dominates over diffusion [66]. Thus, characterising the fluid flow is a prerequisite for understanding solute transport.

The system can be used to study a broad range of biological reactions. These often have complex mechanisms of action and involve interactions between multiple solute species and cell types. However, we restrict the scope of our analysis to a single solute species which can undergo just two reaction processes of solute production and solute degradation, with these reactions further restricted to the spheroidal cell culture. This enables us to focus on the fundamental properties of transport and mixing within the system and explore problems common to most typical applications. Furthermore, these simple reaction processes serve as a useful foundational model for more complex processes that the system is used to study, since they are the constituents from which more complex reaction mechanisms are constructed.

Finally, we note that additional physical mechanisms may affect flow and transport in the system in practice. These include the evaporation of culture medium at the free surface, the absorption of solutes at the device walls or the free surface, changes to

fluid rheology due to the presence of cells and solutes, surfactant gradients which alter the surface tension, and further molecular effects on the contact angles [54]. Typically, these effects are expected to be small and we do not include them in developing our model of the system. We return to some of these mechanisms in chapter 6 where we discuss potential extensions of our model.

2.4 Governing equations for fluid flow

We present a continuum model for fluid flow in the twin-well system, which is formulated for a system with general well geometry. The system setup is illustrated in figure 2.3 which highlights many key quantities and variables. We model the spheroidal cell cultures as two rigid and impermeable spheres that are fixed in place in each culture chamber. Beginning with this simple framework enables us to focus our modelling on other aspects of the flow, namely the free surface dynamics, while providing a suitable foundation for future extensions.

We introduce Cartesian coordinates $\mathbf{x}^* = (x^*, y^*, z^*)$ with associated basis vectors $\{\mathbf{e}_x, \mathbf{e}_y, \mathbf{e}_z\}$, where asterisks are used to denote dimensional variables. The base of the system lies on the plane $z^* = 0$ and the coordinate axes are aligned with the sides of the rectangular microfluidic channel (as indicated in figure 2.3) with the channel midpoint taken as the coordinate origin. This coordinate system is fixed in the frame of the device and we work in this rotating device frame as the system is tilted.

The device is assumed to tilt about the y-axis and the angle of elevation of the negative x-axis to the horizontal is $\theta(t^*)$ as indicated in figure 2.3, where t^* denotes time. The angular velocity of the device is therefore $\mathbf{\Omega}^* = \Omega^*(t^*)\mathbf{e}_y$, where $\Omega^* = \dot{\theta}$ and a dot denotes differentiation with respect to time. Gravity acts vertically downwards, which in our rotating coordinate system corresponds to the direction $\sin\theta\,\mathbf{e}_x - \cos\theta\,\mathbf{e}_z$, and the magnitude of gravitational acceleration is g^*.

The fluid domain is denoted by $\mathcal{D}$ with boundary $\partial\mathcal{D}$. The cell cultures occupy regions $\mathcal{D}_{C_i}$ where the subscripts $i = 1, 2$ are used to index the left and right wells, respectively. The portion of the fluid boundary in contact with the solid walls of the

device is denoted by $\partial\mathcal{D}_S$, the portions in contact with each cell culture by $\partial\mathcal{D}_{C_i}$, and the portions forming the free surface boundaries between the culture medium and the air above by $\partial\mathcal{D}_{F_i}$. The outward-pointing unit normals at the solid wall, cell culture, and free surface boundaries are denoted by $\mathbf{n}_S$, $\mathbf{n}_{C_i}$, and $\mathbf{n}_{F_i}$, respectively.

The location of the free surface $\partial\mathcal{D}_{F_i}$ in each well is denoted by $z^* = h_i^*(x^*, y^*, t^*)$ for $(x^*, y^*) \in \mathcal{B}_i$, which denotes the projection of the interior of the well reservoir onto the x-y plane. We assume that the free surface can be parameterised in this way at all times. This assumption captures the aforementioned requirement that the free surface remains in the reservoir region, with the lower regions of the device immersed in fluid.

Finally, we denote the contact line in the ith well by $\Gamma_i = \partial\mathcal{D}_{F_i} \cap \partial\mathcal{D}_S$, which consists of the points on the free surface in contact with the reservoir wall. We parameterise the contact line by the arc length s^* along the reservoir perimeter so that $\Gamma_i = \{(x_w^*(s^*), y_w^*(s^*), H^*(s^*, t^*)\}$, where $(x_w^*, y_w^*) \in \partial\mathcal{B}_i$ are the x and y coordinates of the reservoir perimeter and H^* denotes the height of contact line above the base of the system. We note that $H^*(s^*, t^*) = h^*(x_w^*(s^*), y_w^*(s^*), t^*)$ and introduce this notation to provide a distinction between the meniscus height h^* and contact-line height H^* for later convenience.

The culture medium is assumed to be an incompressible Newtonian fluid with constant density ρ^* and dynamic viscosity μ^*. The fluid therefore satisfies the incompressible Navier-Stokes equations in a rotating frame, *viz.*

$$\begin{aligned}\rho^*\left(\frac{\partial \mathbf{u}^*}{\partial t^*} + \mathbf{u}^* \cdot \nabla^* \mathbf{u}^*\right) = &- \nabla^* P^* + \rho^* g^* (\sin\theta\ \mathbf{e}_x - \cos\theta\ \mathbf{e}_z) + \mu^* \nabla^{*2} \mathbf{u}^* \\ &- \rho^* (2\boldsymbol{\Omega}^* \times \mathbf{u}^* + \boldsymbol{\Omega}^* \times \boldsymbol{\Omega}^* \times \mathbf{x}^* + \dot{\boldsymbol{\Omega}}^* \times \mathbf{x}^*),\end{aligned} \tag{2.1}$$

and

$$\nabla^* \cdot \mathbf{u}^* = 0, \tag{2.2}$$

where $\mathbf{u}^*(\mathbf{x}^*, t^*) = (u^*, v^*, w^*)$ is the fluid velocity in the device frame, the operator $\nabla^* = (\partial/\partial x^*, \partial/\partial y^*, \partial/\partial z^*)$, and the pressure $P^*(\mathbf{x}^*, t^*)$ is defined relative to atmospheric pressure.

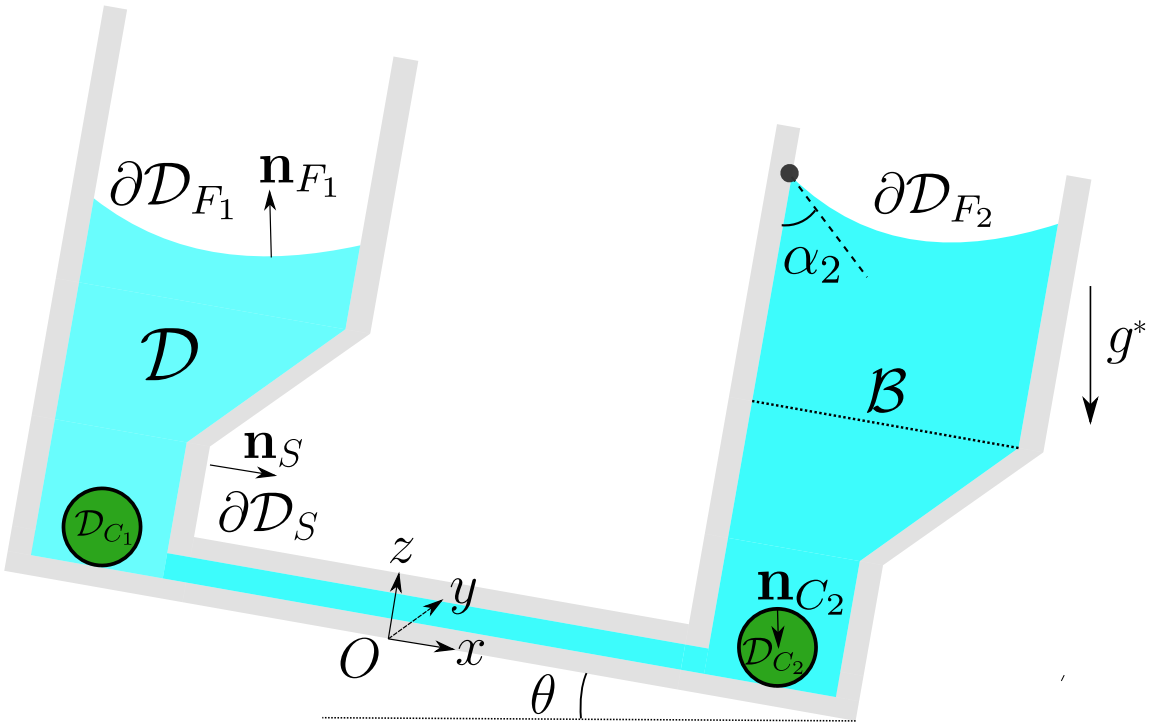

Figure 2.3: Schematic profile view of the system setup showing the fluid domain $\mathcal{D}$ and the boundaries corresponding to the solid device wall $\partial\mathcal{D}_S$, the free surfaces $\mathcal{D}_{F_i}$, and the cell cultures $\mathcal{D}_{C_i}$. The direction of the corresponding surface normal at each boundary is also indicated. The directions of the rotating coordinate axes are shown, with the origin located at the midpoint of the main channel. The elevation angle θ and the (microscopic) contact angle at a point on the contact line α are also shown, while the direction of gravity is indicated as g^*.

At the solid device walls and the cell culture boundaries, which are assumed to be rigid and impermeable, we impose no-flux and no-slip conditions

$$\mathbf{u}^* \cdot \mathbf{n} = 0, \tag{2.3}$$

$$\mathbf{u}^* \cdot \mathbf{t} = 0, \tag{2.4}$$

on $\partial\mathcal{D}_S$ and $\partial\mathcal{D}_{C_i}$, where $\mathbf{n}$ denotes the appropriate unit normal ($\mathbf{n}_S$ or $\mathbf{n}_{C_i}$) and $\mathbf{t}$ any unit tangent to the relevant surface.

Since the no-slip condition (2.4) is incompatible with a moving contact line, we follow the standard hydrodynamic modelling framework and replace it with the Navier-slip condition in the vicinity of the contact line [57, 67]. Thus on the reservoir walls

$\partial\mathcal{D}_S$ we replace (2.4) with

$$\mathbf{u}^* \cdot \mathbf{t} = -2\Lambda^*(\mathbf{t} \cdot \dot{\mathbf{\Gamma}}^* \cdot \mathbf{n}), \tag{2.5}$$

where Λ^* is the slip length, and the rate of strain tensor is defined by

$$\dot{\mathbf{\Gamma}}^* = \frac{1}{2}\Big(\nabla^*\mathbf{u}^* + (\nabla^*\mathbf{u}^*)^\top\Big). \tag{2.6}$$

We assume that the air is inviscid and exerts only atmospheric pressure in the normal direction on the free surface in each well, and that the jump in traction is due to a constant surface tension γ. The kinematic and dynamic boundary conditions on $\partial\mathcal{D}_{F_i}$ are therefore

$$\frac{\partial h_i^*}{\partial t^*} + \mathbf{u}^* \cdot \nabla^* h_i^* = w^*, \tag{2.7}$$

and

$$\boldsymbol{\sigma}^* \cdot \mathbf{n}_{F_i} = -\gamma^* \kappa_i^* \mathbf{n}_{F_i}, \tag{2.8}$$

where $\kappa_i^*(x^*, y^*, t^*) = \nabla^* \cdot \mathbf{n}_{F_i}$ is the mean curvature of the free surface and the Cauchy stress tensor for the fluid is defined by

$$\boldsymbol{\sigma}^* = -P^*\mathbf{I} + 2\mu^*\dot{\mathbf{\Gamma}}^*. \tag{2.9}$$

We adopt the sign convention that a positive curvature is associated with a downwardly concave meniscus (i.e. the menisci in figure 2.3 have negative curvature).

At each contact line Γ_i, we impose the contact angle boundary condition

$$\mathbf{n}_S \cdot \mathbf{n}_{F_i} = -\cos\alpha_i \tag{2.10}$$

where $\alpha_i(s^*, t^*)$ is the microscopic contact angle in the ith well. This is the angle between the free surface and the reservoir wall below it, as indicated in figure 2.3.

We incorporate contact angle hysteresis by prescribing a simple hysteresis law where the microscopic contact angle depends only on the sign of the (normal) contact-line velocity along the solid wall, which is defined by

$$v_{n_i}^*(s^*, t^*) = \frac{\frac{\partial H_i^*}{\partial t^*}}{\sqrt{1 + \left(\frac{\partial H_i^*}{\partial s^*}\right)^2}}. \tag{2.11}$$

Following [68], the hysteresis law is formulated as

$$\begin{aligned} \alpha_i(s^*, t^*) &= \alpha_A \quad \text{if} \quad v^*_{n_i}(s^*, t^*) > 0, \\ \alpha_i(s^*, t^*) &= \alpha_R \quad \text{if} \quad v^*_{n_i}(s^*, t^*) < 0, \\ \alpha_R \leq \alpha_i(s^*, t^*) &\leq \alpha_A \quad \text{if} \quad v^*_{n_i}(s^*, t^*) = 0, \end{aligned} \tag{2.12}$$

where $\alpha_R \leq \alpha_A$ denote the constant microscopic receding and advancing contact angles, respectively.

In other words, at a point on the contact line which is advancing (respectively receding) as defined by the sign of v_{n_i}, the microscopic contact angle takes the value of the advancing contact angle α_A (respectively the receding contact angle α_R). Where the contact line is stationary, the microscopic contact angle lies between these two extreme values. We emphasise that a point along the contact line can also be stationary when the contact angle takes the advancing or receding value. We also note that this hysteresis law is expressed in terms of the microscopic contact angle; an expression for the apparent or macroscopic contact angle, which may vary due to hydrodynamic effects, is to be found as part of the solution.

Initially, we take the fluid to be at rest with

$$\mathbf{u}^* = \mathbf{0} \quad \text{at } t^* = 0, \tag{2.13}$$

and prescribe $h_i^*(x^*, y^*, 0)$, which gives the initial shape of the free surface in each reservoir. The free surface shape also specifies the initial contact angle configuration for which we require $\alpha_i(s^*, 0) \in [\alpha_R, \alpha_A]$. The form of the elevation angle $\theta(t^*)$ must also be specified to close the problem.

In summary, the dependent variables of the continuum model are the fluid velocity $\mathbf{u}^*$, the pressure P^* and the free surface height h_i^*, which sets the fluid domain and from which both the contact-line velocity and microscopic contact angles can be determined. The parameters on which the model depends are discussed further in §2.6, where we provide a table of typical values.

2.4.1 The elevation angle

In an experiment, a rocker system allows custom variations in the elevation angle to be prescribed. In our analysis, we consider both fixed elevation angles and oscillatory

elevation angles. These include both sinusoidal oscillations of the form

$$\theta(t^*) = \theta_A \sin(2\pi f^* t^*), \tag{2.14}$$

where θ_A is the oscillation amplitude and f^* the oscillation frequency, and piecewise linear oscillations which consist of linear transitions between the horizontal and the maximum/minimum elevation angles $\pm\theta_A$ in transition time T^*_{tr}, with pauses of length T^*_p at $\theta = \pm\theta_A$. These piecewise linear oscillations better reflect typical experimental operating conditions.

2.5 Governing equations for solute transport and reactions

We present a continuum model for the transport of a passive solute due to advection and diffusion, with solute reactions able to occur at the spheroidal cell cultures and in the bulk solute. We consider the same setup and coordinate system as previously outlined for the fluid flow problem in §2.4.

The solute concentration $c^*(\mathbf{x}^*, t^*)$ is governed by the reaction-advection-diffusion equation

$$\frac{\partial c^*}{\partial t^*} + \mathbf{u}^* \cdot \nabla^* c^* = D^* \nabla^{*2} c^* + R^*, \tag{2.15}$$

in the fluid domain $\mathcal{D}$, where $\mathbf{u}^*(\mathbf{x}^*, t^*)$ is the velocity field determined from the fluid-flow problem, D^* is the solute diffusion coefficient which is assumed to be constant, and $R^*(c^*, \mathbf{x}^*, t^*)$ represents general solute reactions occurring in the bulk fluid.

At the impermeable device walls and across the free surface, we impose no diffusive solute flux

$$\mathbf{n} \cdot \nabla^* c^* = 0, \tag{2.16}$$

on $\mathcal{D}_S$ and $\mathcal{D}_{F_i}$, where $\mathbf{n}$ is the appropriate outward pointing unit normal. At the spheroidal cell culture boundaries, we impose the condition

$$D^* \mathbf{n}_{C_i} \cdot \nabla^* c^* = J_i^*(c^*, \mathbf{x}^*, t^*), \tag{2.17}$$

on $\partial\mathcal{D}_{C_i}$, where $\mathbf{n}_{C_i}$ is the unit normal pointing out of the fluid on these boundaries and the function J_i^* is a flux term capturing solute reactions associated with each cell culture.

We prescribe the initial solute concentration profile $c^*(\mathbf{x}^*, 0)$. To fully specify the problem, we must prescribe the explicit form of the bulk and surface reaction terms R^* and J_i^*, which we discuss below. The velocity field and time-varying fluid domain must also be specified explicitly and are determined from the solution of the fluid flow problem.

2.5.1 Solute reaction terms

The above formulation of the transport problem is sufficiently general to allow a wide range of processes to be modelled in principle. The bulk reaction and surface flux terms can either be prescribed explicitly or coupled to equations modelling intracellular transport or reaction processes. We refer back to §1.3 for further discussion of reaction mechanisms and how they can be incorporated within the continuum modelling framework.

In this thesis, we restrict attention to simple production and degradation reactions, which we model using zeroth and first order kinetics, respectively. This is because our focus is on studying general transport phenomena within the system rather than a specific biological problem. These reactions also serve as representations for more complex reaction mechanisms, which are straightforward to incorporate into our modelling framework. Further details are provided in chapter 5 where we consider the solute transport and reaction problem. We also introduce an additional simplification by representing the effects of the cell culture via appropriate solute source and sink terms rather than modelling the spheroid explicitly.

2.6 Physical and geometrical parameter values

In this section, we summarise the geometrical and physical parameters associated with the twin-well system and the fluid and transport problems. The geometrical

parameters for the twin-well system, which are as indicated previously in figure 2.2, are shown in table 2.1 along with their values taken from the dimensions of the Akura Twin Microplate [64]. Other physical parameters are shown in table 2.2 along with their typical values.

Symbol	Definition	Typical values	Units
L_A^*	Reservoir length	3.5	mm
W_A^*	Reservoir width	3.5	mm
H_A^*	Reservoir height	10	mm
W_B^*	Connecting component width	3.5	mm
H_B^*	Connecting component height	1	mm
L_C^*	Culture chamber diameter	1	mm
H_C^*	Culture chamber height	1	mm
L_D^*	Channel length	3.5	mm
W_D^*	Channel width	1.6	mm
H_D^*	Channel height	0.1	mm
L_{sep}^*	Reservoir separation	4.5	mm

Table 2.1: Geometrical parameter descriptions and values for the Akura Twin Microplate.

Symbol	Definition	Typical values	Units
ρ^*	Fluid density (water)	1×10^3	kg m^{-3}
μ^*	Fluid viscosity (water)	1×10^{-3}	kg m^{-1} s^{-1}
γ^*	Surface tension coefficient (water/air)	7.2×10^{-2}	kg s^{-2}
g^*	Gravitational acceleration	9.81	m s^{-2}
Λ^*	Slip length	~ 1	nm
α_R	Microscopic receding contact angle	15	deg
α_A	Microscopic advancing contact angle	50	deg
θ_A	Elevation angle amplitude	0 – 15	deg
f^*	Elevation angle frequency	0.01 – 1	s^{-1}
T_{tr}^*	Elevation angle transition time	10 – 100	s
T_p^*	Elevation angle pause time	0 – 100	s
D^*	Solute diffusion coefficient	10^{-12} – 10^{-9}	m^2 s^{-1}

Table 2.2: Physical parameters associated with the fluid and transport problem, with typical values or ranges for these parameters shown.

The culture medium is modelled as a Newtonian fluid with the same properties as water, which is a common assumption in modelling bioreactor and microfluidic systems and is sufficient for our characterisation of flow in the system. We note in

reality the properties of the culture medium can differ from those of water due to the solute content, but this is typically a good approximation [69].

The typical values for the advancing and receding contact angles are estimated using the sessile drop method [70] on a tilted substrate of the same material as the device itself, with data provided by our collaborators at InSphero. We note that contact angle measurements are prone to error, while the values of the contact angles themselves are sensitive to the precise constitution of the culture medium and the presence of solutes and surfactants. In our analysis, we therefore consider a range of values for the contact angles based on these measured values.

Values for the slip length vary across the literature and in numerical studies it is often used as a fitting parameter when comparing theoretical predictions with experimental data [56]. It is normally regarded to be on the scale of nanometres, and we adopt 1 nm as a representative value [71]. We anticipate that for our typical flow rates, the slip length is sufficiently small that results will be independent of its precise value.

Typical experimental operating procedure for the device consists of slow, small amplitude oscillations in the elevation angle, since more forceful shaking is detrimental to the cell culture. Representative parameter values for these oscillations are shown, though we consider a wider range of oscillation regimes in our analysis.

For the transport problem, the diffusivity of relevant solutes varies over several orders of magnitude from $\sim 10^{-12}$ m^2/s for larger proteins up to $\sim 10^{-9}$ m^2/s for small molecules such as nutrients or simple drug compounds [72]. While this range is broad, the diffusivity of all solutes is generally small, which results in advective transport dominating. Values for specific molecules, which also depend on the properties of the culture medium, can be estimated experimentally or theoretically using the Stokes-Einstein relation [73].

2.7 Scaling and non-dimensionalisation

In this section, we define the representative length, time, and velocity scales associated with the fluid flow and transport problems, which we use to non-dimensionalise the governing equations. We also summarise and discuss the key dimensionless parameters on which these equations depend.

We use the reservoir half-width $L_0^* = L_A^*/2$ as the characteristic length scale for the system and the corresponding capillary pressure scale $P_0^* = \gamma^*/L_0^*$ for the pressure. We set the velocity scale to be $U_0^* = (\rho^* g^* W_D^* {H_D^*}^3)/(12\mu^* L_D^* L_0^*)$, which is the characteristic velocity scale in the reservoir region for a flow driven by hydrostatic pressure differences across the channel; this choice is motivated by the fact that we consider gravity driven flows and anticipates our use of lubrication theory across the channel in deriving the reduced model for the volume flow rate (see §2.9). The characteristic time scale is chosen to be the advective timescale $T_0^* = L_0^*/U_0^*$. Finally, for the transport problem we write C_0^* for the scale of the typical solute concentration, which depends on solute reaction processes.

We introduce the following dimensionless variables

$$\mathbf{x}^* = L_0^*\mathbf{x}, \quad t^* = T_0^* t, \quad h_i^* = L_0^* h_i, \quad \mathbf{u}^* = U_0^*\mathbf{u}, \quad P^* = P_0^* P, \quad c^* = C_0^* c. \tag{2.18}$$

2.7.1 Dimensionless equations for fluid flow

For the fluid flow problem, the dimensionless governing equations are written as follows. The incompressible Navier-Stokes equations are given by

$$\begin{aligned}\mathrm{CaRe}\left(\frac{\partial \mathbf{u}}{\partial t} + \mathbf{u}\cdot\nabla\mathbf{u}\right) =& -\nabla P + \mathrm{Bo}(\sin\theta\ \mathbf{e}_x - \cos\theta\ \mathbf{e}_z) + \mathrm{Ca}\nabla^2\mathbf{u} \\ & - \mathrm{CaRe}(2\boldsymbol{\Omega}\times\mathbf{u} + \boldsymbol{\Omega}\times\boldsymbol{\Omega}\times\mathbf{x} + \dot{\boldsymbol{\Omega}}\times\mathbf{x}),\end{aligned} \tag{2.19}$$

and

$$\nabla\cdot\mathbf{u} = 0, \tag{2.20}$$

where $\nabla = (\partial/\partial x, \partial/\partial y, \partial/\partial z)$ is a dimensionless operator, $\boldsymbol{\Omega} = \boldsymbol{\Omega}^* T_0^*$ is the dimensionless angular velocity, and the Reynolds, Bond, and capillary numbers are

respectively defined by

$$\mathrm{Re} = \frac{\rho^* U_0^* L_0^*}{\mu^*}, \quad \mathrm{Bo} = \frac{\rho^* g^* L_0^{*2}}{\gamma^*}, \quad \mathrm{Ca} = \frac{\mu^* U_0^*}{\gamma^*}.$$

The boundary conditions at the solid device walls and cell culture boundaries are

$$\mathbf{u} \cdot \mathbf{n} = 0, \tag{2.21}$$

$$\mathbf{u} \cdot \mathbf{t} = 0, \tag{2.22}$$

for outward pointing unit normal $\mathbf{n}$ and any unit tangent $\mathbf{t}$ to the relevant surface. The no-slip condition (2.22) is replaced with the Navier-slip condition

$$\mathbf{u} \cdot \mathbf{t} = -2\lambda(\mathbf{t} \cdot \dot{\mathbf{\Gamma}} \cdot \mathbf{n}), \tag{2.23}$$

in the reservoir region, where $\lambda = \Lambda^*/L_0^*$ is the dimensionless slip length and the dimensionless strain-rate tensor is

$$\dot{\mathbf{\Gamma}} = \frac{1}{2}\Big(\nabla\mathbf{u} + (\nabla\mathbf{u})^\top\Big). \tag{2.24}$$

At the free surface, the kinematic and dynamic boundary conditions are

$$\frac{\partial h_i}{\partial t} + \mathbf{u} \cdot \nabla h_i = w, \tag{2.25}$$

and

$$-\boldsymbol{\sigma} \cdot \mathbf{n}_{F_i} = \kappa_i \mathbf{n}_{F_i}, \tag{2.26}$$

where the dimensionless mean curvature is $\kappa_i = \nabla \cdot \mathbf{n}_{F_i}$ and the dimensionless Cauchy stress tensor is

$$\boldsymbol{\sigma} = -P\mathbf{I} + 2\mathrm{Ca}\dot{\mathbf{\Gamma}}. \tag{2.27}$$

On the contact line, the contact angle boundary condition is unchanged with

$$\mathbf{n}_S \cdot \mathbf{n}_{F_i} = -\cos\alpha_i, \tag{2.28}$$

while the contact-line hysteresis law is

$$\begin{aligned} \alpha_i(s,t) &= \alpha_A \quad \text{if} \quad v_{n_i}(s,t) > 0, \\ \alpha_i(s,t) &= \alpha_R \quad \text{if} \quad v_{n_i}(s,t) < 0, \\ \alpha_R \le \alpha_i(s,t) &\le \alpha_A \quad \text{if} \quad v_{n_i}(s,t) = 0, \end{aligned} \tag{2.29}$$

for dimensionless contact-line velocity

$$v_{n_i}(s,t) = \frac{\frac{\partial H_i}{\partial t}}{\sqrt{1+\left(\frac{\partial H_i}{\partial s}\right)^2}}. \tag{2.30}$$

The dependent variables are the fluid velocity $\mathbf{u}$, the pressure p, and the free surface shape h_i. Initially the fluid is assumed to be at rest with the initial free surface shape $h_i(x,y,0)$ prescribed in each well. The form of the elevation angle $\theta(t)$ must also be specified; the dimensionless form of the elevation angle described by (2.14) is $\theta(t) = \sin(\omega t)$, where $\omega = 2\pi f^* T_0^*$ is the dimensionless angular frequency.

2.7.2 Dimensionless transport equations

The dimensionless reaction advection diffusion equation for solute transport is

$$\frac{\partial c}{\partial t} + \mathbf{u}\cdot\nabla c = \mathrm{Pe}^{-1}\nabla^2 c + R, \tag{2.31}$$

where $\mathbf{u}$ is the dimensionless velocity field, $\mathrm{Pe} = T_0^*/(L_0^{*2}D^*)$ is the Péclet number, and $R = R^* T_0^*/C_0^*$ is the dimensionless reaction term.

The no-flux boundary conditions

$$\mathbf{n}\cdot\nabla c = 0 \tag{2.32}$$

apply on the device walls and free surface, where $\mathbf{n}$ is the appropriate outward-pointing unit normal on these boundaries. The flux condition at the spheroidal cell culture boundary is

$$\mathrm{Pe}^{-1}\mathbf{n}_{C_i}\cdot\nabla c = J_i(c,\mathbf{x},t), \tag{2.33}$$

where $\mathbf{n}_{C_i}$ is the outward pointing unit normal and $J_i = T_0^* J_i^*/(L_0^* C_0^*)$ is the dimensionless solute flux.

We prescribe the initial solute concentration profile $c(\mathbf{x},0)$ and the form of the reaction terms R and J_i. We note that while we typically work on the advective timescales T_0^*, further timescales are often associated with the transport problem. These include the diffusive timescale $T_D^* = L_0^{*2}/D^*$ and timescales associated with solute reaction rates, which will be relevant in our subsequent analysis.

2.7.3 Dimensionless parameters

We now briefly discuss the key dimensionless parameters introduced in our non-dimensionalisation. In addition to those previously introduced, we define the channel aspect ratio $\epsilon = H_D^*/L_D^*$, the dimensionless reservoir separation distance $\ell = L_{sep}^*/L_0^*$, and the dimensionless channel length, width, and height denoted by $l_c = L_D^*/L_0^*$, $w_c = W_D^*/L_0^*$, and $h_c = H_D^*/L_0^*$, respectively. The channel aspect ratio is typically small, as the channel is long and thin, while the dimensionless reservoir separation distance and channel length are both of order unity. We also define the Strouhal number by $\mathrm{St} = \theta_A \omega$.

For the fluid flow problem, the Reynolds number gives the ratio of inertial to viscous stresses. The Bond number is the ratio of gravitational to capillary forces, while the capillary number gives the ratio of viscous to capillary stresses, both of which are relevant for quantifying surface tension effects. The Strouhal number gives the ratio of the angular velocity to the chosen velocity scale, and thus quantifies the importance of the oscillatory motion. Meanwhile, the Péclet number gives the ratio of the diffusive and advective timescales for the solute transport problem.

Expressions and typical values for the dimensionless parameters are summarised in table 2.3. These representative values motivate the parameter regimes explored in our subsequent work and we exploit the size of various parameters in our asymptotic analysis.

In particular, our derivation of the leading-order equations for the meniscus shape and the Cox-Voinov contact-line law relating the macroscopic and microscopic contact angles relies on the assumption that the capillary number, slip length, and Reynolds number are small. Furthermore, to derive the reduced hydraulic electric circuit analogy for the volume flow rate in the channel in §2.9, we additionally exploit the small channel aspect ratio and make use of lubrication theory. In chapter 5, we continue to exploit the small Reynolds number to neglect inertial effects, so that the leading-order flow profile in the wells is governed by Stokes equations. We note that the Strouhal number is typically at most order unity, which allows inertial rotational effects to be

Symbol	Definition	Expression	Typical values
ϵ	Channel aspect ratio	H_D^*/L_D^*	0.03
ℓ	Dimensionless reservoir separation	L_{sep}^*/L_0^*	2.57
l_c	Dimensionless channel length	L_D^*/L_0^*	2.0
w_c	Dimensionless channel width	W_D^*/L_0^*	0.91
h_c	Dimensionless channel height	H_D/L_0^*	0.06
Re	Reynolds number	$\rho^* U_0^* L_0^*/\mu^*$	0.37
Bo	Bond number	$\rho^* g^* L_0^{*2}/\gamma^*$	0.42
Ca	Capillary number	$\mu^* U_0^*/\gamma^*$	3×10^{-6}
ω	Angular frequency	$2\pi f^* T_0^*$	0.01–20
St	Strouhal number	$\theta_A \omega$	0.001–5
λ	Slip length	Λ^*/L_0^*	$\times 10^{-7}$
τ	Relaxation parameter	$\mathrm{Ca}\log(1/\lambda)$	$\sim 10^{-5}$
Pe	Péclet number	$L_0^{*2}/(T_0^* D^*)$	$5 \times 10^1 - 5 \times 10^4$

Table 2.3: Dimensionless model parameters and typical values.

neglected when Re is small. Additionally, in chapter 5, we work in the high Péclet regime where diffusive transport effects can be neglected or simplified.

Finally, we observe that while the Bond number is typically small, which can at times be exploited to simplify expressions for the meniscus shape, we shall mostly explore the general regime $\mathrm{Bo} = O(1)$, where both capillary and gravitational forces are important in the system. This is because the interplay between these two effects is a key theme of our analysis of fluid flow in the system, as discussed extensively in regards to both the contact-line dynamics in chapter 3 and the volume flow rate in chapter 4.

2.8 Contact-line dynamics and the Cox-Voinov contact-line law

In this section, we present our first reduction of the governing equations for fluid flow and derive the leading-order equations for the evolution of the fluid meniscus and contact line. As part of this derivation, we introduce the Cox-Voinov contact-line law [55, 59] which provides an explicit relation between the observed macroscopic contact angle and the contact-line velocity. While this contact-line law does not form part of the leading-order model under the typical parameter values, appearing instead

as a higher-order correction, we choose to retain this term in order to regularise solutions. We provide an outline of the small slip asymptotic analysis for the contact-line law, following [58], in two dimensions in Appendix A. This serves to highlight the key aspects of the derivation, which remain applicable for the three-dimensional geometry.

2.8.1 Asymptotic Structure

We work in a regime where the dimensionless slip length and capillary number are small. Specifically, we consider the distinguished limit of $\lambda, \mathrm{Ca} \ll 1$ with $\tau = \mathrm{Ca}\log(1/\lambda) \ll 1$, which we refer to as the relaxation parameter. This parameter is associated with the timescale of a spreading droplet or relaxing contact line relative to the advective timescale, as set by the imposed flow. In addition, we take $\mathrm{Re} \ll 1$, meaning that inertial terms can be neglected throughout, and assume the Bond and Strouhal numbers are at most order unity. This regime is consistent with the standard parameter values of the physical system outlined in §2.7.3.

We consider the flow in a single well reservoir, which we divide into three asymptotic regions. These consist of an outer region on the length scale of the entire reservoir, an inner region close to the contact line on the scale of the dimensionless slip length λ, and an intermediate region across which solutions are matched. We note that this intermediate region is required only in the more general case where $\tau = O(1)$.

In the outer region, we exploit the small capillary number to determine the leading-order expression for the free surface shape, which serves to define the outer or macroscopic contact angle ϕ. We determine the leading-order free surface shape in the inner region, which depends on the microscopic contact angle α, similarly. In both cases, the free surface shape can be found without solving for the flow field, although we state the leading-order fluid flow equations in the outer region, which are relevant for our later analysis of solute transport in chapter 5.

For $\tau \ll 1$, the inner and outer regions overlap and so matching can be performed directly [59]. Matching via the free surface tangent, in a plane normal to

the contact line at each contact point, we find that the macroscopic and microscopic contact angles are equal at leading order. For $\tau = O(1)$, the microscopic and macroscopic contact angles no longer agree and logarithmic terms necessitate matching via the intermediate region; we outline this procedure in Appendix A. The asymptotic structure is shown in figure 2.4.

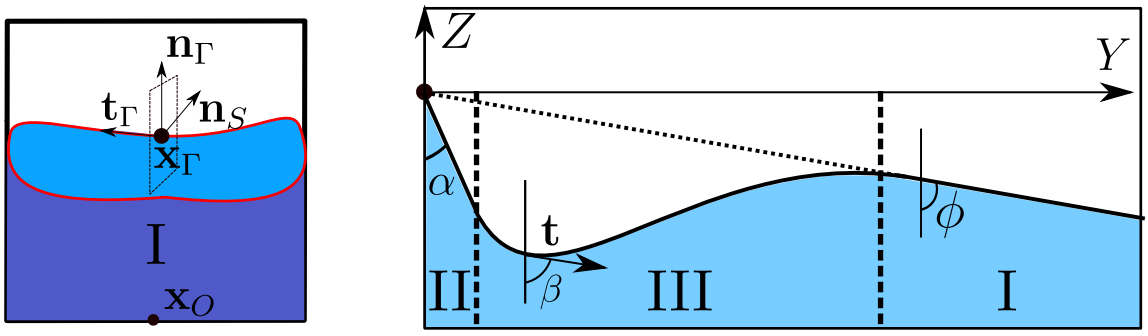

Figure 2.4: Asymptotic structure for the moving contact-line problem. Left: well reservoir showing the outer region (I) and the outer coordinate origin $\mathbf{x}_O$ at the centre of the reservoir base and a general point $\mathbf{x}_\Gamma$ on the contact line (red), at which the reservoir wall normal $\mathbf{n}_S$ and contact-line tangent $\mathbf{t}_\Gamma$ and normal $\mathbf{n}_\Gamma$ are shown. Right: view of the plane normal to the contact line with Y and Z axes aligned with the directions $-\mathbf{n}_S$ and $\mathbf{n}_\Gamma$, respectively. The inner region (II), at a distance $O(\lambda)$ from the contact line, the intermediate region (III) and the outer region (I) are indicated. The shape of the free surface, showing viscous bending in the intermediate region, is indicated as is the free surface tangent $\mathbf{t}$, forming an angle β to the negative Z axis, which is used for matching across the intermediate region. The tangent angle tends to the microscopic or macroscopic contact angle in the inner and outer regions, respectively, which are denoted by α and ϕ.

2.8.2 Outer region

We consider the solution of the fluid-flow problem (2.19)-(2.30) in the outer region, which consists of a single well reservoir. For convenience, we shift the origin of the coordinate system to the midpoint of the reservoir base, denoted by $\mathbf{x}_{O_i}$, by writing $\mathbf{x}' = \mathbf{x} - \mathbf{x}_{O_i}$. We define the total fluid volume in the ith reservoir by

$$V_i(t) = \int\int_{\mathcal{B}_i} h'(x', y')\, \mathrm{d}x'\mathrm{d}y'. \tag{2.34}$$

Since we restrict attention to a single well reservoir in this section, we omit the dashes and the subscripts used to index each well henceforth. It is convenient to write the

total pressure as

$$P(\mathbf{x},t) = P_O(t) + \mathrm{Bo}(x\sin\theta - z\cos\theta) + p(\mathbf{x},t), \tag{2.35}$$

which consists of a spatially uniform term P_O, a hydrostatic pressure component, and a modified pressure term p.

We consider an asymptotic expansion in powers of Ca and write

$$\mathbf{u} \sim \mathbf{u}_0 + \mathrm{Ca}\mathbf{u}_1 + \cdots, \quad p \sim p_0 + \mathrm{Ca}p_1 + \cdots, \quad h \sim h_0 + \mathrm{Ca}h_1 + \cdots,$$

expanding quantities derived from the meniscus height (namely H, V, and α) similarly. We note that the above expressions will in general be functions of the slip length λ. However, since λ only appears in (2.23), p_0 and h_0 are in fact independent of the slip length.

The leading-order momentum equation (2.19) is

$$\nabla p_0 = \mathbf{0}, \tag{2.36}$$

from which we deduce that the modified pressure is spatially uniform to leading order. Since this can be absorbed into the P_O term, we take $p_0 = 0$ without loss of generality. P_O therefore gives the total pressure at the origin to leading order.

The leading-order normal component of the stress condition at the free surface boundary (2.26) is

$$P_O + \mathrm{Bo}(x\sin\theta - h_0\cos\theta) = \kappa_0, \tag{2.37}$$

which is the Young-Laplace equation, where $\kappa_0 = \nabla\cdot\mathbf{n}_{F_0}$ is the curvature and the outward pointing unit normal of the leading-order free surface is $\mathbf{n}_{F_0} = \nabla(z-h_0)/|\nabla(z-h_0)|$.

The relevant boundary conditions are

$$h_0(x_w(s), y_w(s), t) = H_0(s,t), \tag{2.38}$$

where H_0 is the leading-order contact-line height and

$$\mathbf{n}_{F_0}\cdot\mathbf{n}_S = -\cos\phi_0, \tag{2.39}$$

which defines the leading-order macroscopic contact angle $\phi_0(s,t)$, where $\mathbf{n}_S$ is the outward pointing unit normal at the reservoir wall. The Young-Laplace equation (2.37) is solved subject to an imposed fluid volume constraint

$$\int\int_{\mathcal{B}} h_0 \, \mathrm{d}x\mathrm{d}y = V_0(t), \tag{2.40}$$

which determines the value of the leading-order pressure P_O.

The macroscopic contact angle does not necessarily agree with the corresponding leading-order microscopic contact angle α_0 and our solution is generally not valid close to the contact line, on the scale of the slip length, which necessitates examining an inner region in this vicinity.

Before examining the inner region, we state the leading-order equations for the fluid-flow problem in the outer region, which are relevant in our later analysis. We expand $\mathbf{u}_0$ and p_1 in powers of λ writing

$$\mathbf{u}_0 \sim \mathbf{u}_{00} + \lambda \mathbf{u}_{10} + \cdots, \quad p_1 \sim p_{10} + \lambda p_{11} + \cdots,$$

so that $\mathbf{u}_{00}$ is the leading-order velocity field in both Ca and λ. We recall that h_0 is independent of λ.

The velocity field satisfies Stokes equations

$$\nabla p_{10} = \nabla^2 \mathbf{u}_{00}, \qquad \nabla \cdot \mathbf{u}_{00} = 0, \tag{2.41}$$

on the fluid domain, which is set by the shape of the leading-order free surface $z = h_0$. At the reservoir wall, the fluid satisfies the no-flux and no-slip boundary conditions,

$$\mathbf{u}_{00} \cdot \mathbf{n}_S = 0, \qquad \mathbf{u}_{00} \cdot \mathbf{t}_S = 0, \tag{2.42}$$

where $\mathbf{t}_S$ is any tangent to the reservoir wall. We observe that the Navier-slip condition reduces to the no-slip condition in the outer region to leading order in λ.

At the free surface, we impose the kinematic boundary condition and the tangential component of the dynamic boundary condition

$$\frac{\partial h_0}{\partial t} + \mathbf{u}_{00} \cdot \nabla h_0 = w_{00}, \qquad \mathbf{n}_{F_0} \cdot \dot{\mathbf{\Gamma}}_{00} \cdot \mathbf{t}_0 = 0, \tag{2.43}$$

where $\mathbf{t}_0$ is any tangent to the free surface. We note that the normal component of the dynamic boundary condition (2.26) is not required to determine the leading-order flow field; these terms set the $O(\mathrm{Ca})$ correction to the free surface shape. Finally, to close the problem, we must match the fluid velocity profile across the reservoir base $z = 0$ with the flow in the remainder of the system.

2.8.3 Inner region

For each point $\mathbf{x}_\Gamma = x_w(s)\mathbf{e}_x + y_w(s)\mathbf{e}_y + H(s,t)\mathbf{e}_z$ on the contact line, we consider an inner region in the plane normal to the contact line at this point and on the length scale of the slip length λ. Specifically, at any point along the contact line, the outward pointing unit normal to the reservoir wall and the unit tangent and unit normal to the contact line are respectively defined by

$$\mathbf{n}_S = y_w'\mathbf{e}_x - x_w'\mathbf{e}_y, \quad \mathbf{t}_\Gamma = \frac{x_w'\mathbf{e}_x + y_w'\mathbf{e}_y + h_s\mathbf{e}_z}{\sqrt{1+h_s^2}}, \quad \mathbf{n}_\Gamma = \frac{-x_w'h_s\mathbf{e}_x - y_w'h_s\mathbf{e}_y + \mathbf{e}_z}{\sqrt{1+h_s^2}}.$$

We work in the plane with normal direction $\mathbf{t}_\Gamma$ and introduce a local coordinate system (Y, Z) within this plane, writing $\mathbf{x} = \mathbf{x}_\Gamma + \lambda Y\mathbf{e}_Y + \lambda Z\mathbf{e}_Z$, for $\mathbf{e}_Y = -\mathbf{n}_S$ and $\mathbf{e}_Z = \mathbf{n}_\Gamma$. This is shown in figure 2.4.

We introduce rescaled inner variables $p = \tilde{p}/\lambda$ and $\kappa = \tilde{\kappa}/\lambda$ and the free surface is described by $Z = \tilde{h}(Y,t)$. We note that there is no rescaling of the fluid velocity field, which scales according to the velocity of the contact line.

We consider an asymptotic expansion in powers of Ca as before and write

$$\mathbf{u} \sim \mathbf{u}_0 + \mathrm{Ca}\mathbf{u}_1 + \cdots, \quad \tilde{p} \sim \tilde{p}_0 + \mathrm{Ca}\tilde{p}_1 + \cdots, \quad \tilde{h} \sim \tilde{h}_0 + \mathrm{Ca}\tilde{h}_1 + \cdots.$$

The leading-order momentum equation (2.19) gives

$$\frac{\partial \tilde{p_0}}{\partial Y} = \frac{\partial \tilde{p_0}}{\partial Z} = 0, \tag{2.44}$$

while the normal component of the dynamic boundary condition (2.26) is

$$\tilde{p}_0 = \tilde{\kappa}_0. \tag{2.45}$$

Thus the leading-order pressure and curvature are spatially uniform. Since the curvature of the contact line is assumed to be $O(1)$, $\tilde{\kappa}_0$ consists only of the curvature

component in the plane normal to the contact line. Furthermore, in order for the free surface to extend and match the outer solution as $Y \to \infty$, we require $\tilde{p}_0 = \tilde{\kappa}_0 = 0$ and so the free surface is planar on this length-scale to leading order.

Applying the microscopic contact angle boundary condition (2.28) we find that

$$\tilde{h}_0(Y,t) = -Y \tan \alpha_0, \tag{2.46}$$

for $Y > 0$, where $\alpha_0(s,t)$ is the leading order microscopic contact angle.

We do not state the leading-order equations for fluid flow in the inner region here since they are not required for matching. However, we note that in the inner region, slip enters at leading order, via the Navier-slip boundary condition, relieving the singularity in the contact line, and we obtain the 2D Stokes equations for the flow in each plane normal to the contact line at leading order.

2.8.4 Cox-Voinov contact-line law

In the regime $\tau \ll 1$, matching can be performed directly across the inner and outer regions to find that $\phi_0 = \alpha_0$, as described in [59]. We outline a more general matching procedure via the intermediate region, which remains valid for $\tau = O(1)$, in Appendix A for a two-dimensional well geometry.

For $\tau \ll 1$, the equations governing the evolution of the free surface and contact line consist of the quasi-static Young-Laplace problem (2.37)-(2.40). According to the hysteresis law (2.29), the leading-order contact angles are restricted to the hysteresis range $[\alpha_R, \alpha_A]$ and the contact-line velocity vanishes except at the end points. The meniscus shape remains in an equilibrium configuration and responds instantaneously as the reservoir volume $V_0(t)$ and elevation angle $\theta(t)$ vary.

It can be shown that the Young-Laplace equation has a unique solution, provided it exists, when subject to either prescribed contact angle (Neumann) or prescribed contact height (Dirichlet) boundary conditions, in addition to the imposed volume constraint [49]. However, the appropriate boundary data for our problem is more complex due to contact angle hysteresis. For a given volume and elevation angle, the contact angle at each point is not specified uniquely but lies within the hysteresis

range, while the permissible values of the contact height depend on the contact angle and specifically on whether or not the meniscus is locally advancing or receding via the hysteresis law (2.29).

The dependence between the contact height and contact angle adds to the complexity of any numerical scheme. One possible approach is to determine the appropriate equilibrium configuration iteratively over sufficiently small time steps: the contact angle is first updated while the contact height remains fixed, and the contact height is subsequently adjusted in regions where the contact angle is outside the range $[\alpha_R, \alpha_A]$. An iterative scheme following this approach, where hysteresis on the contact line is modelled by an empirical friction force, is employed in [74], for instance.

This approach has limitations however, particularly for the problems we consider where the contact-line motion is driven both by an imposed flow and varying elevation angle and so the contact line can be both advancing and receding at different points. We therefore introduce the Cox-Voinov contact-line law, modified to account for contact angle hysteresis, in order to regularise the problem. We replace the condition $\phi_0 = \alpha_0$ with the equation

$$\tau \frac{H_{0t}}{\sqrt{1 + H_{0s}^2}} = F(\phi_0; \alpha_R, \alpha_A), \tag{2.47}$$

where

$$F(\phi; \alpha_R, \alpha_A) = \begin{cases} G(\phi, \alpha_A), & \text{for } \phi > \alpha_A \\ 0, & \text{for } \alpha_R \leq \phi \leq \alpha_A \\ G(\phi, \alpha_R), & \text{for } \phi < \alpha_R. \end{cases} \tag{2.48}$$

is the modified contact-line law accounting for contact angle hysteresis according to (2.29) and

$$G(\phi, \alpha) = \int_\alpha^\phi \frac{\phi' - \sin\phi' \cos\phi'}{2 \sin\phi'} \, \mathrm{d}\phi'. \tag{2.49}$$

is the usual Cox-Voinov contact-line law [55, 59].

The contact-line law provides an explicit relation between the contact angles and the velocity of the contact line, and thereby provides an evolution equation for the contact-line height H_0. This allows H_0 simply to be stepped forward at each timestep; the quasi-steady Young-Laplace equation can then be solved subject to

Dirchlet boundary conditions (2.38), providing a unique solution even in the case of contact angle hysteresis. This formulation has the additional advantage of accounting for contact angles outside the hysteresis range and remains applicable in the regime $\tau = O(1)$, where the microscopic and macroscopic contact angles can differ significantly.

The contact-line law arises by retaining correction terms of $O(\tau)$ in the matching between microscopic and macroscopic contact angles. We outline the derivation of the contact-line law and this matching procedure in a two-dimensional geometry in Appendix A.

2.8.5 Summary of the reduced model

In summary, the reduced model consists of the leading-order equations for the evolution of the free surface $h(x, y, t)$ and contact line $H(s, t)$ in a single well geometry under a varying fluid volume $V(t)$ and elevation angle $\theta(t)$. These consist of the Young-Laplace problem (2.37)-(2.40) in the outer region, where the contact height boundary condition (2.38) is imposed, while (2.39) defines the macroscopic contact angle, and the contact-line law (2.47) serves as an additional non-linear boundary condition. This reduced model is the focus of our analysis in chapter 3, where we examine solutions under a prescribed volume flow rate $Q(t)$, which sets the reservoir fluid volume as

$$\frac{\mathrm{d}V}{\mathrm{d}t} = Q(t). \tag{2.50}$$

We observe that the reduced model equations apply equally to each reservoir of a twin-well system. However, in this case the volume flow is not externally imposed but driven by pressure differences across the channel. We derive the appropriate form of the volume flow rate in the twin-well system in §2.9.

2.9 Twin-well dynamics

We present the derivation of a reduced model for the volume flow rate in the twin-well system valid for small channel aspect ratios. We work in the same parameter regime

as outlined for the derivation of the contact-line law in §2.8, with the additional assumption that the channel aspect ratio ϵ is small. In particular we work in the distinguished limit $\lambda, \mathrm{Ca} \ll \epsilon \ll 1$ with $\tau = \mathrm{Ca}\log(1/\lambda)$ at most order unity and $\mathrm{Ca} = O(\epsilon^3)$. This final condition is consistent with our choice of pressure and velocity scale.

We therefore consider an asymptotic expansion in the small parameter ϵ and the asymptotic structure is outlined as follows. We divide the device into three asymptotic regions, consisting of the two well reservoirs (region I), the thin channel (region III), and a thin connecting region between the well and channel (region II) which consists of an annular region of width $O(\epsilon)$ in the channel and extending to a height of $O(\epsilon)$ into each well. These regions are illustrated in figure 2.5.

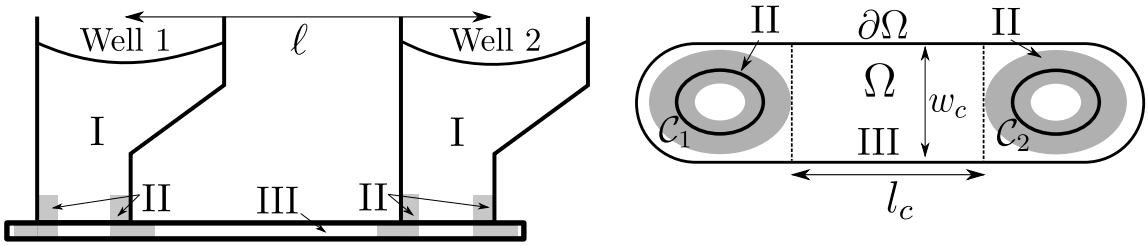

Figure 2.5: Asymptotic regions for the derivation of the reduced hydraulic electric circuit model shown as part of a profile view of the entire system (left) and a top-down view of the channel (right). The asymptotic regions are the outer well regions (I), the channel region (III) and the small intermediate region (II) which connects the two. This consists of the $O(\epsilon)$ annular region surrounding the culture chamber and channel boundary $\mathcal{C}_i$. The dimensionless channel length and width l_c and w_c and the dimensionless reservoir separation distance ℓ are also shown.

We work in terms of the standard Cartesian coordinate system centred on the centre of the channel base, as shown in figure 2.5. We again decompose the total pressure as

$$P = \mathrm{Bo}(x\sin\theta - z\cos\theta) + p, \tag{2.51}$$

where p is a modified pressure term. We note that this modified pressure differs by a constant from the modified pressure defined in §2.8.

The volume flow rate through the channel is

$$Q(t) = \int\int_{\mathcal{S}} \mathbf{u}\cdot\mathbf{n}\,\mathrm{d}S \tag{2.52}$$

where $\mathcal{S}$ is any surface spanning the channel cross section and $\mathbf{n}$ is the rightward facing unit normal. Thus a positive volume flow rate is associated with net fluid flow from well 1 into well 2. Global volume conservation ensures this flow rate is well defined and that the evolution of the fluid volume V_i in each reservoir (defined in (2.40) satisfies

$$\frac{\mathrm{d}V_2}{\mathrm{d}t} = -\frac{\mathrm{d}V_1}{\mathrm{d}t} = Q(t). \tag{2.53}$$

The purpose of our asymptotic analysis is to derive a leading-order expression for the flow rate Q.

2.9.1 Region I: the wells

In the well region (I), we pose expansions

$$\mathbf{u} \sim \mathbf{u}_0 + \epsilon \mathbf{u}_1 + \cdots, \quad p \sim p_0 + \epsilon p_1 + \cdots,$$

for the velocity field and modified pressure as $\epsilon \to 0$. The analysis in this region is identical to that for the outer region considered for the derivation of the contact-line law in §2.8, where we work to leading-order in λ. In particular, the leading-order modified pressure is spatially uniform in this region, and the leading-order equations for the velocity field in this region are identical to those presented in §2.8.2 for the outer reservoir problem, with suitable matching conditions between region I and II.

Details of the flow field in this region are not required to derive the leading-order volume flow rate. We note however, that the appropriate matching conditions are $\mathbf{u}_0 = \mathbf{0}$ on the well base $z = 0$ except on the circular well boundary $\mathcal{C}_i$ where there is a line source or sink of strength $Q(t)/2$, which follows from conservation of mass.

We let $p_0^{(i)}$ denote the spatially uniform pressure in each well for $i = 1, 2$. Making use of our previous analysis in §2.8.2, where we found the total pressure at the reservoir base $\mathbf{x}_{O_i}$ to be P_{O_i} and given by the solution of the Young-Laplace problem (2.37), we find that

$$p_0^{(i)} = \begin{cases} P_{O_1} - \mathrm{Bo}(\sin\theta \mathbf{e}_x - \cos\theta \mathbf{e}_z) \cdot \mathbf{x}_{O_1} & \text{for } i = 1, \\ P_{O_2} - \mathrm{Bo}(\sin\theta \mathbf{e}_x - \cos\theta \mathbf{e}_z) \cdot \mathbf{x}_{O_2} & \text{for } i = 2. \end{cases} \tag{2.54}$$

Thus, the modified pressure difference between the two wells is

$$\Delta p = (P_{O_2} - P_{O_1}) - \mathrm{Bo}\ell \sin\theta, \tag{2.55}$$

where ℓ is the dimensionless reservoir separation distance.

2.9.2 Region II and III

For consistency with our analysis in §2.8, the velocity is scaled according to the typical well velocity scale so that $\mathbf{u} = O(1)$ in the well region. Consequently, in the connecting regions (II) and the thin channel (III), the velocity field is $\mathbf{u} \sim \epsilon^{-1}U\mathbf{e}_x + \epsilon^{-1}V\mathbf{e}_y$ by conservation of mass with $U, V = O(1)$.

In the connecting regions (II), the leading-order terms of the momentum equation (2.19) are

$$\nabla p_0 = \mathbf{0}, \tag{2.56}$$

and thus the pressure is spatially uniform in this region. Hence the leading-order pressure is transmitted through these regions and we can match the pressure at the channel entrance and the well base.

In the channel region (III), we introduce the rescaled velocity components $(u, v, w) = (\epsilon^{-1}U, \epsilon^{-1}V, W)$ and position $(x, y, z) = l_c(X, Y, \epsilon Z)$, where $l_c = O(1)$ is the dimensionless channel length as indicated in figure 2.5. These scales are motivated by the channel dimensions and conservation of mass, while no rescaling of pressure is required.

Writing $U \sim U_0, V \sim V_0$ as $\epsilon \to 0$, the leading-order momentum equations (2.19) are the lubrication equations

$$12k(p_{0X}, p_{0Y}) = (U_{0ZZ}, V_{0ZZ}), \quad p_{0ZZ} = 0, \tag{2.57}$$

for $(X, Y) \in \Omega$ and $0 \leq Z \leq 1$, where Ω is the projection of the channel cross section onto the (X, Y) plane and $k^{-1} = \mathrm{Bo}w_c l_c$, which arises from the fact that $\mathrm{Ca} = \mathrm{Bo}w_c l_c^2 \epsilon^3/12$ due to our choice of scaling. Following standard lubrication theory

and making use of the no-slip conditions on the top and bottom of the channel $Z = 0, 1$, we find the depth-averaged flow, defined by

$$(\bar{U}_0, \bar{V}_0) = \int_0^1 (U_0, V_0)\ \mathrm{d}Z,$$

to be

$$(\bar{U}_0, \bar{V}_0) = -k(p_{0X}, p_{0Y}). \tag{2.58}$$

From mass conservation, the leading-order pressure satisfies

$$p_{0XX} + p_{0YY} = 0, \tag{2.59}$$

on Ω subject to the boundary conditions

$$\frac{\partial p_0}{\partial n} = 0, \tag{2.60}$$

on $\partial\Omega$ and

$$p_0 = p_0^{(i)}, \tag{2.61}$$

on $\mathcal{C}_i$, which arises from matching with the pressure in the well as defined in (2.54).

This Hele-Shaw problem (2.59)-(2.61) must typically be solved numerically. From the solution, we can determine the leading-order depth-averaged flow from (2.58). Furthermore, we can normalise this problem in terms of the pressure difference between the left and right wells by writing $p_0 = p_0^{(2)} - (\Delta p_0)\hat{p}_0$. The boundary conditions (2.61) are then $\hat{p}_0 = 1, 0$ on $\mathcal{C}_1$ and $\mathcal{C}_2$ respectively.

The leading-order volume flow rate is given by

$$Q_0(t) = \mathrm{Bo}^{-1}\Delta p_0 \left(\frac{l_c}{w_c} \int_{-w_c/2l_c}^{w_c/2l_c} \left.\frac{\partial \hat{p}_0}{\partial X}\right|_{X=0} \mathrm{d}Y \right). \tag{2.62}$$

We observe that the Bond number appears since we have scaled pressure according to the capillary pressure but the velocity is based on hydrostatic pressure differences. We observe that (2.62) is the dimensionless form of the standard hydraulic electric circuit analogy equation

$$Q^*(t) = -\Delta P^*/R_h^*, \tag{2.63}$$

where we identify the dimensionless hydraulic resistance as

$$R_h = -\frac{l_c}{w_c}\int_{-w_c/2l_c}^{w_c/2l_c} \left.\frac{\partial \hat{p}_0}{\partial X}\right|_{X=0} \mathrm{d}Y > 0, \tag{2.64}$$

which depends solely on the system geometry. Furthermore, in the special case where the channel is fully rectangular $R_h = 1$, and we recover the hydraulic resistance of a rectangular channel (see [43]) in the limit of a small aspect ratio

$$R_h^* = \frac{12\mu^* L_D^*}{{H_D^*}^3 W_D^*}. \tag{2.65}$$

2.9.3 Summary of twin-well dynamics

We have obtained the equation

$$Q(t) = -\Delta p / R_h, \tag{2.66}$$

for the leading-order volume flow rate $Q(t)$ in the system in terms of the pressure difference across the channel and the dimensionless hydraulic resistance of the channel, defined by (2.64). The pressure difference is

$$\Delta p = \mathrm{Bo}\ell \sin\theta + P_{O_2} - P_{O_1}, \tag{2.67}$$

where the first term is due to tilting. The remaining pressure terms are found by solving the Young-Laplace equation in each reservoir, as stated in §2.8.5. By conservation of mass, the volume of fluid in each well satisfies

$$\frac{\mathrm{d}V_2}{\mathrm{d}t} = -\frac{\mathrm{d}V_1}{\mathrm{d}t} = Q(t). \tag{2.68}$$

We examine the solutions for the volume flow rate in chapter 4 in a two-dimensional system geometry. We note that this leading-order model provides only the volume flow rate, with further analysis required to determine the velocity profile in the relevant regions. We consider numerical solutions for the velocity field in a two-dimensional system in chapter 5 when we examine the problem of solute transport.

Chapter 3

Single-well analysis

3.1 Introduction

In this chapter we examine the evolution of the moving contact line and the fluid free surface in a single well geometry. This restriction is motivated by two factors. Firstly, it allows us to examine the moving contact line problem in a simpler setting, as we study the impact of an imposed flow regime on the meniscus shape and capillary pressure in isolation, removing the feedback between the pressure difference and the flow that occurs in the twin-well system. Secondly, it enables us to explore the moving contact line problem in greater depth, which includes a range of three-dimensional well geometries and various operating regimes that, due to the computational complexity of the resulting Young-Laplace equation for the meniscus shape, are more difficult to incorporate directly when examining the full twin-well system. Key features of our analysis can nevertheless be used to support our modelling of the full twin-well system, which we consider in chapter 4.

The structure of this chapter is outlined as follows. We begin in §3.2 by briefly describing the configuration of the single well system for a general well cross section and discussing the structure and properties of the equations governing the evolution of the free surface and contact line under an imposed volume flow rate. In §3.3 we describe the numerical scheme used to solve the single well problem. In particular, we introduce the *Surface Evolver* software package [63] which forms a key component of the numerical scheme. We employ Surface Evolver to solve the Young-Laplace

equation and efficiently compute the free surface shape for a general well geometry. Subsequent sections are dedicated to analysing different single-well geometries under a range of flow and operating conditions supported by this numerical scheme.

Specifically, we consider the following scenarios presented in order of increasing complexity. We begin in §3.4 with a well of circular cross section, first examining solutions in the simplest case of a purely horizontal system where the motion of the contact line is driven by an imposed inlet or outlet flow. In this case, it is possible to obtain exact or simple asymptotic expressions for the shape of the free surface. In §3.5 we first study the behaviour of a circular well where the motion of the contact line is instead driven by a varying elevation angle in the absence of an imposed flow, which requires computing the free surface shape numerically using Surface Evolver. We then combine these two scenarios to consider a circular well with both a varying elevation angle and an imposed flow.

Finally, in §3.6 we summarise our analysis of the single-well geometry and discuss the relevance of our conclusions to the operation of the twin-well system. This forms the basis of our detailed analysis of a (two-dimensional) representation of the twin-well system in chapter 4.

3.2 The single-well system

We consider a modification of the twin-well system where a single well is isolated and connected, via the inlet that would otherwise connect to the horizontal channel in a twin-well system, to an external pumping system. This external pump controls the prescribed flow of fluid into or out of the single-well system. The device is then placed on a laboratory rocker which tilts the system to provide a prescribed variation in the elevation angle.

We model the evolution of the free surface and contact line subject to imposed variations in reservoir volume $V(t)$ and elevation angle $\theta(t)$, accounting for both gravitational and capillary effects. We focus in particular on the impact of contact angle hysteresis and hydrodynamic effects that arise from the Cox-Voinov contact-line

law. Since we are interested in the free surface rather than the details of the flow, we model only the upper well reservoir of the physical system and thus effectively consider a well of uniform cross section. We refer to §2.8 for a description of the single-well geometry and coordinate system as well as a derivation of the model equations. A summary of the system setup is shown in figure 3.1 and we restate the dimensionless model equations for ease of reference below.

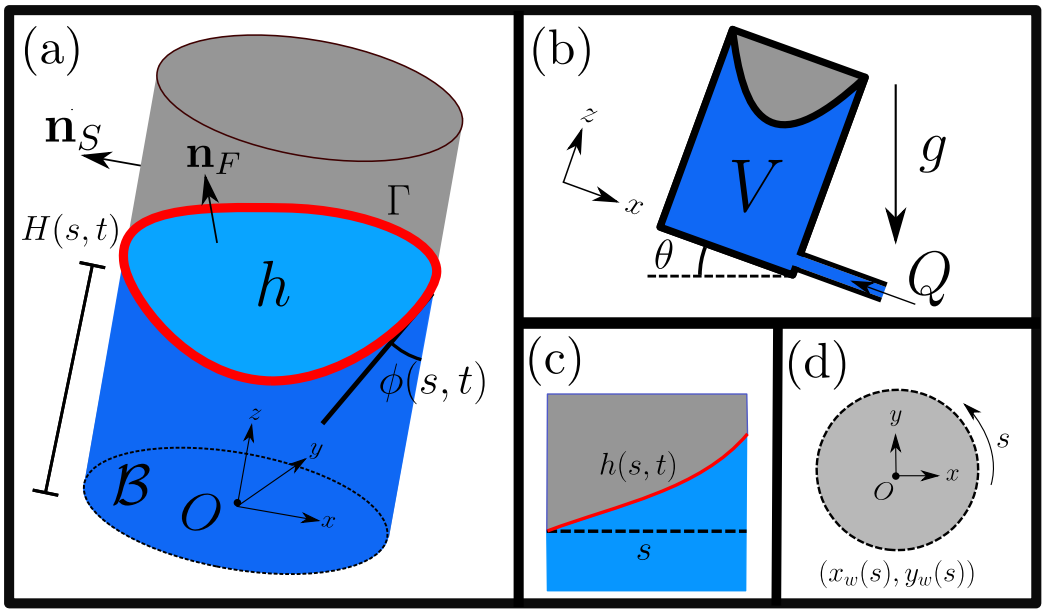

Figure 3.1: Schematics showing the dimensionless single-well system. (a) Three-dimensional view of the single-well system illustrating the free surface h, the contact line Γ (red) and the associated contact-line height H and contact angle ϕ, and the outward pointing unit normals to the free surface $\mathbf{n}_F$ and well wall $\mathbf{n}_S$. The alignment of the Cartesian coordinate axes is also shown, with the origin at the base of the well. (b) Profile view (along plane $y = 0$) illustrating the angle of elevation θ of the system to the horizontal. The flow rate Q and fluid volume V are shown, and the direction of gravity is indicated by g. (c) Close-up view of the contact line illustrating the variation of the contact height h as a function of the well perimeter arc length s. (d) Top-down view illustrating the base of the well and the well perimeter (x_w, y_w), which is parameterised by the perimeter arc length s.

3.2.1 Reduced model equations

The reduced model for the evolution of the contact line in a single well takes the form of the quasi-steady Young-Laplace equation

$$\mathrm{Bo}(x\sin\theta - h\cos\theta) + P = \kappa, \tag{3.1}$$

for the meniscus height $h(x, y, t)$, where $P(t)$ is the uniform pressure term and $\kappa = \nabla \cdot \mathbf{n}_F$ is the curvature with $\mathbf{n}_F = \nabla(z-h)/|\nabla(z-h)|$ the outward unit normal to the free surface. The boundary conditions are

$$h = H \tag{3.2}$$

$$\tau \frac{h_t}{\sqrt{1+h_s^2}} = F(\phi; \alpha_R, \alpha_A) \tag{3.3}$$

on the contact line Γ, which is parametersied by the arc length s. These correspond to an imposed contact-line height $H(s,t)$ and the Cox-Voinov contact-line law, with F defined by (2.47), relating the contact-line velocity to the macroscopic contact angle, which is defined by

$$\mathbf{n}_F \cdot \mathbf{n}_S = -\cos\phi(s,t), \tag{3.4}$$

where $\mathbf{n}_S$ is the outward-pointing unit normal to the well wall. Finally, the volume constraint is

$$\int\int_{\mathcal{B}} h \, \mathrm{d}x\mathrm{d}y = V. \tag{3.5}$$

The initial contact-line height $H(s,0)$ is prescribed as are the forms of the fluid volume $V(t)$ and elevation angle $\theta(t)$. The reservoir volume can also be specified in terms of the volume flow rate as $Q(t) = V_t(t)$.

We observe that the reduced model can equivalently be viewed as an evolution equation (3.2) for the contact-line height $H(s,t)$, with the Young-Laplace equation (3.1) serving as an associated boundary value problem to determine the contact angle and thus the contact-line velocity. This view is convenient both for obtaining numerical solutions of the reduced model and in presenting our analysis of the single-well dynamics, where we divide the problem into its two constituent parts of the quasi-static Young-Laplace problem for the meniscus shape and the dynamic problem for the evolution of the contact line.

3.2.2 Model variables and parameters

Important quantities that we can extract from the solution for the meniscus height h are the contact-line height H, the macroscopic contact angle ϕ, the total fluid volume V, and the total pressure P. For later convenience in comparing gravitational and capillary effects, we decomposed the pressure into a hydrostatic and capillary component by writing $P = P_h + P_\gamma$ with

$$P_h(t) = \frac{\mathrm{Bo} V(t)\cos\theta(t)}{A}, \tag{3.6}$$

$$P_\gamma(t) = -\frac{1}{A}\int_\Gamma \cos\phi(s,t)\mathrm{d}s, \tag{3.7}$$

where A is the cross-sectional area of the well. These expressions are obtained by integrating (3.1) over the well base $\mathcal{B}$ and using Green's theorem, while making use of the volume constraint (3.5) and the definition of the contact angle (3.4).

These model outputs provide additional physical insight and often prove more relevant to our analysis than the full solution for the meniscus height. For instance, the total pressure P is a key output of our model, which is important to understand ahead of our analysis of the twin-well system, where pressure differences drive the flow in the channel. In addition, we shall typically describe the state of the single-well system in terms of the fluid volume and contact angle configuration (V, ϕ), since they provide the most meaningful physical representation for the reasons we outline in §3.2.3.

The reduced model equations depend on four dimensionless parameters. These are the Bond number Bo, which gives the ratio of the strength of gravitational and capillary forces, the microscopic receding and advancing contact angles $\alpha_R \leq \alpha_A$, and the capillary relaxation parameter τ, which gives the ratio of the spreading and advective timescales. The estimated values of these parameters for the physical system were given in §2.6, although in this chapter we explore the behaviour of the system across a range of parameter values.

We note that the Bond number is typically of order unity, meaning that the meniscus shape is determined by the interplay of both capillary and gravitational

forces, while the difference between the microscopic receding and advancing contact angles suggests hysteresis effects will also be important. Furthermore, the relaxation parameter is typically small and in the regime $\tau \ll 1$ we expect behaviour akin to a fast-slow dynamical system, with the contact line undergoing slow quasi-steady motion except when $Q = 0$, which we examine in §3.4.3.

3.2.3 Properties of the Young-Laplace problem

In this section, we discuss properties of the static Young-Laplace problem, which will prove useful for our analysis and serve to motivate expressing solutions in terms of the fluid volume and contact angle configuration (V, ϕ). The Young-Laplace equation (3.1) with volume constraint (3.5) can be solved subject to either an imposed contact-line height (3.2) or an imposed contact angle (3.4), with the solution to each of these problems unique when it exists [49]. Thus, there is an equivalence between the contact-line height H and contact angle ϕ: the meniscus shape at any given time can be fully determined by specifying either the fluid volume and contact-line height (V, H) or the fluid volume and contact angle configuration (V, ϕ). In our analysis we adopt the convention of specifying solutions in terms of the latter.

One reason for this is that the Young-Laplace problem exhibits solutions for the free surface h which share the same overall shape and contact angle configuration but differ only by the mean fluid height, which is defined as $\bar{h} = V/A$. Physically, these solutions correspond to single-well systems that differ only in the total fluid volume. To show this translational invariance, we observe that solutions to the Young-Laplace problem with prescribed contact angle boundary conditions and volume constraint (3.1), (3.4), and (3.5) are invariant under suitable shifts in the volume, meniscus height, and hydrostatic pressure constant given by

$$V \to V + \delta V, \quad P_h \to P_h + \delta V(\mathrm{Bo}\cos\theta)/A, \quad h \to h + \delta V/A, \tag{3.8}$$

with the contact angle configuration and capillary pressure unchanged. The relative meniscus height, defined by $\tilde{h} = h - \bar{h}$, is also invariant across these solutions.

This invariance can be exploited to simplify the procedure for solving the Young-Laplace equation. It is only necessary to solve (3.1) for the zero-volume solution $V = 0$ in which $P_h = 0$ by (3.6). The corresponding free surface for a general volume V is then obtained via a translation by $\bar{h}$ in the z-direction.

A further consequence of this invariance is that the variables V and ϕ independently specify the following quantities. The fluid volume V specifies the mean fluid height $\bar{h}$ and hydrostatic pressure by (3.6), while the contact angle configuration ϕ determines the capillary pressure by (3.7) and the relative meniscus height $\tilde{h}$ via the solution of the zero-volume Young-Laplace problem. In contrast, the contact-line height H cannot be used to independently specify the free surface shape or capillary pressure without knowledge of the fluid volume. While the relative contact height $\tilde{H} = H - \bar{h}$ can be used instead, it is less physically meaningful than the contact angle configuration. The combination (V, ϕ) therefore provides a more concise and informative description of the state of the system.

Furthermore, the translational invariance of the Young-Laplace problem extends to the reduced model itself as, up to appropriate translations, the system dynamics are independent of the initial volume. This allows us to work in physically unrealistic regimes (e.g. regimes for which the volume is non-positive) when characterising the model mathematically. Such results can then easily be translated to a physical system.

We conclude this section by observing that while these properties do apply to a general well geometry, further complications can arise when the well perimeter is not smooth.

3.3 Numerical methods and Surface Evolver

We outline the numerical scheme we employ for solving the reduced model equations for the evolution of the meniscus and contact line. We view the problem as an evolution equation for the contact-line height H with the associated Young-Laplace boundary value problem providing the contact-line velocity. The evolution of H is determined using a finite difference scheme outlined in §3.3.1. The Young-Laplace

boundary value problem is typically more challenging and computationally intensive, particularly in cases where the contact line is non-uniform. We therefore use the *Surface Evolver* software to solve the variational form of the Young-Laplace problem using a finite element method [63]. This solution scheme is applicable to the general Young-Laplace problem for arbitrary well geometries and elevation angles, in addition to a non-uniform contact line.

In this chapter, we typically prescribe a volume flow rate $Q(t)$ that can be integrated analytically to obtain the fluid volume $V(t)$. For more general flows, however, the volume can be found numerically using a fourth-order Runge-Kutta method, which we implement in Python using the standard `scipy` library. This is relevant when extending our analysis to the twin-well problem in chapter 4, where the volume flow rate is driven by pressure differences.

3.3.1 Finite difference scheme for contact-line height

We solve the contact-line evolution equation (3.3) for H, given (3.2), using a finite difference scheme. We discretise the contact-line position by considering n equally spaced points along the well perimeter at points s_i at which the contact-line height is $H(s_i, t)$. To determine the height at time $t + \Delta t$ we apply the forward Euler scheme

$$H(s_i, t + \Delta t) = H(s_i, t) + \tau^{-1} \Delta t \sqrt{1 + H_s(s_i, t)^2} F_{hys}(\phi(s_i, t)), \tag{3.9}$$

using the central difference scheme

$$H_s(s_i, t) \approx \frac{H(s_{i+1}, t) - H(s_{i-1}, t)}{2\Delta s} \tag{3.10}$$

to approximate the gradient term, where Δs is the distance between successive points on the well perimeter. We note that for small values of the relaxation parameter τ a sufficiently small time step size is needed for numerical stability.

We implement the above scheme in Python. We note that at each timestep we require the value of the contact angle $\phi_i(s_i, t)$ to determine the contact-line velocity using the contact-line law (3.3), which necessitates solving the static Young-Laplace problem using Surface Evolver. The use of the forward Euler scheme is motivated

by the fact that this is generally computationally intensive. We replace (3.9) with a higher-order Runge-Kutta scheme in the cases where solutions to the Young-Laplace equation are readily available, such as the horizontal system we consider in §3.4.

3.3.2 Surface Evolver

The *Surface Evolver* software programme, developed by Brakke [63], is designed for solving the problem of minimising the total energy of a surface subject to imposed constraints. It has been widely used to study a range of energy minimisation problems corresponding to different physical phenomena, including the shape of fluid in a container under microgravity conditions [75, 76], the formation of thin filaments at sharp corners [77], the shape of a capillary drop on a rough surface or surface with isolated ridges and grooves [78, 79], and electrowetting effects [80, 81]. While many applications pertain to finding the static equilibrium shape of a capillary surface, Surface Evolver has also been used to investigate dynamic problems such as the evolution of the contact line. Indeed, further relevant applications include modelling contact angle hysteresis of a droplet on a planar surface through variations in the drop volume and surface heterogeneity [82] or tilting of the plane [74, 83, 84]. We apply a similar methodology to study the contact angle hysteresis of the capillary surface in the single-well system.

Surface Evolver uses a finite-element method with surfaces represented by simplicial complexes of triangular elements. The total surface energy is defined in terms of an energy functional and is typically formed from multiple components, including surface tension, gravitational potential energy, and other user-defined energies that represent additional physics such as the contact angle condition. This energy functional is minimised, subject to imposed constraints, using the method of gradient descent, which iteratively evolves the surface until it converges to an equilibrium state which is a (local) minimum of the total energy. Specifically, at each iterative step, the forces on each vertex are calculated from the gradient of the energy and the vertices are moved accordingly. Constrained vertices are projected back onto the feasible set defined by the constraints. A variety of in-built tools exist to refine, remesh, and

visualise the surface and to extract relevant quantities such as the surface energy or pressure. We refer to [63] and the [85] for further details.

In our analysis, we make use of Surface Evolver to solve the quasi-steady Young-Laplace problem for the system under general conditions. We use Surface Evolver, rather than other FEM schemes, since it is a powerful, purpose-built tool for finding such equilibrium surfaces. Furthermore, it allows us to consider the quasi-steady Young-Laplace and dynamic contact-line problems separately, although it is straightforward to integrate these solutions into the general procedure for solving the dynamic contact-line problem using the finite difference scheme outlined above. We outline our implementation below.

3.3.3 Implementation of the Surface Evolver scheme

Since Surface Evolver takes a variational approach of minimising the total energy of the surface, we convert the Young-Laplace equation (3.1) with imposed contact-line height boundary conditions (3.2) and volume constraint (3.5) to variational form (see [85] for instance).

To define the geometry of the surface itself, which is represented by triangular facets, we approximate the well cross-section as a polygon. In particular, for the circular well geometry that we consider in our analysis, we approximate the well cross-section as a regular n-sided polygon. The appropriate energy integrals can be defined within the Surface Evolver software, which automatically imposes a volume constraint for the specified fluid volume. Further constraints are imposed manually, which include restricting the surface to lie within the interior of the well geometry.

To determine the initial meniscus shape at time $t = 0$, we supply the initial volume $V(0)$, elevation angle $\theta(0)$, and contact-line height $H(s_i, 0)$. We must also supply an initial guess for the meniscus shape: for a uniform contact-line height we take this to be the simplest guess of a flat meniscus with $h = H$, although we note that this can be improved upon for a circular well geometry by using the analytic solution available when $\mathrm{Bo} = 0$ (see §3.4), for example. In practice and for computational efficiency, we begin with a relatively coarse mesh which is refined at later stages of the iteration as

the surface approaches equilibrium. Convergence of solutions is ensured by confirming that the energy undergoes no significant change upon further iterations. Empirically, we find that convergence is fast and typically requires between 20 and 50 iterations after the final mesh refinement, depending on the contact angle, with contact angles closer to 90° requiring fewer iterations.

Relevant quantities such as the total pressure P and the contact angle ϕ can easily be extracted from the Surface Evolver software. We note that the contact angle ϕ must be calculated from the surface normal, which is determined from the normal to the triangular facet. As noted in [74], this approach is dependent on the mesh size and can result in inaccuracies even for relatively fine meshes. We therefore adopt an alternative method for measuring the contact angle, which entails use of vertices of neighbouring facets to better estimate the surface normal. For the standard mesh size, this results in a maximum error of 0.3% in the contact angle range $[5°, 175°]$ for the circular well geometry, which improves on the standard method by an order of magnitude.

When solving the dynamic contact-line problem, we use the above procedure to determine the meniscus shape at $t = 0$. To determine the meniscus shape at subsequent timesteps, we first update the contact-line height H following (3.9) using the current contact angle configuration. We also update the fluid volume and elevation angle. We then use Surface Evolver to find the new equilibrium shape of the meniscus, using the current meniscus shape with updated contact-line height position as our initial guess. We note therefore that this typically requires a smaller number of iterative steps (for the same mesh refinement) than for the initial configuration, provided the time step is small, since the system is already close to equilibrium.

The above scheme applies to both the circular and square well geometries, although we note that small modifications are required for the square well geometry under certain circumstances. This is due to the formation of thin filaments at the well corners, which can occur for certain contact angle configurations.

The standard parameter values for the numerical scheme in the case $\tau = 1$ are summarised in table 3.1. These are the number of mesh vertices on the contact line

n and in total N_v, the time step size Δt for the forward Euler scheme (3.9), and the number of iterations in Surface Evolver when solving the (static) Young-Laplace problem at $t = 0$, with an initial guess of a flat meniscus $h = H$, and the (dynamic) problem at subsequent time steps. The value of Δt is reduced accordingly for smaller values of τ so that $\Delta t \tau^{-1}$ remains small.

Symbol	Parameter	Value
n	Number of vertices on contact line	~ 200
N_v	Total number of mesh vertices	~ 4000
Δt	Time step size	0.01
N_{static}	Number of iterations (static)	100
N_{dyn}	Number of iterations (dynamic)	20

Table 3.1: Key parameters for the numerical scheme with standard values shown for $\tau = 1$. N_{static} denotes the number of iterations in Surface Evolver to determine the initial free surface shape starting from a horizontal surface, while N_{dyn} denotes the number of Surface Evolver iterations at each timestep for the dynamic contact-line problem.

Finally, verification of the numerical method is achieved by comparison of solutions obtained using the Surface Evolver scheme with either exact or alternative numerical solutions, obtained using a finite difference method, which are available for the simple scenario of a horizontal system with a circular well geometry, which we consider in §3.4. Good agreement between these solutions is observed for both the static equilibrium problem for the meniscus shape and the moving contact-line problem under the standard numerical parameter values, which are chosen to balance accuracy and computational efficiency, with relative errors below 1% for the standard contact angle range $[15°, 50°]$.

3.4 Horizontal circular well

We begin our analysis of the single-well system by examining the dynamics of a well with circular cross section and restricting attention to the horizontal regime where $\theta = 0$. This regime exhibits axisymmetric solutions for the meniscus shape, where the contact angle and contact height are uniform along the contact line. Focusing on these

solutions allows us to reveal the fundamental behaviour of the system and introduce core concepts while avoiding the added complexities of a non-uniform contact line, which we consider in later sections.

We consider a circular well with unit radius and restrict attention to axisymmetric solutions of the form $h(r,t)$, where r is the radial coordinate for the base of the well. The contact height $H(t)$ and contact angle $\phi(t)$ are therefore uniform along the contact line. We prescribed the volume flow rate $Q(t)$ from which we obtain the fluid volume $V(t)$.

In the axisymmetric case, the equation for the evolution of the contact-line height (3.3) is

$$\tau \frac{\mathrm{d}H}{\mathrm{d}t} = F(\phi; \alpha_R, \alpha_A), \tag{3.11}$$

while the associated Young-Laplace equation (3.1) with imposed contact-line height (3.2) and volume constraint (3.5) is

$$-\mathrm{Bo}h + P = -\frac{1}{r}\frac{\partial}{\partial r}\left(\frac{rh_r}{\sqrt{1+h_r^2}}\right) \tag{3.12}$$

subject to

$$h(1,t) = H(t), \tag{3.13}$$

$$2\pi \int_0^1 rh(r,t)\ \mathrm{d}r = V(t). \tag{3.14}$$

From (3.4), the macroscopic contact angle satisfies

$$\cot\phi(t) = h_r(1,t). \tag{3.15}$$

We prescribe the initial volume as $V(0) = 0$ without loss of generality, and the initial contact height $H(0)$. We typically express solutions in terms of the volume and contact angle $(V(t), \phi(t))$ however, which offers more physical insight.

We examine both the Young-Laplace problem and the dynamic contact-line problem in turn. Initially, we consider the case $\mathrm{Bo} = 0$ where, in the absence of gravity, the meniscus shape is determined by surface tension effects alone. The solutions to the Young-Laplace problem take the form of a spherical cap meniscus. We characterise these solutions by examining the relationship between the contact angle, contact

height, and capillary pressure, for which exact expressions are available. We further introduce the concept of the meniscus cap volume, which provides an alternative way to characterise the meniscus shape and proves useful in subsequent analysis.

Making use of our solutions for the meniscus shape, we then examine the dynamics of the system under an imposed flow. We focus on how the solutions, and in particular the evolution of the contact line, depend on the relaxation parameter τ, highlighting behaviour such as the pinning and relaxation of the contact line. Furthermore, in the parameter regime $\tau \ll 1$, we obtain a further reduction to the single-well equations by exploiting the small relaxation parameter. In this reduction, which we call the fast relaxation model to reflect the behaviour of the contact line, the evolution of the contact line is independent of the exact form of the contact-line law to leading order. This reduction is both physically relevant, due to the typical parameter values of the twin-well system, and applicable to more general geometries and operating regimes, which we consider in subsequent sections.

Finally, we consider how the behaviour of the system changes when gravitational effects are included, finding that while the meniscus shape is altered, the overall qualitative dynamics of the contact line are unchanged. Here we also discuss the variation in time of the hydrostatic and capillary pressure, which are key outputs of our modelling and relevant to the twin-well system.

3.4.1 Spherical cap solutions to the Young-Laplace problem

In the regime $\mathrm{Bo} = 0$, we can write down the exact solution of the axisymmetric Young-Laplace problem (3.12)-(3.14). For a given fluid volume V, solutions exist provided $|H - \bar{h}| \leq 2/3$, where $\bar{h} = V/\pi$ is the mean fluid height. We parameterise these solutions according to the value of the contact angle $0 \leq \phi \leq \pi$. The free surface shape corresponds to either a spherical cap or a flat plane and is given explicitly in terms of the relative meniscus height $\tilde{h}(r;\phi) = h(r,t;\phi) - \bar{h}(t)$ by

$$\tilde{h} = \begin{cases} \tan\phi + \tilde{H}(\phi) - \sqrt{\sec^2\phi - r^2}, & \text{if } 0 \leq \phi < \pi/2, \\ \tan\phi + \tilde{H}(\phi) + \sqrt{\sec^2\phi - r^2}, & \text{if } \pi/2 < \phi \leq \pi, \\ \tilde{H}(\pi/2) = 0, & \text{if } \phi = \pi/2, \end{cases} \tag{3.16}$$

where

$$\tilde{H}(\phi) = \frac{1}{3}(\tan\phi - \sec\phi)^2(2\sec\phi + \tan\phi) \tag{3.17}$$

is the contact height relative to the mean fluid height $\bar{h}$. The hydrostatic component of the pressure vanishes since $\mathrm{Bo} = 0$, while the capillary component is

$$P_\gamma(\phi) = -2\cos\phi. \tag{3.18}$$

We note that a contact angle of $\phi = \pi/2$ corresponds to a flat meniscus with zero curvature or capillary pressure, while for $\phi < \pi/2$ or $\phi > \pi/2$ solutions correspond to a (downwardly) convex meniscus with negative capillary pressure (see figure 2.3 for instance) and (downwardly) concave meniscus with positive capillary pressure, respectively.

Before considering the system dynamics under an imposed flow, it is convenient to also define the (signed) meniscus cap volume. For an arbitrary fluid volume V, the cap volume V_{cap} is defined as the volume of fluid above the plane $z = H(\phi)$ which intersects the well at the contact line. The cap volume is

$$V_{cap}(\phi) = 2\pi \int_0^1 r(h(r) - H(\phi))\ \mathrm{d}r = -\pi\tilde{H}(\phi), \tag{3.19}$$

and we observe that for a particular contact angle this cap volume is independent of the total fluid volume V. Furthermore, this volume is negative for a convex meniscus with $\phi < \pi/2$.

The cap volume and capillary pressure are both strictly increasing functions of the contact angle. They therefore provide an equivalent characterisation of the meniscus shape and by extension the state of the system. For the majority of this section, it is both preferable and more intuitive to describe the meniscus in terms of the contact angle, from which we can obtain the above quantities. However, in practice an experimenter will have direct control of volumes via the imposed flow rate and so there are aspects of our analysis for which the cap volume proves more useful. An example of this is given in §3.4.4 when we consider hysteresis of the contact angle.

3.4.2 Contact-line dynamics

We now examine the dynamics of the contact line for the horizontal well with Bo = 0. We present the initial conditions in terms of the initial contact angle $\phi(0)$ and the initial volume $V(0) = 0$, which together specify $H(0)$. The key model parameters are the microscopic advancing and receding contact angles α_A and α_R and the relaxation parameter τ. We shall generally consider simple alternating flows where the flow rate $Q(t)$ has a constant magnitude but alternates in sign at regular intervals, possibly with a fixed period of zero flow between these intervals (see figure 3.2(d) for instance).

We begin by presenting the key dynamics of the contact line while also exploring the effect of the relaxation parameter. Figure 3.2 illustrates the behaviour of the system under a prescribed alternating flow rate $Q(t)$ and shows the variation of the contact angle, the contact height, and the fluid volume for a range of different relaxation parameters. Here the microscopic contact angles are set to their standard values $(\alpha_R, \alpha_A) = (15°, 50°)$, which correspond to typical values for the physical system, but the qualitative behaviour of the system is representative of any contact angle pairing.

The contact-line dynamics can be divided into two distinct phases: the pinned phase, where the contact-line velocity vanishes and so its position remains fixed, and the unpinned phase, during which the contact line advances or recedes. From the contact-line law (2.29), the pinned phase corresponds to $\alpha_R \leq \phi \leq \alpha_A$ while the unpinned phase corresponds to either $\phi > \alpha_A$ (advancing motion) or $\phi < \alpha_R$ (receding motion).

Overall, the typical behaviour can be summarised as follows. As the volume increases, the contact angle also increases, with the contact line remaining pinned until it exceeds the advancing contact angle, beyond which the contact line begins to advance. Conversely, for a decreasing fluid volume, the contact angle decreases until the receding angle is reached, at which point the contact line becomes unpinned and begins to recede. Finally, we observe that at times where the volume flow rate vanishes (indicated by grey shading in figure 3.2), if the contact angle is outside the pinned range, then the contact angle relaxes back to the advancing or receding angle.

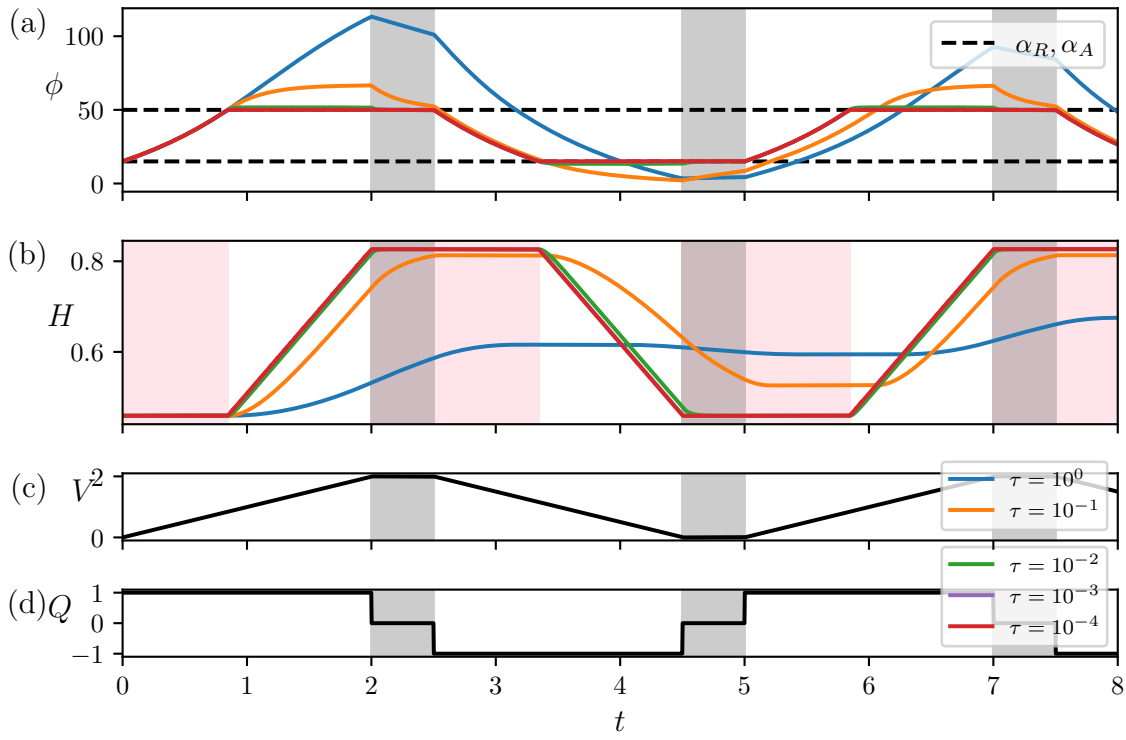

Figure 3.2: Single-well contact-line dynamics as the relaxation parameter τ varies over several orders of magnitude as indicated. An alternating volume flow rate is prescribed, and the initial conditions are $(V(0), \phi(0)) = (0, 15°)$ with $(\alpha_R, \alpha_A) = (15°, 50°)$. (a) Evolution of the contact angle $\phi(t)$ with the microscopic contact angles indicated. (b) Evolution of the contact-line height $H(t)$ with time periods during which the contact line is pinned indicated for the particular case of $\tau = 10^{-4}$ by red shading. (c) Variation of the fluid volume $V(t)$ and (d) the imposed volume flow rate $Q(t)$. Periods during which no flow is imposed are indicated by grey shading.

This relaxation occurs more quickly for smaller values of τ, while for larger values this relaxation may not be complete before the flow resumes.

It can be seen from the governing equations that the dynamics during the pinned phase are independent of the relaxation parameter τ. In this case, the change in the contact angle due to the changing fluid volume is determined solely from the quasi-steady Young-Laplace problem. This can be seen from the contact angle plots in figure 3.2(a). Since the flow rate is a piecewise constant function, during each pinned phase, where $\alpha_R \leq \phi \leq \alpha_A$, increasing or decreasing solutions between the horizontal dashed lines share a common shape and will collapse to a single curve if shifted in time.

The unpinned dynamics do depend on the relaxation parameter however and solutions exhibit qualitatively different behaviour as τ varies across the indicated orders of magnitude. The deviation between the microscopic advancing or receding contact angle and the dynamic macroscopic contact angle ϕ during the unpinned dynamics depends on the relaxation parameter, with the magnitude of this deviation decreasing as τ decreases. This in turn affects the capillary pressure, which is a function of the macroscopic contact angle.

We can broadly divide solutions into two classes of qualitative behaviour in the unpinned phases based on the magnitude of τ. For sufficiently small relaxation parameters (i.e. $\tau \ll 1$ and in practice $\tau \lesssim 10^{-3}$), the macroscopic contact angle remains approximately equal to the advancing or receding contact angle during the unpinned phase, resulting in near identical solutions. In actuality, the contact angle is very slightly above or below these values when the contact line is in motion. Solutions are virtually indistinguishable for $\tau \lesssim 10^{-3}$ and solutions in purple and red overlap in figure 3.2. Indeed, we shall show that for $\tau \ll 1$ the contact angle remains bounded to leading order in τ throughout the dynamics by the microscopic contact angles so that $\phi \in [\alpha_R, \alpha_A]$ and the capillary pressure is therefore also bounded to leading order.

Furthermore, the contact-line motion during the unpinned phase is significantly simpler for small τ. Since the contact angle is approximately constant so too is the meniscus shape. The free surface now simply translates as the contact height changes in a manner proportional to the change in volume. This can be seen in figure 3.2(b), where the contact heights for $\tau \lesssim 10^{-3}$ (shown by the red curve) are either constant during pinned phases (red shaded regions) or vary linearly with the uniform volume flow rate during unpinned phases (unshaded regions).

In contrast, for larger values of τ both the contact-line height and contact angle vary during the unpinned phase, which can be seen in figure 3.2 for solutions with $\tau \geq 10^{-1}$. In this case, the contact height variation is no longer linear for a uniform flow rate, and the meniscus shape continues to change as the contact line advances or recedes. This is a result of the interplay between the contact-line law and the Young-Laplace problem.

3.4.3 Small relaxation parameter dynamics

The simpler dynamics exhibited for $\tau \ll 1$ reflect the fact that further model reduction is possible in this regime, which we outline in this section. This reduction, which we refer to as the fast relaxation model, is underpinned by the fact that the system exhibits fast-slow dynamics for small τ. By considering the dynamics on the slow timescale, which is associated with the volume flow rate, as well as the distinct pinned and unpinned phases of the contact line, we show that in this regime, the leading order contact-line motion is independent of the contact-line law while the macroscopic contact angle remains bounded within the hysteresis range to leading order.

Firstly, for flows on the slow advective timescale ($Q = O(1)$ and $t = O(1)$), the leading-order equation for the evolution of the contact line (3.11) reduces to the algebraic equation $F(\phi; \alpha_R, \alpha_A) = 0$. From the definition of F in (2.48) we conclude that

$$\begin{array}{rll} \phi \sim \alpha_A & \text{if} & H_t > 0, \\ \phi \sim \alpha_R & \text{if} & H_t < 0, \\ \alpha_R \leq \phi \leq \alpha_A & \text{if} & H_t = 0, \end{array} \tag{3.20}$$

and thus the macroscopic contact angle is restricted to the range $\alpha_R \leq \phi \leq \alpha_A$ to leading order.

Furthermore, in the unpinned phase of the contact-line motion, where we assume $H_t = O(1)$, a regular perturbation analysis of (3.11) shows that $\phi \sim \alpha + \tau\phi_1$, where α is either the microscopic receding or advancing contact angle as per (3.20). The $O(\tau)$ correction to the contact angle ϕ_1 is obtained from expanding the contact-line law F on the right hand side of (3.3) for small τ, and we find that

$$\phi_1 = \frac{H_t}{G_\phi(\alpha, \alpha)}, \tag{3.21}$$

where G is defined by (2.49).

As discussed in §3.2.3, the meniscus height h can be written in terms of the mean and relative meniscus heights denoted by $\bar{h}(t) = V(t)/A$ and $\tilde{h}(r; \phi)$ respectively, where the latter is independent of the fluid volume and depends only on the macroscopic contact angle. For $\phi = \alpha + O(\tau)$, we find that $h = \bar{h}(t) + \tilde{h}(r; \alpha) + O(\tau)$

and thus, by differentiating (3.14) with respect to time, the leading-order contact-line velocity is

$$\frac{\mathrm{d}H}{\mathrm{d}t} \sim \frac{Q}{A}. \tag{3.22}$$

Combining (3.21) and (3.22) we obtain the expression

$$\phi_1 = \frac{Q}{AG_\phi(\alpha;\alpha)}, \tag{3.23}$$

for the correction to the macroscopic contact angle in terms of the volume flow rate. The expression in (3.23) shows good agreement with numerical simulations for small τ for both an advancing and receding contact line, which is shown in figure 3.3. Meanwhile equation (3.22) shows the contact-line velocity to be independent of the form of the contact-line law and is proportional to the volume flow rate, which explains the linear variation of the contact height under a uniform flow rate in figure 3.2.

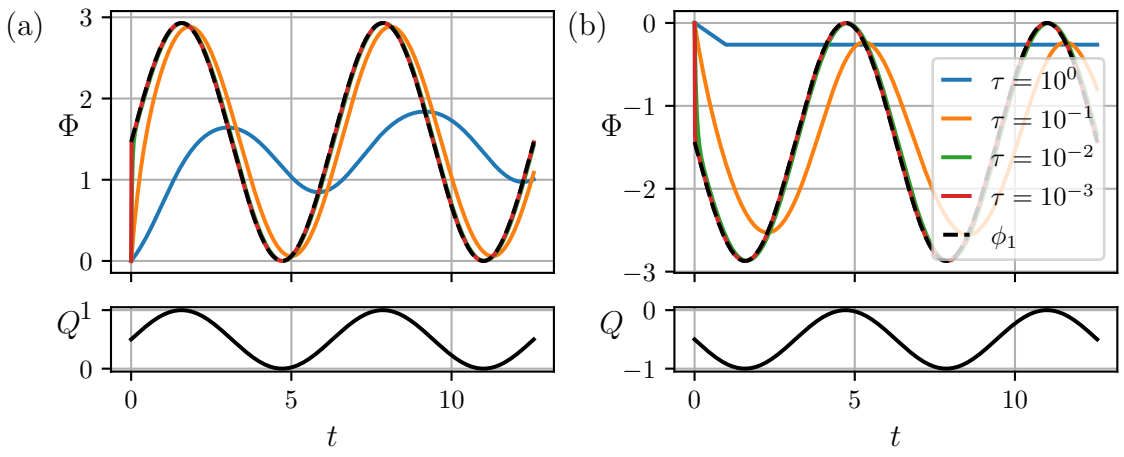

Figure 3.3: Scaled deviation $\Phi = (\phi - \alpha)/\tau$ between the macroscopic and microscopic contact angles calculated from numerical solutions with a prescribed oscillating volume flow rate Q as indicated for a range of values of the relaxation parameter τ. The first-order deviation ϕ_1 predicted by equation (3.23) is also shown by a dashed line. Close agreement is observed for sufficiently small τ. (a) Deviation from the advancing angle α_A under a positive flow rate and (b) deviation from the receding angle α_R under a negative flow rate.

We also examine the dynamics on the fast timescale t/τ for $Q = 0$, which is relevant for when the flow rate vanishes before changing sign. In this case, if the contact angle is outside of the pinned range (i.e. $\phi \notin [\alpha_R, \alpha_A]$) then (3.11) shows that

it must relax back to equilibrium at either $\phi = \alpha_R$ or $\phi = \alpha_A$ on the fast relaxation timescale. The relaxation of the contact line, which can be seen in the previous section in figure 3.2 during periods of zero flow, is further illustrated in figure 3.4. We note that this fast relaxation also occurs when $Q = O(1)$ if the initial contact angle lies outside the hysteresis range with a deviation larger than $O(\tau)$.

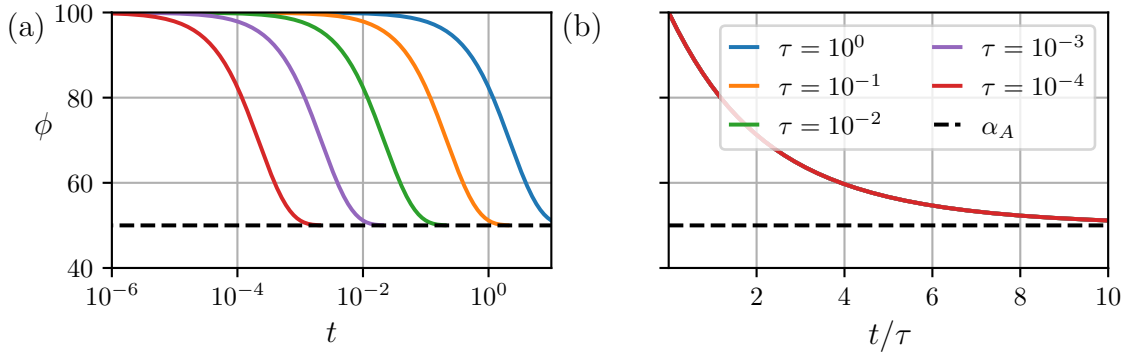

Figure 3.4: (a) Relaxation of the macroscopic contact angle ϕ to the microscopic advancing contact angle $\alpha_A = 50°$ in the absence of an imposed rate from an initial contact angle of $\phi(0) = 100°$. The relaxation is shown for a range of values for the relaxation parameter τ as indicated. (b) The relaxation curves collapse onto a single plot when time is normalised by the relaxation parameter τ, which provides the timescale for relaxation.

These results form the basis of the fast relaxation reduction, which we state below. We stress that the model as stated relies on the contact line being uniform and thus applies only for the horizontal circular geometry, although it remains valid for non-zero Bond numbers. However, aspects of this analysis, in particular the distinct pinned and unpinned phases of the contact line, remain applicable in the case of a non-uniform contact line, which we discuss in §3.5.

We consider the regime $\tau \ll 1$ and work to leading order in τ in both the contact height H and contact angle ϕ, as well as derived quantities such as the capillary pressure. We assume that the initial conditions are such that $\phi(0) \in [\alpha_R, \alpha_A]$, since we have established that otherwise the contact line will rapidly relax back to lie within this range, and the imposed flow rate $Q(t)$ is at most of order unity.

The reduction entails replacing the equation governing the evolution of the contact-line position (3.3) with the leading order expression obtained in (3.22). This equation

is therefore

$$\frac{\mathrm{d}H}{\mathrm{d}t} = \frac{Q(t)}{A}\mathbb{I}_{[\phi \notin (\alpha_R, \alpha_A)]}(\phi), \tag{3.24}$$

where $\mathbb{I}$ is the indicator function taking a value of one when the indicated condition is satisfied and zero otherwise. The remaining model equations are unchanged.

The fast relaxation model is simpler than the standard reduced model since the leading-order contact-line velocity is independent of the exact form of the contact-line law. This simplifies the computation of numerical solutions and avoids the inherent stiffness associated with small values of τ. Moreover, this regime is particularly relevant to the physical problems under consideration, since relaxation of the contact line is typically rapid in comparison to the timescale associated with the imposed flow.

This model also explains the simpler unpinned contact-line dynamics observed when the relaxation parameter is small. Specifically, during the unpinned phase, the contact angle remains fixed to leading order at the advancing or receding contact angle, and it is only the contact height which varies with the flow. Furthermore, the leading-order contact-line velocity is set by the imposed flow rate, being equal to the rate of increase of the mean fluid height, and is independent of the contact-line law.

Another key feature of the small relaxation parameter regime is that the macroscopic contact angle ϕ remains restricted to the range $[\alpha_R, \alpha_A]$ at leading order in τ. Consequently, the capillary pressure and meniscus cap volume are similarly bounded at leading order and satisfy $P_\gamma(\alpha_R) \leq P_\gamma(\phi) \leq P_\gamma(\alpha_A)$, and $V_{cap}(\alpha_R) \leq V_{cap}(\phi) \leq V_{cap}(\alpha_A)$. We note that the contact line is pinned when the contact angle is in the interior of its given range (i.e. $\phi \in (\alpha_R, \alpha_A)$) but at the endpoints the contact line is typically unpinned, though in the absence of flow it may be pinned at these values.

Figure 3.5 shows the typical dynamics in the small relaxation parameter regime, highlighting the pinned and unpinned phases of the contact line as well as the variation in the meniscus shape. We use the same alternating flow rate as for previous solutions in §3.4.2 but without any periods of zero flow to more clearly illustrate the distinction between pinned and unpinned phases. We observe that the meniscus shape and

contact angle, and thus the capillary pressure, remain constant to leading order during unpinned phases of the contact line.

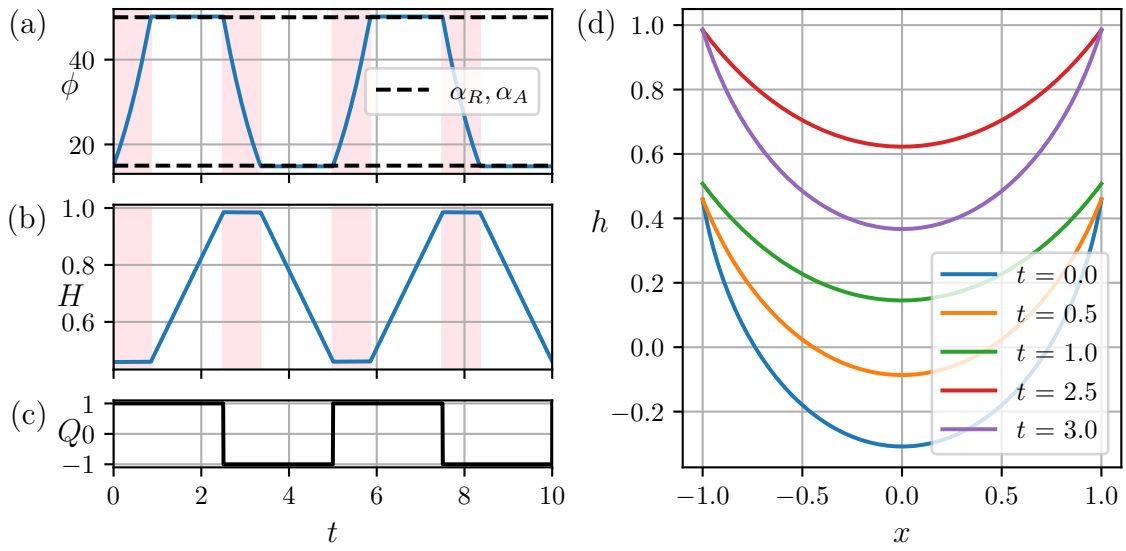

Figure 3.5: Single-well dynamics for the small relaxation parameter regime $\tau \ll 1$. The alternating volume flow rate $Q(t)$ is prescribed and the initial conditions are $(V(0), \phi(0)) = (0, 15°)$ with $(\alpha_R, \alpha_A) = (15°, 50°)$. (a) The variation in the contact angle $\phi(t)$ and (b) the variation of the contact height $H(t)$. The pinned phases of the contact line are shown by red shading and the microscopic advancing and receding contact angles are indicated. (c) The imposed volume flow rate $Q(t)$. (d) The free surface profile h (viewed along the plane $y = 0$) at various times to illustrate the motion of the meniscus. The profiles at $t = 0$ and $t = 0.5$ share the same contact height (at $x = \pm 1$) and illustrate how the meniscus shape changes during the initial pinned phase. Meanwhile the profiles at $t = 1$ and $t = 2.5$ share the same shape and contact angle and illustrate the first unpinned phase as the contact line advances. The profile at $t = 3$ is during the second pinned phase after the flow direction is reversed and shares the same contact height as the profile at $t = 2.5$ which is the point of flow reversal.

3.4.4 Contact angle hysteresis

We now examine the effects of contact angle hysteresis, focussing on the small relaxation parameter regime due to its physical relevance. In this regime, the hysteresis range $[\alpha_R, \alpha_A]$ also sets the range of possible values for the macroscopic contact angle, capillary pressure, and meniscus cap volume. A greater hysteresis range results in a greater range for these quantities, while in the absence of hysteresis, where $\alpha_R = \alpha_A$,

the values of these three quantities are also fixed.

In the simple hysteresis-free case, there is no contact-line pinning for non-zero flow rates, and therefore the contact angle is constant in time, serving merely as a parameter to set the initial shape of the meniscus. This shape is itself invariant and the free surface translates uniformly during the subsequent dynamics according to the flow rate. Furthermore, in this case the state of the system depends solely on the current fluid volume; it is fully reversible and independent of the flow history. In particular, the contact height can be expressed as a function of the fluid volume and the equation governing the contact-line evolution (3.24) can be reparametrised accordingly to remove any explicit time dependence.

However, in the general case with hysteresis where $\alpha_R \neq \alpha_A$, two variables, taken to be the pairing (V, ϕ), are required to describe the state of the system. It is not usually possible to reparametrise and write $\phi = \phi(V; \phi(0))$, thereby describing the system in terms of the fluid volume $V(t)$ alone. This is because the general dynamics do depend on the history of the system, specifically the points at which the contact line transitions between its pinned and unpinned phases, and not just on the current fluid volume. As the flow oscillates, the contact-line state need not be the same at times which share the same fluid volume. Two exceptions can occur for $\alpha_R \neq \alpha_A$, these are if the flow is unidirectional or the flow is sufficiently small so that the contact line remains pinned throughout the entire motion.

The hysteresis of the contact angle is illustrated in figure 3.6 under a range of flow regimes. The typical hysteresis curve is shown in figure 3.6(a). We see that any period of unpinned contact-line motion followed by a reversal in the flow direction results in hysteresis, and the contact angle can no longer be parameterised by the fluid volume. In contrast, if the contact line remains pinned for all time, the hysteresis loop collapses to a single curve which can be parameterised by the fluid volume. This is shown in figure 3.6(b), while figure 3.6(c) illustrates the contact angle behaviour under a unidirectional flow, where the contact angle can also be parameterised by the fluid volume.

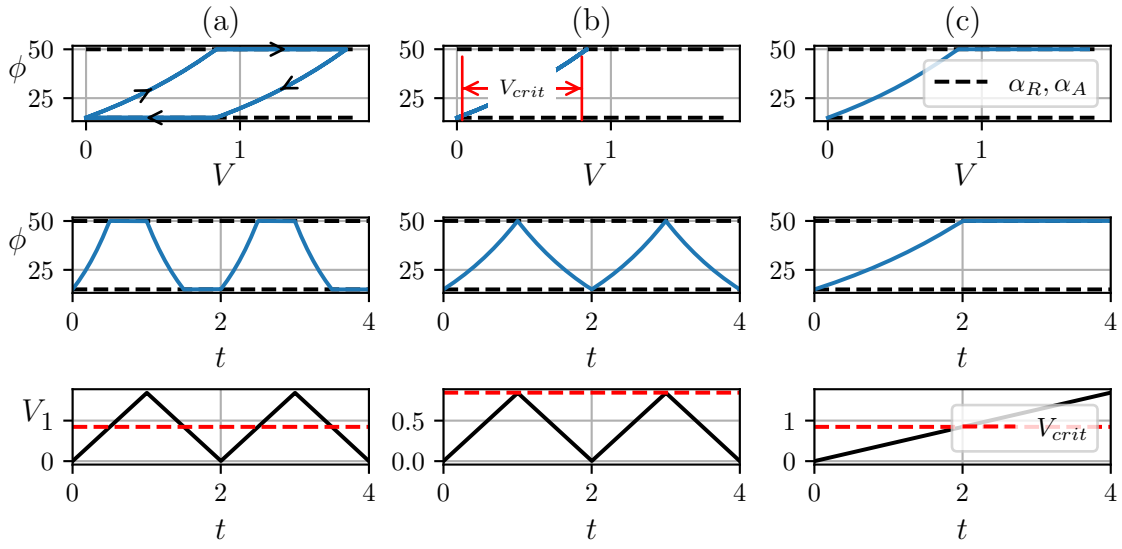

Figure 3.6: Contact angle hysteresis curves for $\tau \ll 1$ showing the variation of the macroscopic contact angle ϕ with the fluid volume V for a variety of prescribed volume flow rates (as indicated by the fluid volume). The corresponding variation of both the contact angle and fluid volume with time are also shown. In all cases, the initial conditions are $(V(0), \phi(0)) = (0, 15°)$ and the microscopic receding and advancing contact angles are $(\alpha_R, \alpha_A) = (15°, 50°)$, which are indicated. The critical transfer volume V_{crit} (as defined in the main text) required for the system to transition from the receding contact angle to the advancing contact angle is also shown. (a) General oscillatory flow rate exhibiting a typical hysteresis loop which includes unpinned contact-line dynamics, (b) smaller amplitude oscillatory flow rate to ensure the contact line remains pinned to exhibit a collapsed hysteresis curve, and (c) a constant unidirectional flow rate. The latter two flow regimes are examples of special cases for which the contact angle can be parameterised in terms of the fluid volume.

In a practical setting, contact angle hysteresis is generally undesirable because it results in variability of the macroscopic contact angle and the state of the system. While it is straightforward for an experimenter to measure and control volumes via the imposed flow rate, measuring the initial contact angle at the beginning of each experiment is cumbersome and such measurements are also prone to error. However this information is needed to model the subsequent evolution of the system. Furthermore, ideally an experimenter performs repeated runs of the same experiment under identical conditions, which requires controlling the initial contact angle configuration rather than simply measuring it.

Our analysis provides a method to overcome this difficulty and convert the system

to a known state with a specified contact angle from an arbitrary starting state. This method relies on the fact that if the contact line is advancing or receding under an imposed flow, then the macroscopic contact angle relaxes back to either the advancing or receding contact angle once the flow stops. Consequently, if a sufficient volume of fluid is injected or removed from the system, via the imposed flow rate, so as to ensure that the contact line becomes unpinned, then the contact angle at the end of this influx or efflux is known to be equal to either the advancing or receding contact angle.

The volumes required to be injected or removed from the system can be calculated in terms of the meniscus cap volume. Specifically, we define the transfer volume by

$$V_{tr}(\phi_1 \to \phi_2) = V_{cap}(\phi_2) - V_{cap}(\phi_1), \tag{3.25}$$

which for $\phi_1, \phi_2 \in [\alpha_R, \alpha_A]$ gives the change in fluid volume required for a transition from contact angle configuration ϕ_1 to ϕ_2 during which the contact line remains pinned. Thus for an arbitrary initial contact angle configuration $\phi \in [\alpha_R, \alpha_A]$, the magnitude of the injected fluid volume for the system to reach the advancing contact angle is $V_{tr}(\phi \to \alpha_A)$ while the magnitude of the fluid volume to be removed from the system to reach the receding contact angle is $|V_{tr}(\phi \to \alpha_R)|$.

The magnitude of both of these quantities is bounded by the critical transfer volume, defined by

$$V_{crit} = V_{tr}(\alpha_R \to \alpha_A) = V_{cap}(\alpha_A) - V_{cap}(\alpha_R). \tag{3.26}$$

This is the fluid volume required to be pumped into the well for a meniscus initially at the receding contact angle to reach the advancing contact angle. By symmetry, it is also the fluid volume required to be pumped out of the well for a meniscus initially at the advancing contact angle to reach the receding contact angle. We note that the magnitude of the critical volume is set by the hysteresis range and this volume is indicated in figure 3.6.

It follows that regardless of the initial contact-line configuration, any influx or efflux of fluid that exceeds this critical transfer volume is sufficient to ensure the

contact line becomes unpinned and thus reaches a known contact angle configuration. From this known state, we can then add or remove the appropriate volume of fluid, as given by the transfer volume (3.25), to reach a given contact angle configuration ϕ. The initial steps of this procedure are illustrated in figure 3.7.

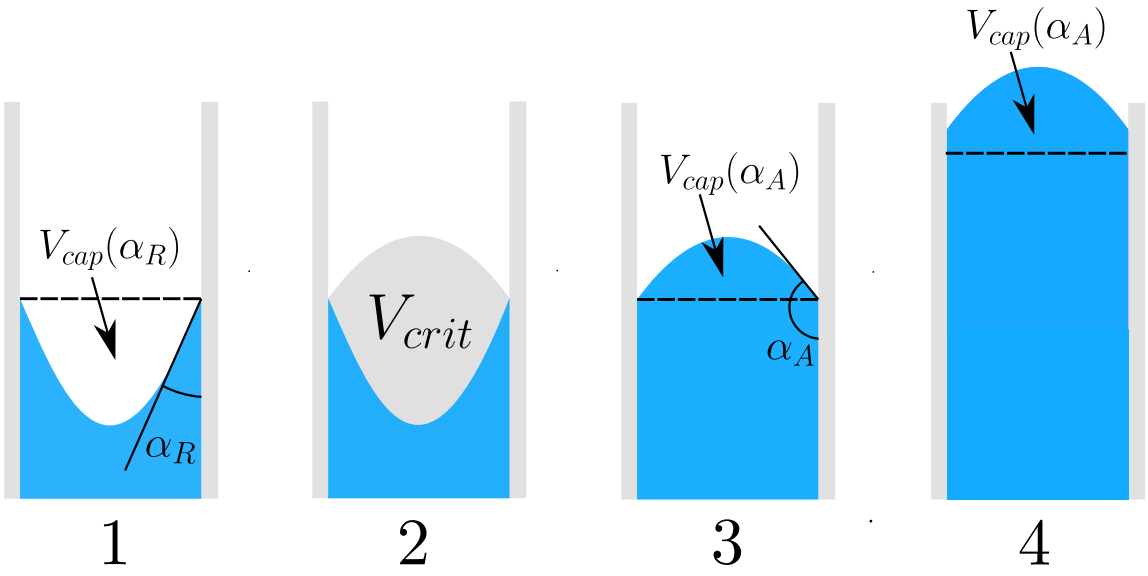

Figure 3.7: Schematic illustrating the critical transfer volume V_{crit} and the procedure to convert the system to the known state at the advancing contact angle configuration. (1) The system is initially at equilibrium at the receding contact angle α_R. (2) A volume of fluid equal to the critical volume V_{crit} is injected into the system by the imposed flow rate. (3) During this time, the contact line remains pinned and the macroscopic contact angle increases until it reaches the advancing contact angle α_A, at which point the meniscus is on the edge of moving. (4) If the injected volume exceeds the critical volume then the contact line will become unpinned, however once the flow stops the contact angle will relax back to the advancing contact angle α_A.

Thus it is possible to experimentally set the system in a known initial state, from which point our model can be used to determine the subsequent dynamics of the contact line. Furthermore, by controlling the specific initial state an experimenter can ensure repeatability of experiments. We note that this method is not restricted to the small relaxation parameter regime, although for larger τ we must wait longer to ensure the relaxation of the contact line is complete. However, it does require knowledge of the microscopic advancing and receding contact angles, which can be obtained by prior measurement.

The transfer volume and meniscus cap volume can also be used to inform the optimal flow rate for desired system dynamics. For instance, we can identify the appropriate oscillatory flow rate to ensure that the contact angle and thus the capillary pressure remain within some desired interval, or to ensure that the contact line remains pinned throughout the dynamics, as in figure 3.6(b). Ultimately, this understanding provides an experimenter with direct control over the state of the system, and thus the capillary pressure, through the imposed volume flow rate. These ideas are also applicable to the twin-well system, and we shall develop these concepts further in chapter 4.

3.4.5 Gravitational effects: the Young-Laplace problem

We now consider the effect of gravity on the dynamics of the horizontal circular well system. We note that in the previous analysis for $\mathrm{Bo} = 0$ the assumption that $\theta = 0$ was not strictly necessary. The axisymmetric spherical cap solutions for the meniscus shape remain valid for $\theta \neq 0$ since the Young Laplace equation (3.12) has no dependence on the elevation angle for $\mathrm{Bo} = 0$. Consequently, under the reduced model (which assumed sufficiently slow variations in the elevation angle as part of the derivation) the contact-line dynamics are not affected by tilting the system in the absence of gravity. However, for non-zero Bond numbers, the assumption $\theta = 0$ is required to admit axisymmetric solutions of the Young-Laplace equation (3.12).

In this section, we consider the behaviour of a horizontal system for non-zero Bond numbers. We find that while gravitational effects do alter the shape of the free surface, the resulting dynamics of the contact line do not differ significantly from the zero Bond number solutions. In this section, we briefly examine the Young-Laplace problem for the meniscus shape for non-zero Bond numbers and discuss the moving contact-line problem in §3.4.6.

We seek axisymmetric solutions of the Young-Laplace problem with non-zero Bond number subject to an imposed contact-line height and fluid volume, corresponding to equations (3.12)-(3.14) as stated in §3.4. For a given fluid volume we label solutions according to the value of the contact angle ϕ which satisfies (3.15). For $\mathrm{Bo} \neq 0$, these

equations do not have an exact solution, and we cannot find closed-form expressions for the meniscus shape. However, it is straightforward to solve the system numerically, while asymptotic solutions are readily available in the limits of both small and large Bond numbers [47], and small Bond number solutions are illustrated in figure 3.8(c). Furthermore, it is not necessary to use the Surface Evolver scheme to solve the axisymmetric problem, and we instead use the standard boundary value problem solver implemented in `scipy`, which uses a fourth-order collocation method to solve the problem and is less computationally intensive than the Surface Evolver scheme.

The meniscus shape for the zero-volume solution and for a representative contact angle is shown in figure 3.8(a) for a range of Bond numbers. The spherical cap solution for $\mathrm{Bo} = 0$, is also shown for comparison. As the Bond number increases, the meniscus shape becomes flatter as gravitational effects become more significant. For large Bond numbers, gravitational effects dominate and the meniscus is almost completely flat. This is exemplified by the solution for $\mathrm{Bo} = 100$, although we shall generally restrict attention to Bond numbers of order at most unity. This corresponds more closely to typical experimental regimes where gravitational and capillary effects are comparable.

From these numerical solutions for the meniscus shape we can extract the relationship between the contact-line height and contact angle $H(\phi)$. Furthermore, for axisymmetric solutions the meniscus cap volume V_{cap} remains defined by equation (3.19) and satisfies $V_{cap}(\phi) = -\pi H(\phi)$. As before, the cap volume provides an alternative way to characterise the relationship between the contact angle and contact height and will again prove useful in relating the imposed flow rate to changes in the meniscus shape. Meanwhile, the hydrostatic and capillary pressures, defined by equations (3.6) and (3.7), are given respectively by $P_h = \mathrm{Bo}\bar{h}$ and $P_\gamma = -2\cos\phi$.

The relations between these key quantities are summarised in figure 3.8. Figure 3.8(b) shows the variation of the meniscus cap volume with the contact angle for a range of Bond numbers, while figure 3.8(d) shows the corresponding variation of the capillary pressure with the cap volume. Plots for the spherical cap meniscus $\mathrm{Bo} = 0$ are also shown for comparison. It can be seen overall that the magnitude of the cap

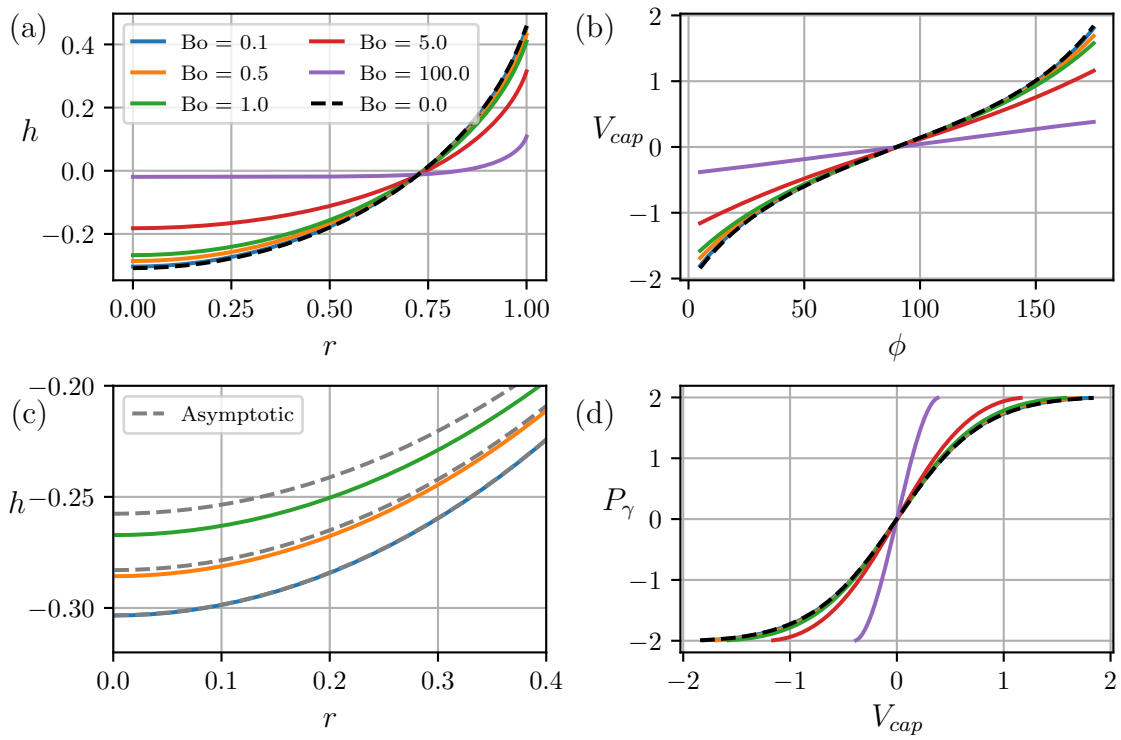

Figure 3.8: (a) Exemplar zero-volume axisymmetric meniscus profiles $h(r)$ for a uniform contact angle $\phi = 15°$ shown for a range of Bond numbers as indicated. (c) Comparison of numerical and asymptotic solutions for the meniscus shape showing good agreement for small Bond numbers. (b) Meniscus cap volume V_{cap} as a function of the contact angle ϕ and (d) the capillary pressure P_γ as a function of the meniscus cap volume for a range of Bond numbers. Solutions corresponding to Bo = 0 are shown by a dashed line for comparison.

volume decreases with Bond number and that this decrease is most significant for more extreme contact angles further from 90°. This agrees with physical intuition: as the Bond number increases the meniscus shape becomes flatter and so the cap volume decreases. Furthermore, contact angles closer to 90° correspond to solutions which are nearer to a flat meniscus for any Bond number. Indeed the meniscus is flat for $\phi = 90°$ even in the absence of gravity.

Solving the Young-Laplace problem and determining the relationship between the contact-line height and contact angle allows us to examine the moving contact-line problem for non-zero Bond numbers. The similarity of the solution curves relating the contact angle and meniscus cap volume in figure 3.8 suggests that the qualitative

differences in the system dynamics will be limited as the Bond number varies. We do however expect a quantitative difference from the zero-Bond number solutions, with a more significant difference for both larger Bond numbers and more extreme contact angles, and we discuss these differences in the next section.

3.4.6 Gravitational effects: the moving contact line

The impact of the Bond number on the contact-line dynamics is felt primarily through the Young-Laplace problem. For a horizontal system where the contact-line motion is driven by an imposed flow, the overall dynamics remain as outlined in §3.4.2 onwards for the zero-Bond number solutions. To summarise this briefly, the dynamics can be divided into pinned and unpinned phases of motion, which are set by the contact angle and the hysteresis range, and the relaxation parameter governs the deviation between the macroscopic and microscopic contact angles. In our discussion of the contact-line motion for non-zero Bond number, we continue to restrict attention to the small relaxation parameter regime $\tau \ll 1$. Furthermore, we present results for the standard hysteresis range $(\alpha_R, \alpha_A) = (15°, 50°)$, noting that the qualitative behaviour of the system is the same across all (non-zero) hysteresis ranges.

Figure 3.9(a) illustrates the typical dynamics of the contact line by showing the hysteresis of the contact angle for a range of experimentally relevant small Bond numbers under an imposed alternating flow regime, shown in figure 3.9(d). The typical behaviour of the system remains the same across all Bond numbers, though there are some quantitative differences that result from the changing relationship between the contact height and contact angle. In particular, the critical transfer volume V_{crit}, which is the change in volume associated with a transition between the advancing and receding contact angle, decreases as the Bond number increases for a fixed hysteresis range. This is summarised in figure 3.9(b).

More generally, as the Bond number increases, the same change in fluid volume has a more significant impact on the shape of the meniscus and results in a larger change in the contact angle and capillary pressure during pinned phases. Such quantitative differences must be accounted for when calculating the appropriate flow rates for the

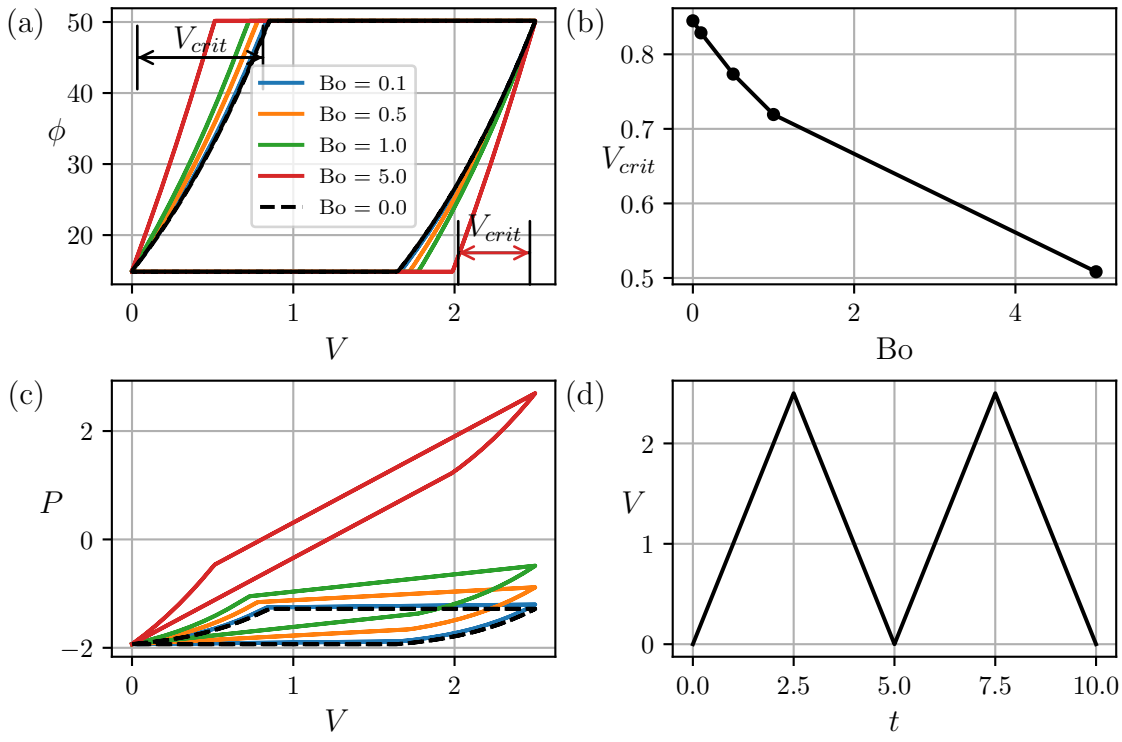

Figure 3.9: (a) Contact angle hysteresis curves for $\tau \ll 1$ showing the variation of the macroscopic contact angle ϕ with the fluid volume V for a variety of Bond numbers as indicated under an alternating volume flow rate. In all cases, the initial conditions are $(V(0), \phi(0)) = (0, 15°)$ and the standard hysteresis range is used. The critical transfer volume V_{crit} required for the system to transition from the receding contact angle to the advancing contact angle is also highlighted for the Bo = 0 and Bo = 5 solutions. (b) The variation of the critical transfer volume V_{crit} with Bond number. (c) The corresponding hysteresis curve for the variation of the total pressure P with the fluid volume V. (d) The prescribed variation of the fluid volume V with time t under the alternating flow rate.

desired operation of the system, such as in determining the critical transfer volume or prescribing imposed flow rates so that the contact line remains pinned.

We note that while the contact angle and thus capillary pressure are more sensitive to changes in volume for larger Bond numbers, the range of the contact angle and capillary pressure remains the same and is set by the hysteresis range in the small relaxation parameter regime. However, the variation and range of the total pressure do increase with Bond number, as shown by the pressure hysteresis curves in 3.9(c). This is because, for non-zero Bond numbers, the pressure now has a hydrostatic

component which continues to vary during pinned phases of the contact-line motion. We discuss this pressure variation in further detail below.

3.4.7 Pressure variation

The total pressure is divided into a hydrostatic and capillary component, as defined by (3.6) and (3.7). The hydrostatic pressure is determined by the current fluid volume while the capillary pressure is set by the contact angle. We note that the hydrostatic pressure scales with the Bond number and so becomes more significant as gravitational effects increase. Meanwhile, the capillary pressure remains bounded to leading order with $P_\gamma(\alpha_R) \leq P_\gamma \leq P_\gamma(\alpha_A)$ in the regime $\tau \ll 1$, and this range is independent of the Bond number.

The pressure is a key output of our model as it is important in understanding the twin-well system, where pressure differences ultimately drive the fluid flow. Thus it is the pressure change that is of most interest rather than the absolute pressure. We observe that both the hydrostatic and capillary pressure change more rapidly with the fluid volume for larger Bond numbers, which can be seen, for instance, from figure 3.8(c) for the capillary pressure.

To examine the variation in pressure under an imposed flow we define the total pressure difference from the initial value by $\delta P = P(t) - P(0)$. Figure 3.10(a) shows the variation of the total pressure difference with an increasing fluid volume as the system transitions from the receding contact angle to the advancing contact angle for a range of Bond numbers. Figures 3.10(b) and (d) show the hydrostatic and capillary components of this pressure change, while figure 3.10(c) shows the percentage contribution of the capillary pressure to the total pressure change.

We observe that both the hydrostatic and capillary components of pressure initially increase with the fluid volume and that, as expected, this increase is more rapid for larger Bond numbers for both pressure components. However, the capillary pressure remains constant (to leading order) once the advancing contact angle is attained, while the hydrostatic pressure continues to increase proportionally to the fluid volume.

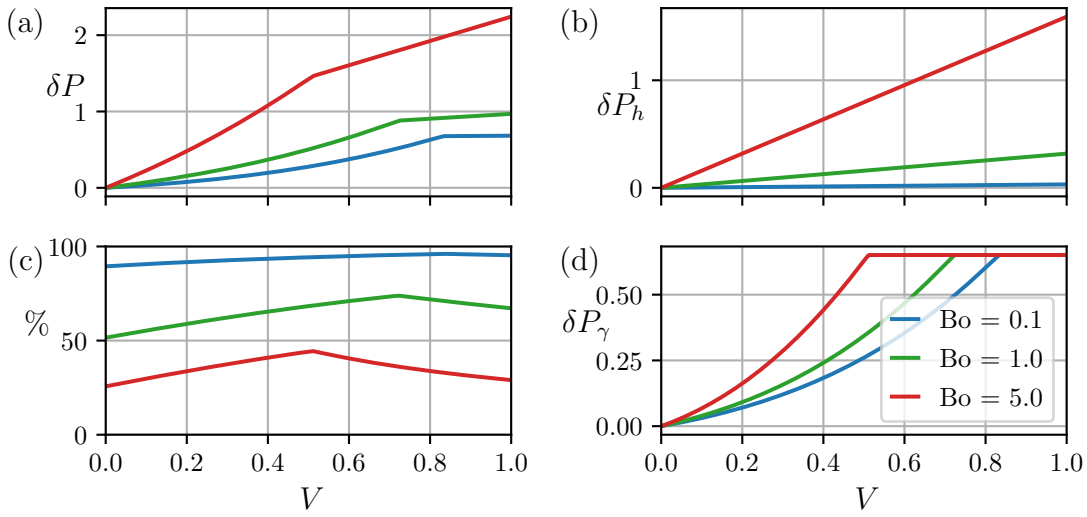

Figure 3.10: (a) Variation of the total pressure difference δP as the fluid volume V increases. (b) The variation in the hydrostatic pressure difference δP_h. (c) The percentage contribution of the capillary pressure difference to the total pressure difference. (d) The variation in the capillary pressure difference δP_γ. Solutions are shown for a range of Bond numbers as indicated; in all cases the initial conditions are $(V(0), \phi(0)) = (0, 15°)$ and the standard hysteresis range is used.

For larger Bond numbers, the capillary pressure constitutes a smaller overall percentage of the total pressure change. However, for the Bond numbers considered the capillary pressure initially constitutes a significant proportion (at least 25% for Bo ≤ 5) of the total pressure change and typically increases more rapidly than the hydrostatic pressure until the advancing contact angle is attained. We note that similar behaviour is observed for a decreasing fluid volume when the system begins at the advancing contact angle, where the pressure is instead decreasing, although the corresponding figures are omitted here.

Figure 3.10 highlights that for Bond numbers of order unity, the magnitude of the capillary and hydrostatic pressure changes are comparable. While for a purely unidirectional flow, the hydrostatic pressure will ultimately dominate since the capillary pressure is bounded, this is not representative of typical operating conditions where the flow direction alternates. At each point of flow reversal, we expect variations in the capillary pressure to be important.

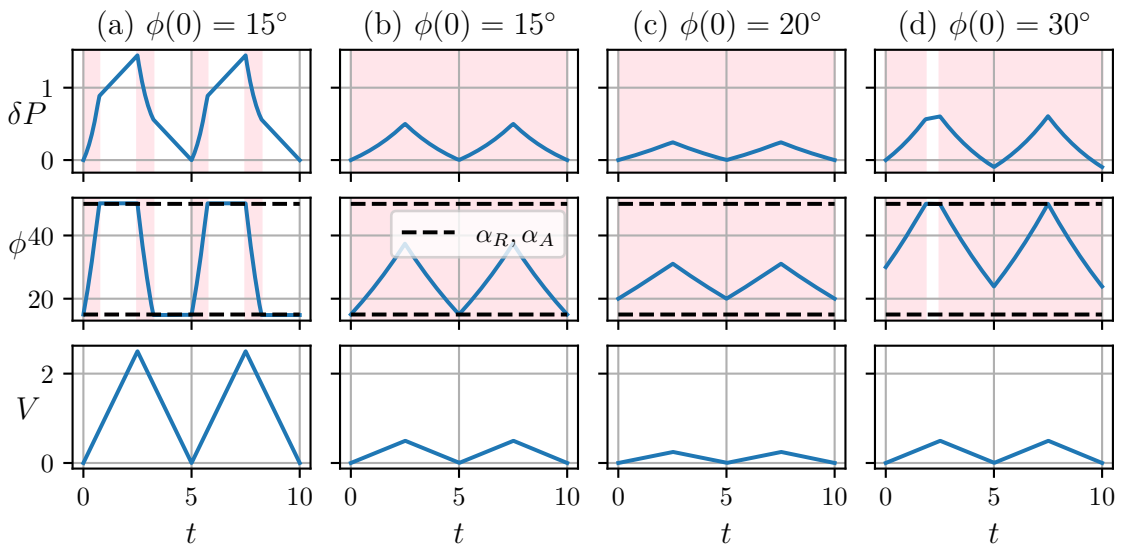

Figure 3.11: Four solutions of the dynamic contact-line problem under an alternating volume flow rate with different volume amplitudes and initial contact angle configurations, which are indicated. The total pressure difference δP, the contact angle ϕ, and the fluid volume V are shown in each case as a function of time t. Pinned phases of the contact line are indicated by red shading. In all cases, the initial fluid volume is $V(0) = 0$, the Bond number is $\mathrm{Bo} = 1$, and the standard hysteresis range is used.

The variation of pressure under a range of representative operating conditions is shown in figure 3.11, which also shows the corresponding variation in the contact angle and the imposed alternating flow rate. Overall, oscillations in the fluid volume of fixed amplitude and period which arise from an alternating flow rate produce oscillations of the same period in the total pressure. The precise form of the oscillating pressure depends on the flow amplitude and the initial contact angle configuration and figure 3.11 demonstrates the possible behaviour of the system.

Unless $\alpha_R = \alpha_A$, in which case there is no contact angle hysteresis, the total pressure does not vary uniformly in time. The total pressure varies more quickly during pinned phases of the contact line (indicated by red shading) since both pressure components vary. However during unpinned phases, the leading-order contact angle is constant and so only the hydrostatic pressure changes, which varies in proportion to the fluid volume.

Figures 3.11(a) and (b) show solutions for which the contact angle is initially equal

to the receding contact angle but with different flow amplitudes. In the former, the flow amplitude is such that the contact line ultimately becomes unpinned, as the fluid volume transferred is greater than the critical transfer volume, while in the latter, the smaller flow amplitude means that the contact line is pinned throughout. In both cases, provided the initial flow rate is positive, periodic oscillations in the fluid volume result in periodic oscillations in the pressure. Similar behaviour occurs for a system which begins at the advancing contact angle when the flow is initially negative.

Slightly different behaviour is observed when the initial contact angle is not equal to the receding or advancing angle initially. If the oscillation amplitude is small, so that the contact line remains pinned (see 3.11(c)), then periodic oscillations in the volume again produce periodic oscillations in the pressure. However, if the contact line becomes unpinned (see 3.11(d)), there is an initial transient period and periodic oscillations in the pressure begin only from the point at which the flow direction is reversed.

The behaviour illustrated by the examples in figure 3.11 is common across the full range of Bond numbers and hysteresis ranges. The precise value of the critical transfer volume, which affects the observed behaviour, will vary with these parameters however. We recall that it is straightforward to set up the system to control the initial contact angle configuration, and therefore the pressure variation can also be controlled via the imposed flow rate. Furthermore, for regular periodic flows, it is typically only necessary to model a single flow period, since with the exception of some initial transient behaviour due to contact angle hysteresis, the response of the system is also periodic.

3.4.8 Summary

In this section we have explored axisymmetric solutions of the moving contact-line problem, including the associated Young-Laplace problem, for a horizontal system. We have considered the behaviour of the system under a range of parameter regimes, focussing particularly on the experimentally relevant small relaxation parameter regime

$\tau \ll 1$ for which distinct behaviour is observed. We note that the qualitative behaviour of the system remains mostly unchanged as the remaining parameters of the Bond number and the microscopic advancing and receding contact angles vary. Special cases of note include the zero gravity limit ($\mathrm{Bo} = 0$), where exact solutions to the Young-Laplace problem are available, and the hysteresis-free limit where $\alpha_R = \alpha_A$, in which the system dynamics are greatly simplified since the contact angle, capillary pressure, and meniscus shape are all constant in time.

Through our analysis, we have introduced concepts such as the pinned and unpinned phases of the contact-line motion and the critical transfer volume. These concepts are important for characterising the behaviour of the system and will be developed further in subsequent sections for both the single and twin-well systems. We have also discussed the practical applications of this modelling work, including how our results can be exploited to prepare the system in a known contact angle configuration via the imposed volume flow rate, or to determine the appropriate flow operating conditions to achieve desired variations in the total pressure. The total pressure is a key output of our single-well model due to its importance for the dynamics of the twin-well system, where it drives the flow.

While many key features of the single-well dynamics can be shown through our analysis of the horizontal system under an imposed flow, in practice the system may also be subject to oscillations in the elevation angle. In such cases, gravitational effects have a more significant impact on the system dynamics than in the case of a horizontal system. We extend our analysis to investigate the impact of a varying elevation in the next section.

3.5 Tilted circular well

We extend our analysis of the single-well system with a circular cross-section to incorporate the effects of a varying elevation angle. A tilting system results in additional complexity since solutions of the Young-Laplace problem for the meniscus shape are no longer axisymmetric in general. Thus, the contact angle and contact height vary

along the contact line, and the relationship between these two quantities can no longer be reduced to a function of a single variable, of the form given in (3.17) for instance, as for a uniform contact line.

We predominantly use the Surface Evolver numerical scheme to solve the model equations, due to the increased complexity of the Young-Laplace problem. However, for small elevation angles asymptotic analysis can provide additional insights and can be used to further validate the numerical scheme.

We consider the system dynamics under a range of illustrative parameter and operating regimes, prescribing the volume flow rate $Q(t)$ and the elevation angle $\theta(t)$ independently. Initially, we consider the effects of tilting in the absence of flow. We then consider the combined effects of a varying elevation angle and an imposed volume flow rate, and we compare our results with the axisymmetric solutions for a horizontal system under the corresponding flow regime to highlight the impact of tilting.

3.5.1 Parameters and variables

In this section, we restrict attention to the physically relevant fast relaxation regime by setting $\tau = 10^{-3}$ in our numerical solutions. We present the system dynamics for a range of illustrative Bond numbers and hysteresis ranges, as set by the microscopic receding and advancing contact angles α_R and α_A. We restrict attention to non-zero Bond numbers since, as discussed in §3.4, in the absence of gravity solutions are insensitive to the elevation angle.

For non-zero elevation angles, the contact line is typically non-uniform and the contact angle $\phi(s,t)$ and contact height $H(s,t)$ vary along the well perimeter, which is parameterised by the polar angle / perimeter arc length s. To better describe the state of the contact line, it is convenient to identify the left and right halves of the contact line with those points satisfying $x < 0$ and $x > 0$ respectively, where $x = \cos s$ is the usual Cartesian x-coordinate. We further define the left and rightmost contact angles by $\phi^-(t) = \phi(\pi, t)$ and $\phi^+(t) = \phi(0, t)$ respectively, with the corresponding left and rightmost contact heights given by $H^-(t) = H(\pi, t)$ and $H^+(t) = H(0, t)$.

Finally, we define the effective mean contact angle $\bar{\phi}(t)$ which satisfies

$$P_\gamma = -2\cos\bar{\phi}, \tag{3.27}$$

and corresponds to the value of the contact angle in a system with a uniform contact line for a given capillary pressure. The effective mean contact angle supports comparison with the corresponding axisymmetric solutions and often provides a more intuitive description of the state of the contact line than the capillary pressure.

Finally, as in previous sections, we consider zero initial volume solutions without loss of generality so that $V(0) = 0$. Furthermore, to simplify our analysis and to match typical experimental conditions, we suppose that the system is initially horizontal with $\theta(0) = 0$ and with no variation along the contact line. Thus the initial meniscus shape is axisymmetric and we specify the initial contact angle configuration via $\phi(s, 0) = \phi_0$.

3.5.2 Tilting without flow

We consider variations of the elevation angle in the absence of flow. Specifically, we consider simple oscillations of the elevation angle with $\theta(t)$ varying linearly between $\theta = 0^\circ$ and $\theta = \pm\theta_A$, where θ_A is the oscillation amplitude. These transitions occur in transition time T_{tr}, so that the total oscillation period is $4T_{tr}$.

We note however that in the fast relaxation regime $\tau \ll 1$ the equations are autonomous to leading order in τ, assuming $\dot{\theta} = O(1)$. The leading-order contact-line dynamics are therefore invariant, up to a suitable rescaling of time, to changes in the transition time as well as the functional form of the transitions, provided these remain monotonic. We therefore take $T_{tr} = 1$ here without loss of generality.

We first consider the behaviour of the contact line during the initial elevation from the horizontal to the maximum amplitude (i.e. up to time T_{tr}). This is illustrated in figure 3.12 for a variety of hysteresis ranges $[\alpha_R, \alpha_A]$, while other parameters are fixed, to illustrate the possible behaviour of the contact line. For each example, a profile view of the contact height and the corresponding variation in the contact angle at various stages of the initial elevation are shown, along with the variation of the mean, left, and right contact heights and contact angles with the elevation angle.

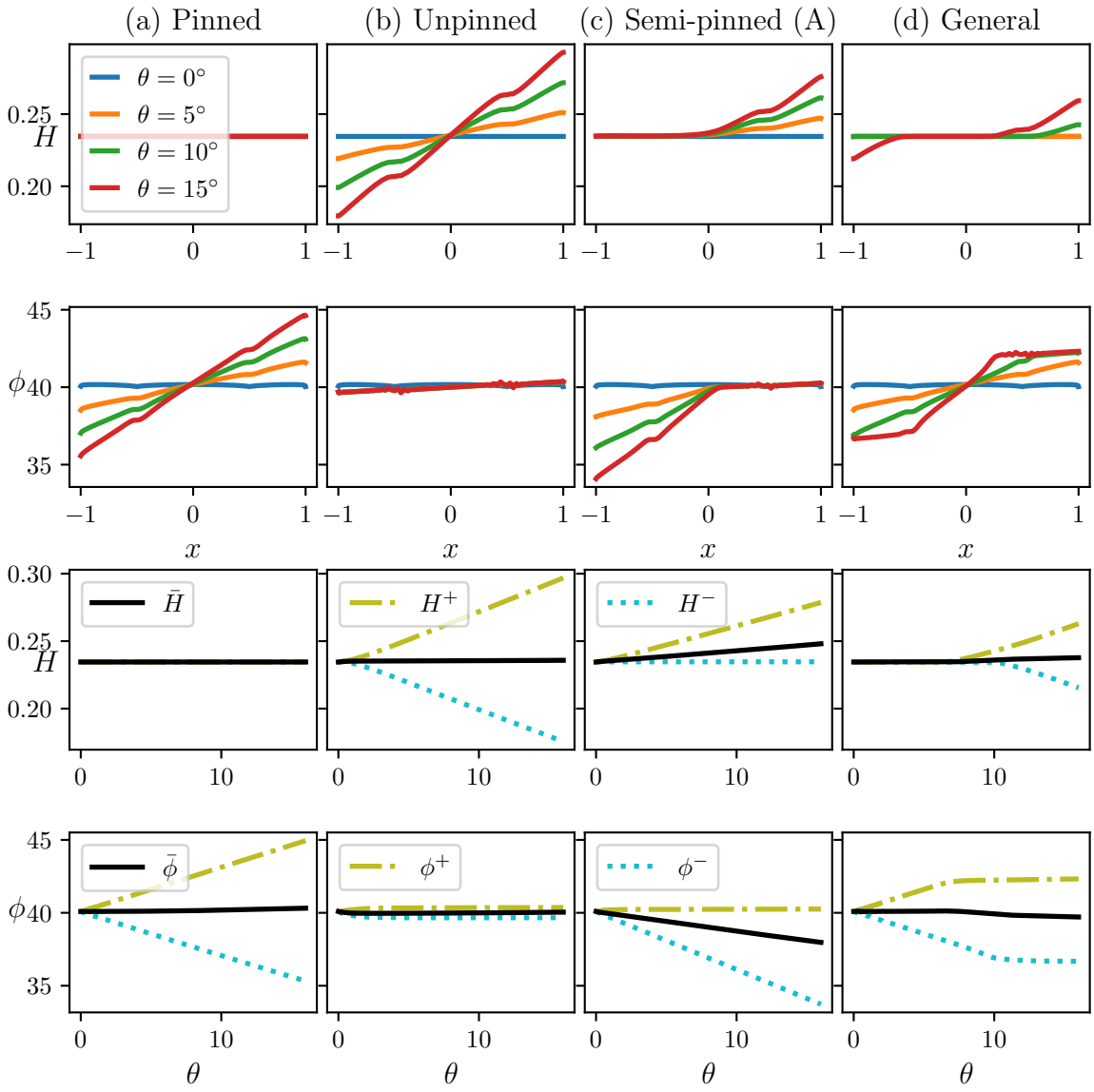

Figure 3.12: Variation of the contact-line height H and the contact angle ϕ along the front portion of the contact line ($y < 0$) viewed in profile at various stages of the initial elevation for each regime. The evolution of mean, left and rightmost contact heights $\bar{H}$ and H^- and H^+ as well as the effective mean contact angle $\bar{\phi}$ and left and rightmost contact angles ϕ^- and ϕ^+ as a function of the elevation angle θ are also shown. In all cases, solutions are obtained for Bo $= 1$, $\theta_A = 15°$, and $\phi_0 = 40°$. The hysteresis range $[\alpha_R, \alpha_A]$ corresponding to each regime is $[0°, 180°]$ for the pinned regime, $[40°, 40°]$ for the unpinned regime, $[0°, 40°]$ for the semi-pinned advancing (A) regime, and $[30°, 50°]$ for the general example.

In general, see 3.12 (d), as the elevation angle increases the contact angles along the right-hand portion of the contact line increase until the advancing angle is reached, at which point the contact line will advance. Meanwhile the contact angles along the

left-hand portion of the contact line decrease with the contact line receding once the receding contact angle is obtained. Importantly, the contact line does not vary uniformly with points closer to the left and rightmost edges (corresponding to $x = -1$ and $x = 1$ respectively) changing most rapidly. Consequently, the contact line can be in a variety of different states, with some portions of the contact line pinned while other portions are in motion.

In addition to the representative general example in 3.12 (d), which illustrates the partial pinning of the contact line, three special regimes are shown. These regimes are where (a) the contact line remains fully pinned throughout, (b) the contact line is fully unpinned throughout, with one half advancing and the other half receding, and (c) the contact line is semi-pinned where one half of the contact line is advancing or receding, and the other half is pinned.

In figure 3.12, these regimes are obtained by an appropriate choice of the hysteresis range. In particular, fully pinned behaviour is obtained for a suitably wide hysteresis range, while fully unpinned behaviour occurs only in the case of no contact angle hysteresis where $\alpha_R = \alpha_A = \phi_0$. A pure semi-pinned contact line is obtained for non-zero hysteresis ranges in cases where either $\alpha_A = \phi_0$, for an advancing contact line (as shown), or $\alpha_R = \phi_0$, for a receding contact line (not shown here). In general however, the contact-line behaviour is a combination of these regimes, consisting of an initial pinned period followed by partial unpinning of the contact line and depends on the relationship between the system parameters and initial contact angle.

3.5.3 Variations in pressure

The above categorisation of the contact line is also useful in understanding the variation of pressure in a tilting system. We recall that the hydrostatic pressure component (3.6) can be determined in terms of the volume and elevation angle, without solving for the motion of the contact line. Thus we restrict our discussion to the capillary pressure P_γ, or equivalently the effective mean contact angle $\bar{\phi}$, defined by (3.7) and (3.27), respectively.

Figure 3.13(a) summarises the percentage increase in the capillary pressure relative to its initial magnitude for the four exemplar solutions presented in figure 3.12, with the pressure variation for the semi-pinned receding solution additionally shown. The change in capillary pressure is significantly lower for the pinned and unpinned regimes than it is for the semi-pinned regimes. Furthermore, for the representative general example the initial change in capillary pressure is small, but a more significant decrease is observed once the contact line becomes partially unpinned.

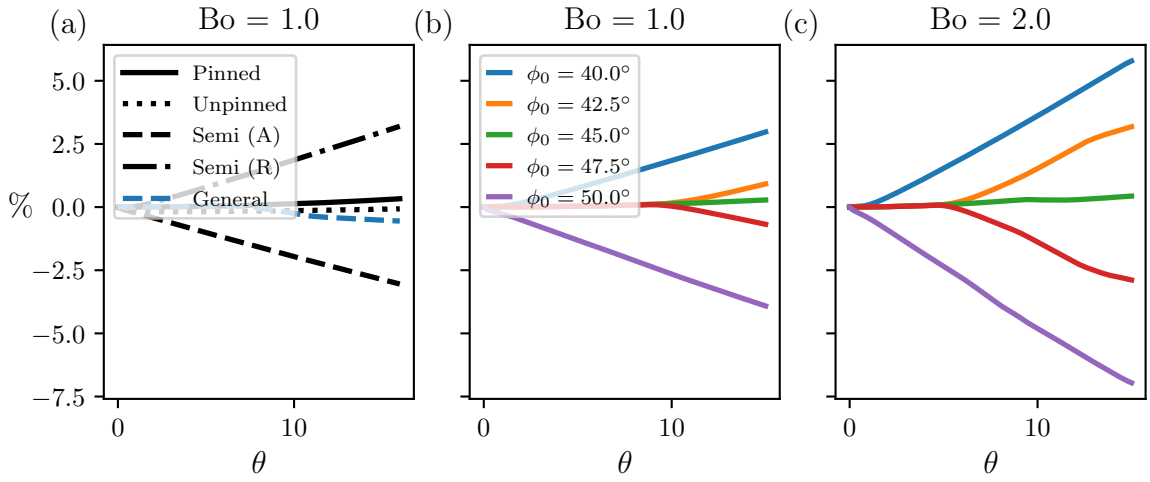

Figure 3.13: Percentage increase in the capillary pressure (relative to its initial magnitude $|P_\gamma|$) as a function of the elevation angle θ for a range of operating regimes. (a) Capillary pressure increase for the examples shown in 3.12 with $\phi_0 = 40°$; the semi-pinned receding (R) regime with hysteresis range $[40°, 180°]$ is also shown. (b) and (c) Capillary pressure increase for solutions corresponding to a fixed hysteresis range $[40°, 50°]$ for various initial contact angles ϕ_0 and Bond numbers as indicated.

Intuitively, these observations can be explained by noting that in the fully pinned regime, the contact angle increases on one half of the contact line and decreases on the other, and these deviations from the initial uniform value approximately cancel when integrated to obtain the capillary pressure. Meanwhile in the fully unpinned regime, the contact angle is fixed and thus the capillary pressure is unchanged. Conversely, in the semi-pinned regime, or more generally when the contact line is only partially pinned, the variation along the contact line is no longer symmetric, which results in more significant changes to the capillary pressure. We observe that, for fixed values of

θ_A, Bo, and ϕ_0, the two semi-pinned solutions result in the most significant pressure deviation, since contact line asymmetry occurs from the outset.

For the small elevation angles that we typically consider, we can explain these observations more formally by considering asymptotic solutions for the meniscus shape, which are viewed as perturbations to the axisymmetric solution. Posing expansions for h, ϕ, H and P_γ in the small parameter θ, it is straightforward to see that for the fully pinned and unpinned solutions the leading-order correction to the capillary pressure must be $O(\theta^2)$. This is because the change in capillary pressure is independent of the elevation direction, with solutions invariant under $\theta \to -\theta$ and $x \to -x$. This symmetry is lost if the contact line is only partially pinned, in which case there is a larger $O(\theta)$ correction to the capillary pressure.

Restricting attention to a pinned contact line, we can obtain a leading-order expression for the contact angle configuration at a given elevation angle θ. By expanding in powers of $\sin\theta$, we find that

$$\phi(s) \sim \phi_0 + (\mathrm{Bo}\ H_0 \sin\theta \sec\phi_0)\cos s, \tag{3.28}$$

where H_0 is the initial contact-line height corresponding to the axisymmetric solution with uniform contact angle ϕ_0. The derivation of this expression follows the approach presented in [83] for the similar problem of a pinned droplet on a tilted plane. This approach considers the balance of forces acting on the surface to determine an expression for the contact angle without finding the full shape of the meniscus.

We see from the above expression that the leading-order deviation in the contact angle is proportional to $\mathrm{Bo}\sin\theta$, which corresponds physically with the magnitude of the gravitational force in the x-direction. It also depends on the initial contact angle ϕ_0. This term does not contribute to the leading-order capillary pressure deviation, however numerical solutions show that the pressure deviation increases with both the elevation angle and Bond number in all contact line regimes. Figures 3.13(b) and (c) illustrate this by showing the percentage capillary pressure increase with elevation angle for two different Bond numbers. These plots also stress how the contact-line behaviour depends on the initial contact angle and the hysteresis range; here the

hysteresis range is fixed and the initial contact angle varies in contrast to the previous examples. We observe that larger Bond numbers result in a greater deviation in the capillary pressure, with the contact line becoming unpinned at smaller elevation angles (see figures 3.13(b) and (c) for $42.5 \leq \phi_0 \leq 47.5$, for example). However, for typical parameter regimes we find that the total deviation in the capillary pressure is small, for instance the deviation is below 5% for Bo ≤ 1 and $\theta \leq 15°$ for the illustrative hysteresis range $[40°, 50°]$.

3.5.4 Oscillating contact line

The above discussion pertains only to the initial elevation of the system. We now extend our analysis to the full oscillation cycle. Figure 3.14 shows the variation of the effective mean contact angle under periodic oscillations for examples of the pinned, unpinned, and semi-pinned regimes. A clear distinction can again be seen between these regimes.

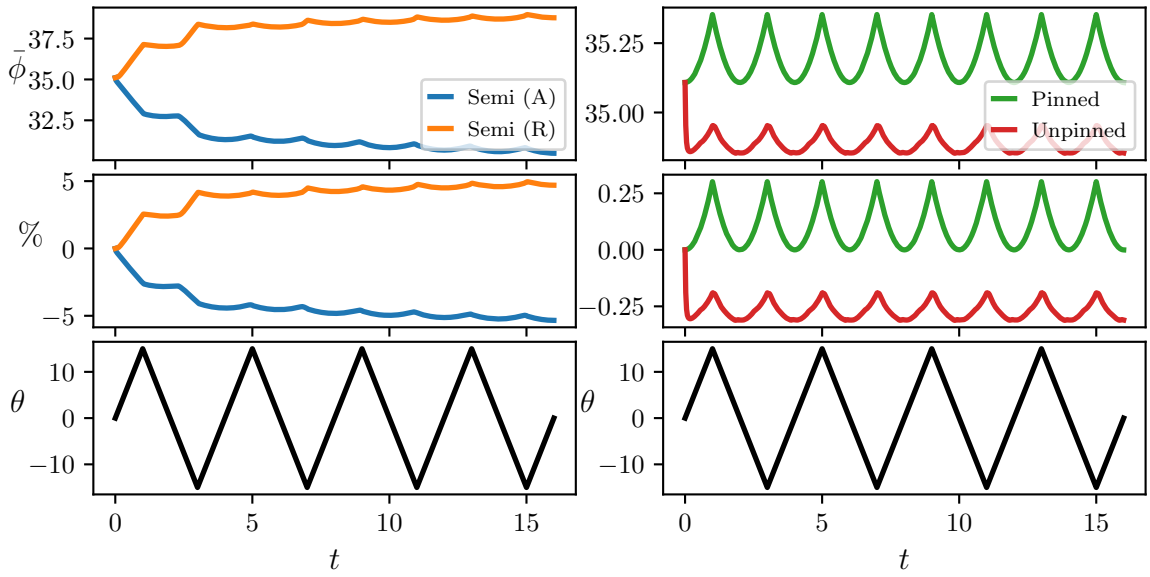

Figure 3.14: Variation of the effective mean contact angle $\bar{\phi}$ and the percentage change in the capillary pressure (relative to the magnitude of its initial value) under regular periodic oscillations in the elevation angle θ as shown. Solutions for the pinned, unpinned, semi-pinned (advancing) and semi-pinned (receding) regimes are shown, which are obtained by appropriately varying the hysteresis range for a fixed initial contact angle.

Firstly, we see that the fully pinned and unpinned regimes both result in similar periodic oscillations in the mean contact angle and thus capillary pressure. This is because the contact-line dynamics are fully reversible in these cases, with any changes in the contact line reversed as the system returns to the horizontal. For the pinned regime, this follows immediately from the fact that solutions depend only on the Young-Laplace equation, while for the unpinned regime this is a consequence of the small relaxation parameter. Thus solutions depend only on the current elevation angle and not the oscillation history.

In contrast, semi-pinned and partially pinned solutions exhibit dependence on the oscillation history due to contact angle hysteresis. For example, in the semi-pinned advancing regime, the right-hand portion of the contact line advances while the left-hand portion is pinned during the initial elevation. However, upon the return to the horizontal the right-hand portion of the contact line is pinned, while the left-hand portion later begins to advance as the elevation angle decreases further.

The asymmetry in the contact-line dynamics, which results from contact angle hysteresis, has a corresponding effect on the capillary pressure. After multiple oscillation cycles, the pressure variations ultimately begin to undergo regular oscillations. However, since the initial elevation changes result in the most significant change in capillary pressure, due to the asymmetric contact-line motion, these oscillations are not usually centred on the initial value. However, if the hysteresis range is sufficiently large, the amplitude of these oscillations is small as the contact line remains mostly pinned throughout the later oscillations.

There are parallels between the contact-line dynamics for a tilting system and for a horizontal system under an imposed flow rate. For non-zero hysteresis ranges, the contact-line dynamics are reversible (depending not on the history but only on the current elevation angle or volume respectively) only when the contact line remains pinned throughout. In our analysis of the horizontal system, we identified the critical fluid volume beyond which the contact line becomes unpinned. For an oscillating system, we can similarly define a critical oscillation amplitude θ_c, beyond which the

contact line becomes unpinned. Indeed, we can make use of (3.28) to obtain an asymptotic expression for this threshold, which is given implicitly by

$$\mathrm{Bo}\ \tilde{h}_0 \sin\theta_c \sec\phi_0 = \min\left\{\phi_0 - \alpha_R, \alpha_A - \phi_0\right\}, \tag{3.29}$$

and depends on the Bond number, initial elevation angle, and hysteresis range.

In principle, the critical elevation amplitude is useful as it can be used to inform device operating regimes for which the variation in the capillary pressure is minimised due to the contact line remaining pinned. While the capillary pressure deviation is significantly larger in cases where the contact line is partially unpinned due to contact angle hysteresis, the percentage difference under typical operating conditions is still not too large for $\mathrm{Bo} \leq 1$. However, in practice tilting the devices also induces a net fluid flow in each well, and thus it is important to investigate the combined effects of flow and tilting on the contact line.

3.5.5 Flow and tilting

We examine tilting of the single-well system under an imposed flow rate, which is chosen to be representative of the tilting induced flows of the twin-well system, which we examine in chapter 4. We illustrate the contact-line dynamics under the combined tilting and flow regimes and compare the variation of the mean contact angle and capillary pressure with the corresponding flow regime in a horizontal system. We thereby assess the significance of tilting on the capillary pressure under typical operating regimes. We find in general that the variation in the capillary pressure due to tilting is less significant than that due to an imposed flow rate. Furthermore, the imposed flow rate can act to oppose the asymmetry introduced by tilting and thus reduce the deviation from the axisymmetric solution.

To demonstrate the single-well dynamics, we consider solutions for $\mathrm{Bo} = 1$ under the hysteresis range $[30°, 50°]$. As in the previous section, we vary the initial contact angle ϕ_0 to obtain different contact-line regimes. Furthermore, we consider two distinct flow regimes which are representative of flows in the twin-well system. The first is the simultaneous flow regime, where the volume flow rate is proportional to

the variation in the elevation angle. The second is the sequential flow regime, where tilting and the volume flow occur separately and sequentially.

3.5.5.1 Simultaneous flow

We begin by considering the simultaneous flow regime where the volume flow rate is

$$Q(t) = k\dot{\theta}(t), \tag{3.30}$$

for some constant of proportionality k. This form is motivated by the typical flow rates achieved in the twin-well system when driven by a slowly varying elevation angle, which we demonstrate in §4.3. Since we continue to consider oscillations in the elevation angle with amplitude θ_A and transition time T_{tr}, the volume flow rate is an alternating piecewise constant function taking values $\pm k\theta_A/T_{tr}$. We take $k = 1$, $\theta_A = 10^\circ$ and $T_{tr} = 1$ in this section to provide illustrative results.

For these simultaneous flows, the variation in the effective mean contact angle is shown in figure 3.15 for a variety of different initial contact angles corresponding to particular contact-line pinning regimes. These are a general partially pinned scenario and the semi-pinned advancing and receding regimes. The corresponding variation in the contact angle for a horizontal system under the same imposed flow rate is also shown, indicated as the axisymmetric solution (AS).

Overall, there is only a limited difference between the mean contact angles for the tilted and horizontal solutions, which continues over the course of multiple oscillation cycles. The corresponding percentage difference between the capillary pressure for these solutions is no more than 2% for these examples, which is representative of other typical parameter regimes.

Furthermore, the percentage difference in capillary pressure between the two solutions is markedly smaller than the percentage difference that results from tilting only, as we considered in the previous section. This is particularly pronounced in the semi-pinned regimes, which were associated with the greatest change in capillary pressure in the case of tilting alone. This is because while tilting acts on each side of the contact line differently, moving one side towards an advancing state and the

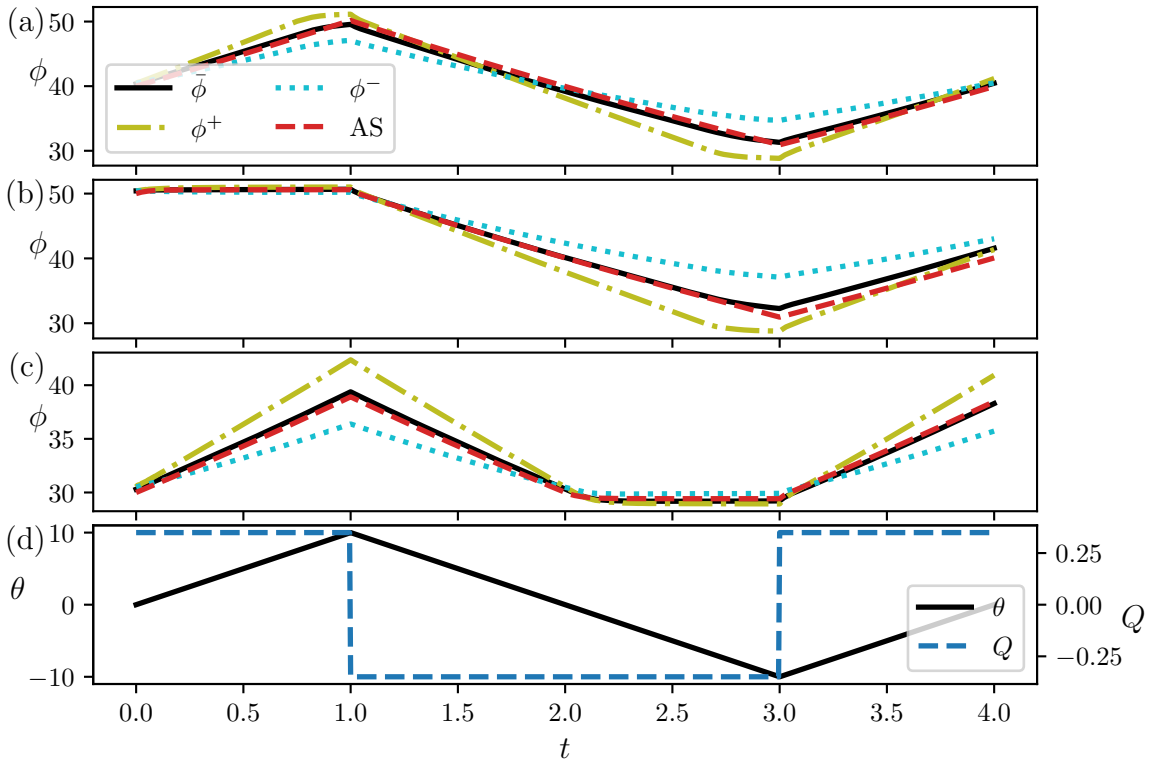

Figure 3.15: Variation of the effective mean contact angle $\bar{\phi}$ and the leftmost and rightmost contact angles ϕ^- and ϕ^+ under prescribed oscillations in the elevation angle θ and volume flow rate Q corresponding to the simultaneous tilt and flow regime. Illustrative examples for (a) a general partially pinned scenario, (b) the semi-pinned (advancing) and (c) the semi-pinned (receding) regimes are shown, which are obtained by varying the initial contact angle ϕ_0 for the fixed hysteresis range $[15°, 50°]$. The corresponding contact angle for the axisymmetric solution (AS) under the same flow rate but without tilting is shown for comparison.

other towards the receding state, the volume flow rate acts uniformly. In semi-pinned scenarios, it therefore acts to mitigate the asymmetry in the contact line due to tilting.

We conclude therefore that the change in volume has a more significant impact on the capillary pressure than the change in elevation angle, as evidenced by the good agreement between the axisymmetric and tilted solutions. In this flow regime, the axisymmetric solution can therefore serve as a good approximation to the full tilting system if we are primarily interested in the mean contact angle / capillary pressure rather than the details of the contact line. This is typically the case for the twin-well system and thus this approximation can offer significant computational savings.

3.5.5.2 Sequential flow

We now consider the second flow regime of sequential tilting and flow. Here, the elevation angle oscillates with amplitude θ_A and transition time T_{tr}, with pauses of the same duration at the oscillation maxima, minima, and midpoint. As the system tilts the volume flow rate is zero, while during pauses in the elevation angle the flow is uniform, with amplitude $\pm k\theta_A/T_{tr}$ as for the simultaneous flow regime. We note a full cycle now takes total time $8T_{tr}$ and we again take $k = 1$, $\theta_A = 10^\circ$ and $T_{tr} = 1$ for illustrative results, which are shown in figure 3.16.

We observe that there is a more significant difference between the tilting and axisymmetric solutions in this regime, particularly where the contact line is semi-pinned. This difference is most apparent for the semi-pinned receding solution in 3.16(c), due to the initial asymmetry introduced by tilting the system without flow. We note in contrast that for the semi-pinned advancing solution in 3.16(b), this initial asymmetry is quickly counteracted by the positive flow rate.

However, while we observe a starker difference between solutions than for the simultaneous tilt and flow regime, the percentage difference in capillary pressure is still typically small at $\sim 2.5\%$ for these solutions. Thus we can also conclude that the axisymmetric solution serves as a good approximation in this operating regime.

3.5.6 Summary

In this section we have considered the contact-line dynamics of an oscillating system both with and without an imposed volume flow rate. Tilting in the absence of flow served to highlight the typical contact-line dynamics from which we identified various contact-line regimes. These regimes are related to the behaviour of the capillary pressure; smaller changes in the capillary pressure are associated with the pinned and unpinned regimes due to the symmetry and reversibility of the contact line in these cases.

We highlighted the impact of the model parameters, with the hysteresis range and initial contact angle affecting the observed contact-line regime, while larger gravita-

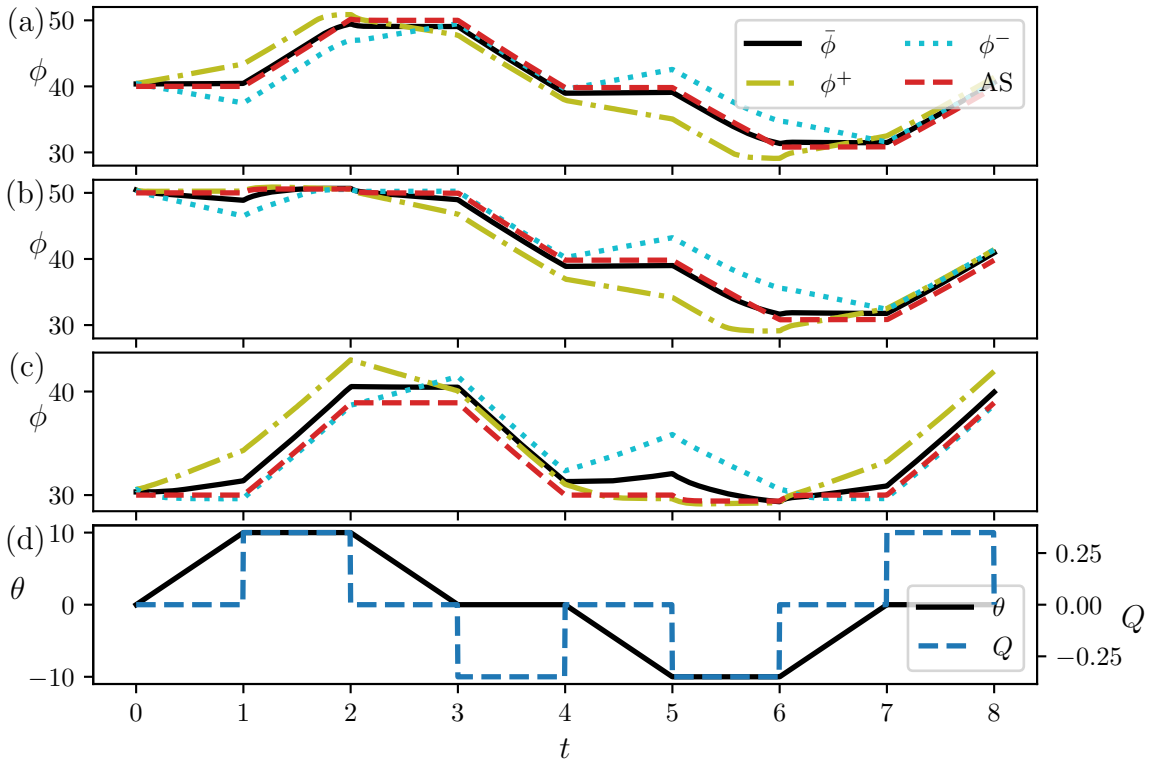

Figure 3.16: Variation of the effective mean contact angle $\bar{\phi}$ and the leftmost and rightmost contact angles ϕ^- and ϕ^+ under prescribed oscillations in the elevation angle θ and volume flow rate Q corresponding to the sequential tilt and flow regime. Illustrative examples for (a) a general partially pinned scenario, (b) the semi-pinned (advancing) and (c) the semi-pinned (receding) regimes are shown, which are obtained by varying the initial contact angle ϕ_0 for the fixed hysteresis range $[15°, 50°]$. The corresponding contact angle for the axisymmetric solution (AS) under the same flow rate but without tilting is shown for comparison.

tional effects, quantified through the Bond number and elevation angle, both increase the capillary pressure change with tilting. Through asymptotic analysis, we also identified a critical elevation angle to keep the contact line pinned, and thus limit the capillary pressure change. However, typical deviations in capillary pressure due to tilting were small in most cases across the typical parameter values. Furthermore, under continuous oscillations deviations in capillary pressure do not increase indefinitely but settle down to regular oscillations.

For tilting with flow, we considered two regimes representative of typical flow conditions in the twin-well system. We observed that the difference between tilted and axisymmetric solutions under the same flow regimes are comparable, with only a

small percentage difference in capillary pressure. This suggests that the axisymmetric solution can be used as an approximation for twin-well dynamics, where we care about the capillary pressure and its effects on the volume flow rate rather than the details of the contact line.

3.6 Discussion

In this chapter, we have characterised the evolution of the free surface and contact line in a single-well system for a range of experimentally relevant operating regimes under the reduced model. The reduced model can be divided into two parts: the associated Young-Laplace problem for the meniscus shape, through which we relate the contact-line height and contact angle, and the evolution equations for the fluid volume and contact-line height, which depend on the contact-line law. The Young-Laplace problem also determines the capillary pressure in terms of the contact angle, which is a key output of our model due to its role in driving the flow in the twin-well system.

Our discussion of the model structure in §3.2 highlighted the dependence of each sub-problem on the system parameters and the different computational challenges associated with each of them. Solving the Young-Laplace problem typically presents the most difficulty, particularly for a general well geometry and elevation angle, and thus in §3.3 we introduced a numerical scheme based on the *Surface Evolver* software package to tackle this problem. We also highlighted the simplifications that are possible in certain special cases for the circular well, which includes the translational invariance of the Young-Laplace problem, and the existence of exact solutions, asymptotic solutions, or simpler numerical solution schemes in certain parameter regimes corresponding to a horizontal system or for small elevation angles.

The evolution of the contact line depends on the value of the macroscopic contact angle through the contact-line law. In §3.4 we first illustrated the dynamics in the simplest case of a horizontal circular system, with the contact-line motion driven by an imposed flow rate, before extending this analysis to an oscillating system in

§3.5. We showed how the dynamics of the contact line are affected by contact angle hysteresis, expressed in terms of the microscopic contact angles. Hysteresis results in distinct pinned and unpinned phases of the contact-line dynamics, which are relevant for characterising the general behaviour and understanding the capillary pressure. While in the case of a horizontal circular system the contact line is uniform (i.e. either entirely pinned or unpinned) at any point in time, tilting the system induces partial pinning and a non-uniform contact line, which results in more complex dynamics.

In addition to contact angle hysteresis, we also showed the important role that the relaxation parameter plays in the contact-line dynamics. This parameter sets the timescale for relaxation to equilibrium in the absence of an imposed flow rate or varying elevation angle, as well as the magnitude of the deviation between the microscopic and macroscopic contact angle of an unpinned contact line. We focussed on the physically relevant small relaxation parameter regime $\tau \ll 1$ which serves to simplify the unpinned contact-line dynamics by ensuring that the contact angles, and thus the capillary pressure, remain bounded to leading-order in τ, with this bound set by the hysteresis range.

Our characterisation of the system also provided insights of practical relevance for use in experiments. For example, in §3.4.4 we identified the critical transfer volume, associated with transitions between a fully advancing and fully receding contact line. Injecting or removing a volume of fluid greater than this critical transfer volume provides a method of preparing the system in a known state at the advancing or receding contact angle. This serves to mitigate the uncertainty associated with the existence of a range of stable contact angle configurations which results from contact angle hysteresis, an issue compounded by the difficulty of measuring contact angles in practice. Meanwhile, for an oscillating system we identified the critical elevation angle in §3.5.4, below which the contact line is guaranteed to remain unpinned. This again serves to account for the complexity of contact angle hysteresis, in this case by ensuring the dynamics are time-reversible and controlling the variation of the capillary pressure.

Overall, our work in this chapter has focussed on understanding how the device operating regime impacts the contact-line dynamics and the capillary pressure. This understanding lays the foundation for the twin-well system, where the flow is driven by the pressure difference across the wells. We note that concepts introduced in this chapter, such as transfer volume or critical elevation angle, will prove useful as we consider similar criteria in a twin-well system that remove the variability introduced by contact angle hysteresis.

Additionally, our analysis suggests potential methods for approximating the contact-line dynamics, which are particularly useful when extending to the case of a twin-well system. For instance, our analysis of an oscillating system showed that tilting has only a small impact on the capillary pressure provided the contact line remains unpinned, while in the general case of both flow and tilting, the axisymmetric solution of the Young-Laplace problem, which neglects the varying elevation angle, often provides a good approximation to the capillary pressure. We shall revisit these ideas in the context of the twin-well system, particularly as our focus shifts from the contact-line dynamics to the pressure difference and flow rate. However, in order to retain the effects of tilting in a non-uniform contact line while keeping computation of the contact-line dynamics feasible, we opt to consider a two-dimensional well geometry as we extend our analysis to flow in a twin-well system in chapter 4.

Chapter 4

Fluid flow in a twin-well system

4.1 Introduction

In this chapter, we examine the volumetric flow in a twin-well microfluidic system through analysis of the reduced hydraulic electric circuit analogy model derived in chapter 2. In this model, the flow rate is proportional to the pressure difference across the channel, which consists of both a hydrostatic and a capillary component. The capillary component depends on the contact angle and meniscus shape which we studied in detail in chapter 3, while the hydrostatic component results from differences in fluid volume and from the varying elevation angle.

The goal of our analysis in this chapter is to evaluate the impact of capillary effects on gravity-driven flows in the twin-well system. This builds on our analysis of the evolution of the contact line in chapter 3, however we now focus on the flow rate and volume of fluid in each well rather than the dynamics of the contact line itself. We first characterise the flow rate under various elevation regimes in the absence of surface tension. We then assess how these flows are modified if surface tension effects are incorporated and quantify the difference between the two scenarios in terms of the relevant parameters of the reduced model.

Our model extends previous analysis of similar gravity-driven twin-well systems, which have either neglected capillary effects or considered only a constant capillary pressure in the context of a horizontal system [14, 86], by incorporating the effects of a varying capillary pressure and a non-uniform contact line due to tilting. In addition,

we continue to highlight the practical applications of our analysis, which include how the variability introduced by capillary effects may be controlled through the design and operation of the system.

In this chapter, we restrict attention to a two-dimensional representation of the twin-well system. This simplifies the computation of the associated Young-Laplace boundary value problem for the capillary pressure, while retaining the effects of tilting on the capillary pressure via the non-uniform contact line. This simplification allows us to focus on exploring the qualitative dynamics of the twin-well system, which can in principle be extended to the full three-dimensional geometry. We still make use of the insights obtained from our analysis of the three-dimensional contact-line dynamics in chapter 3 however, as the dynamics of the contact line are similar.

The structure of this chapter is as follows. In §4.2 we briefly outline the two-dimensional system geometry and summarise the reduced model equations, variables, and key parameters. In §4.3 we begin our analysis of this model in the surface tension free sublimit where capillary effects are neglected. We present results for a variety of operating regimes including a horizontal system, with flow driven by volume differences across the wells, and an oscillating system, where we explore the effect of varying the oscillation amplitude and frequency. This analysis serves to introduce the typical behaviour of the twin-well system and acts as a reference for comparison with solutions where surface tension effects are included. We consider these solutions in §4.4 and §4.5 where we consider a horizontal and oscillating system respectively. In each regime we investigate how surface tension effects complicate the twin-well dynamics and discuss how our analysis can be used to inform practical steps which can be taken to mitigate or account for these complications. Finally, we discuss our results and their applications in §4.6.

4.2 Two-dimensional system

In this chapter we consider a two-dimensional representation of the microfluidic system. This is formed from the three-dimensional system geometry, as described in

§2.3 and shown in figure 2.2, by restricting attention to the plane $y^* = 0$. The two-dimensional geometry is illustrated in the schematic diagram in figure 4.1.

We non-dimensionalise the system with lengths scaled according to the reservoir half-width $L_0^* = L_A^*/2$, however it is now more convenient to scale pressure according to the hydrostatic pressure scale $P_0^* = \rho^* g^* L_0^*$ rather than the capillary pressure scale. Furthermore, in two-dimensions, the appropriate velocity scale is $U_0^* = \rho^* g^* {H_D^*}^3/12\mu^* L_D^*$ and we scale time according to the advective timescale $T_0^* = L_0^*/U_0^*$.

Both the Cox-Voinov contact-line law and reduced model for the volume flow rate in the twin-well system continue to apply in two dimensions, with their derivation remaining essentially unchanged (see §2.8 and §2.9). We observe that in two dimensions the well reservoir is rectangular and the contact 'line' consists of just two points at each edge, which we refer to as the left and right-hand contact points. Furthermore, the dimensionless hydraulic resistance for the rectangular channel is $R_h = 1$ with our choice of scaling, with dimensional hydraulic resistance given by $R_h^* = 12\mu^* L_D^*/{H_D^*}^3$ in two dimensions.

We state the reduced model equations in dimensionless form below. We note that these equations consist of a restatement of the equations for the evolution of the contact line analysed in chapter 3 (see §2.8 for statement and derivation) in a two-dimensional geometry and these equations apply to each well of the twin-well system. However, the (two-dimensional) volume flow rate is no longer freely prescribed but determined from the pressure difference between the two wells as derived in §2.9.

4.2.1 Reduced model equations

The reduced model for the twin-well system consists of six state variables (three for each well) governed by ordinary differential equations with respect to time which are coupled to two associated boundary value problems. For each well, indexed by $i = 1, 2$, these variables are the fluid reservoir volume $V_i(t)$ and the left and right contact heights $H_i^{\pm}(t)$, which are measured relative to the reservoir base. The system

along with key reduced model variables and other relevant quantities are shown in figure 4.1.

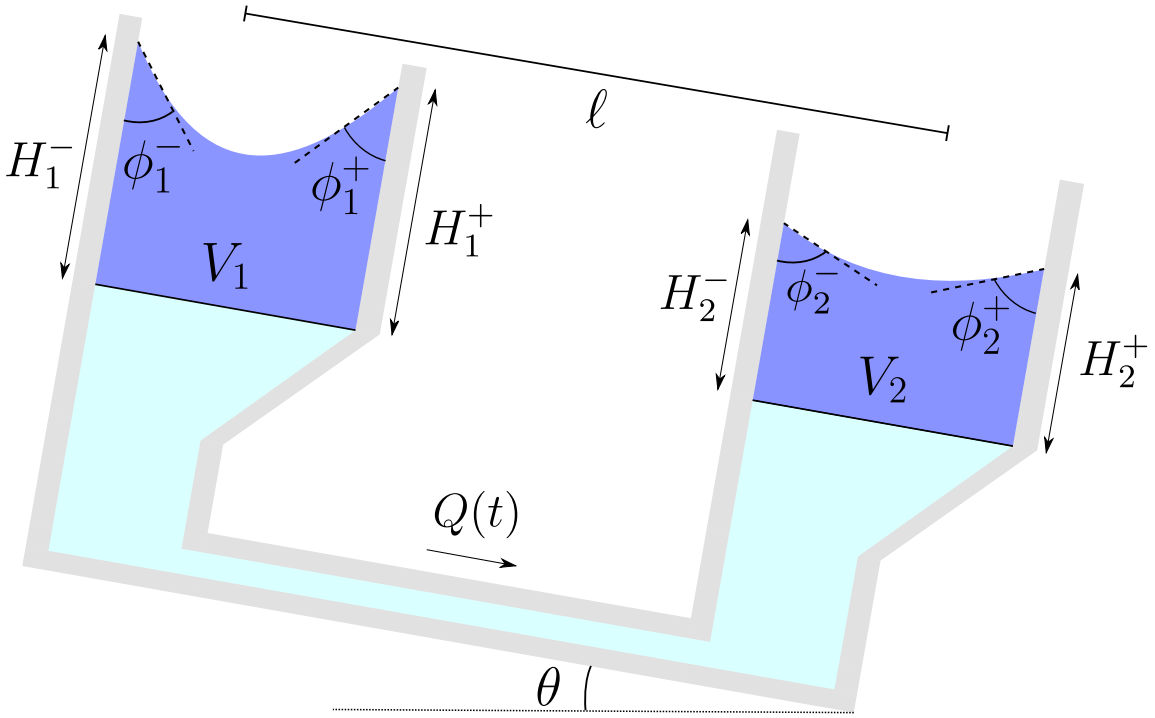

Figure 4.1: Diagram of the two-dimensional system showing the key dependent variables (V_i, H_i^+, H_i^-) for $i = 1, 2$ of the reduced model in addition to the macroscopic contact angles $\phi_i^\pm$. Dark blue shading indicates the fluid volume in the reservoir region. The elevation angle $\theta(t)$, the direction of the volume flow rate $Q(t)$, and the reservoir separation distance ℓ are also shown.

The dimensionless evolution equations are

$$\frac{\mathrm{d}V_2}{\mathrm{d}t} = -\frac{\mathrm{d}V_1}{\mathrm{d}t} = Q(t), \tag{4.1}$$

$$\tau \frac{\mathrm{d}H_i^\pm}{\mathrm{d}t} = F(\phi_i^\pm; \alpha_R, \alpha_A), \tag{4.2}$$

where $Q(t)$ is the (two-dimensional) volume flow rate from well 1 into well 2, $\phi_i^\pm(t)$ denotes the left and right (macroscopic) contact angles in each well, and the contact-line law F is as defined in (2.48).

The contact heights and contact angles in each well are related via solutions of the associated Young-Laplace boundary value problem

$$x \sin\theta - h_i \cos\theta + P_i = -\mathrm{Bo}^{-1} \frac{h_{ixx}}{(1 + h_{ix}^2)^{3/2}}, \tag{4.3}$$

for the meniscus height $h_i(x,t)$ above the reservoir base on the domain $-1 \leq x \leq 1$. This is solved subject to either imposed contact-line height boundary conditions

$$h_i(\pm 1, t) = H_i^{\pm}(t), \tag{4.4}$$

or imposed contact angle boundary conditions

$$\frac{\partial h_i}{\partial x}(\pm 1, t) = \cot \phi_i^{\pm}(t), \tag{4.5}$$

and the volume constraint

$$\int_{-1}^{1} h_i(x,t)\ \mathrm{d}x = V_i(t). \tag{4.6}$$

The spatially uniform pressure term $P_i(t)$ in the Young-Laplace equation (4.3) is determined as part of the solution. It is composed of a hydrostatic and capillary term which are given by

$$P_{h_i} = \frac{V_i \cos\theta}{2}, \quad P_{\gamma_i} = -\frac{1}{2\mathrm{Bo}}(\cos\phi_i^{+} + \cos\phi_i^{-}), \tag{4.7}$$

respectively, with $P_i = P_{h_i} + P_{\gamma_i}$. These expressions can be found by integrating (4.3) across the reservoir base.

Finally, the volume flow rate depends on the modified pressure difference Δp across the channel and is given by

$$Q(t) = -\Delta p = -(\Delta P_h + \Delta P_\gamma - \ell \sin\theta), \tag{4.8}$$

where the first two terms are the total hydrostatic and capillary pressure differences ($\Delta P_h = P_{h_2} - P_{h_1}$ and $\Delta P_\gamma = P_{\gamma_2} - P_{\gamma_1}$) and the final term is due to tilting the system. We observe that solving the Young-Laplace equation is necessary for computing the volume flow rate.

The initial volume $V_i(0)$ and contact heights $H_i^{\pm}(0)$ in each well must be prescribed, as must the form of the elevation angle $\theta(t)$. The reduced model depends on five dimensionless parameters: the Bond number Bo, the microscopic receding and advancing contact angles α_R and α_A, the relaxation parameter τ, and the reservoir separation distance ℓ. We refer to table 2.3 in §2.7.3 for the typical values of these

parameters, and we note that with the exception of the reservoir separation distance these parameters were discussed in detail in the context of the dynamic contact-line problem. We work in the physically relevant small relaxation parameter regime $\tau \ll 1$. In addition, we note that this model is formulated on the assumption that the meniscus remains in the fluid reservoir region of each well at all times.

4.2.2 Model structure, variables, and properties

The overall structure of the reduced model is similar to the dynamic contact-line problem in a single well considered in chapter 3, except that the volume flow rate is now set by the pressure difference rather than imposed externally. Thus many properties and results established for the dynamic contact-line problem continue to apply. We briefly summarise the relevant features as they relate to the reduced hydraulic electric model here.

Firstly, we note that the state of the system can be described in terms of the reservoir volume and contact heights $(V_i, h_i^{\pm})$ for each well, as above, or equivalently the reservoir volume and contact angles $(V_i, \phi_i^{\pm})$ can be used. As before, the description of the system in terms of the contact angles is preferable since they independently provide information on the meniscus shape and capillary pressure. This is based on the translational invariance of the Young-Laplace problem which is outlined chapter 3 (see §3.2.3).

We recall that a consequence of translational invariance is that solutions of the dynamic contact-line problem with the initial contact angle configuration prescribed are independent of the initial fluid volume for a single-well system. For the twin-well system, we observe from (4.1) that the total fluid volume is conserved, while the hydrostatic pressure difference (4.7) depends only on the difference in volume between the two wells. We conclude therefore that the dynamics of the twin-well system are independent of the total volume and that the state of the system can be described in terms of just five variables: the volume difference $\Delta V = V_2 - V_1$ and the four contact angles $\phi_i^{\pm}$, which we write as $\mathbf{\Phi} = (\phi_1^+, \phi_1^-, \phi_2^+, \phi_2^-)$. In our theoretical analysis we take the total fluid volume to be zero without loss of generality.

We observe that the hydrostatic pressure difference is a function of ΔV alone while the capillary pressure difference is a function of $\mathbf{\Phi}$ alone. We additionally define the net influx of fluid from well 1 into well 2 by

$$V_{in}(t) = \int_0^t Q(t') \, \mathrm{d}t' = \frac{1}{2}(\Delta V(t) - \Delta V(0)), \tag{4.9}$$

which is typically of more practical relevance than the volume difference ΔV, which is useful for our theoretical analysis.

4.2.3 Numerical solutions

Numerical solutions for the reduced model are obtained with Python using standard routines. In particular, the ordinary differential equations (4.1)-(4.2) are solved using the initial value problem solver `solve-ivp` from the `scipy.integrate` package, which uses an explicit fifth-order Runge-Kutta method. Absolute and relative tolerances of 10^{-8} are used.

The associated Young-Laplace boundary value problem (4.3)-(4.6) can be solved subject to either prescribed contact-line height or contact angle boundary conditions using the boundary value problem solver `solve-bvp` from the `scipy.integrate` Python package, which uses a fourth-order collocation algorithm. In our analysis, we precompute solutions over the full range of prescribed contact angle pairings (ϕ^+, ϕ^-) and elevation angles θ for a given Bond number. We note that solutions need only be computed in this way for $V = 0$, as solutions with non-zero volumes can be determined using translational invariance (i.e. $h \to h + V/2$ as described in §3.2.3). From these solutions we extract the mapping between the contact angles and contact-line heights, which is required for solving (4.2).

In solving the Young-Laplace problem, we use the exact (2D) circular cap solution corresponding to $\mathrm{Bo} = 0$ and $\theta = 0$ as the initial guess for the boundary value problem solver for low Bond numbers and subsequent solutions are obtained by continuation as the parameters Bo and θ vary. We set a tolerance of 10^{-8}, which is measured in terms of the L2 norm, and refined the grid size until the solutions converged.

4.3 Surface tension free dynamics

We first examine flows in the absence of surface tension and outline the relevant equations and physical mechanisms in this case. Many previous studies of similar gravity-driven systems do not consider capillary effects or argue that they can be neglected [14, 35, 86, 87]. This simplifies the modelling of fluid flow in these systems and can provide a good approximation to the dynamics under certain conditions, as we shall highlight for our particular twin-well system. However, under typical parameter regimes, in particular where $\mathrm{Bo} = O(1)$, we expect gravitational and capillary effects to be comparable in the system. Thus our solutions in this section serve as a reference point for comparison with later analysis where capillary effects are included, in addition to illustrating the typical system dynamics in a simplified setting.

We assume that the flow is driven only by hydrostatic pressure differences with $\Delta P_\gamma \equiv 0$. From the evolution equations for the fluid volume in each well (4.1) we obtain the equation

$$\frac{\mathrm{d}}{\mathrm{d}t}(\Delta V) = 2Q(t) = 2\ell \sin\theta - \Delta V \cos\theta, \tag{4.10}$$

for the volume difference ΔV, which makes use of conservation of fluid volume. Since we do not consider capillary pressure differences, there is no need to consider the evolution of the contact line or the associated Young-Laplace boundary value problem for the meniscus shape as the two ordinary differential equations (4.1) and (4.2) decouple, with (4.1) forming a closed system for the fluid volume. We prescribe the initial volume difference $\Delta V(0)$ and the form of the elevation angle $\theta(t)$. We observe that in this special case of zero surface tension the equation (4.10) is linear in ℓ and so we consider numerical solutions with $\ell = 1$ without loss of generality.

4.3.1 Physical mechanisms

The surface tension free equation (4.10) can be recovered from the reduced model under two parameter regimes. These are the high Bond number regime and the small contact angle hysteresis regime. Both of these regimes are associated with the surface

tension parameter, which we define by $S = \mathrm{Bo}^{-1}|\cos\alpha_A - \cos\alpha_R|$, being small but correspond to different physical mechanisms, which we now outline. We note that the (leading-order) free surface shape in each well is different for each mechanism.

The simplest regime in which we recover the surface tension free model is where the Bond number is large ($\mathrm{Bo} \gg 1$) and so gravitational effects dominate over capillary effects. By posing an expansion of the dependent variables V_i and $H_i^{\pm}$ in powers of the small parameter Bo^{-1} and retaining only leading-order terms in the reduced model equations (4.1)–(4.5) we recover the surface tension free model (4.10).

Although it is not necessary for determining the volume flow rate, we observe that in this case the leading-order solution to the Young-Laplace equation (4.3)–(4.6) with prescribed contact angle boundary conditions (4.5) is a flat meniscus $h = \bar{h} + x\tan\theta$ with a small inner region to account for the prescribed contact angle. Furthermore, the leading-order spatially uniform pressure P_i from the solution to the Young-Laplace equation (4.3) in each *individual* well is hydrostatic and given by $P_i = V_i/2$.

The second parameter regime where the capillary pressure difference can be neglected is where the hysteresis range is small. We define the small hysteresis limit as $S = \mathrm{Bo}^{-1}|\cos\alpha_A - \cos\alpha_R| \ll 1$ with $\mathrm{Bo} = O(1)$ at most. This makes precise the sense in which the difference between the advancing and receding contact angles is small relative to the Bond number. In this regime we also require $\tau \ll 1$. By posing an expansion of the dependent variables in powers of S we again recover the surface tension free equation (4.10) from the leading order volume flow rate.

In this limit, the Bond number itself may still be small meaning that capillary effects are still important in the system as a whole. For example, and in contrast to the large Bond number regime, the meniscus in each reservoir is typically curved and there is an associated capillary pressure contribution to the leading order pressure term P_i in the Young-Laplace equations (4.3). However, this pressure term depends on the macroscopic contact angle and, in the small hysteresis limit, the resulting capillary pressure *difference* between the two reservoirs can be neglected.

Unlike the large Bond number limit, this case relies on the fact that the relaxation parameter is small and so the macroscopic contact angles are bounded by the

microscopic advancing and receding contact angles to leading order in τ, as shown in §3.4.3. Consequently the capillary pressure difference is bounded with $|P_\gamma| \leq S$. In cases where contact angle hysteresis is small but $\tau = O(1)$, the capillary pressure difference is generally of order unity due to a different *dynamic* contact angle in each well, which in turn affects the flow rate. However, we restrict attention to the experimentally relevant small relaxation parameter regime in this chapter.

While the underlying cause may differ, the surface tension free model is ultimately recovered in both of the above regimes because the capillary pressure difference can be neglected as $|\Delta P_\gamma| \ll |\Delta P_h|$. In showing this, we have assumed that $\Delta P_h = O(1)$ which is consistent with the geometry and typical parameter values for the experimental system where the reservoir height, width, and separation distance are comparable and so in particular $\ell = O(1)$.

More generally, larger reservoir separation distances can also be used to amplify gravitational effects. In this case, hydrostatic pressure differences dominate, providing $S/\ell \ll 1$, and we can recover the surface tension free model in this limit. However, in this regime tilting the system results in large changes in fluid volume and so it is more appropriate to scale the fluid height according to the reservoir separation distance rather than the reservoir width. Hence the condition for recovering the surface tension free model is equivalent to a large modified Bond number $\ell\mathrm{Bo} \gg 1$.

4.3.2 Flow in a static system

We first suppose that the microfluidic system is static and held at some fixed elevation angle θ with the flow driven by a difference in the initial fluid volume in each reservoir. In this scenario the system dynamics are particularly simple. The surface tension free equation (4.10) has the exact solution

$$\Delta V(t) = \Delta V_{eq} + (\Delta V(0) - \Delta V_{eq}) \exp(-t \cos\theta), \tag{4.11}$$

where $\Delta V(0)$ is the initial volume difference and $\Delta V_{eq}(\theta) = 2\ell \tan\theta$ is the equilibrium volume difference which is approached on a dimensionless timescale of $O(\sec\theta)$. For feasible elevation angles (i.e. $|\theta| \leq 30°$) this timescale is of order unity.

The equilibrium volume is such that the hydrostatic pressure difference due to volume differences balances the pressure difference due to tilting and increases with both ℓ and θ. The corresponding difference in the mean fluid height between the two reservoirs at equilibrium is $\ell \tan\theta$ in the device frame. This means that the fluid height in each reservoir is equal when measured in the lab frame, which is expected on physical grounds for the hydrostatic pressure to equilibrate.

The dimensionless drainage timescale depends on the elevation angle, although this dependence is relatively weak for typical elevation angles. In dimensional terms, the timescale to reach equilibrium is set by

$$T_0^* = \frac{12\mu^* L_D^* L_0^*}{\rho^* g^* {H_D^*}^3} = R_h^* \frac{L_0^*}{\rho^* g^*}, \tag{4.12}$$

where R_h^* is the hydraulic resistance of the two-dimensional channel. For the typical parameter values $T_0^* \approx 7.5$s which sets the timescale for equilibration. We therefore expect the static system to fully equilibrate within approximately 30 seconds to a minute.

This timescale can be altered by varying the geometry of the system and is particularly sensitive to variations in the channel height H_D^*. Thinner channels constrict the flow and increase the time taken for the system to equilibrate. This can be used to inform the design of the twin-well system and optimise for desired flow rates, drainage timescales, and shear stresses ([14]).

4.3.3 Flow in an oscillating system

We now consider flows in a sinusoidally oscillating system with elevation angle $\theta(t) = \theta_A \sin\omega t$, where θ_A is the oscillation amplitude and ω the dimensionless oscillation frequency. We suppose that the flow is driven by this tilting rather than an initial volume difference and set $\Delta V(0) = 0$ so that the system is initially in equilibrium. The equation (4.10) no longer has an exact analytic solution in this case but numerical solutions can be readily determined using the standard method (see §4.2.3) while we also consider asymptotic solutions available in certain parameter regimes. We recall that (4.10) is linear in ℓ and so we take $\ell = 1$ for numerical solutions in this section.

We first investigate the effects of varying the oscillation frequency with fixed amplitude, taking $\theta_A = 10°$ as a representative value. The volume difference as a function of both time and elevation angle is shown in figure 4.2 for three representative frequency values corresponding to low, moderate, and high frequency oscillations relative to the drainage timescale. In each case, after a short transient response solutions ultimately reach steady state oscillations with the same frequency as the oscillating elevation angle.

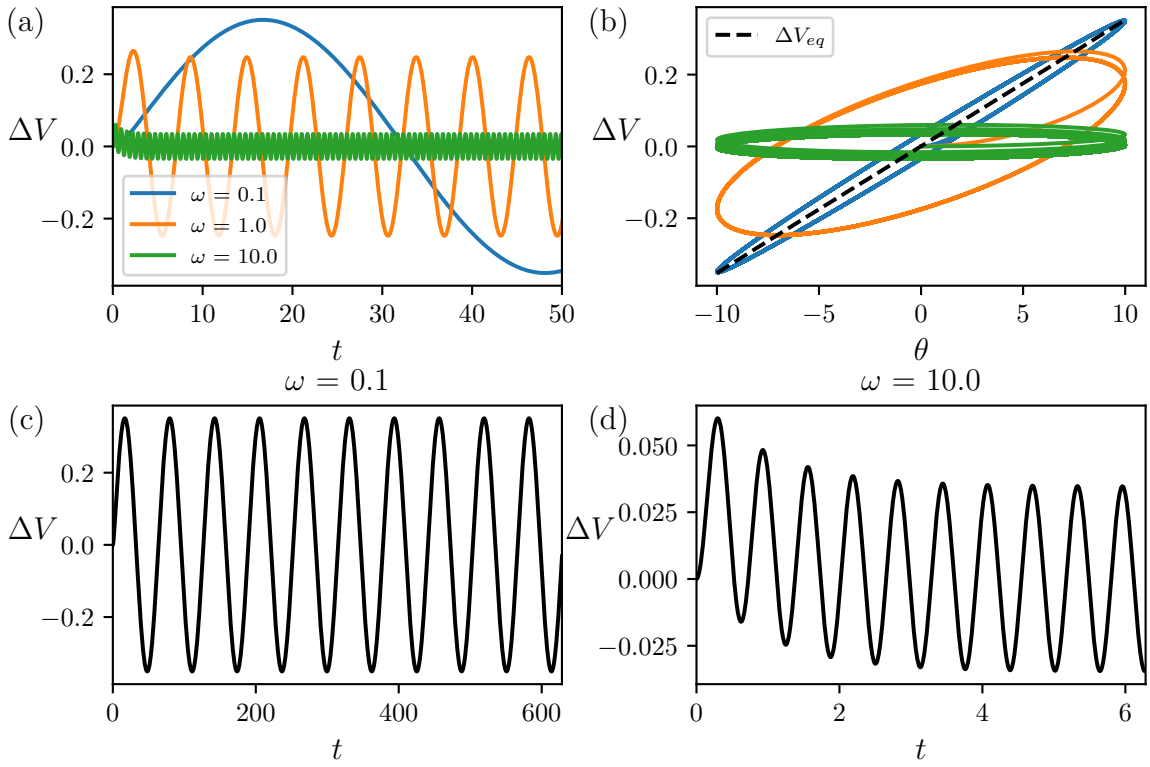

Figure 4.2: (a)-(b) Oscillations in the volume difference ΔV under sinusoidal oscillations in the elevation angle with $\theta_A = 10°$ shown as both a function of time t and elevation angle θ for a range of illustrative oscillation frequencies ω. The equilibrium volume difference $\Delta V_{eq}(\theta)$ for the current elevation angle is also indicated. (c)-(d) Individual plots showing the oscillations in the volume difference ΔV as a function of time t over the first ten oscillation cycles for both low ($\omega = 0.1$) and high ($\omega = 10$) frequency oscillations.

The amplitude of the steady state volume oscillations depends on the oscillation frequency, with higher frequency oscillations resulting in smaller volume amplitudes. The observed behaviour can be explained by considering the underlying physics of the

system and the drainage to the equilibrium that occurs when the system is held at a fixed elevation angle. For high-frequency oscillations, there is insufficient time for significant drainage of fluid between the two wells over the course of each oscillation cycle, which results in only a small volume of fluid being transferred between each well. Conversely, sufficiently low frequency oscillations allow the fluid volume to approximately equilibrate during the oscillation cycle. The fluid volume varies slowly with the volume difference approximately equal to the equilibrium height difference for the current elevation angle $\Delta V \approx \Delta V_{eq}(\theta) = 2\ell \tan\theta$. This equilibrium volume difference is also illustrated in figure 4.2 and solutions track this equilibrium more closely as the oscillation frequency decreases.

Figure 4.3 summarises the amplitude of the steady state oscillations in the volume difference and the volume flow rate, which are denoted by ΔV_A and Q_A respectively, for oscillation frequencies across several orders of magnitude. These amplitudes are normalised by the elevation amplitude θ_A. High frequency oscillations correspond to small volume amplitudes $\Delta V_A = O(\omega^{-1})$ with flow rates of order unity $Q_A = O(1)$. Conversely for low frequency oscillations $\Delta V_A = O(1)$ while the flow rate is small with $Q_A = O(\omega)$. In this case fluid is quasi-steady as it tracks the slowly varying equilibrium volume.

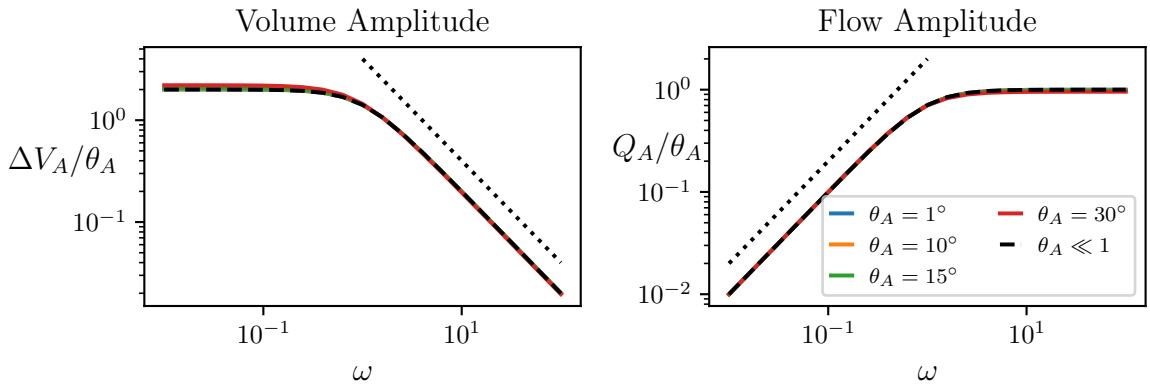

Figure 4.3: Amplitude of the late time steady state oscillations in the volume difference ΔV_A and volume flow rate Q_A (normalised by the elevation amplitude θ_A) as they vary with oscillation frequency ω for a range of indicated elevation amplitudes. The corresponding normalised amplitudes obtained from the leading order solution for small elevation amplitude $\theta_A \ll 1$ (see (4.13)) are also shown and dotted lines of slope ± 1 are included for reference.

Furthermore, both ΔV_A and Q_A scale with θ_A with the normalised solutions approximately collapsing onto a single curve. This is because for the small elevation amplitudes we consider (4.10) is approximately linear in θ_A. Indeed, by making use of the small-angle approximation it can be readily shown that the leading-order solution to (4.10) is

$$\Delta V(t) \sim \frac{2\ell\theta_A}{\sqrt{1+\omega^2}}\bigg(\sin(\omega t - \arctan(\omega)) + \sin(\arctan(\omega))\exp(-t)\bigg), \tag{4.13}$$

in the small amplitude limit $\theta_A \ll 1$.

The steady state volume and flow rate amplitudes obtained from the solution (4.13) are also shown in figure 4.3 and demonstrate excellent agreement with the numerical solutions. Thus the asymptotic solution can be used as an approximation even for the largest amplitudes considered. Furthermore, this asymptotic solution explains key features observed in the numerical solutions, including the phase shift of $\arctan(\omega)$ most noticeable for high frequency oscillations, the transient response which decays on the $O(1)$ drainage timescale, and the amplitude of the steady state oscillations in volume and flow rate. Indeed, we see that for low frequency oscillations $\Delta V_A \sim 2\ell\theta_A$, $Q_A \sim \ell\theta_A\omega$ while for high frequency oscillations $\Delta V_A \sim 2\ell\theta_A\omega^{-1}$, $Q_A \sim \ell\theta_A$

We can extend this analysis to consider flows driven by an initial volume difference with $\Delta V(0) \neq 0$ in addition to the oscillating elevation angle. However, this simply introduces an additional transient response with the initial volume difference equilibrating on the drainage timescale before the system settles down to the steady state oscillations driven by the elevation angle.

4.3.4 General low frequency oscillations

It is also straightforward to extend this analysis to more general oscillations in the elevation angle. We briefly outline solutions in the limit of low-frequency oscillations here, which is motivated by the distinct behaviour observed in this case. An asymptotic solution is available for general oscillations in the high-frequency limit via a

multiple-scales analysis, though we omit the details here since this regime is less relevant to the operation of the physical system. Such high frequency oscillations may be relevant in other scenarios however, for instance in systems where the channel is engineered to promote mixing [10].

We consider general oscillations of the elevation angle with angular frequency ω and introduce the oscillation time variable $T = \omega t$ so that $\theta(T)$ is a 2π-periodic function. We seek the leading order solutions to (4.10) in the low frequency regime $\omega \ll 1$ with initial condition $\Delta V(0) = 0$. We pose an asymptotic expansion in powers of the small parameter ω and find that

$$\Delta V \sim 2\ell \tan\theta(T), \tag{4.14}$$

to leading order, which we note is equal to the equilibrium volume difference $\Delta V_{eq}(\theta(T))$. The corresponding volume flow rate is

$$Q \sim \ell\omega\theta_T(T)\sec^2\theta(T), \tag{4.15}$$

and thus we again find that the flow is quasi-steady and tracks the equilibrium volume with flow rate $O(\omega)$. We note that solutions with $\Delta V(0) \neq 0$ results in an additional initial period of faster flow on the $O(1)$ drainage timescale driven by this volume difference, before solutions settle down to the steady state (4.14).

Under typical operating conditions, the device cannot be tilted too rapidly meaning that device operating regimes correspond to low to moderate oscillation frequencies $\omega \leq 1$. Furthermore, the device is generally not tilted continuously but instead subject to paused oscillations where the system is held fixed for a pause time at the maximum and minimum elevation amplitudes. We consider flows under this operating regime in the next section.

4.3.5 Paused oscillations

Experimentally relevant paused oscillations are described by three parameters: the elevation amplitude θ_A, the transition time T_{tr} and the pause time T_p. The system transitions linearly between the horizontal and the maximum and minimum elevation

angle $\pm\theta_A$ in time T_{tr}, where it is held fixed for time T_p. The total oscillation period is therefore $4T_{tr} + 2T_p$.

For small amplitude oscillations we expect the flow to scale with θ_A. Indeed we can again find a simple asymptotic solution for $\theta_A \ll 1$ which provides excellent agreement with numerical solutions even for larger oscillation amplitudes. We therefore investigate the effects of varying the transition and pause times.

Flows exhibit distinct qualitative behaviour depending on the magnitude of T_{tr} and T_p. This behaviour is illustrated in figure 4.4 which presents examples showing the variation of the volume difference and volume flow rate for a range of T_{tr} and T_p pairings for representative amplitude $\theta_A = 10°$. In all cases, the system eventually settles down to steady-state oscillations after the decay of the transient response on the drainage timescale.

When the pause time is small the system essentially undergoes periodic oscillations with frequency proportional to T_{tr}^{-1}, and so the previous results for a general oscillating system apply. In particular, the volume amplitude and flow rate depend on the transition time T_{tr}. Low-frequency oscillations are quasi-steady and track the equilibrium volume difference, while high-frequency oscillations result in a small transfer of fluid. Examples of this are illustrated in the first two columns of figure 4.4.

When the pause time is large the system is able to drain to equilibrium although there are two cases to consider. If the transition time is also large, then the volume difference tracks the equilibrium volume throughout as for low frequency oscillations and so there is limited flow during the pause time as the system is already close to equilibrium. Conversely if the transition time is small, then the system drains to equilibrium during the pause time, as for a static system, which can result in larger flow rates. These two scenarios are illustrated in the second two columns of figure 4.4.

In practice, the pause time is typically sufficiently long (e.g. 1 or 2 minutes corresponding to $T_{tr} \sim 10$) compared with the drainage time-scale (approximately 10 seconds) that the system can equilibrate during this period. The transition time can

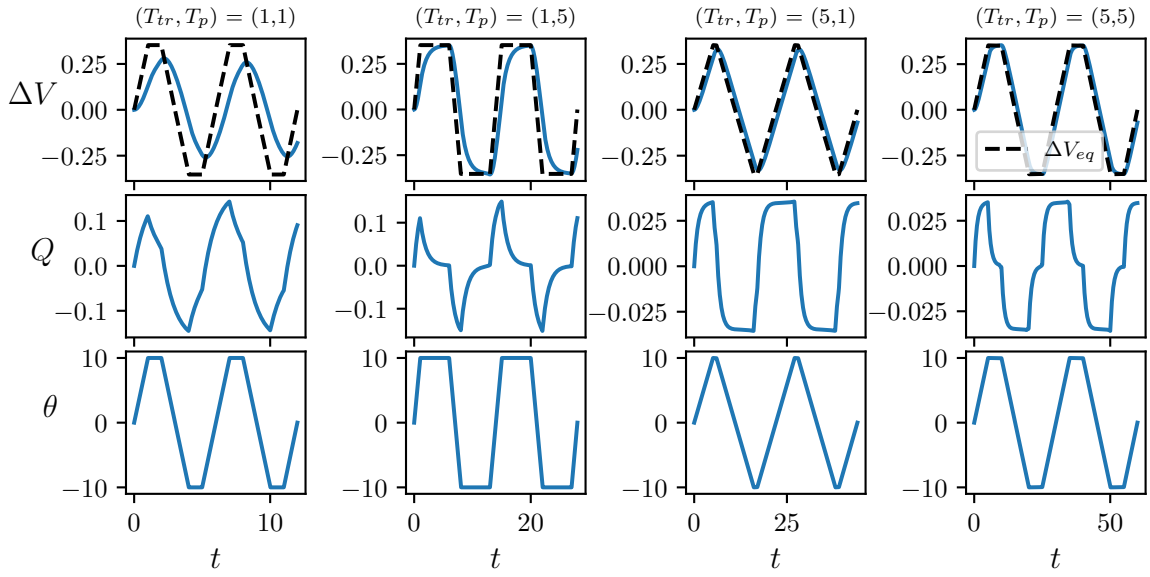

Figure 4.4: Variation in the volume difference ΔV and flow rate Q with time t for a range of prescribed paused oscillations in the elevation angle θ with amplitude $\theta_A = 10°$ and transition and pause time (T_{tr}, T_p) as indicated. The equilibrium volume difference ΔV_{eq} is indicated by a dashed line, and low-frequency oscillations approximately track this volume, as can be seen for solutions with $T_p = 5$.

vary but is typically shorter (e.g. 10 or 20 seconds corresponding to $T_{tr} \sim 1$). Thus we investigate the long pause time regime for various transition times below.

Figure 4.5 shows the volume difference and volume flow rate as a function of time for a range of transition times (for a large fixed value of T_p) during the initial phase of the paused oscillation cycle, which consists of the initial transition and pause. In all cases, solutions ultimately reach the final equilibrium volume difference $\Delta V_{eq}(\theta_A) = 2\ell \tan \theta_A$. Fast transitions result in limited fluid transfer during the transition itself, but fluid drains to equilibrium during the pause time on the $O(1)$ drainage timescale. Meanwhile slow transitions allow transfer of fluid during over this transition period, resulting in slower flows and only a small amount of drainage during the pause period.

Consequently, fast transitions are associated with larger initial flow rates which decay exponentially in the same manner as the static solutions, while slow transitions have low but constant flow rates that are inversely proportional to the transition time. As T_{tr} is reduced the initial flow rate is bounded by $Q_{max} = \ell \tan \theta_A$, which is the flow

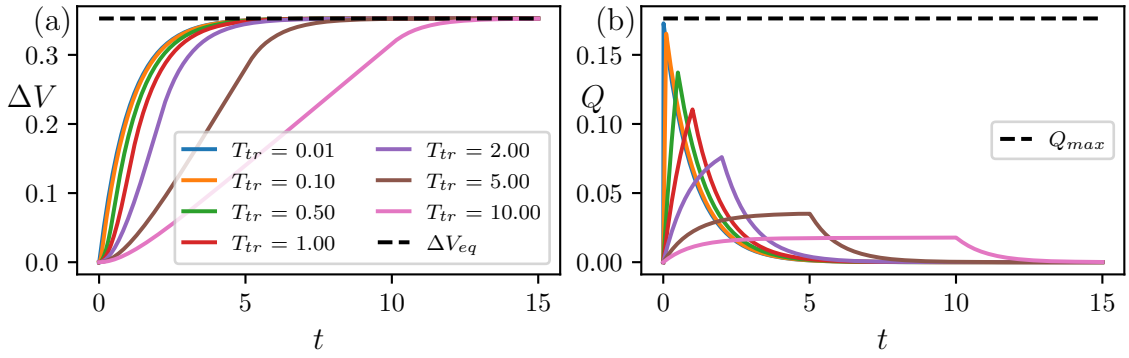

Figure 4.5: Variation in volume difference ΔV and flow rate Q with time t for paused oscillations with a range of transition times T_{tr}, as indicated, but with fixed amplitude $\theta_A = 10^\circ$ and pause time $T_p = 20$. The equilibrium volume difference ΔV_{eq} and theoretical maximum flow rate Q_{max} associated with instantaneous tilting are also indicated.

rate associated with instantaneous tilting. During later oscillations, the magnitude of the initial flow rate doubles for small T_{tr} values since these transitions are between the minimum and maximum amplitudes $-\theta_A$ and θ_A.

We note that the typical flows under fast and slow transition times are consistent with the elevation and flow regimes we explored in §3.5.5 for a single-well system. There we defined the simultaneous flow regime where $Q \propto \dot{\theta}$, which we see from (4.15) corresponds to low frequency oscillations, and the sequential flow regime where tilting and flow occurred sequentially. This sequential flow regime corresponds to the behaviour of the twin-well system under paused oscillations with long pause times and short transition times.

Finally, the analysis of the paused oscillation regime can be used to determine optimal experimental conditions. For long pause times, the elevation amplitude determines the net volume of fluid transferred between the wells in each oscillation cycle, which is equal to $\Delta V_A = 2\ell \tan\theta_A$. This amplitude can be chosen to optimise transport between the wells, which we consider in more detail in chapter 5. A first approximation, however, is to take the amplitude ΔV_A to be comparable to the volume of the culture chamber to ensure mixing between solutes in these regions.

Meanwhile the transition time sets the flow rate, with fast transition times result-

ing in the fastest transfer, which is limited by the drainage timescale, while slower transition times are limited by the oscillation frequency. The optimal transition time can be set based on the desired mixing time between the two wells as well as the flows that the cell cultures can experience.

Furthermore, it is straightforward to extend our analysis to more general paused oscillations consisting of a sequence of transitions between different fixed elevation angles with pauses between them. In particular, transitions from θ_1 to θ_2 result in a net transfer of fluid $\ell(\tan\theta_2 - \tan\theta_1)$. For slow transitions, the flow rate is approximately uniform with $Q \sim \ell(\tan\theta_2 - \tan\theta_1)/T_{tr}$ while for fast transitions the fluid drains with exponentially decaying flow rate with maximum flow rate $Q_{max} \sim \ell(\tan\theta_2 - \tan\theta_1)$. Such general paused oscillations provide a simple method to vary the volume of fluid transferred and the volume flow rate throughout an experiment.

Our characterisation of the surface tension free regime provides a useful starting point for identifying optimal experimental operating regimes. However, in practice we expect surface tension effects to be important and modify the flow. Quantifying and accounting for these effects is important if precise control of fluid between wells is desired. Thus we extend our analysis to investigate how surface tension effects modify the solutions for both a static and oscillating system.

4.4 Capillary effects in a static system

In this section we consider capillary effects for the case of a static system with θ fixed to examine the impact of surface tension on the system dynamics and equilibrium state. We recall that in general the state of the system can be described by five state variables $(\Delta V(t), \mathbf{\Phi}(t))$, where $\mathbf{\Phi} = (\phi_1^+, \phi_1^-, \phi_2^+, \phi_2^-)$. To match typical experimental usage, we consider solutions which are driven only by an initial hydrostatic pressure difference $\Delta P_h(0) \neq 0$, due to a difference in fluid volume between the two wells, with no initial capillary pressure difference $\Delta P_\gamma(0) = 0$. Without loss of generality we restrict attention to positive initial flow rates $Q(0) > 0$. We use the standard parameter values listed in table 2.3 unless otherwise stated with $\tau = 10^{-3}$, which

corresponds to the small τ regime and thus $\phi \in [\alpha_R, \alpha_A]$ to leading order. The equations (4.1)—(4.5) are solved using the numerical scheme outlined in §4.2.3, and we compare solutions with the equivalent solutions in the absence of capillary effects or contact angle hysteresis (i.e. $S = 0$) which are driven by the same initial hydrostatic pressure difference.

4.4.1 Horizontal system dynamics

We first illustrate the system dynamics in the case of a horizontal system with $\theta = 0$, which is representative of any fixed elevation angle. Moreover, in this special case the meniscus in each well exhibits symmetric solutions. Thus to more clearly highlight the key behaviour and physics we restrict attention to solutions which are symmetric in each well and so the left and right contact angles and contact heights are equal (i.e. $\phi_i^+ = \phi_i^-$ and $h_i^+ = h_i^-$) throughout.

Figure 4.6 illustrates the typical dynamics for a horizontal system driven by an initial hydrostatic pressure difference. The evolution of the volume flow rate, the volume and pressure differences, and the (normalised) contact heights and contact angles are shown, as are corresponding quantities for the equivalent surface tension free solution. The accompanying schematic in figure 4.7 provides a snapshot of the system at key points during the dynamics.

The solution exhibits a decreasing flow rate with the volume difference ultimately approaching an equilibrium value on a timescale of order unity, much like the surface tension free solution. However, in the absence of surface tension this equilibrium is $\Delta V = 0$, corresponding to an equal volume of fluid in each well, while with surface tension the equilibrium corresponds to a balance between the hydrostatic and capillary pressures and has $\Delta V < 0$. Thus, the fluid volumes in each well are not equal and less fluid is transferred between the two wells when surface tension effects are included.

This difference can be explained by considering the physics of the contact-line dynamics and the additional capillary pressure term. As fluid is transferred across the

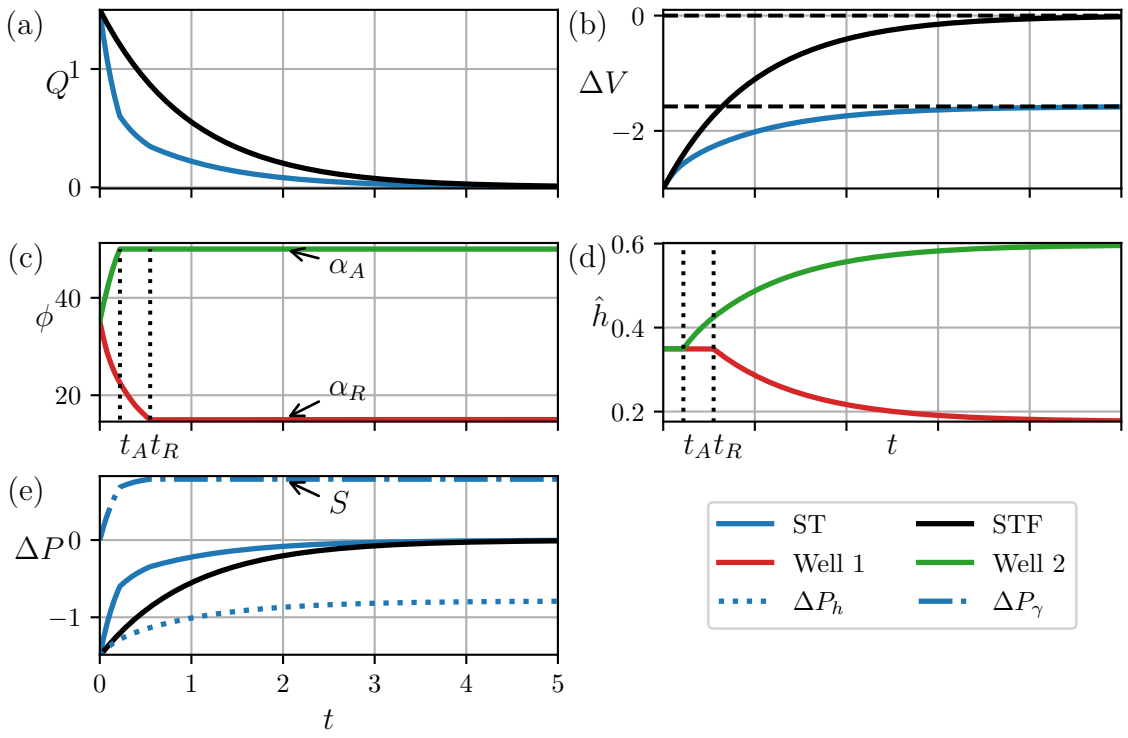

Figure 4.6: Typical solution for the horizontal system showing the evolution with time t of (a) the volume flow rate Q, (b) the volume difference ΔV (c) the contact angles ϕ, (d) the contact heights (normalised by the initial mean meniscus height) $\hat{h}$, and (e) the pressure difference ΔP, which is decomposed into its hydrostatic and capillary components ΔP_h and ΔP_γ. The initial state is $(\Delta V(0), \phi_1(0), \phi_2(0)) = (-3, 35°, 35°)$ and the standard parameter values are used. The flow rate, volume difference and total pressure difference for the surface tension free (STF) model with the equivalent initial state are also shown. The horizontal dashed lines in (b) indicate the equilibrium volumes for each solution. The vertical dotted lines in (c) and (d) indicate the times t_A and t_R at which the contact angles reach their advancing and receding values α_A and α_R, at which point the contact line in the relevant well becomes unpinned. The capillary pressure difference attains its maximal value S when both contact lines are unpinned.

wells the change in both the hydrostatic and capillary pressure components act to oppose the flow rate. For this particular example where $Q(0) > 0$ and $\Delta V(0) < 0$, both ΔV and ΔP_h are increasing which reduces the flow rate. Furthermore, as discussed in our analysis of the single-well system in chapter 3, the contact angle and capillary pressure are increasing functions of the fluid volume in each well. This can be seen in figure 4.6, where the contact angle in well 2 increases until the contact line becomes

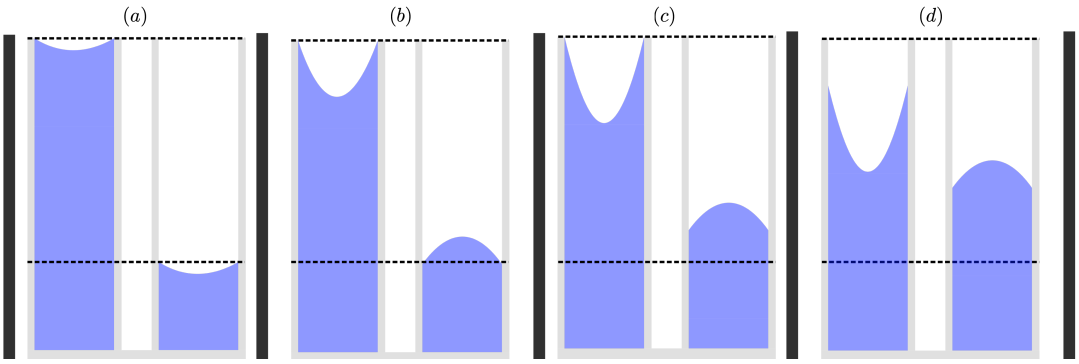

Figure 4.7: Snapshots of the system at four key times during the dynamics showing (a) the initial configuration of the system at $t = 0$, (b) the time $t = t_A$ when the meniscus in well 2 reaches the advancing contact angle and becomes unpinned, (c) the time $t = t_R$ when the meniscus in well 1 reaches the receding contact angle and becomes unpinned, and (d) the final equilibrium state with an unequal volume of fluid in each well. The horizontal dotted lines indicate the initial meniscus height in each well for reference.

unpinned at the advancing angle, while the contact angle in well 1 decreases until the contact line becomes unpinned at the receding angle. Ultimately, the contact-line dynamics in each well results in an increasing capillary pressure difference ΔP_γ, which acts to further reduce the flow rate compared with solutions without surface tension.

Once both the advancing and receding angles are obtained, the capillary pressure remains constant at its maximum value, which is given in terms of the surface tension parameter $\Delta P_\gamma = S$. Moreover, we observe that once the advancing and receding contact angles are obtained in each well (as indicated by dashed lines in figure 4.6), the decrease in volume flow rate becomes less rapid, since the capillary pressure in the corresponding well remains fixed from this point onward. There is a significant difference between both the flow rates and equilibrium volumes for solutions with and without surface tension, which highlights that capillary effects cannot typically be neglected in this parameter regime.

This behaviour is representative of flows at fixed elevation angles driven by an initial volume difference. The flow induces pressure changes which oppose the flow and decrease the volume flow rate, with the system eventually reaching equilibrium where the total pressure difference vanishes. For a non-zero elevation angle, the

timescale for equilibration is $O(\sec\theta)$, as is the case for the dynamics without surface tension, and the left and right contact angles in each well may not be equal, although this does not substantially alter the typical dynamics. Furthermore, similar system dynamics are observed for flows driven by an initial difference in capillary pressure or a combined hydrostatic and capillary pressure difference. However, we do not consider these scenarios as they are not representative of the typical operation of the gravity-driven system.

4.4.2 Equilibrium volume

For a static system at a fixed elevation angle, all solutions ultimately reach an equilibrium state. These are defined as states $(\Delta V, \mathbf{\Phi})$ where time derivatives on the left-hand side of equations (4.1) and (4.2) vanish. We note immediately from the contact-line law (2.48) that this requires $\phi_i^{\pm} \in [\alpha_R, \alpha_A]$ exactly (i.e. not just to leading order in τ) to ensure the contact line is stationary. For a given contact angle configuration $\mathbf{\Phi}$ satisfying this condition, the corresponding equilibrium volume difference for which the flow rate and total pressure difference vanish is found by considering (4.8) to be

$$\Delta V_{eq}(\mathbf{\Phi}, \theta) = \Delta V_{eq}^{(h)}(\theta) - 2\Delta P_\gamma(\mathbf{\Phi}) \sec\theta, \tag{4.16}$$

where $\Delta V_{eq}^{(h)}(\theta) = 2\ell \tan\theta$ is the hydrostatic equilibrium obtained in the absence of capillary effects. We recall that this is the volume difference required to balance the hydrostatic pressure difference due to the tilting of the device, while the second term in (4.16) is the volume difference required to balance the capillary pressure difference.

Capillary effects and in particular contact angle hysteresis result in a range of possible equilibrium volume differences, with the hydrostatic equilibrium $\Delta V_{eq}^{(h)}(\theta)$, which is the unique equilibrium in the absence of surface tension or hysteresis effects (i.e. $S = 0$), forming the midpoint of this range. Furthermore, since the capillary pressure difference is bounded with $|\Delta P_\gamma| \leq S$, the range is proportional to the surface tension parameter S with

$$|\Delta V_{eq} - \Delta V_{eq}^{(h)}| \leq 2S \sec\theta. \tag{4.17}$$

Figure 4.8(a) illustrates the range of potential equilibrium volume differences as a function of the elevation angle. The hydrostatic equilibrium $\Delta V_{eq}^{(h)}$ increases with the elevation angle and is also proportional to the reservoir separation distance ℓ. The range depends on the hysteresis range and Bond number via the surface tension parameter S, and depends weakly on the elevation angle.

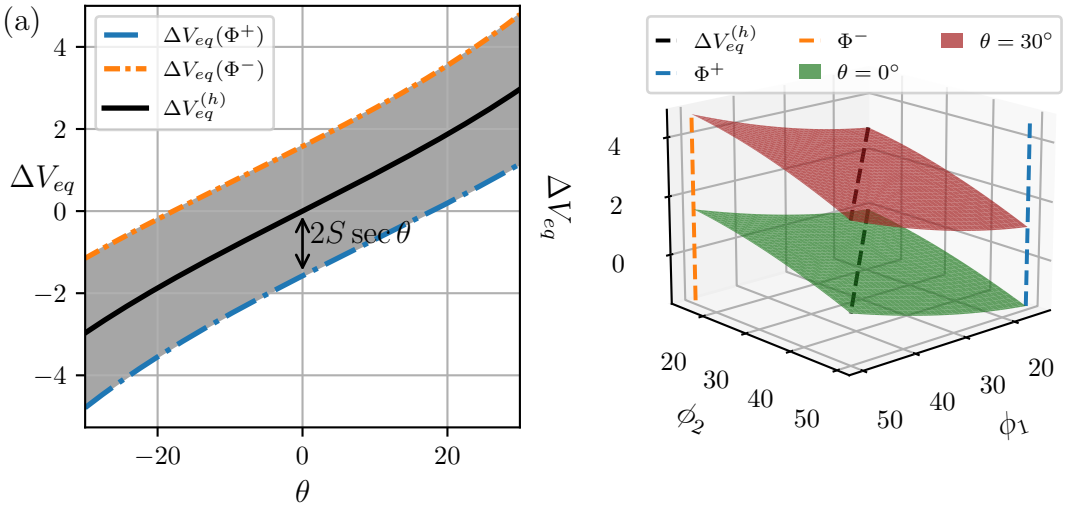

Figure 4.8: (a) Variation of the hydrostatic equilibrium volume difference $\Delta V_{eq}^{(h)}$ and the range (shaded) of possible equilibrium volume differences with elevation angle θ. The minimum and maximum equilibrium volume differences $\Delta V_{eq}(\mathbf{\Phi}^+)$ and $\Delta V_{eq}(\mathbf{\Phi}^-)$, which correspond to a fully unpinned meniscus in each well, are also indicated. (b) Three-dimensional plot of the equilibrium surfaces for various elevation angles. ΔV_{eq} is a function of the contact angle pair (ϕ_1, ϕ_2) under the assumption that the left and right contact angles in each well are equal. The fully unpinned contact angle configurations $\mathbf{\Phi}^+$ and $\mathbf{\Phi}^-$ are also indicated, which coincide with the minimum and maximum equilibrium volume difference at any given elevation angle. The hydrostatic equilibrium $\Delta V_{eq}^{(h)}$ is indicated by a dashed line in each case. The standard system parameter values are used.

For the case of a horizontal system where the meniscus in each well is symmetric, the potential equilibrium states form a surface in three-dimensional state space $(\Delta V, \phi_1, \phi_2)$. This is illustrated in figure 4.8(b). We observe that multiple contact angle configurations result in the same equilibrium volume difference. For instance, if the contact angles in the two wells are equal then the equilibrium volume difference is equal to the hydrostatic equilibrium $\Delta V_{eq}^{(h)}$. Meanwhile, for a general elevation angle

where the menisci are not symmetric, the equilibrium states form a four-dimensional hypersurface in the five-dimensional state space $(\Delta V, \mathbf{\Phi})$. In this case, contact angle configurations where the capillary pressures in each well are equal and so $\Delta P_\gamma = 0$ result in an equilibrium volume difference equal to the hydrostatic equilibrium.

For given system parameter values, the maximum and minimum equilibrium volume differences are associated with the contact angle configurations $\mathbf{\Phi}^- = (\alpha_A, \alpha_A, \alpha_R, \alpha_R)$ and $\mathbf{\Phi}^+ = (\alpha_R, \alpha_R, \alpha_A, \alpha_A)$, respectively. These configurations correspond to the meniscus in each well reaching a fully unpinned state and the capillary pressure difference attaining its minimal or maximal value with $\Delta P_\gamma(\mathbf{\Phi}^\pm) = \pm S$. Since the contact angles in each well are increasing functions of the well volume, the contact angle configuration $\mathbf{\Phi}^+$ is associated with positive flow rates while $\mathbf{\Phi}^-$ is associated with negative flow rates. The equilibrium volume difference associated with these states are indicated in the plots in figure 4.8 and illustrated by the schematic in figure 4.9, which also shows the hydrostatic equilibrium for reference.

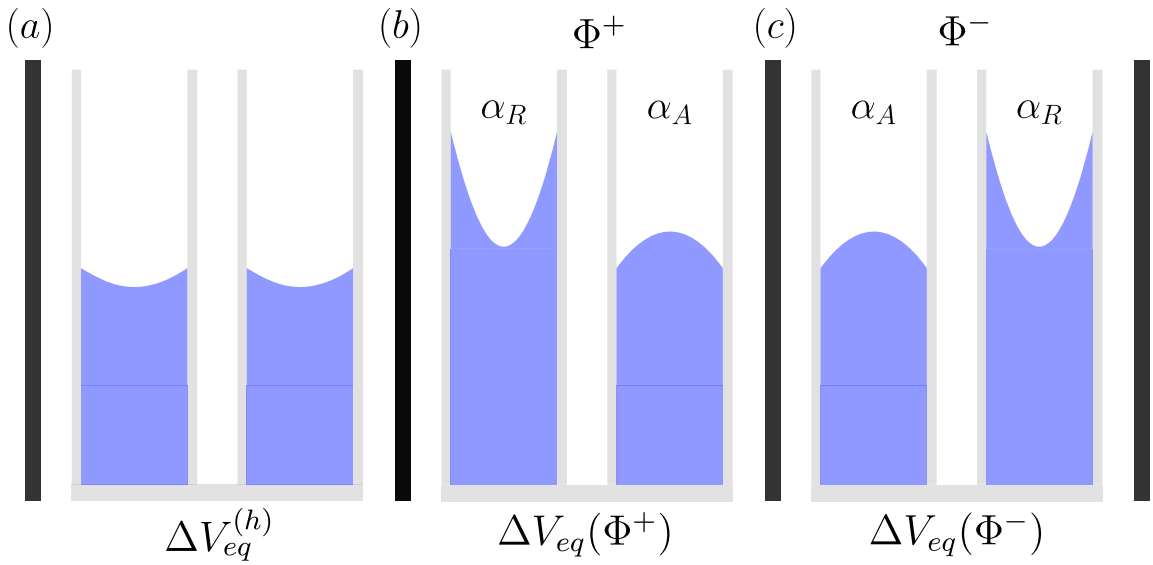

Figure 4.9: Schematic diagram illustrating some potential equilibrium states of the horizontal system. These are the hydrostatic equilibrium $\Delta V_{eq}^{(h)}$ where the contact angles in the two wells are equal and the two fully unpinned equilibria $\Delta V_{eq}(\mathbf{\Phi}^+)$ and $\Delta V_{eq}(\mathbf{\Phi}^-)$, which are associated with the fully unpinned contact angle configurations $\mathbf{\Phi}^+$ and $\mathbf{\Phi}^-$ which are also indicated.

4.4.3 Sensitivity to initial conditions

The range of potential equilibrium states is set by the system parameters, while the particular equilibrium obtained in any experiment depends on the initial conditions. We investigate this dependence on the initial conditions in this section. Without loss of generality, we predominantly restrict discussion to non-negative flow rates $Q(t) \geq 0$. In this case, ΔV and ΔP_γ are both increasing functions of time, with $\phi_1^{\pm}$ decreasing and $\phi_2^{\pm}$ increasing. Equivalent results are applicable in the case $Q(t) \leq 0$ by symmetry.

We first restrict attention to a horizontal system where the meniscus in each well is symmetric. Figure 4.10 shows the system dynamics in terms of the volume difference ΔV for various initial states $(\Delta V(0), \phi_1(0), \phi_2(0))$. A range of final equilibrium volumes are obtained which depend on both the initial volume difference and the initial contact angle configuration. For each initial volume difference the corresponding surface tension free solution ($S = 0$) is also shown for reference.

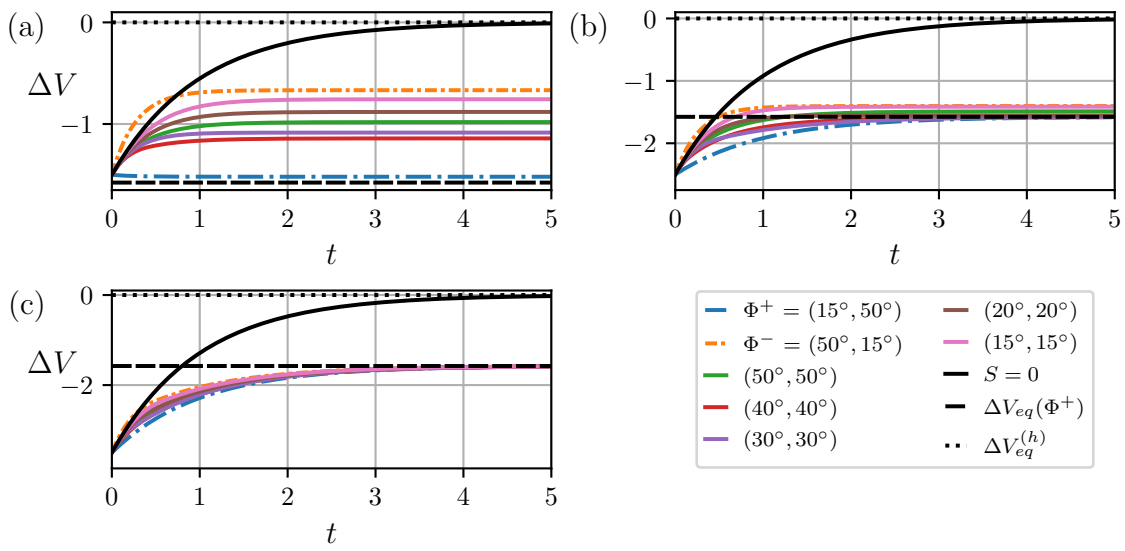

Figure 4.10: Volume difference in a horizontal system for various initial states. For each solution, the initial contact angle pairing (ϕ_1, ϕ_2) is shown in the legend and the surface tension free solution ($S = 0$) is also shown. The minimum unpinned equilibrium $\Delta V_{eq}(\mathbf{\Phi}^+)$ and hydrostatic equilibrium $\Delta V_{eq}^{(h)} = 0$ are indicated with a horizontal dashed line. The initial volume differences are (a) $\Delta V(0) = -1.5$, (b) $\Delta V(0) = -2.5$, (c) $\Delta V(0) = -3.5$, and the standard system parameters are used.

For a fixed initial volume difference, all solutions with surface tension are bounded above by the solution with $\mathbf{\Phi}(0) = \mathbf{\Phi}^-$ and below by the solution with $\mathbf{\Phi}(0) = \mathbf{\Phi}^+$, which are indicated in the plots. These correspond to the minimal or maximal initial capillary pressure difference respectively. Solutions with a lower initial capillary pressure difference have faster initial flow rates and potentially a greater volume of fluid transferred across the wells.

The hydrostatic and unpinned equilibrium volume differences, $\Delta V_{eq}^{(h)}$ and $\Delta V_{eq}(\mathbf{\Phi}^+)$ are also indicated in figure 4.10 by dashed horizontal lines. The unpinned equilibrium is especially relevant since many solutions obtain this equilibrium, particularly as the magnitude of the initial volume difference increases. The solutions in figure 4.10 highlight three possible scenarios depending on the size of $|\Delta V(0)|$, which we describe below.

Firstly, in figure 4.10(a), $|\Delta V(0)|$ is small with $\Delta V(0) > \Delta V_{eq}(\mathbf{\Phi}^+)$. Thus if $Q(0) > 0$, no choice of initial contact angles can achieve the unpinned equilibrium $\Delta V_{eq}(\mathbf{\Phi}^+)$. In fact, this is true even for initial conditions with $Q(0) < 0$, since in this case the contact angles will be moving away from the configuration $\mathbf{\Phi}^+$ and towards $\mathbf{\Phi}^-$. In figure 4.10(b), $|\Delta V(0)|$ is larger but the equilibrium state is still sensitive to the initial contact angles: some initial configurations obtain $\Delta V_{eq}(\mathbf{\Phi}^+)$ and some do not. Finally, figure 4.10(c) corresponds to the largest value of $|\Delta V(0)|$ and $\Delta V_{eq}(\mathbf{\Phi}^+)$ is reached for any initial contact angle configuration.

These observations can be explained physically as follows. Variations in the final equilibrium state and sensitivity to the initial conditions result from the capillary pressure term. A larger absolute initial volume difference corresponds to a larger absolute hydrostatic pressure difference. If this pressure difference is sufficiently large it can overcome the opposing capillary pressure difference and ensure that, before equilibrium is obtained, a sufficient volume of fluid is transferred across the system so that all contact points become unpinned during the motion. For positive initial flow rates, this corresponds to obtaining the unpinned contact angle configuration $\mathbf{\Phi}^+$, from which the only possible equilibrium volume difference is $\Delta V_{eq}(\mathbf{\Phi}^+)$.

If the magnitude of the initial volume difference is sufficiently large, the contact line in each well will become fully unpinned regardless of the initial contact angle configuration. However, as $|\Delta V(0)|$ decreases, the initial hydrostatic pressure difference will only be sufficient to overcome the capillary pressure difference for a smaller range of initial contact angle configurations until ultimately either $\Delta V(0) > \Delta V_{eq}(\mathbf{\Phi}^+)$ or $Q(0) < 0$, making it impossible to reach the unpinned equilibrium state $\Delta V_{eq}(\mathbf{\Phi}^+)$.

4.4.4 Critical initial volume difference

The practical applications of the above observations are discussed at the end of this section. We first formalise this physical intuition by identifying a criterion on the initial volume difference which ensures that the initial flow is positive and that the unpinned equilibrium state $\Delta V_{eq}(\mathbf{\Phi}^+)$ is obtained for a particular initial contact angle configuration. This criterion can be extended to a sufficient condition valid for any initial contact angle configuration, thereby removing the sensitivity to the initial conditions. Since these conditions correspond to a larger absolute initial volume difference, for a positive initial flow rate, they take the form of an upper bound on $\Delta V(0)$, which corresponds to a sufficiently large volume of fluid in well 1 relative to well 2.

To find a condition that ensures the contact line in each well becomes unpinned we can make use of our single-well analysis in chapter 3. In §3.4.4, we defined the transfer volume $V_{tr}(\phi \to \phi')$ for $\phi, \phi' \in [\alpha_R, \alpha_A]$. This gives the change in fluid volume associated with a transition between uniform contact angle configurations ϕ and ϕ' in a horizontal single-well system. Exact expressions are available for the transfer volume in the case of a spherical cap meniscus with $\mathrm{Bo} = 0$ for both three and two-dimensional well geometries, while for $\mathrm{Bo} > 0$ this can be calculated numerically from the Young-Laplace equation. Furthermore, in two dimensions it is straightforward to extend the definition of the transfer volume to non-zero elevation angles where the contact angles are not symmetric (i.e. $\phi^+ \neq \phi^-$) by solving the dynamic contact-line problem numerically, although for notational convenience we suppose each meniscus is symmetric in our discussion below.

Returning to the twin-well system, for any given initial contact angle configuration, which we write as $\mathbf{\Phi} = (\phi_1, \phi_2)$, we calculate the transfer volumes $V_{tr}(\phi_1 \to \alpha_R) \leq 0$ and $V_{tr}(\phi_2 \to \alpha_A) \geq 0$. These give the required volume change in each well for the meniscus to become fully unpinned under a positive flow rate. We let $V_{tr}^{\max}(\mathbf{\Phi}) = \max\{|V_{tr}(\phi_1 \to \alpha_R)|, V_{tr}(\phi_2 \to \alpha_A)\}$, which is the net transfer volume between the two wells required for the contact line in both wells to become fully unpinned.

Thus a condition on the initial volume difference for the system to become fully unpinned, and therefore reach the equilibrium $\Delta V_{eq}(\mathbf{\Phi}^+)$ is $\Delta V \leq \Delta V_{bnd}$ where

$$\Delta V_{bnd}(\mathbf{\Phi}) = \Delta V_{eq}(\mathbf{\Phi}^+) - 2V_{tr}^{\max}(\mathbf{\Phi}). \tag{4.18}$$

This condition ensures that $Q > 0$ up until the point that both contact lines become unpinned, and thus the system cannot reach equilibrium before becoming unpinned.

Furthermore, since $V_{tr}^{\max}$ is bounded above by the critical transfer volume defined by $V_{crit} = V_{tr}(\alpha_R \to \alpha_A)$, we introduce the critical volume difference

$$\Delta V_{crit} = \Delta V_{eq}(\mathbf{\Phi}^+) - 2V_{crit}. \tag{4.19}$$

The condition $\Delta V(0) \leq \Delta V_{crit}$ is therefore a sufficient condition for the system to obtain the unpinned equilibrium $\Delta V_{eq}(\mathbf{\Phi}^+)$ which is independent of the initial contact angle configuration. We note that $\Delta V_{crit} = \Delta V_{bnd}(\mathbf{\Phi}^-)$, which is consistent with solutions in figure 4.10 being bounded above by those with $\mathbf{\Phi}(0) = \mathbf{\Phi}^-$ since $\Delta V_{eq}(\mathbf{\Phi}^+)$ is the minimum equilibrium value.

Figure 4.11 illustrates the equilibrium volume $\Delta V_{eq}(\phi_1, \phi_2)$ for a horizontal system along with the basin of attraction ΔV_{bnd} defined by (4.18) for the unpinned equilibrium $\Delta V_{eq}(\mathbf{\Phi}^+)$. The critical volume difference ΔV_{crit} is also shown as are a selection of trajectories in $(\Delta V, \phi_1, \phi_2)$ space that correspond to solutions shown in figure 4.10. We see that only solutions starting within the basin of attraction boundary reach the unpinned equilibrium ΔV_{eq}.

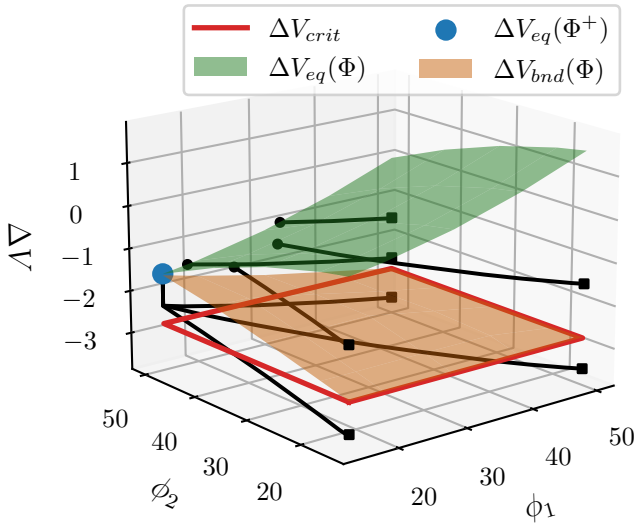

Figure 4.11: Three dimensional plot showing the equilibrium volume differences ΔV_{eq} and boundary volume difference $\Delta V_{bnd}(\mathbf{\Phi})$ for a horizontal system. The minimum unpinned equilibrium $\Delta V_{eq}(\mathbf{\Phi}^+)$ and the critical volume difference ΔV_{crit} are also indicated. Trajectories of solutions (with their final equilibrium values and initial values indicated by black circles and squares respectively) show how $\Delta V_{bnd}(\mathbf{\Phi})$ forms the boundary for the basin of attraction of $\Delta V_{eq}(\mathbf{\Phi}^+)$.

4.4.5 Discussion of system parameters

The critical volume difference ΔV_{crit} depends on both the elevation angle and the system parameter values. Figure 4.12(a) illustrates the variation of the critical volume difference ΔV_{crit} and the unpinned equilibrium volume difference $\Delta V_{eq}(\mathbf{\Phi}^+)$ with the elevation angle for the standard system parameters. The critical volume difference V_{crit} is also indicated, which exhibits a slight variation with the elevation angle as shown in figure 4.12(b).

From the definition in (4.19), the critical volume difference ΔV_{crit} is defined in terms of $\Delta V_{eq}(\mathbf{\Phi}^+)$ and V_{crit}. The unpinned equilibrium volume difference is

$$\Delta V_{eq}(\mathbf{\Phi}^+) = 2\ell \tan\theta - 2S \sec\theta, \tag{4.20}$$

which depends on the reservoir separation distance ℓ. Dependence on the Bond number and microscopic contact angles is only through the surface tension parameter $S = \mathrm{Bo}^{-1}|\cos\alpha_A - \cos\alpha_R|$.

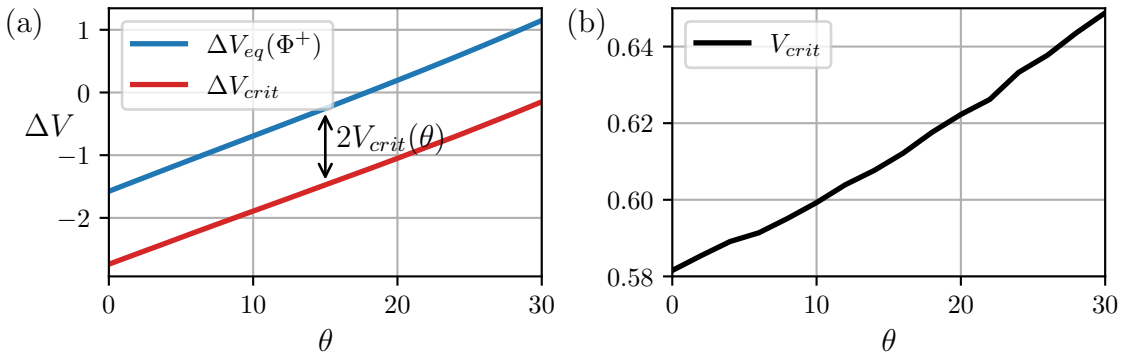

Figure 4.12: (a) Variation of the critical volume difference ΔV_{crit} and minimum unpinned equilibrium volume difference $\Delta V_{eq}(\mathbf{\Phi}^+)$ with elevation angle θ for the standard system parameter values. (b) Corresponding variation of the critical transfer volume V_{crit} with elevation angle.

The critical volume difference meanwhile in general does not have a closed form expression. It depends on the contact-line dynamics in a single well and thus depends on the Bond number and microscopic contact angles. Figure 4.13 shows how V_{crit} depends on the Bond number for a range of microscopic contact angle pairings. We see that V_{crit} increases with the surface tension parameter S via both the decreasing Bond number and increasing hysteresis range. Furthermore, V_{crit} is bounded with the maximum value occurring in the limit Bo $= 0$ of the spherical cap meniscus and at the maximum hysteresis range $(\alpha_R, \alpha_A) = (0°, 180°)$.

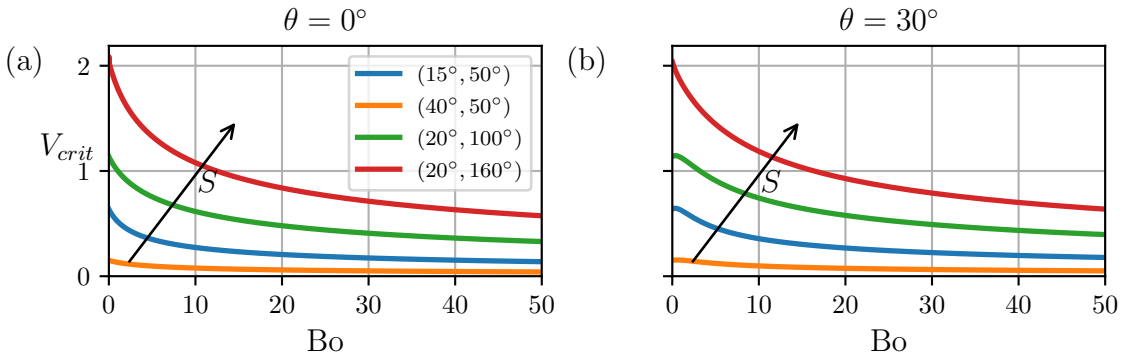

Figure 4.13: Variation of the critical volume difference V_{crit} with Bond number for a range of contact angle pairings (α_R, α_A) as indicated for (a) a horizontal system $\theta = 0°$ and (b) an elevated system with $\theta = 30°$.

4.4.6 Discussion

Capillary effects modify the dynamics of the system at a fixed elevation angle by reducing the volume of fluid transferred across the wells due to the additional capillary pressure term which opposes the flow. In addition, contact angle hysteresis introduces a degree of variability in the system, which manifests through a range of potential equilibrium states and a sensitivity to initial conditions. The surface tension parameter $S = \mathrm{Bo}^{-1}|\cos\alpha_A - \cos\alpha_R|$, which gives the maximum magnitude of the capillary pressure difference in the small τ regime and thus measures the strength of capillary forces in the system, can be used to quantify both the deviation from the surface tension free solution and the variability in equilibrium states.

While in principle capillary effects can be controlled by reducing the surface tension parameter S (e.g. by increasing the Bond number through the system design or properties of the culture medium, or by reducing the hysteresis range through use of a coating to control the contact angles) in practice capillary effects are an inherent part of the current system design with the typical system parameters corresponding to a value of S of order unity. The resulting sensitivity to the initial state of the system is undesirable however, since it introduces variability across repeated experiments. Our results highlight that care must be taken in preparation of the system to ensure that it begins at a known contact angle configuration in order to accurately predict the resulting dynamics.

However, controlling or even measuring the initial contact angle configuration in each reservoir is challenging in practice. Thus for flows driven by an initial difference in volume between the wells, our analysis identifies a criterion for the magnitude of this difference, based on the critical initial volume difference ΔV_{crit}, which ensures the system reaches a known final equilibrium state, the minimum unpinned equilibrium $\Delta V_{eq}(\mathbf{\Phi}^+)$, regardless of the initial contact angle configuration. Physically, this corresponds to a sufficiently high initial hydrostatic pressure difference to overcome the variability that results from the capillary pressure difference.

The critical volume difference provides a method of shifting the system from an

arbitrary unknown state to a fully determined one, provided the system parameters are known. In practice, it provides a method of setting up the system to achieve a known initial state before continuing to the next stage of an experiment, since this knowledge allows the subsequent dynamics to be accurately modelled and controlled. Typically, the subsequent motion is driven by varying the elevation angle rather than volume differences and we move on to consider these regimes next.

4.5 Capillary effects in an oscillating system

We now explore how capillary effects alter the dynamics of an oscillating system. To match typical experimental operations, we consider the paused oscillation regime outlined in §4.3.5 and further restrict attention to oscillations with sufficiently long pause times, which allow the system to equilibrate. We fix the transition and pause times at $T_{tr} = 1$ and $T_p = 8$ (total period 20), which are representative of the typical dynamics for oscillations with long pause times, and investigate the impact of varying the oscillation amplitude θ_A. We suppose that the system is initially horizontal and at equilibrium with the initial volume difference therefore $\Delta V(0) = \Delta V_{eq}(\mathbf{\Phi}(0))$ for the prescribed initial contact angle configuration $\mathbf{\Phi}(0)$. For simplicity we suppose the meniscus in each well is symmetric initially. We compare results with the equivalent solutions in the absence of capillary effects ($S = 0$), which are driven by the same oscillating elevation angle and with initial volume difference $\Delta V(0) = 0$.

4.5.1 Oscillatory dynamics

Figure 4.14 illustrates the typical dynamics of an oscillatory system under the standard system parameter values. We present solutions in terms of volume difference, $\Delta V(t)$ and the net volume of fluid transferred across the wells, $V(t) = (\Delta V(t) - \Delta V(0))/2$, which is useful for comparing solutions with different initial volume differences as well as being a more relevant quantity experimentally. The surface tension free solution is also shown for comparison.

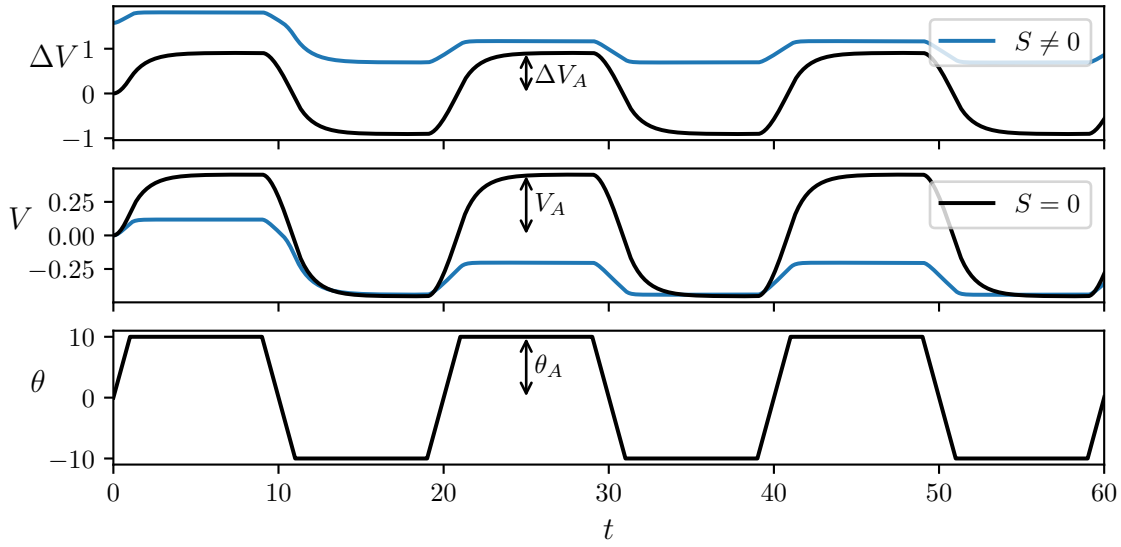

Figure 4.14: Example of oscillatory dynamics showing the evolution of the volume difference ΔV and transfer volume V with time t for prescribed paused oscillations in the elevation angle θ with amplitude θ_A as shown. Solutions are shown with capillary effects ($S \neq 0$) for initial contact angle $\phi(0) = 35°$ and in the absence of capillary effects ($S = 0$). The steady state amplitudes ΔV_A and V_A are also indicated for the case $S = 0$.

We observe that oscillatory dynamics both with and without capillary effects are similar. The pause time is sufficiently long to allow drainage to equilibrium during each half oscillation cycle, and the fluid volume undergoes regular, steady-state oscillations after the first oscillation cycle. The amplitude and midpoint of the steady state oscillations in the volume difference are denoted by ΔV_A and ΔV_m, respectively, and are set by the equilibrium values obtained during the forward and backward oscillations. The corresponding amplitude and midpoint of the oscillations in the transfer volume are $V_A = \Delta V_A/2$ and $V_m = (\Delta V_m - \Delta V(0))/2$, respectively.

In the absence of surface tension $\Delta V_A = \ell \tan \theta_A$, which is set by the hydrostatic equilibrium, and the oscillation midpoint is zero. Surface tension reduces the amplitude of the volume oscillations and the midpoint of these oscillations is no longer zero in general for both ΔV and V. Furthermore, the oscillation amplitude and midpoint can depend on the initial contact angle configuration.

4.5.2 Sensitivity to initial conditions

Figure 4.15 shows the oscillations in ΔV and V for a range of solutions with different initial contact angle configurations and elevation amplitudes. For the majority of solutions we take the initial contact angle in each well to be equal, and thus $\Delta V(0) = 0$, however solutions corresponding to the unpinned initial states $\mathbf{\Phi}^- = (\alpha_A, \alpha_R)$ and $\mathbf{\Phi}^+ = (\alpha_R, \alpha_A)$ are also shown. As for the static system, these solutions, where the capillary pressure is minimal or maximal, form upper and lower bounds for all other solutions.

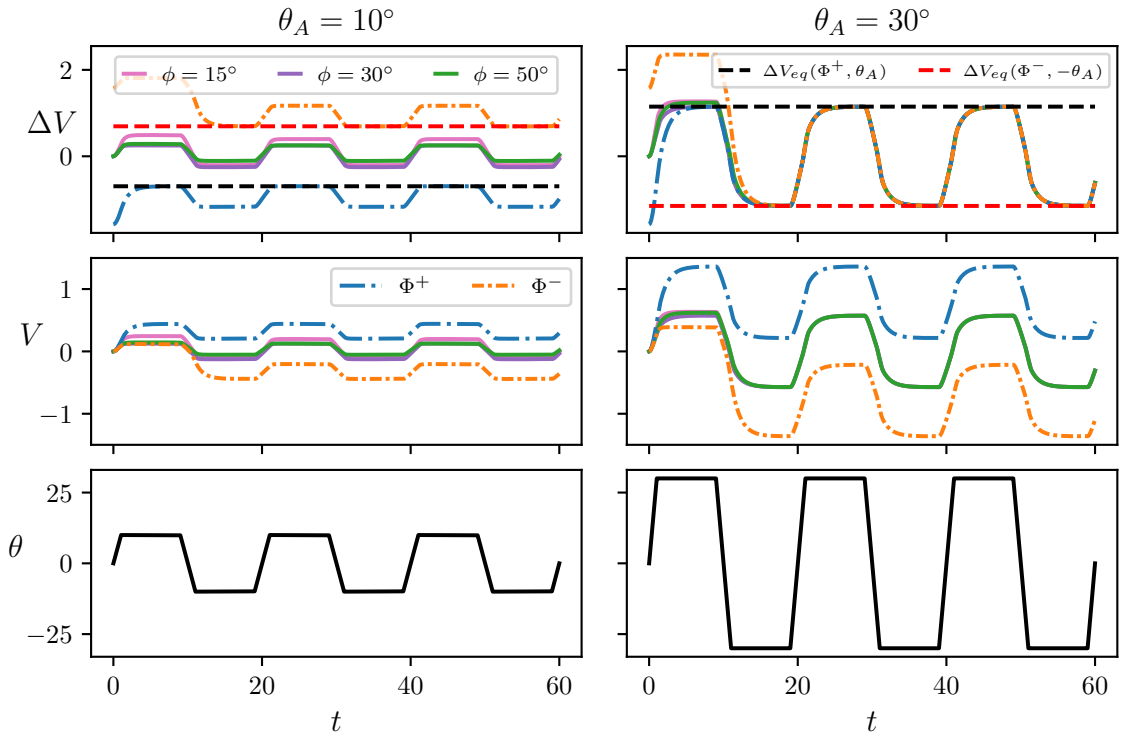

Figure 4.15: Solutions showing the evolution of the volume difference ΔV and transfer volume V with time t for two different elevation amplitudes and for a range of initial contact angle configurations. They include configurations where the initial contact angle ϕ is the same in both wells, and the two fully unpinned initial configurations $\mathbf{\Phi}^+ = (\alpha_R, \alpha_A)$ and $\mathbf{\Phi}^- = (\alpha_A, \alpha_R)$.

Figure 4.15 highlights two possible cases depending on the magnitude of the elevation amplitude. For small elevation amplitudes, solutions with different initial conditions are generally distinct, although solutions with similar initial conditions

are naturally similar. The equilibrium volume differences attained on the forward and backward portions of the oscillation cycle are sensitive to the initial contact angle configuration. However, in all cases they remain bounded with

$$\Delta V_{eq}(\mathbf{\Phi}^+, \theta) \leq \Delta V_{eq} \leq \Delta V_{eq}(\mathbf{\Phi}^-, \theta) \tag{4.21}$$

for $\theta = \pm\theta_A$.

For larger elevation amplitudes, solutions with different initial conditions ultimately coalesce and attain the same steady state oscillations in ΔV, which can be seen for solutions with $\theta_A = 30°$. In this case, all steady state solutions in ΔV have midpoint zero and amplitude $\Delta V_A = \Delta V_{eq}(\mathbf{\Phi}^+, \theta_A)$. This corresponds to solutions attaining the minimum unpinned equilibrium state $\Delta V_{eq}(\mathbf{\Phi}^+, \theta_A)$ during the forward portion of the oscillation and the maximal unpinned equilibrium state $\Delta V_{eq}(\mathbf{\Phi}^-, -\theta_A) = -\Delta V_A$ during the reverse oscillation. These equilibria are indicated in figure 4.15; we note by symmetry that

$$\Delta V_{eq}(\mathbf{\Phi}^\pm, \theta_A) = -\Delta V_{eq}(\mathbf{\Phi}^\mp, -\theta_A) \tag{4.22}$$

from the definition in (4.16). Meanwhile, steady state solutions for the transfer volume V all have the same amplitude $V_A = \Delta V_{eq}(\mathbf{\Phi}^+, \theta_A)/2$, but may have different midpoints, which are set by the initial volume difference.

There are parallels between these two cases and the behaviour of the static system, where a sufficiently large hydrostatic pressure difference could overcome the sensitivity to initial conditions and ensure all solutions attain the unpinned equilibrium state. For the static system, this pressure difference was provided by a difference in volume but here it results from a change in elevation angle. Thus we can identify a criterion based on the elevation amplitude rather than the initial volume difference to remove the sensitivity to initial conditions.

4.5.3 Critical elevation angle

The criterion which ensures all solutions reach the same steady state regardless of initial conditions takes the form $\theta_A > \theta_{crit}$, where θ_{crit} is the critical elevation amplitude. This critical elevation amplitude depends on the system parameters, namely

the hysteresis range, Bond number, and reservoir separation distance. It is straightforward to determine θ_{crit} numerically since it is sufficient to evaluate solutions where the contact angle configuration is unpinned $\mathbf{\Phi}^{\pm}$ initially, since these bound all other solutions. Furthermore by symmetry we can restrict attention to either one of these initial states.

We can also obtain an approximation to θ_{crit} by considering a similar physical argument to the one used to determine the critical volume difference for a static system. We consider the solution with initial contact angle configuration $\mathbf{\Phi}^{-}$, which must attain the unpinned equilibrium state $\Delta V_{eq}(\mathbf{\Phi}^{-}, -\theta_A)$ during the negative portion of the oscillation cycle. If after the next transition $-\theta_A \to \theta_A$ this solution attains the unpinned equilibrium state $\Delta V_{eq}(\mathbf{\Phi}^{+}, -\theta_A)$ then all solutions must reach the same steady state.

We assume the change in elevation angle is sufficiently rapid that there is limited fluid transferred between the wells, and further neglect any changes in the contact angle during this period. Following similar arguments used to determine ΔV_{crit}, a condition for the system to become fully unpinned is

$$\Delta V(\mathbf{\Phi}^{+}, \theta_A) > V_{crit}(\theta_A), \tag{4.23}$$

where the critical transfer volume $V_{crit}(\theta_A)$ is the volume of fluid transferred between the two wells for both menisci to transition between the advancing and receding states. This condition ensures that $Q > 0$ up until the point that the $\mathbf{\Phi}^{+}$ contact angle configuration is reached. This condition determines the critical elevation amplitude.

We recall that $\Delta V(\mathbf{\Phi}^{+}, \theta) = 2\ell \tan\theta - S$, while $V_{crit}(\theta)$ depends on the microscopic contact angles and Bond number. As discussed in §3.4.6, V_{crit} increases with stronger capillary effects, through either a smaller Bond number or larger hysteresis range, as does the surface tension parameter S.

The critical elevation angle therefore also increases with stronger capillary effects. Figure 4.16(a) shows how the critical elevation amplitude varies with the hysteresis range with $15^\circ \leq \alpha_R \leq \alpha_A \leq 50^\circ$ while the remaining system parameters of the Bond number and reservoir separation distance remain fixed at the standard values. The

critical elevation angle generally increases for larger hysteresis ranges, although its precise value depends on the two microscopic contact angles individually. This is reinforced by the scatter plot in figure 4.16(b) of the critical elevation amplitude against the surface tension parameter S, although there is naturally a strong correlation with S.

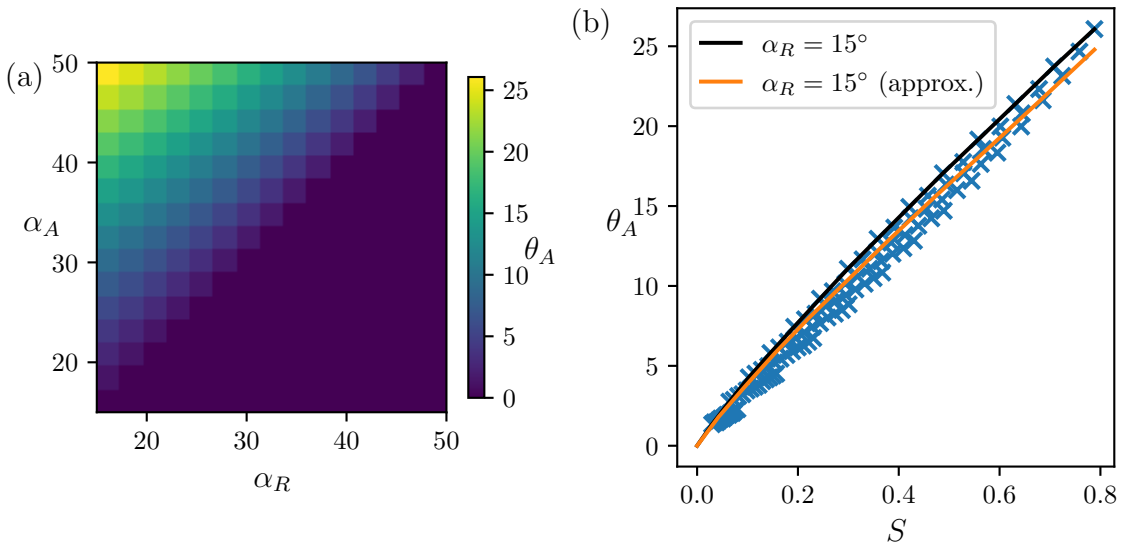

Figure 4.16: (a) Critical elevation amplitude θ_A as a function of the microscopic contact angles $\alpha_R \leq \alpha_A$. (b) Scatter plot of the critical elevation angle against the surface tension parameter S. The critical elevation angle as a function of S for fixed $\alpha_R = 15°$ is also shown from both direct numerical simulations and an approximation based on the critical transfer volume. The standard values of Bo and ℓ are used in all cases.

Figure 4.16(b) also highlights the critical elevation angle for fixed α_R while α_A varies. The approximation based on the critical transfer volume is also shown in this case and there is good agreement between the two values particularly for smaller values of α_A. The approximation is less good for larger hysteresis ranges, since the increased oscillation amplitudes required result in more significant changes to the contact angle as the system is tilted, which are neglected in the approximation based on the critical transfer volume.

Overall, the critical elevation amplitude increases with capillary effects, through an increasing hysteresis range or a decreasing Bond number. However, it can be reduced

by increasing the reservoir separation distance ℓ, which amplifies the hydrostatic pressure difference induced by tilting. Much like the critical volume difference, the critical elevation amplitude provides a means of removing the variability induced by contact angle hysteresis and ensuring all initial conditions result in the same steady state for ΔV.

4.5.4 Transfer volume

In practice, the transfer volume V is more relevant for a typical biological experiment than the volume difference ΔV, since the volume of fluid transferred between the wells determines the mixing of solutes. If we are concerned with the mixing of a solute that is continuously produced by the cell cultures, then it is only the amplitude of the steady state oscillations which matters, since the duration of a typical experiment is long compared with the length of a single oscillation cycle (i.e. days compared with minutes). Conversely, if we are interested in the mixing of an initial solute distribution then both the amplitude V_A and midpoint V_m of these oscillations are relevant. We primarily restrict our discussion to the first mixing problem which requires determining the relationship between the elevation amplitude θ_A and the volume amplitude V_A, through which we can identify the optimal tilting regime for a desired exchange of volume between the two wells.

Figure 4.17(a) summarises the variation of the volume amplitude V_A with the initial contact angle configuration for a range of elevation amplitudes θ_A. We consider the standard system parameters and restrict attention to initial states where each meniscus is symmetric and the initial contact angle ϕ is the same in both wells. For a given elevation amplitude, there is generally only a small variation in the volume amplitude with the initial contact angle, with V_A increasing as ϕ is reduced. This is explained by the fact that the capillary pressure depends on the cosine of the contact angle and thus varies more slowly for contact angles further from 90°. Furthermore, above the critical elevation amplitude ($\theta_{crit} \approx 26°$ for the standard parameter values) there is no variation in amplitude with the initial contact angle, since all solutions obtain the same steady state in this case.

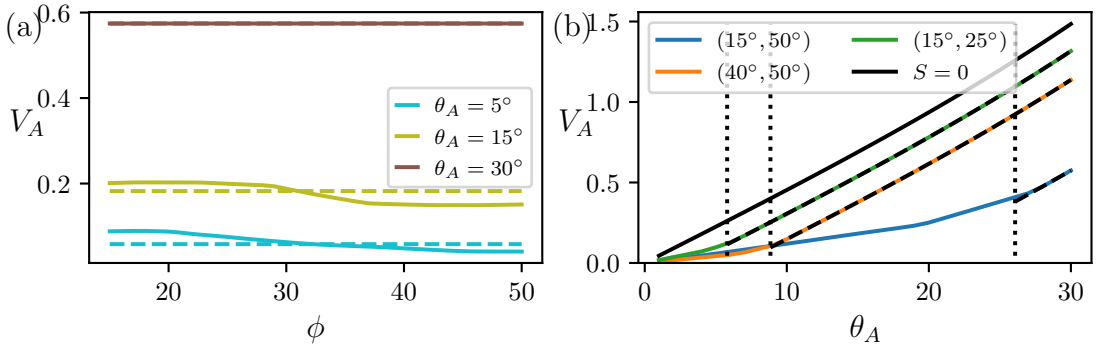

Figure 4.17: (a) Dependence of the steady-state amplitude of the transfer volume V_A on the initial contact angle configuration, where ϕ is the initial contact angle in both wells, for a selection of elevation amplitudes θ_A. In each case the volume amplitude corresponding to the fully unpinned initial configuration $\mathbf{\Phi}^+$ is also shown by a dashed line. (b) Transfer volume amplitude as a function of the elevation amplitude for the initial configuration $\mathbf{\Phi}^+$. Solutions are shown for a range of hysteresis ranges and for the surface tension free regime $S = 0$. For solutions with surface tension, the critical elevation amplitude is indicated by a dotted vertical line, while the theoretical equilibrium volume for $\theta_A > \theta_{crit}$ given in (4.24) is indicated by a dashed line

Figure 4.17(a) also shows the corresponding volume amplitude associated with the initial equilibrium state $\mathbf{\Phi}^+ = (\alpha_R, \alpha_A)$ by a dashed line. This is typically close to the mean value across all initial contact angles, since it corresponds to contact angles at either end of the hysteresis range. We therefore adopt this value as a measure of the average volume amplitude for a particular elevation amplitude, which is further justified by the fact that we can prepare the system in the $\mathbf{\Phi}^+$ state using the critical volume difference.

Figure 4.17(b) shows the volume amplitude V_A corresponding to the initial state $\mathbf{\Phi}^+$ as a function of the elevation amplitude θ_A. The amplitude is shown for a variety of hysteresis ranges as well as in the absence of capillary effects / contact angle hysteresis ($S = 0$). In each case, the critical elevation angle is indicated by a dashed vertical line.

The volume amplitude V_A naturally increases with elevation amplitude θ_A. Furthermore, above the critical elevation angle we can determine an explicit expression

for the volume amplitude, which is

$$V_A = \ell \tan\theta_A - S \sec\theta_A, \tag{4.24}$$

for $\theta_A > \theta_{crit}$. In this case, the reduction in amplitude from the surface tension free solution is $S \sec\theta_A$ and so can be quantified in terms of the surface tension parameter S. For $\theta_A < \theta_{crit}$, we must rely on numerical simulations since we do not have an explicit expression for the volume amplitude. We again find that stronger capillary effects decrease the volume amplitude for a given elevation angle, while stronger gravitational effects increase the volume amplitude.

This analysis allows us to calculate the appropriate elevation amplitude θ_A for a desired volume amplitude V_A. This is illustrated in figure 4.18, where we show that the same volume amplitude can be achieved for different hysteresis ranges by judicious selection of the elevation amplitude. All solutions have steady state amplitude $V_A = 0.5$, including the surface tension free solution.

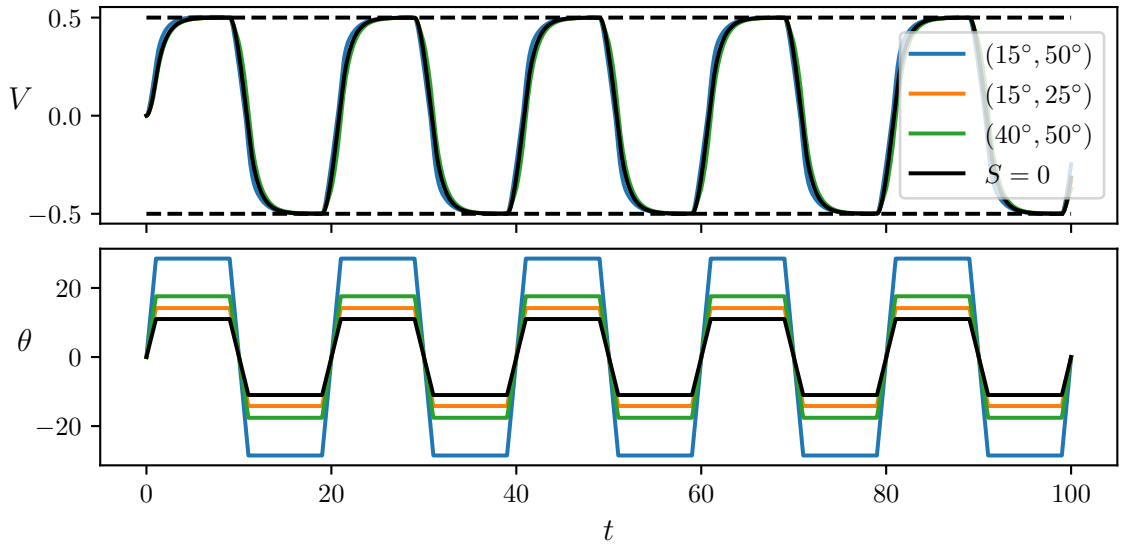

Figure 4.18: Oscillation in the transfer volume $V(t)$ for three distinct hysteresis ranges and in the absence of surface tension ($S = 0$). In each case, the amplitude of the oscillation in the elevation angle θ is chosen to obtain a steady state volume amplitude $V_A = 0.5$, as indicated by the dashed horizontal line. The initial condition and contact angle configuration correspond to $\Delta V(0) = 0$ and ensure that the oscillation midpoint is $V_m = 0$ in each case.

In addition, for each solution we select initial conditions which ensure the oscillations have midpoint $V_m = 0$ by setting $\Delta V(0) = 0$. We note that this choice does not affect the oscillation amplitude since in all cases $\theta_A > \theta_{crit}$. In practice however, it can be difficult to prepare the system in a known state in this way, and so control of the midpoint V_m can instead be achieved by adjusting the elevation regime. This involves considering oscillations in the elevation angle, which are not zero-centred or more general transitions between different elevation amplitudes to achieve the desired fluid volumes and flow rates.

Finally, the examples presented in figure 4.18 show how a desired volume amplitude can be achieved for given system parameter values by varying the elevation amplitude alone, which is useful for an experimenter to select the appropriate operating regime. However, for some parameter values it may not be possible to achieve the desired volume flows, for instance if capillary effects are too strong that it would require an elevation amplitude beyond the feasible device operating regimes. In such cases, our analysis can be used to inform modifications to the design of the system to achieve the desired transfer of fluid between the wells. This includes varying the system geometry through a longer channel length to increase gravitational effects, or by reducing capillary effects by, for instance, increasing the reservoir width or reducing the hysteresis range.

4.6 Discussion

In this chapter, we have characterised the dynamics of gravity-driven flows in a two-dimensional twin-well system under both static and oscillatory operating conditions. Our initial analysis in §4.3 analysed the volume flow rate in the absence of surface tension effects, which served to introduce the general dynamics. In this scenario, flows in a static system drained to equilibrium on a timescale set by the hydraulic resistance of the channel. This depends on the channel geometry and is particularly sensitive to the channel height, which can be used to adjust the time to equilibrium as has been studied previously [14]. In an oscillatory system, the fluid volume ultimately

undergoes steady-state oscillations with an amplitude dependent on both the elevation amplitude and frequency. For low-frequency oscillations, which reflect experimental operating conditions, the flow rate is small and the volume varies slowly, tracking the equilibrium state.

The surface tension free model serves as a first approximation for flow in the system, and indeed, often capillary effects are neglected entirely in similar gravity-driven systems [35, 86]. In §4.4 and §4.5 we examined how the dynamics are modified by the inclusion of capillary effects. Overall, capillary forces, and in particular hysteresis of the contact angle, serve to reduce the flow rate and transfer of fluid across the wells. In a static system, contact angle hysteresis introduces a range of potential equilibrium states, with the final state sensitive to the initial conditions. Similarly for an oscillating system, the steady state amplitude is reduced compared with the surface tension free solution and the midpoint and amplitude of these oscillations are again sensitive to the initial conditions, in addition to depending on the system parameters and hysteresis range.

Through our analysis, we identified criteria, based on the initial volume difference for a static system and the elevation amplitude for an oscillating system, that remove the dependence on initial conditions, ensuring all solutions obtain the same equilibrium state or oscillation amplitude. Both of these criteria are related to the concept of the critical transfer volume, as discussed in our single-well analysis, which is the required volume for the meniscus in a single well to transition between the advancing and receding contact angle configurations. This highlights the importance of understanding the contact-line dynamics and their effect on the flow rate.

In addition, our analysis allows capillary effects to be quantified with the surface tension parameter $S = \mathrm{Bo}^{-1}|\cos\alpha_A - \cos\alpha_R|$ proving a useful measure of the strength of capillary effects in the system. This gives the maximum capillary pressure difference and thus the equilibrium volume or oscillation amplitude typically depend on this quantity. Controlling this parameter through physical adjustments to the system can in principle reduce capillary effects, although in practice some capillary effects are inevitable. Thus our analysis focussed on ways in which capillary effects can

be accounted for through the operation of the system, which include achieving the desired flow rates or transfer of fluid across the system.

In this chapter we have restricted attention to a two-dimensional representation of the system for computational efficiency, although we expect our characterisation of the general qualitative behaviour to remain applicable to a three-dimensional geometry. Extending our analysis to the three-dimensional system to obtain quantitative predictions relevant to the physical system is a natural direction of future work. The key change in moving from two to three dimensions is the form of the Young-Laplace equation and the resulting boundary data maps. Thus in some operating regimes, for example a static horizontal system for which axisymmetric solutions for the meniscus shape are readily available, this extension is reasonably straightforward. For a tilting system however, we require the more computationally intensive numerical scheme based on Surface Evolver to fully account for the contact-line dynamics in both wells.

However, we recall that our analysis of the single-well contact-line dynamics in chapter 3 showed that the effects of tilting on the capillary pressure can often be neglected under standard operating conditions, with the capillary pressure approximated from the axisymmetric horizontal solution of the Young-Laplace problem. A similar symmetric approximation for the two-dimensional twin-well system also performs well, both for low amplitude oscillations in the elevation angle and for larger amplitudes provided $\theta_A > \theta_{crit}$, although we omit the details of this analysis here. This suggests that the axisymmetric approximation is a suitable approach to simplify the computation of the three-dimensional system dynamics under typical operating conditions.

Further extensions of our analysis in this chapter include the application of the reduced model to different system designs and geometries. This includes multi-well systems, where additional wells are connected in sequence, or larger and more complex networks of wells and channels [64].

Finally, a key motivation for understanding the flow in the system is its role in driving transport and mixing of solute between the two wells. Our analysis in this chapter provides a relationship between the device operating conditions through the

variation of the elevation angle and the resulting flow, allowing an experimenter to optimise the operating conditions to achieve a desired flow rate. The next stage of this problem is therefore to understand the relationship between the flow rate and the transport of solute, and thus identify exactly what flow rate is desirable, which is the focus of the next chapter.

Chapter 5

Solute transport and reactions in two dimensions

5.1 Introduction

In this chapter we study solute transport and reactions in the twin-well system. This builds on our previous analysis of fluid flow since under typical experimental operating conditions advective transport is the predominant transport mechanism. Due to computational limitations, we continue to restrict attention to a simplified two-dimensional representation of the system. Our analysis captures the key qualitative features of solute transport from which we can extract useful insights to inform optimal experimental procedure.

The structure of this chapter is outlined as follows. We provide a brief overview of solute transport and reaction problems in microfluidic systems in §5.2. In §5.3 we present a summary of the two-dimensional system geometry and the relevant transport and reaction processes we consider, along with the associated transport equations and modelling assumptions. We also introduce the particle-based numerical scheme we implement to solve the corresponding reaction-advection-diffusion equation. In §5.4 we discuss the concept of mixing within the microfluidic system, which is integral to the transport problems we consider, and define relevant measures of mixing. In §5.5 we extend our analysis of the fluid flow problem, which until now has only concerned the volume flow rate, to determine the flow profile, which is required to study advective transport. In §5.6 we examine the mixing of an initial solute con-

centration under advective and diffusion transport and in §5.7 we incorporate simple solute production reactions. Both of these scenarios serve as simple representations of the mixing problems associated with the typical experimental use of the system. Finally in §5.8 we summarise our key findings and discuss potential extensions of our modelling and analysis.

5.2 Overview of solute transport and reactions

Understanding and controlling solute distribution in microfluidic systems is of vital importance, from ensuring adequate nutrient supply and waste removal for cell culture growth in bioreactor systems to delivering exact drug concentrations to each microfluidic chamber in advanced organ-on-a-chip devices for pharmaceutical studies [26, 88]. In the context of pharmaceutical drug development, *in vitro* microfluidics systems are routinely used to estimate reaction rates for pharmacokinetic studies [89, 90]. These parameter estimates are typically based on a compartmental modelling framework, which relies on the assumption that each microfluidic chamber constitutes a well-mixed system [39]. Thus it is important to ensure typical experimental operating conditions result in a well-mixed system. On the other hand, spatial variations in solute concentration play an important role in other pharmaceutical studies. Examples include studies of spatial heterogeneity in drug metabolism in the liver and chemotactic transport of immune cells for immunotherapy treatments, which require establishing precise concentration gradients across the microfluidic system [36, 91].

However, the nature of microfluidic systems can make controlling solute transport challenging, particularly in cases where rapid mixing is desirable. For instance, many solutes, including larger drugs and biomolecules, have low diffusivity meaning that mixing by diffusion is limited despite the small device length scales [10]. Thus, mixing in these systems generally relies on advective transport and an imposed flow rate, but effective mixing is often hampered by the laminar and reversible flows associated with low Reynolds numbers [10]. This has motivated the development of a variety of mixing strategies for microfluidic systems. These include active stirring techniques to disrupt

the interface between parallel fluid layers, and passive techniques, which can involve modifying the system geometry using herringbone channels or obstacles to modify the flow, for example [12, 92]. Many of these mixing strategies are examples of chaotic mixing [11].

Solute transport in microfluidic systems can be modelled using a range of frameworks. Pharmacokinetic modelling generally favours compartmental models for their simplicity, where transport processes are described by ordinary differential equations. Reaction kinetics can similarly be modelled via ordinary differential equations with a range of well-established models for typical biological processes [93]. However, in cases where spatial variation is important solute transport and reactions are typically modelled by reaction-advection-diffusion (RAD) equations.

In all but the simplest cases, RAD equations must be solved numerically, with their complexity and utility in modelling many physical phenomena resulting in the development of a large range of numerical solution schemes. Classical partial differential equation methods for solving these equations include finite difference schemes, finite element schemes, and spectral methods [94, 95]. All these methods have advantages and limitations, and their suitability depends on the specifics of the problem at hand. Some typical challenges associated with RAD problems include the disparity in timescales of different processes, the presence of non-linear reaction terms, and finding solutions within complex domains [96]. The first of these issues is particularly relevant for our problem, which features large Péclet numbers due to low solute diffusivity and the nature of the flow.

Classical finite difference and finite element methods can struggle to resolve solute transport in these high Péclet regimes, with solutions exhibiting oscillatory behaviour or instability. Many transport problems fall into this regime and so numerous modifications to these schemes have been developed to address these challenges, including upwind schemes or the inclusion of artificial diffusion [97]. Further refinements in the case of disparate timescales include the use of operator splitting techniques, in which the RAD equation is split into two or more subproblems representing the individual

transport processes which are then solved sequentially over suitably small intervals, enhancing computational efficiency [98].

The aforementioned methods are typically grid or mesh-based Eulerian schemes. Lagrangian methods, which follow the fluid particle trajectories, have also been developed and are particularly useful in high Péclet number problems where transport is advection-dominated. Such schemes include particle-based numerical methods which range in complexity from simple particle tracing approaches [99, 100], with diffusion and reactions incorporated via stochastic processes [101, 102], to more sophisticated approaches and semi-Lagrangian schemes which combine both Eulerian and Lagrangian approaches [103]. Particle-based approaches are common in studying mixing in microfluidic systems, due to a combination of simple laminar flows and high Péclet number regimes, which allows systems to be analysed using approaches from dynamical systems theory [11, 104].

Motivated by the high Péclet number for our RAD problem, we adopt a simple particle-based scheme, which is outlined in §5.3.3.

5.3 Problem setup

We consider solute transport, via advection and diffusion, and simple solute production reactions. These processes are described by a reaction-advection-diffusion equation, which was outlined for general reaction processes in §2.5. To simplify our analysis while retaining key features of solute transport within the system we make the following modifications to the aforementioned setup.

Firstly, as in chapter 4 we consider a two-dimensional well geometry, with the further simplification that we take each well to have a uniform width (i.e. the culture chamber and reservoir have equal width). Additionally, we do not specify a maximum well height and instead take each well to be semi-infinite. This simplified geometry is representative of the full system while being easier to analyse, and enables us to capture the key qualitative features of solute transport. Furthermore, we are primarily concerned with solute distribution in the lower regions of the well close to the cell

cultures, which we assume are located far from the free surface. The semi-infinite well assumption is not expected to significantly alter the flow profile in these regions, and therefore provides a good approximation to concentration, particularly for the high Péclet regimes we consider. Finally, for simplicity we also neglect the effect of the cell cultures on the flow and incorporate their effect on solute concentration through source and sink reaction terms in appropriate regions.

5.3.1 System geometry

The two-dimensional system geometry that we consider is shown in figure 5.1, which is non-dimensionalised according to the well width. We denote the regions consisting of the left-hand and right-hand wells by $\mathcal{D}_1$ and $\mathcal{D}_2$ respectively, the channel is denoted by $\mathcal{D}_0$, and the solid device wall by $\partial\mathcal{D}$. For later convenience in analysing the concentrations in different parts of the device, each well is divided into ascending square subregions of unit width and height which are labelled alphabetically. Thus $\mathcal{D}_{iA}$ corresponds to the culture chamber and $\mathcal{D}_{iB}$ the connecting region in the ith well, with higher regions corresponding to the well reservoir. We work in a 2D Cartesian coordinate system $\mathbf{x} = (x, y)$ with origin located at the midpoint of the channel base.

The dimensionless length and height of the channel are denoted by l and h respectively. Within the left-hand culture chamber, we identify a circular reaction region of diameter d, which is denoted by $\mathcal{R}$ and indicated in figure 5.1. The reaction region corresponds to the typical size and location of a cell culture and is used to define the appropriate source and sink terms in the reaction-advection-diffusion equation. We limit our analysis to solute production reactions in a single culture chamber, although it is straightforward to extend this analysis to two spheroids by including an additional reaction region in the right-hand culture chamber.

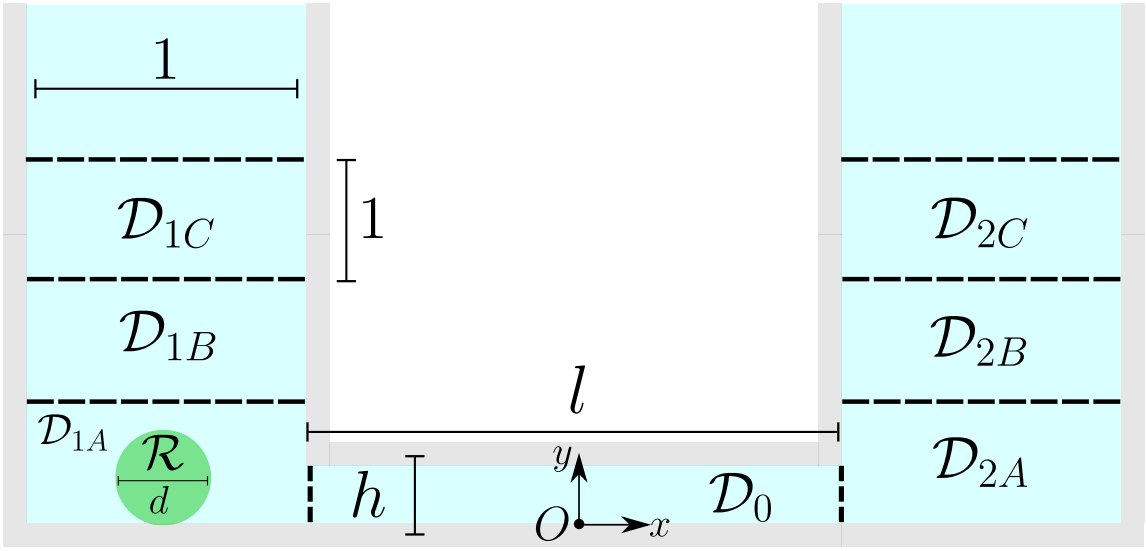

Figure 5.1: Illustration of the simplified two-dimensional geometry showing two semi-infinite wells $\mathcal{D}_i$ for $i = 1, 2$ of uniform unit width connected by a thin horizontal channel $\mathcal{D}_0$ with dimensionless height h and length l. Each well is divided into ascending square subregions labelled alphabetically, with region A corresponding to the culture chamber. The circular reaction region $\mathcal{R}$ of diameter d, which we note is not an explicit boundary, is also shown in the left-hand well.

5.3.2 Transport equations

The dimensionless transport equation for a single solute species is the reaction-advection-diffusion equation

$$\frac{\partial c}{\partial t} + \mathbf{u} \cdot \nabla c = \mathrm{Pe}^{-1} \nabla^2 c + f, \tag{5.1}$$

where $c(\mathbf{x}, t)$ is the solute concentration, $\mathbf{u}(\mathbf{x}, t)$ is the dimensionless velocity field, Pe is the Péclet number, and f is the reaction term. We impose the no diffusive solute flux condition

$$\mathbf{n} \cdot \nabla c = 0 \quad \text{on } \partial\mathcal{D}, \tag{5.2}$$

where $\mathbf{n}$ is the outward pointing unit normal to the solid walls and the far field condition $c \to 0$ as $y \to \infty$. For simple solute production in the left-hand well, the reaction term takes the form

$$f = r\mathbb{I}_{\mathcal{R}}(\mathbf{x}), \tag{5.3}$$

where r is the dimensionless solute production rate and

$$\mathbb{I}_{\mathcal{R}}(\mathbf{x}) = \begin{cases} 1, & \mathbf{x} \in \mathcal{R} \\ 0, & \mathbf{x} \notin \mathcal{R} \end{cases} \tag{5.4}$$

is the indicator function for the reaction region $\mathcal{R}$.

To complete the statement of the problem, we prescribe the initial solute concentration profile $c(\mathbf{x}, 0)$ as well as the explicit form of the velocity field $\mathbf{u}$, which is discussed in §5.5.

We have non-dimensionalised the system of equations by scaling lengths according to the well width L_C^*, time according to the advective timescale $t_A^* = L_C^*/U_0^*$, where U_0^* is the representative velocity scale and concentration according to the representative concentration C_0^*, which is set by the initial solute concentration or production rate. We note that the Péclet number is given by $\mathrm{Pe} = U_0^* L_C^*/D^*$, where D^* is the solute diffusivity coefficient and it is convenient for our later analysis to define the diffusive timescale by $t_D^* = {L_C^*}^2/D^* = \mathrm{Pe}\, t_A^*$. We refer to §2.6 for the typical values of the dimensional parameters. Standard values of the relevant dimensionless parameters are summarised in table 5.1.

l	Channel length	3.5
h	Channel height	0.1
d	Reaction region diameter	0.4
ϵ	Channel aspect ratio	0.03
Pe	Péclet number	$10 - 10^5$

Table 5.1: Dimensionless parameters and typical values for the reaction-advection-diffusion problem.

5.3.3 Numerical scheme

We employ a particle-based numerical scheme to solve the reaction-advection-diffusion equation. This entails tracking the evolution of many particles which represent units of concentration. The evolution of an individual particle is determined by advection along flow streamlines, with diffusive transport and reactions modelled as stochastic processes. Specifically diffusion is modelled as Brownian motion, while reactions

correspond to the addition or removal of particles according to a Poisson process. We refer to [101, 102] for further details on stochastic modelling of reaction-advection-diffusion systems and outline the numerical method we employ, which follows the Euler–Maruyama (EM) solution scheme, below.

The position of an individual particle $\mathbf{X}(t)$ evolves at each time step Δt according to the equation

$$\mathbf{X}(t+\Delta t) = \mathbf{X}(t) + \mathbf{u}(\mathbf{X}, t)\Delta t + \sqrt{2\mathrm{Pe}^{-1}\Delta t}\boldsymbol{\xi}, \tag{5.5}$$

where $\boldsymbol{\xi}$ is a random variable with a standard normal distribution. We note that this is equivalent to the usual finite-difference Euler scheme for solving the ordinary differential equation for particle position in the flow field, with an additional stochastic term to incorporate diffusion. At each time step, we also apply reflective boundary conditions to ensure all particles remain within the domain, which accounts for the no-solute-flux boundary condition. We must specify the initial particle distribution and note that the far-field condition is automatically satisfied.

Particle production is modelled by the addition of particles via a Poisson process with rate parameter $\nu = r|R|$, where r is the reaction rate and $|R|$ the area of the reaction region. At each time step, N particles, distributed uniformly at random within the reaction region $\mathcal{R}$, are added to the system, where N has a Poisson distribution with mean $N_F\nu\Delta t$. The normalising factor N_F corresponds to the number of particles per unit area that equates to a unit solute concentration.

The solute concentration in an arbitrary region $\mathcal{A}$ is defined as

$$c(\mathcal{A}, t) = \frac{1}{N_F A}\int_{\mathcal{A}} \sum_{i=1}^{N} \delta(\mathbf{x} - \mathbf{X}_i)\ \mathrm{d}^2\mathbf{x}, \tag{5.6}$$

where δ is the Dirac delta function and A is the area of $\mathcal{A}$. While the region $\mathcal{A}$ is arbitrary, the area must be sufficiently large (relative to the total particle density) for these concentration measurements to be meaningful. We find that $N_F = 10^4$ is generally sufficient for examining concentrations on the scale of each culture chamber, but take $N_F = 10^6$ when studying concentration variations on smaller scales within the culture chamber.

The appropriate time step depends on the relative magnitude of the advective, diffusive and reaction terms. We note that the numerical error can be split into the following components. Firstly, there is the usual numerical error associated with the deterministic Euler component of this scheme, which corresponds to advection, for which the global error is $O(\Delta t)$. Secondly, while the diffusion term is a stochastic process and so the conventional error is not defined, we can instead consider the error in expected values. It can be shown that the EM numerical scheme has weak convergence $O(\Delta t)$ and strong convergence $O(\sqrt{\Delta t})$ [101]. Additionally, there is the error associated with splitting the transport and reaction processes, which is an issue we shall return to in later discussion. To reduce this error we require the time step to be sufficiently small to allow diffusive effects to occur throughout the process.

Since the Péclet number is typically large, with $\mathrm{Pe} \gtrsim 50$, we expect the error associated with advection to be the most significant. We take $\Delta t = 0.01$ unless otherwise stated, which ensures the size of the diffusive displacement is no larger than that of the advective displacement. The contributions to particle displacement are comparable for the smallest Péclet numbers considered and thus the advective component will be larger in most scenarios.

In cases where Pe is very large, so that the advective component contributes most to the overall error, we may modify the EM scheme as follows. We replace the deterministic Euler component representing advection with the Runge-Kutta fourth order (RK4) scheme, where the expected global error is $O(\Delta t^4)$. Thus the numerical scheme can be summarised as solving the advective component of the transport problem using the RK4 scheme while adding a stochastic term to represent diffusion at the end of this step.

We implement the above algorithm in Python using standard inbuilt routines for both the Euler/RK4 numerical method and for simulating the random variables for Brownian motion and the Poisson process. This implementation is validated by comparison with a range of simple test cases for which the exact solution to the deterministic reaction-advection-diffusion is known. These include a single isolated square culture chamber with rectangular reaction region or a twin-well system in which the

culture chamber and channel have the same height. In both cases the problem is reduced to a one-dimensional reaction-advection-diffusion problem for which analytic solutions exist. We omit the details for brevity.

5.4 Measures of mixing

Our analysis of transport and reaction processes is motivated by questions relating to solute mixing, a term which can be beset by ambiguity due to common informal usage. Thus it is important to clarify exactly what is meant by the concept of mixing within the system and introduce some measures to quantify this mixing.

The potential ambiguity of the term *mixing* is discussed extensively in [13], where it is defined in the context of stirring problems as 'the operation by which a system evolves under stirring from one state of simplicity — the initial segregation of the constituents — to another state of simplicity —their complete uniformity'. In particular, a distinction is drawn between the concepts of *blending* and *stirring*, both of which may be viewed as a rearrangement of solute driven by advection, and true mixing. True mixing requires diffusion: a perfectly *well-mixed* solute corresponds to a homogeneous solute on the molecular scale, while a blended or stirred solute may appear to be well mixed at larger length scales but still exhibit inhomogeneous structure when viewed on a smaller scale.

It is therefore important to be clear about the scale upon which we consider mixing. For our system, we distinguish between two types of mixing. The first is *inter-well* mixing on larger length scales. In this case we consider each culture chamber, or other regions of comparable size, as a whole. Here we are primarily interested in the *transfer* of solute between these regions rather than the exact solute distribution within them. In contrast, the second type of mixing we consider is *intra-well* mixing, which concerns the mixing and spread of solute on a smaller length scale within a particular region. This is closer to the definition of mixing given above, although for our purposes the term *stirring* encapsulates the flow that results from the oscillatory motion of the device.

There are many quantities which can be used to measure the degree of mixing within a system [11, 105] and we introduce three useful measures here. For a general region in the system, which we denote by $\mathcal{A}$ with dimensionless area A, these are the mean solute concentration

$$C_{\mathcal{A}}(t) = \frac{1}{A}\int_{\mathcal{A}} c(\mathbf{x},t)\ \mathrm{d}^2\mathbf{x}, \tag{5.7}$$

the standard deviation of solute concentration

$$\sigma_{\mathcal{A}}(t) = \sqrt{\frac{1}{A}\int_{\mathcal{A}} (c(\mathbf{x},t) - C_{\mathcal{A}}(t))^2\ \mathrm{d}^2\mathbf{x}}, \tag{5.8}$$

and the maximum deviation of solute concentration

$$M_{\mathcal{A}}(t) = \max_{\mathbf{x}\in\mathcal{A}} |c(\mathbf{x},t) - C_{\mathcal{A}}(t)|. \tag{5.9}$$

The first of these is useful for quantifying inter-well mixing by comparing the mean solute concentration across the two culture chambers or other regions of the system. The two remaining measures are relevant to intra-well mixing as they quantify the mixing of solute within a given region, with larger values corresponding to a greater degree of inhomogeneity, while $\sigma, M \to 0$ in a fully well-mixed system. We observe that in general the two measures of deviation scale according to the mean concentration C, and so in cases where this mean concentration varies with time or when comparing mixing in regions with different mean concentrations it is often useful to consider these measures normalised by the mean concentration.

While the standard deviation is a natural measure of the spread of solute, the maximum deviation is often more relevant for practical applications [13]. For instance, in the context of microfluidic systems, solute concentrations above a certain critical level may be detrimental to the cell cultures. A further example, more relevant to the applications we consider, is that experimentally measuring the concentration in a culture chamber involves sampling a small volume of culture medium. Additionally, the degree of inhomogeneity within a region is important in developing models of reaction processes within the system, where spatial uniformity or a well-mixed system is often a key underlying assumption for compartment-based models [40].

In our preliminary analysis of solute transport we shall mostly focus on inter-well mixing and present our results in terms of the mean solute concentration for different regions of the system, although we discuss intra-well mixing where relevant. We adapt the definition (5.7) of the mean concentration for our particle-based scheme in the natural way by making use of the definition (5.6) for the solute concentration in a given region.

5.5 Fluid velocity profile

We begin our analysis by examining the form of the fluid velocity profile, which extends our previous analysis of the fluid-flow problem. In particular, in chapter 4 we analysed the volume flow rate in the two-dimensional system, without considering the details of the flow profile. We recall that the flow was driven by the varying elevation angle, however the leading-order equations for the velocity field do not depend on the elevation and so in this chapter we simply prescribe the flow rate $Q(t)$ directly. This proves more convenient for our analysis, although practically it is more useful to an experimentalist to specify the device operating conditions via the elevation angle θ instead. Our results from chapter 4, characterising the relationship between Q and θ, facilitate converting between the two.

To determine the flow profile, we solve the leading-order equations for fluid flow, which were stated in §2.8.2 in the context of a general three-dimensional system. These equations continue to apply in our two-dimensional setup with some slight modifications to account for the simplified geometry; we summarise the leading-order flow problem here.

In the channel interior, we exploit the small channel aspect ratio and use lubrication theory to find the leading-order Poiseuille flow profile. In the remainder of the system, the fluid is governed by the incompressible Stokes equations to leading order as the Reynolds number is small. The no-slip and no-flux boundary conditions apply at the device walls. For our semi-infinite well geometry, we replace the free surface boundary conditions with a far-field outlet condition specifying fully developed flow.

We restrict attention to the right-hand well and a region of the connecting channel of length $O(h)$, which acts as an inlet region. We introduce a local Cartesian coordinate system (X, Y) with origin located on the well base at the well-channel interface, as illustrated in figure 5.2.

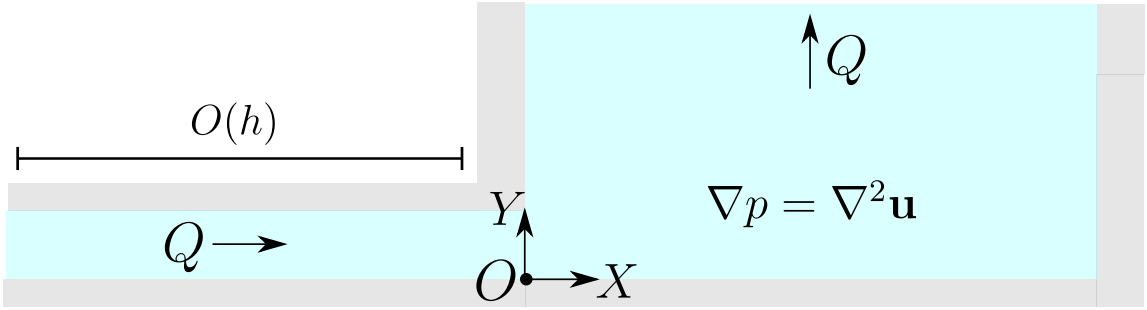

Figure 5.2: Diagram showing the domain for the Stokes flow problem which consists of the right-hand well with a small inlet region of length $O(h)$. The origin of the local Cartesian coordinate system (X, Y) is also indicated. No slip and no flux boundary conditions apply at the solid device walls, while inlet and outlet conditions, based on the flow rate Q, are imposed in the inlet region and as $Y \to \infty$.

The leading-order dimensionless equations for fluid flow are

$$\nabla p = \nabla^2 \mathbf{u}, \quad \nabla \cdot \mathbf{u} = 0, \tag{5.10}$$

subject to the no-flux and no-slip boundary conditions

$$\mathbf{u} = \mathbf{0}, \tag{5.11}$$

on the solid device walls $\partial\mathcal{D}$. We apply the inlet condition

$$\mathbf{u}(X, Y) = \frac{6Q(t)}{h^2} y(h - Y)\mathbf{e}_X, \tag{5.12}$$

in the connecting channel and the far-field outlet condition

$$\mathbf{u}(X, Y) \to 6Q(t)X(1 - X)\mathbf{e}_Y, \tag{5.13}$$

as $Y \to \infty$, where $Q(t)$ is the imposed volume flow rate (per unit length).

These equations describe fluid flow in the right-hand well, from which it is straightforward to determine the flow profile in the remainder of the system. In the channel,

the leading-order Poiseuille profile matches the inlet condition while the flow in the left-hand well is found by symmetry. Furthermore, by linearity of Stokes flow the solution is linear in the imposed volume flow rate. Thus $\mathbf{u} = Q(t)\hat{\mathbf{u}}$, where $\hat{\mathbf{u}}$ is the solution for $Q = 1$ and so the flow streamlines are independent of the volume flow rate. This remains valid provided the volume flow rate is slowly varying, so that Stokes equations continue to apply and we can neglect time dependence, which follows from our assumption of a slowly varying elevation angle driving the flow.

We solve the leading-order equations numerically using COMSOL for a time-independent flow rate $Q = 1$. In doing so, we apply the far-field outlet condition at a large but finite height in the well. Global convergence of the numerical scheme is ensured by repeated refinement of the mesh until there is no significant change to the solutions. We note that a stress singularity exists at the sharp corners at the interface between the well and the channel regions. COMSOL employs adaptive mesh refinement to resolve the associated gradients in the velocity field and thus we expect our solution to be accurate except in the immediate vicinity of the corner. While the singularity can be removed by rounding the corner, the current solutions are sufficiently accurate for our analysis of the transport problem. Finally, we verify that the flow profile in the vicinity of the culture chamber is insensitive to increases in height at which the far field condition is applied.

The flow profile for $Q = 1$ is shown in figure 5.3 in various regions of the right-hand well and channel, returning to the Cartesian coordinate system (x, y) with origin located at the centre of the base of the channel. The flow profile can be summarised by considering three key regions: the culture chamber, the reservoir above the culture chamber (corresponding to $y > 1$), and the channel (corresponding to $x < 1.75$). In the latter two regions, the flow exhibits a Poiseuille profile which is set by the inlet and outlet conditions. In the reservoir, the mean velocity is Q while the corresponding velocity in the channel region is a factor of ten greater due to the smaller channel height. Close to the edge of these two regions, the flow deviates from the Poiseuille profile during the transition into or out of the culture chamber. The size of this transition region is smaller for the channel due to the small channel height.

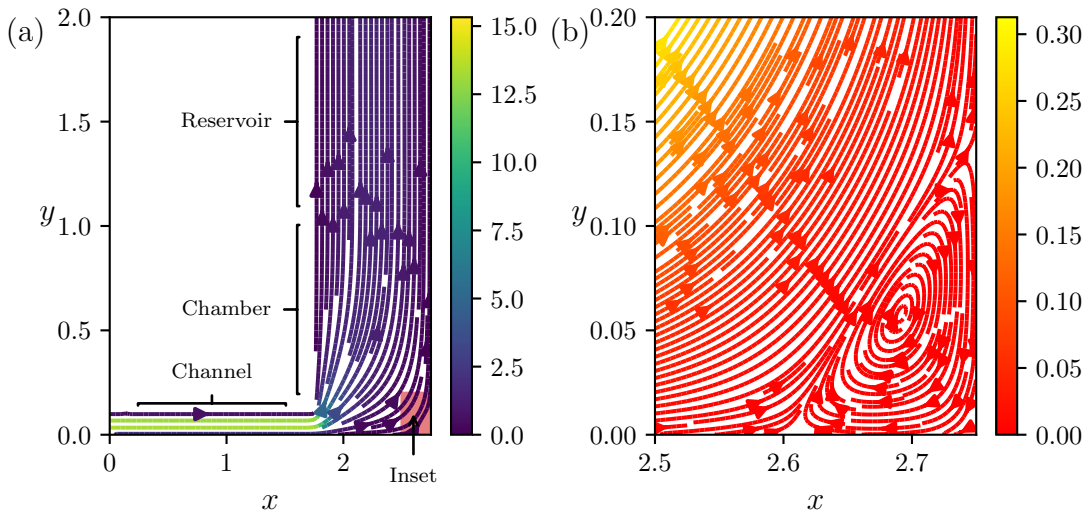

Figure 5.3: (a) Velocity field in the right-hand well and channel for imposed volume flow rate $Q = 1$ with inset region highlighted in red. (b) Inset region showing the lower right-hand corner of the culture chamber to illustrate the largest eddy.

Within the culture chamber itself, the flow exhibits the typical features associated with Stokes flow near a corner [106] and [107]. Faster fluid enters from the inlet channel, slows as it rounds the corner, and ultimately exits into the reservoir. Due to the corner, Stokes separation occurs and a series of eddies form to the right of the separating streamline approaching the corner. This small isolated circulatory region is difficult to see in 5.3(a), and so figure 5.3(b) shows a close-up of this region to highlight the first eddy. The presence of an isolated circulatory region, as well as the low fluid velocity close to the separating streamline, have implications for the effectiveness of advective transport, as we discuss in the next section.

5.5.1 Discussion

Before examining advective transport under this flow profile, we make the following observations. Firstly, while the fluid velocity was found for modified boundary conditions corresponding to an infinite well, it is still valid for a system with finite height under appropriate assumptions. In particular, we assume that each well contains a sufficient volume of fluid so that the free surface remains far from the base of each

reservoir. In this case, we expect the flow to reach a fully developed state within each well before it is affected by the free surface. This is supported by our numerical solutions, where transition to a fully developed flow in the reservoir regions occurs over relatively short length-scales and is independent of the exact position at which the outlet condition is imposed.

Thus our velocity profile is a good approximation to the flow profile in a system with finite height, except in a region close to the free surface. Since we are primarily interested in solute transport within the lower regions of the well (specifically the culture chamber and lower reservoir), such an approximation is acceptable. Most problems we consider involve initial solute distributions, or later solute reactions, which are restricted to the culture chambers themselves, with a small imposed flow rate which restricts solute transport by advection to the lower reservoir regions. Although diffusion will drive solute closer to the free surface, this transport will be limited in high Péclet regimes. Thus we proceed with this approximate flow and exclude the region close to the free surface from our analysis; we highlight cases where this assumption is relevant or in need of refinement as they occur.

This simplified fluid flow problem retains the key features of the physical system and is therefore expected to offer qualitative insights into practical questions. The key features of the flow profile that will prove relevant in our analysis of solute transport include the linearity and reversibility of Stokes flow and the associated characteristics of low Reynolds number mixing [11].

It is straightforward in principle to extend this analysis to different culture chamber geometries, including a three-dimensional system. Furthermore, we can extend our numerical solutions to include the effects of the cell culture on the fluid flow by modelling the region occupied by the cell culture as either a rigid sphere or a porous domain. These extensions require our core modelling assumptions to remain valid: the rocking of the device must be sufficiently small and slow to allow inertial effects to be neglected and the free surface must be sufficiently high within the reservoir so the fully developed flow approximation at the outlet is justified.

Finally, we note that the neglected inertial terms of order $O(\mathrm{Re})$ may be comparable or greater than the diffusive term of order $O(\mathrm{Pe}^{-1})$ for the lowest diffusivity solutes we consider. However, we continue to neglect these terms in our analysis since we are primarily interested in examining the interplay between advection and diffusion. Furthermore, the typical flow regime of paused oscillations results in significant periods where diffusion acts alone and thus is expected to have the greater impact.

5.6 Dispersal of initial solute profile

The first transport problem we examine concerns the dispersal of an initial solute concentration, which, for example, is representative of mixing an initial drug bolus. We consider the transport equations in the absence of solute reactions ($r = 0$) and with the flow profile found in the previous section for a prescribed volume flow rate $Q(t)$. The initial concentration profile is,

$$c(\mathbf{x}, 0) = \begin{cases} 1, & \mathbf{x} \in \mathcal{D}_{1A}, \\ 0, & \mathbf{x} \notin \mathcal{D}_{1A}, \end{cases} \tag{5.14}$$

corresponding to a uniform unit concentration in the left-hand culture chamber. We explore how solutions depend on the imposed flow rate and solute diffusivity and focus on mixing between the culture chambers and other regions. Results are therefore presented in terms of the mean solute concentration C in relevant regions.

5.6.1 Diffusive transport and scaling arguments

The limitations of diffusive transport in the absence of flow can be shown by considering scaling arguments. We recall that the diffusive timescale is defined by $t_D^* = {L_C^*}^2/D^*$, where L_C is the well width and thus represents the typical length scale of the square culture chamber. This is the timescale on which an initial inhomogeneous solute concentration in an isolated culture chamber equilibrates to a uniform concentration profile under diffusive transport alone.

However, we are typically interested in mixing between the two culture chambers, in which case the appropriate timescale for diffusive mixing is expected to scale according to the channel length as $l^2 t_D^*$. For the thin channel we consider here with

$\epsilon \ll 1$, by considering global solute conservation and the rate-limiting solute flux across the channel-well interface, the expected timescale is $\epsilon^{-1} t_D^*$. These scaling arguments support asymptotic analysis of the initial solute dispersal problem under diffusive transport alone in the regime $\epsilon \ll 1$, from which we can determine the mixing time between the two culture chambers for various channel geometries. These results can be confirmed by numerical solutions, which serve to validate the numerical scheme.

We do not include the results of this analysis here as scaling arguments are sufficient to show that diffusive transport alone is insufficient to support mixing across the two culture chambers on the typical timescale of an experiment. Indeed, for the representative values of solute diffusivity, t_D^* ranges from 15 minutes to several hours for higher diffusivity solutes up to several days for the lowest diffusivity solutes. The corresponding timescale for equilibrium between the two culture chambers is increased by a factor of 30 due to the thin channel ($\epsilon \approx 0.03$). Thus equilibrium between the culture chambers, or indeed any meaningful solute mixing, is not possible within the time frame of a six-day experiment for lower diffusivity solutes, while mixing of higher diffusivity solutes is also limited. Furthermore, in practice frequent and rapid mixing of solutes is required to promote continuous reactions between the cell cultures.

This reinforces the principle that advective transport is essential for adequate mixing in microfluidic systems. A static system without flow is not suitable for conducting biological experiments and oscillations to induce flow and enable advective transport are required.

5.6.2 Large Péclet regime

Typical flow conditions correspond to the large Péclet number regime with solute transport dominated by advection. We therefore consider the leading-order approximation where diffusive effects are neglected. In this case, solute transport simply amounts to the *transfer* of solute between different regions of the device and our analysis informs the optimal imposed flow regime for desired solute transfer.

For $\mathrm{Pe} \gg 1$, the right-hand side of (5.1) vanishes at leading order in the absence of reaction terms. Thus the material derivative of solute concentration is zero and the concentration associated with each fluid parcel is conserved. Equivalently, solute particles are simply advected along streamlines, which for Stokes flow do not vary with the imposed volume flow rate $Q(t)$. This allows us to parameterise both particle positions and solute concentrations in terms of the net transfer volume

$$V(t) = \int_0^t Q(t') \, \mathrm{d}t', \tag{5.15}$$

instead of time.

The solution of the initial solute dispersal problem is illustrated in figure 5.4(a), which shows how the mean solute concentration, denoted by $C_{i\alpha}$, varies with the net transfer volume in key regions $\mathcal{D}_{i\alpha}$ of the system. These regions are indicated in the accompanying figure 5.4(b), which also shows a snapshot of the solute particle distribution at key times. We restrict attention to a positive flow rate and thus the concentrations in regions above the culture chamber in the left-hand well are omitted as they remain zero throughout.

We observe that the solute concentration in the channel $\mathcal{D}_0$ and the lower right-hand well $\mathcal{D}_{2A}$ initially increase as solute is transferred. The concentration ultimately reaches a maximum value in each region before decreasing, as solute begins to move further up the well. This can be seen from the solute particle distribution in figure 5.4(b). The shape of the flow profile can also be seen from the solute distribution in the higher well regions.

Meanwhile the solute concentration in the left-hand culture chamber $\mathcal{D}_{1A}$ decreases as fluid is transferred, although this decrease becomes less rapid as more fluid is transferred. From the particle distribution, it can be seen that solute is retained in regions close to the device walls in addition to the lower left-hand corner of the culture chamber. This is explained by the fluid streamlines: solute remains trapped both in the circulatory region itself and along slow streamlines close to this region and the device walls. While some of this solute, along slow-moving streamlines, can

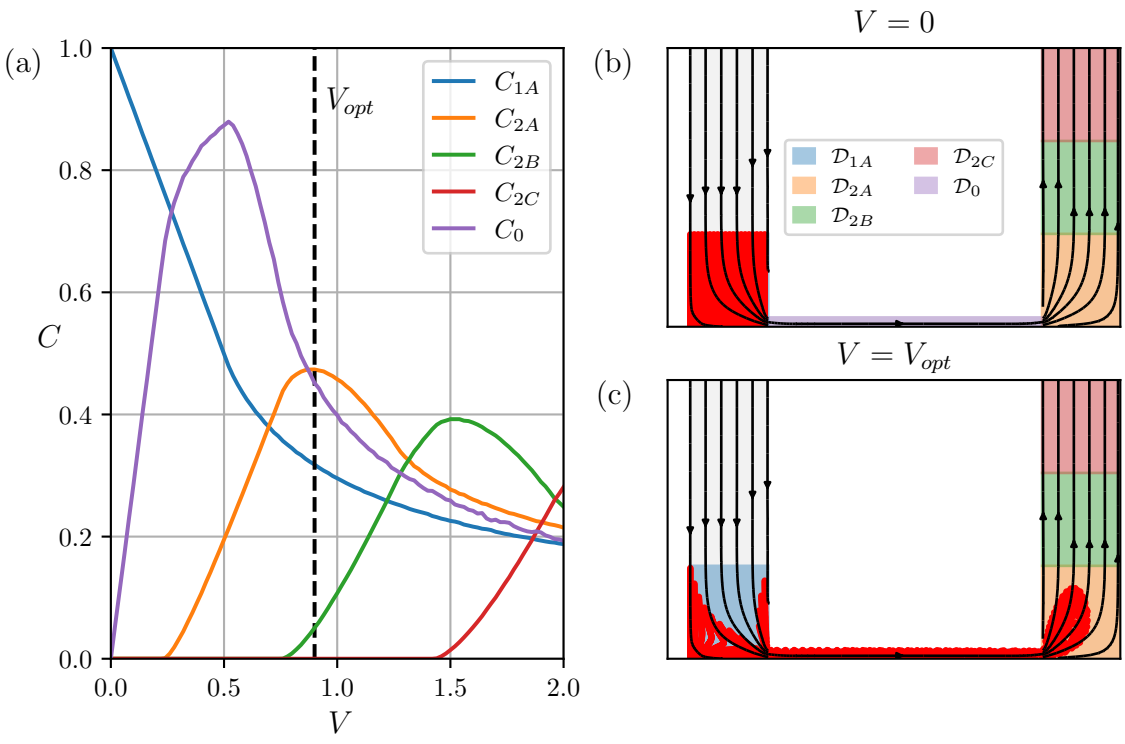

Figure 5.4: (a) Mean concentration $C_{i\alpha}$ in key regions of the device as a function of the net transfer volume V. The optimal transfer volume $V_{opt} \approx 0.9$ for which the concentration in the right-hand culture chamber is maximised is indicated by a vertical dashed line. (b) and (c) Diagrams illustrating the corresponding regions of the device with flow streamlines overlaid and the solute particle distribution (dark red) indicated at both the outset ($V = 0$) and at the optimal transfer volume ($V = V_{opt}$).

be flushed out as more fluid is transferred, the concentration in the culture chamber will never reach zero due to the isolated circulatory region.

Furthermore, flushing out solute close to the device walls is rarely desirable in practice, since it disperses the bulk of the solute further up the right-hand well and away from the culture chamber. Indeed, for this initial solute concentration problem, it is typically desirable to maximise the amount of solute transferred to the right-hand culture chamber $\mathcal{D}_{2A}$. The optimal transfer volume for this is $V_{opt} \approx 0.9$ which is indicated in figure 5.4 by a vertical dashed line and results in a mean concentration in the right-hand well of $C_{2A} \approx 0.47$. The optimal transfer volumes for other regions can be determined similarly and it is straightforward to extend this analysis to other initial solute distributions to study optimal solute transfer between different regions.

We conclude that solute transfer by advection is significantly more effective than transfer by diffusion alone. However, without diffusion there is no mixing between the wells; the blob of transferred solute will not spread out within the right-hand well, and will return fully intact to the left-hand well when the flow is reversed. In reality, small diffusive effects will accumulate over the course of the experiment and we examine the combined effects of advection and diffusion in the next subsection.

However, since advection is solely within the control of the experimenter, our analysis offers valuable insights into the optimal flow regime. Furthermore, while true mixing cannot be achieved without diffusion, in the context of a typical experiment advective transport is sufficient to expose each cell culture to the relevant solutes and thus enable cross-talk and reaction processes.

5.6.3 Advection and diffusion in a single cycle

We now examine combined advective and diffusive transport under an oscillatory flow rate, which is defined in terms of prescribed variation in the transfer volume $V(t)$. We consider paused oscillations in which the net transfer volume transitions linearly between 0 and a maximum amplitude V_A in time T_f, which we term the flow time, where it is subsequently held fixed for time T_p, which we term the pause time. For convenience we define the half-cycle time by $T_c = T_f + T_p$ and thus $2T_c$ is the period of a single oscillation cycle. A representative oscillation cycle is shown in figure 5.5(c). We observe that this regime corresponds to the typical flows produced by slow variations in the elevation angle, as discussed in chapter 4.

The dimensional flow time typically lies in the range $10\text{s} \leq T_f^* \leq 30\text{s}$, although longer flow times are possible, while the pause time is on the order of minutes. We take $T_f^* = 20\text{s}$ as the default value. The flow time sets the advective timescale $t_A^* = T_f^*$ and thus $T_f = 1$. The transport problem therefore depends on three dimensionless parameters, namely V_A, T_p and Pe.

We begin by considering solute transport over a single oscillation cycle. We present solutions for a fixed volume amplitude $V_A = 0.9$, which is chosen based on the approximate value of the optimal transfer volume for advective transport (see figure

5.4), for a range of Péclet numbers. We initially take the flow and pause times to be comparable with $T_f = T_p = 1$. Solutions for the mean concentration in each culture chamber are shown in figure 5.5, the corresponding advection-only solution is also shown for comparison.

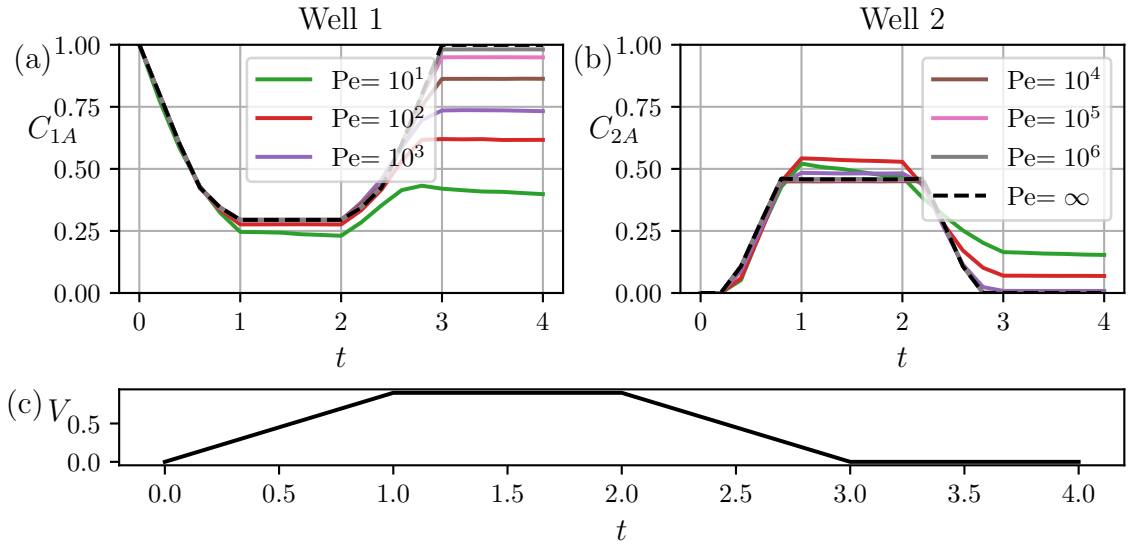

Figure 5.5: Mean solute concentration C in the culture chamber of (a) the left-hand and (b) the right-hand well over the course of a single oscillation cycle for a range of values of Pe as indicated, with the advection-only solution Pe $= \infty$ also shown. (c) The flow oscillation cycle in terms of the prescribed net transfer volume V. The volume amplitude is $V_A = 0.9$ and the pause time is equal to the flow time with $T_f = T_p = 1$ so that the half-cycle time is $T_c = 2$.

We observe that for Pe $\gtrsim 10^3$ very little solute is retained in the right-hand culture chamber after a single oscillation cycle. Smaller Péclet numbers do result in some solute retention however. This is due to solute being transported across the wells during the forward portion of the flow cycle diffusing into regions of fluid that remain in the right-hand culture chamber as the flow is reversed.

We also see that the decrease in solute concentration in the left-hand culture chamber across the course of one oscillation cycle becomes more significant for small Pe values. Furthermore, this decrease in concentration is greater than the corresponding increase in concentration in the right-hand culture chamber, since solute additionally diffuses into the higher regions of the left-hand well.

Under the standard flow regime with $T_f^* = 20$s the Péclet number varies between 50 for the highest diffusivity solutes to 5×10^4 for the lowest. Thus different solutes exhibit different mixing behaviour, with the lowest diffusivity solutes requiring a longer time period and many oscillation cycles for significant mixing between the culture chambers.

5.6.4 Multiple oscillation cycles and sequential mixing

For typical paused oscillatory flow regimes, many thousands of oscillation cycles occur over the course of a six-day experiment. To efficiently compute solutions over the course of many oscillation cycles we make an assumption of sequential mixing [13]. This entails computing advective and diffusive transport separately and sequentially, with diffusive effects incorporated after a period of advective transport. This is equivalent to splitting the advection and diffusion operators [98]. Specifically, we split the total duration time into intervals of length T_{split}. On each interval, we first solve the advective transport problem without diffusion and then solve the diffusive-only transport problem on this interval. Thus, diffusive effects are incorporated but only at the end of each splitting interval.

As discussed in [13], the sequential mixing assumption is common for transport problems in high Péclet regimes, although its validity depends on the underlying geometry and flow regime in addition to the magnitude of Pe. This is because diffusive effects can enhance advective transport in a manner which amounts to more than just the 'sum of their parts' [13]. Examples of this include stretching enhanced diffusion, whereby shear flows stretch the solute to form thin filaments or lamellae, which increases concentration gradients and reduces the distances necessary for effective dispersal by diffusive transport [13]. Taylor dispersion is another classical example of advection enhanced diffusion [108].

However, in addition to the large Péclet number, the typical flow regime and system geometry suggest that the sequential mixing assumption will be appropriate for the solute dispersal problem. Specifically, the paused oscillatory flow provides a natural splitting at the half-cycle time T_c, while the typical flow and pause times

result in short residence times in the channel, where enhanced mixing can occur, and longer residence times in the culture chamber, where stretching of solute is limited.

We make use of the sequential mixing assumption henceforth in our numerical simulations. We validate the sequential mixing assumption by comparison with full numerical simulations over multiple oscillation cycles and confirm that good agreement is observed for the full range of solute diffusivity values when we restrict attention to mean solute concentrations.

Under the sequential mixing assumption there is no distinction between the flow time and pause time, since diffusive effects are only incorporated at the end of each half cycle. It is therefore most convenient to describe the flow regime in terms of the half-cycle time T_c. The quantity $\mathrm{Pe}^{-1}T_c$ captures the total diffusive effects during each half cycle.

Furthermore, we recall that the diffusive timescale t_D^* and advective timescale t_A^* were introduced in §5.3.2 and that $\mathrm{Pe} = t_D^*/t_A^*$. When considering a large number of oscillations it is convenient to work on the diffusive timescale. We use tildes to denote quantities non-dimensionalised according to the diffusive (rather than advective) timescale, noting in particular that $\tilde{t} = t/\mathrm{Pe}$ and $\tilde{T}_c = T_c/\mathrm{Pe}$.

5.6.5 Oscillation frequency

We first examine solutions for oscillations with fixed volume amplitude $V_A = 0.9$ and varying oscillation frequency or cycle time $\tilde{T}_c$. These are shown in figure 5.6 where we plot the mean solute concentration in each culture chamber at the end of each cycle. Smaller half-cycle times result in more effective mixing between the two culture chambers, in the sense that more solute is retained at earlier times. This improved mixing is not unlimited however and ultimately plateaus for sufficiently high frequency oscillations. In this case, solutions appear to converge to a common limiting solution as $\tilde{T}_c \to 0$. We refer to the limiting solution as the high frequency limit, although we stress that this is relative to the diffusion timescale and so in particular we remain in the $\mathrm{Re} \ll 1$ regime. Numerically we find mixing protocols

with $\tilde{T}_c \lesssim 10^{-3}$ are sufficiently close to this limiting solution, with very little change observed by a further increase in the oscillation frequency.

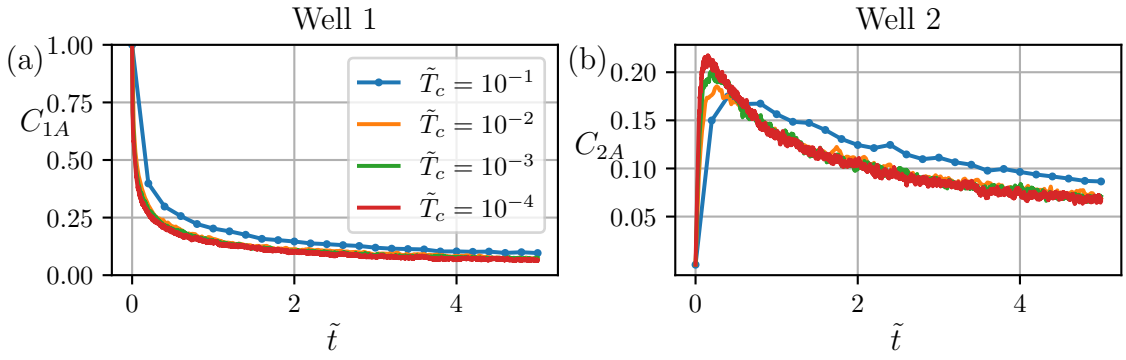

Figure 5.6: Mean solute concentration C in (a) the left-hand culture chamber and (b) the right-hand culture chamber for a range of oscillation frequencies specified by the half cycle time $\tilde{T}_c$. Solute concentration is recorded only at the cycle endpoint, corresponding to times $\tilde{t} = 2n\tilde{T}_c$ for non-negative integers n. The volume amplitude is $V_A = 0.9$ and the experiment duration is $\tilde{T}_{exp} = 5$.

The high frequency limit represents the optimal mixing regime for paused oscillations as it results in the fastest solute transfer and retention between the two culture chambers. The maximum solute concentration in the right-hand culture chamber occurs at $\tilde{t}_m \approx 0.15$ with $C_{2A} \approx 0.21$. This concentration later falls as solute diffuses into higher regions of the well, falling more quickly in the high-frequency limit. Thus lower frequency oscillations may be more desirable in scenarios where the goal is to keep solute in the right-hand culture chamber for longer rather than achieve the fastest transfer.

For typical operating regimes, $\tilde{T}_c$ decreases from 0.1 to 10^{-4} as the solute diffusivity decreases while the experiment duration ($T^*_{exp} = 6$ days varies from $\tilde{T}_{exp} = 5 \times 10^3$ to $\tilde{T}_{exp} = 0.5$. Thus, optimal mixing between the culture chambers is now achievable within the experimental time frame for all solutes.

5.6.6 Oscillation amplitude

We now examine the effects of varying the volume amplitude V_A while restricting attention to the high frequency regime. The evolution of the mean solute concentration

in each culture chamber under a high frequency mixing protocol for a range of volume amplitudes V_A are shown in figure 5.7. The diffusion-only solution (equivalent to zero amplitude oscillations $V_A = 0$) is also shown for comparison.

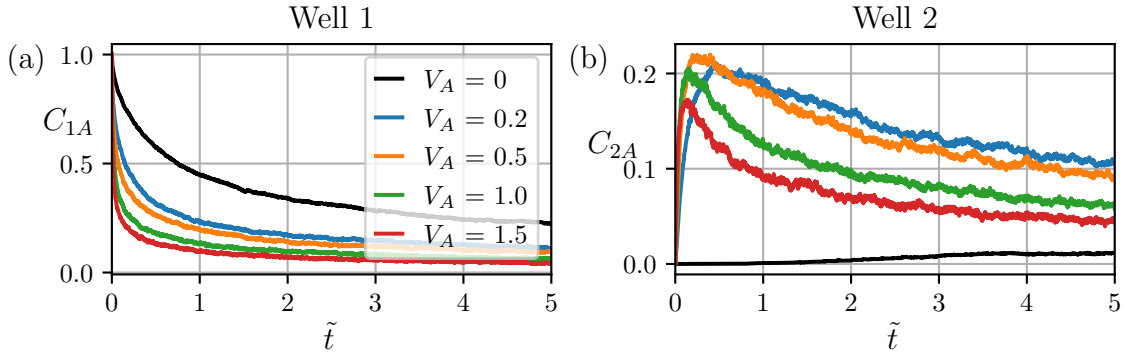

Figure 5.7: Mean solute concentration C in (a) the left-hand and (b) the right-hand culture chamber for a range of volume amplitudes V_A under a high frequency mixing protocol ($\tilde{T}_c = 10^{-4}$). The diffusion-only solution ($V_A = 0$) is also shown for comparison.

Clearly higher amplitude oscillations are expected to increase transport and mixing across the two wells. However, we recall that for mixing between the culture chambers an optimal value of $V_A \approx 0.9$ was found in the large Péclet regime. We see from figure 5.7 that the concentration in the right-hand culture chamber exhibits a rapid rise followed by a more gradual fall. For greater oscillation amplitudes, the concentration attains its maximum value earlier which again demonstrates the increased rate of mixing. However, while the value of this maximum initially increases with the volume amplitude, it subsequently begins to fall. This again results from increased solute transport into the higher regions of the right-hand well.

The efficiency of mixing can be summarised by the transfer time $\tilde{t}_m$ at which the concentration in the right-hand culture chamber attains its maximum value C_m, which are shown in table 5.2 for a representative range of volume amplitudes. We conclude that there is an optimal oscillation amplitude which results in the greatest peak concentration in the right-hand culture chamber and numerically we find this to be approximately equal to the optimal transfer volume for advection-only transport.

However, within the range $0.2 \leq V_A \leq 1.0$ the maximum concentration is not particularly sensitive to variation in the volume amplitude. In contrast, the time at which this maximum concentration is obtained can be reduced substantially by increasing the volume amplitude across this range.

V_A	0.0	0.1	0.2	0.5	0.8	0.9	1.0	1.2	1.5
$\tilde{t}_m$	5.00	1.06	0.47	0.40	0.24	0.15	0.15	0.11	0.14
C_{2A}	0.01	0.17	0.21	0.22	0.22	0.21	0.21	0.19	0.17

Table 5.2: Maximum concentration in the right-hand culture chamber C_{2A} and the time $\tilde{t}_m$ at which this maximum is obtained for a range of oscillation volume amplitudes V_A under the high frequency mixing protocol ($\tilde{T}_c = 10^{-4}$).

We conclude by noting that mixing is improved significantly by incorporating advective transport, as it allows the rapid transfer of solute between the two wells. However, mixing in the sense of solute retention remains fundamentally limited by diffusion, as the time at which the right-hand culture chamber attains its maximum concentration scales with the diffusive timescale t_D^*. High diffusivity solutes achieve significant mixing in a just a few minutes but low diffusivity solutes still require a number of days. This cannot be changed by altering the oscillatory flow regime through the volume amplitude or frequency, although we have shown that these do provide means of optimising mixing for a given solute diffusivity. Furthermore, we can extend our analysis of the oscillation amplitude to optimise mixing between different regions of the system. We discuss how mixing could potentially be enhanced to overcome the limit resulting from solute diffusivity in §5.8.

5.7 Solute production

In experiments, effective mixing of solutes produced by the cell cultures is also desirable to facilitate biological reactions. Our analysis of the initial solute dispersal problem is still relevant to this scenario, as it provides insights into how to promote mixing in the system. However, in this section we consider mixing in conjunction with simple solute production reactions explicitly.

To illustrate solute mixing with production reactions we set the diameter of the reaction region in the left-hand culture chamber to be $d = 0.4$, which is representative of the typical spheroid diameter. Additionally we set the reaction rate to be $r = 1$ without loss of generality, since for zeroth order solute production reactions solutions are linear in r and so the reaction rate can be absorbed into the concentration scale C_0. We use the standard flow conditions of $V_A = 0.9$ with $T_f = 1$ and $T_p = 4$ as considered previously and consider low diffusivity solutes with $\mathrm{Pe} = 5 \times 10^3$. A typical six-day experiment corresponds to around 2500 oscillation cycles and we present results in terms of dimensional time t^*. The dimensionless parameters defined above correspond to $T_f^* = 20$ s and $T_p^* = 80$ s and $D^* = 10^{-11}$ m^{2}s^{-1}.

Solutions are obtained using the particle-based scheme described in §5.3.3, with the sequential mixing approximation used for solutions over multiple oscillation cycles. This approximation is adapted to account for solute reactions by noting that solute particles behave independently and thus we add particles at the end of each oscillation cycle according to their expected distribution after a single cycle. This distribution is calculated from full numerical simulations of an entire cycle.

Figure 5.8 shows how the mean concentration varies in the lower five regions (A–E) of each well over the course of a typical six-day experiment. The concentration in each region increases over time and regions closer to the cell culture have higher concentrations. Furthermore, the concentration in the equivalent regions of each well is comparable, although the concentration in the right-hand well is naturally slightly lower. This demonstrates that frequent and effective solute transfer between the two wells can be achieved by tilting the system, just as for the initial solute dispersal problem.

We compare these results with static conditions in figure 5.9, which shows the concentration in the key measurement regions of just above the cell culture (region B) and the mid-well measurement region (region D). Under static conditions, very little solute reaches region B in the right-hand well even by the end of experiment, while within the left-hand well solute is concentrated towards the lower regions to a greater extent than for the oscillatory solution. These trends agree with experimental data

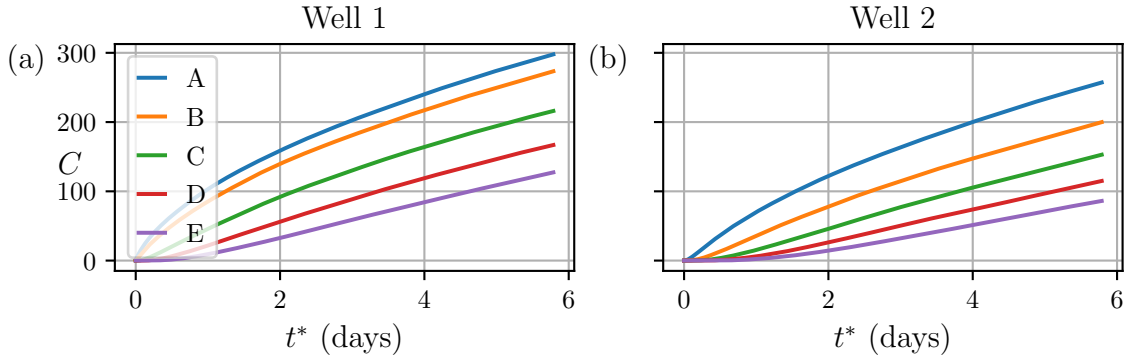

Figure 5.8: Mean solute concentration $C_{i\alpha}$ in the lower five regions of each well for $\mathrm{Pe} = 5 \times 10^3$ over the course of a six-day experiment under the standard oscillatory flow regime.

obtained by collaborators at InSphero, although further work is needed for a detailed quantitative comparison.

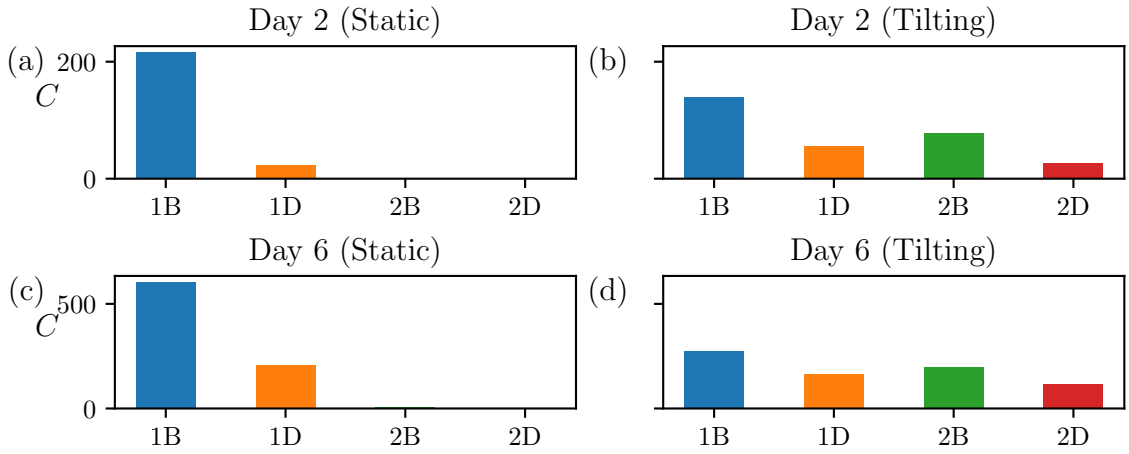

Figure 5.9: Mean solute concentration $C_{i\alpha}$ in key regions of each well after two and six days under both static and oscillatory conditions with $\mathrm{Pe} = 5 \times 10^3$.

5.7.1 Intra-well mixing

Most of our analysis has focussed on mixing between larger regions of the well, with results presented in terms of the mean concentration. However, it is also informative to examine the solute distribution within each well. We find that, at later times, variation in the vertical direction is more significant than horizontal variation. Figure 5.10 shows the horizontally averaged concentration profile $\bar{c}(y)$ in each well on day

2 and day 5, with the standard deviation at this height also indicated. We observe that although the imposed flow regime enhances mixing both between and within the wells, there remains a significant concentration gradient across the lower portion of each well.

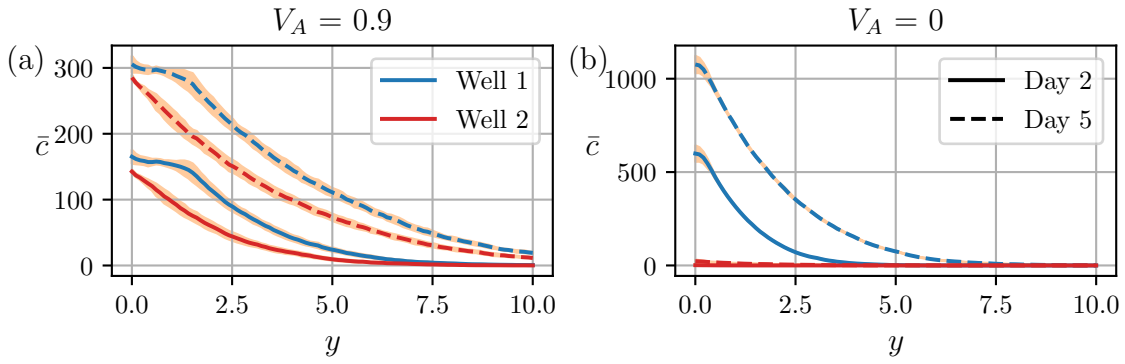

Figure 5.10: Solute concentration averaged in the horizontal direction $\bar{c}(y)$ in each well after a duration of two and six days and under both static conditions ($V_A = 0$) and standard flow conditions ($V_A = 0.9$) for $\mathrm{Pe} = 5 \times 10^3$. The standard deviation for each height is indicated by shading.

This emphasises that, despite enhanced mixing between the two wells, the individual wells are typically not well mixed, due to low solute diffusivity. This spatial variation in the system may need to be accounted for in practice, for example in the context of solute measurement or in developing models of localised reaction processes occurring within the spheroids. For instance, we require an understanding of the concentration distribution to accurately estimate the rate parameter from measured solute concentration and cannot simply use a simple compartment-based model, which requires the well-mixed assumption.

Intra-well mixing naturally improves for higher diffusivity solutes, in which case the well-mixed modelling assumption may be appropriate. However, our model requires further refinement to accurately study higher diffusivity solutes over the entire experiment duration, since in this case solute quickly diffuses into higher regions of the well where the effects of the free surface are important and thus our semi-infinite well assumption is no longer appropriate. We verify that our analysis is valid for $\tilde{t} \lesssim 5$, which covers the typical experiment duration for high diffusivity solutes, by

confirming that 99% of solute remains in the region $y \leq 10$, which corresponds to the typical well height, in this case.

5.8 Discussion

In this chapter we have developed and analysed a simplified model for solute transport in a two-dimensional twin-well system. Our analysis has made use of and extended our study of fluid flow in previous chapters. We have also exploited features of the system geometry and typical operating conditions to perform further model reduction of the transport equation, including the low Reynolds number to calculate the flow profile and the large Péclet number which underpins the sequential mixing simplification of our numerical scheme.

We considered two transport problems, namely the dispersal of a fixed initial solute profile and the dispersal of a continuously produced solute, which are both relevant to the use of the physical system. Our results emphasised the importance of advective transport to enable mixing between the culture chambers on reasonable experimental timescales and identified optimal mixing regimes in terms of the frequency and amplitude of the imposed oscillatory flow. Although further refinement of our model is required before we can obtain quantitative predictions for comparison with the physical system, our analysis nevertheless provides useful insights to support the use of the system in experiments. We have highlighted practical implications of our analysis, which include identifying suitable operating regimes for efficient drug delivery or frequent exchange of solutes between the two cell cultures.

Our preliminary analysis of solute transport can be extended in a variety of ways. Firstly, we have focused on mixing between larger regions of each well, such as the two culture chambers, but a more thorough investigation of intra-well mixing is also important. Understanding solute distribution on this scale can inform experimental measurement protocols or be used to assess the suitability of the system for pharmacokinetic parameter estimation or to study reaction mechanisms, which require a well-mixed system. Extensions to incorporate more complex and biologically relevant

reaction mechanisms that more closely align with the typical use of the twin-well system are also important, which include models of drug clearance, interactions between the two cell cultures, and ultimately immune dynamics which incorporate chemotactic transport.

However, some refinements to our modelling framework are required before studying more realistic reaction mechanisms. These include extending our analysis to a three-dimensional well geometry and removing the assumption of a semi-infinite well by incorporating the dynamics of the free surface, which allows examination of high diffusivity solutes over the entire experimental time frame. Another refinement is to incorporate the spheroidal cell cultures explicitly, either as rigid spheres with surface reactions or as a porous domain, rather than implicitly via source and sink terms in the reaction region.

Lastly, one key finding from our analysis is that while flow enhances mixing significantly, mixing remains diffusion-limited with solute diffusivity setting the timescale for mixing between the two culture chambers. This highlights the challenges associated with mixing in microfluidic systems in low Reynolds number and high Péclet number regimes [11, 13]. Furthermore, this limitation cannot easily be overcome by adjusting the parameters of the oscillatory flow profile, since the flow is reversible with invariant streamlines and limited stretching of solute in the well regions. It would therefore be interesting and useful to explore if more fundamental changes to the flow regime, or modifications to the system geometry, could be used to enhance mixing.

This could be achieved by employing chaotic mixing protocols or enhanced inertial effects to alter the fluid streamlines to promote mixing [11, 109]. The thin channel geometry could also be used to stretch the solute distribution and reduce the size of the interface between regions of different solute concentration [13]. Finally, the hysteresis of the contact line and the resulting asymmetry of the free surface, which played a key role in our analysis of fluid flow, could also be exploited to enhance mixing.

Chapter 6

Conclusions and future work

6.1 Conclusion

In this thesis, we have developed and analysed a suite of models for fluid flow and solute transport in a novel twin-well microfluidic system designed for applications in pharmaceutical drug development. A central focus of our modelling has been to incorporate and examine capillary effects through the dynamics of the moving contact line and contact angle hysteresis, extending traditional models of gravity-driven systems in which these effects are neglected. By employing asymptotic reductions based on disparate length and time scales, we derived reduced model equations that highlight key physical mechanisms, improve computational efficiency, and provide insight of direct experimental and practical relevance.

In chapter 2, we presented the full governing equations for fluid flow and transport of a passive solute. Flow was described by the Navier–Stokes equations, with modifications to the usual boundary conditions to capture hysteresis. Solute transport was described by a reaction–advection–diffusion equation. We identified several dimensionless parameters that formed the basis of our asymptotic reductions and outlined the derivation of reduced models for both the moving contact-line dynamics and the volume flow rate across the channel, which we analysed in chapters 3 and 4.

Specifically, in chapter 3, we analysed the contact-line dynamics in a single-well geometry under an imposed volume flow and varying elevation angle. The free surface was described by the quasi-steady Young-Laplace equation, which provides the

relationship between the contact angle, well volume, and pressure, while the Cox-Voinov contact-line law, modified to account for hysteresis, described the evolution of the contact line. We introduced a numerical framework based on the *Surface Evolver* software to solve the reduced model equations for a general well geometry and elevation angle.

We first illustrated the typical dynamics in a horizontal system and discussed how solutions depend on the dimensionless model parameters. In particular, we found that the relaxation parameter τ plays an important role in setting the deviation between the macroscopic and microscopic contact angles and the timescale for relaxation to equilibrium in the absence of flow, resulting in simpler dynamics in the experimentally relevant small τ regime. We also highlighted the distinct pinned and unpinned phases of the contact-line motion, resulting from contact angle hysteresis. We then extended our analysis to a tilted system, where our numerical results were complemented by an asymptotic analysis applicable for small elevation angles, and the combined tilting and flow regime, which is most relevant to experimental operating conditions. We found that although tilting affected the contact-line dynamics, in many cases it did not significantly alter the capillary pressure due to symmetry, allowing us to use an axisymmetric approximation to simplify the numerical simulations.

In chapter 4, we analysed the flow in a two-dimensional twin-well system using a reduced hydraulic electric circuit analogy obtained by exploiting the small channel aspect ratio. The volume flow rate is proportional to the pressure difference across the channel, which has a hydrostatic and capillary component and is determined from the Young-Laplace equation. Thus our analysis built directly on the work in chapter 3.

We characterised flows driven by initial volume differences and varying elevation angles. We first examined cases without contact angle hysteresis, where capillary effects do not influence the flow. For oscillatory systems, we showed that the dynamics depend on the relative timescales of the oscillation and drainage across the channel and that simplifications were possible for low-frequency oscillations that match typical experimental conditions. We then investigated how contact angle hysteresis

modifies the flow, demonstrating that capillary effects serve to reduce the flow rate and introduce variability by allowing for a range of potential equilibrium configurations. We introduced the surface tension parameter $S = \mathrm{Bo}^{-1}|\cos\alpha_A - \cos\alpha_R|$ to quantify these effects.

In both chapters 3 and 4, we have emphasised the practical relevance of our analysis. In particular, we identified criteria, expressed in terms of the fluid volume or elevation angle, that can be used to remove or minimise the variability introduced by contact angle hysteresis. These criteria inform experimental practice and provide guidance for operating the system to ensure repeatability and reproducibility.

In chapter 5, we examined solute transport in the two-dimensional twin-well system, making some further simplifications to the system geometry to expedite our initial characterisation. We exploited the low Reynolds number to determine the flow profile in the system, building on our previous analysis of the flow, and the large Péclet number, which served to underpin our particle-based scheme and our sequential mixing modelling assumption, where diffusive effects are neglected during the flow.

We considered two representative transport problems: the dispersal of an initially localised solute, which is related to drug delivery, and the dispersal of a continuously produced solute, which is related to biological reactions in cell cultures. Through this analysis, we identified optimal operating conditions that enhance solute mixing between the two culture chambers. These conditions were presented in terms of the amplitude and frequency of the oscillating volume flow rate, but it is straightforward to relate these conditions to the oscillating elevation angle, including adjustments necessary to account for contact angle hysteresis, via our analysis in chapter 4.

Our results demonstrated a significant improvement in mixing efficiency compared with diffusion alone, although mixing ultimately remains limited by the low solute diffusivity and the laminar flow profile. We emphasise that our analysis represents a first detailed study of solute transport in the twin-well system, with substantial scope for further development. Nevertheless, our results provide valuable qualitative

insights into system behaviour and confirm that effective inter-well mixing to facilitate biological reactions is achievable on experimental timescales through rocking the system.

6.2 Future work

There are numerous ways in which the models and analyses presented in this thesis could be extended. The most immediate avenue is the extension of our analysis in chapters 4 and 5 to a three-dimensional geometry. Although we do not anticipate any major qualitative differences from our two-dimensional results, a three-dimensional formulation would provide better quantitative predictions to inform experimental procedure and facilitate direct comparison with experimental data for model validation. While three-dimensional simulations present additional computational challenges, our current analysis provides a foundation for further simplifications and model reduction. For instance, the axisymmetric approximation for the capillary pressure established in chapter 3 can be used to efficiently extend the volume flow analysis in chapter 4 into three dimensions.

A further natural extension involves the study of contact-line dynamics in alternative well geometries, particularly the square well geometry corresponding to the physical system. While the qualitative behaviour is expected to remain broadly consistent with that observed in circular wells, refinements to the model are required to capture features such as the formation of rivulets at well corners, which occur for contact angles below a critical value [46, 50].

Our focus on fluid flow and contact-line motion leaves the modelling of solute transport and reactions as the area with the greatest scope for future development. This includes refinements to our modelling framework, accounting for the free surface and a more sophisticated treatment of the spheroidal cell cultures, and the incorporation of more detailed and realistic biological reaction mechanisms. Such modelling could more directly support experimental studies, for instance by informing optimal measurement protocol, to account for the solute distribution or enabling parameter

estimation for spatially heterogeneous reaction systems where compartmental modelling is not suitable. Given the intended application of the device to the study of immunotherapy treatments, extensions of the transport model to include chemotaxis would also be of relevance.

Finally, the initial results from our analysis of solute transport suggest that further investigation of alternative mixing strategies to overcome the limitations associated with low solute diffusivity and Stokes flow would be worthwhile. This involves incorporating chaotic mixing principles to explore how solute mixing can be enhanced through altering the system geometry or developing intricate mixing protocols [11]. An intriguing possibility is that contact angle hysteresis, the focal point of our analysis of the flow where we sought to mitigate its effects, could be exploited to enhance mixing due to the resulting asymmetry of the free surface motion.

Overall, the modelling and characterisation presented in this thesis provide a foundation for these future developments, while already offering experimentally relevant insights into the operation and optimisation of the twin-well microfluidic systems.

Appendix A

Derivation of the contact-line law

We present an outline of the derivation of the modified Cox-Voinov contact line law (2.49) in two dimensions, which forms part of the reduced model for the evolution of the contact line in §2.8. Following [58, 59] we work in the regime $\mathrm{Ca}, \lambda \ll 1$, but with $\tau = O(1)$ and consider a two-dimensional rectangular reservoir with outer Cartesian coordinates (y, z) and base $\mathcal{B} = \{(y, 0) : -1 \leq y \leq 1\}$. The free surface is defined by $z = h(y, t)$ and the unit tangent to this surface is

$$\mathbf{t} = \sin\beta(y, t)\mathbf{e}_y - \cos\beta(y, t)\mathbf{e}_z, \tag{A.1}$$

where β is the angle of elevation to the negative z-axis (see figure 2.4).

The analysis of the outer regions proceeds as in §2.8.2. We find that the leading-order free surface h_0 satisfies the Young-Laplace equation and

$$h_{0y}(\pm 1, t) = \pm\cot\phi_0^{\pm}(t), \tag{A.2}$$

defines the leading-order macroscopic contact angle $\phi_0^{\pm}$ at the contact points $y = \pm 1$.

We consider an inner region near the left-hand contact point at $y = -1$, noting that treatment of the right-hand contact point is similar. Analysis of the inner region proceeds as in §2.8.3. We introduce the local coordinate system (Y, Z) with $y = -1 + \lambda Y$, $z = h(-1, t) + \lambda Z$ and inner variables $\tilde{p} = p/\lambda$, $\tilde{\kappa} = \kappa/\lambda$ with the free surface written as $Z = \tilde{h}(Y, t)$. We find that

$$\tilde{h}_0(Y, t) = -Z\cot\alpha_0^{-}(t), \tag{A.3}$$

where α_0^{-} is the leading-order microscopic contact angle at the left-hand contact point.

Since $\tau = O(1)$, we require the intermediate region for matching, which is due to the presence of logarithmic terms at higher orders [59]. We introduce a local polar coordinate system (R, Θ) with $Y = R\cos\Theta$ and $Z = -R\sin\Theta$, noting that $\mathbf{e}_R = (\sin\Theta, -\cos\Theta)$ and $\mathbf{e}_\Theta = (\cos\Theta, \sin\Theta)$. The intermediate region corresponds to $1 \ll R \ll \lambda^{-1}$ and so it is useful, as in [58], to introduce the intermediate variable ξ defined by

$$R = \lambda^{\xi-1}, \tag{A.4}$$

noting that the inner region is approached as $\xi \to 1$ and the outer region is approached as $\xi \to 0$. We parameterise the free surface as $\Theta = \Theta_F(\xi, t)$ in the intermediate region.

The free surface curvature can be expressed in terms of the tangent angle as

$$\tilde{\kappa} = -\frac{\partial\beta}{\partial\tilde{\sigma}}, \tag{A.5}$$

where the inner arc length $\tilde{\sigma}$ satisfies

$$\frac{\partial\tilde{\sigma}}{\partial\tilde{R}} = 1 + O(\mathrm{Ca}^2). \tag{A.6}$$

We recall that the leading-order pressure and curvature vanish in the inner region. Furthermore, a local analysis of the outer flow problem as $y \to -1$ or a far-field analysis of the inner flow problem as $R \to \infty$ motivates the rescalings

$$\tilde{p} = \mathrm{Ca}\tilde{P}, \quad \tilde{\kappa} = \mathrm{Ca}\tilde{K}. \ , \tag{A.7}$$

for the intermediate region.

We introduce a streamfunction $\tilde{\psi}$ for the flow field $\mathbf{u} = \frac{1}{R}\frac{\partial\tilde{\psi}}{\partial\Theta}\mathbf{e}_R - \frac{\partial\tilde{\psi}}{\partial\tilde{R}}\mathbf{e}_\Theta$ and seek solutions of the form

$$\tilde{\psi} = \tilde{R}f(\xi, \Theta, t), \quad \tilde{P} = \frac{1}{\tilde{R}}g(\xi, \Theta, t), \tag{A.8}$$

which are consistent with both the far-field and local analyses. Additionally, we rewrite the free surface and tangent angle as

$$\Theta_F = \alpha_0 + \tau\vartheta(\xi, t), \quad \beta = \alpha_0 + \tau B(\xi, t),$$

which is motivated by the expected curvature scaling. The unit tangent and outward unit normal to the free surface are

$$\mathbf{t} = \mathbf{e}_R(\Theta_F) + O(\mathrm{Ca}), \quad \mathbf{n}_F = \mathbf{e}_\Theta(\Theta_F) + O(\mathrm{Ca}) \tag{A.9}$$

respectively, and thus Θ_F and β agree to leading order in Ca.

Omitting subscripts for brevity, the leading-order momentum equations in the intermediate region are

$$\frac{\partial \tilde{P}}{\partial R} = \frac{1}{R}\frac{\partial}{\partial \Theta}(\nabla^2 \tilde{\psi}) \tag{A.10}$$

$$\frac{1}{R}\frac{\partial \tilde{P}}{\partial \Theta} = -\frac{\partial}{\partial R}(\nabla^2 \tilde{\psi}). \tag{A.11}$$

The no-flux and Navier-slip boundary conditions are

$$\tilde{\psi} = 0, \tag{A.12}$$

$$\frac{1}{R}\frac{\partial \tilde{\psi}}{\partial \Theta} = \frac{1}{R^2}\frac{\partial^2 \tilde{\psi}}{\partial \Theta^2}, \tag{A.13}$$

on the solid boundary $\Theta = 0$, where we have simplified the Navier-slip condition in (A.13) by making use of the no-flux condition (A.12). Meanwhile, on the free surface at $\Theta = \Theta_F$, the kinematic boundary condition and the normal and tangential components of the dynamic boundary condition are

$$\frac{\partial \tilde{\psi}}{\partial \tilde{R}} = v_n(t)\sin\Theta \tag{A.14}$$

$$\tilde{P} - 2\left(\frac{1}{\tilde{R}^2}\frac{\partial \tilde{\psi}}{\partial \Theta} - \frac{1}{\tilde{R}}\frac{\partial^2 \tilde{\psi}}{\partial \Theta \partial \tilde{R}}\right) = \tilde{K}, \tag{A.15}$$

$$\frac{1}{2\tilde{R}^2}\frac{\partial^2 \psi}{\partial \Theta^2} - \frac{\tilde{R}}{2}\frac{\partial}{\partial \tilde{R}}\left(\frac{\partial \tilde{\psi}}{\partial \tilde{R}}/\tilde{R}\right) = 0, \tag{A.16}$$

respectively, where $v_n(t) = h_t(-1, t)$ is the contact-line velocity.

Rewriting these equations in terms of the functions f and g and retaining only leading order terms, we obtain,

$$g = -\left(\frac{\partial f}{\partial \Theta} + \frac{\partial^3 f}{\partial \Theta^3}\right), \qquad \frac{\partial g}{\partial \Theta} = f + \frac{\partial^2 f}{\partial \Theta^2}, \tag{A.17}$$

from the momentum equations (A.10) and (A.11), which we combine to obtain

$$\left(\frac{\partial^2}{\partial \Theta^2} + 1\right) g = 0, \qquad \left(\frac{\partial^2}{\partial \Theta^2} + 1\right)^2 f = 0. \tag{A.18}$$

Similarly from the boundary conditions (A.12)–(A.13) on the device wall we obtain

$$f = \frac{\partial f}{\partial \Theta} = 0, \tag{A.19}$$

on $\Theta = 0$. The free surface boundary conditions (A.14)–(A.16) are

$$f = v_n \sin\Theta, \quad f + \frac{\partial^2 f}{\partial \Theta^2} = 0, \quad g = \frac{\mathrm{d}B}{\mathrm{d}\xi} \tag{A.20}$$

on $\Theta = \Theta_F$, where we have written the curvature in terms of the tangent angle using (A.5).

Solving equations (A.17) subject to the boundary conditions (A.19) and (A.20), we find that

$$f = A(\Theta\cos(\Theta - \Theta_F) - \cos\Theta_F \sin\Theta), \qquad g = 2A\cos(\Theta - \Theta_F), \tag{A.21}$$

where

$$A = \frac{v_n(t)\sin\Theta_F}{\Theta_F - \sin\Theta_F\cos\Theta_F}.$$

Since Θ_F and β agree to leading order, from the normal component of the dynamic boundary condition in (A.20), we obtain the equation

$$\frac{1}{\tau}\frac{\partial\beta}{\partial\xi} = -\frac{2v_n(t)\sin\beta}{\beta - \sin\beta\cos\beta} \tag{A.22}$$

with boundary conditions $\beta(0,t) = \phi_0^-(t)$ and $\beta(1,t) = \alpha_0^-(t)$, which follow from matching the unit tangent in the inner and outer regions.

We solve equation (A.22) to obtain a contact-line law relating the contact-line velocity to the microscopic and macroscopic contact angles

$$v_n = \tau^{-1} G(\phi_0, \alpha_0), \tag{A.23}$$

where G is the Cox-Voinov contact-line law defined by (2.49).

We observe that the integrand in (2.49) is positive for contact angles in the range $\phi \in [0, \pi]$. Furthermore, we recall that the hysteresis law (2.29) relating the contact-line velocity to the microscopic contact angle states that the contact-line velocity is non-zero only when the microscopic angle is advancing or receding. We therefore

combine the contact-line law (2.49) and hysteresis law (2.29) to obtain the contact-line law with hysteresis (2.48).

This completes the outline of the derivation of the Cox-Voinov contact-line law with contact angle hysteresis in a two-dimensional well geometry. The approach in three dimensions is similar, but at each point along the contact line, we work in the plane normal to the contact line (see figure 2.4) at this point [58]. In three dimensions, the velocity v_n is the normal contact-line velocity defined by (2.30).

Bibliography

[1] George M Whitesides. The origins and the future of microfluidics. *nature*, 442(7101): 368–373, 2006.

[2] Jaime Castillo-León. Microfluidics and lab-on-a-chip devices: history and challenges. In *Lab-on-a-Chip Devices and Micro-Total Analysis Systems: A Practical Guide*, pages 1–15. Springer, 2014.

[3] Andréas Manz, N Graber, and H Michael Widmer. Miniaturized total chemical analysis systems: a novel concept for chemical sensing. *Sensors and actuators B: Chemical*, 1(1-6):244–248, 1990.

[4] Amid Shakeri, Shadman Khan, and Tohid F Didar. Conventional and emerging strategies for the fabrication and functionalization of pdms-based microfluidic devices. *Lab on a Chip*, 21(16):3053–3075, 2021.

[5] Eric K Sackmann, Anna L Fulton, and David J Beebe. The present and future role of microfluidics in biomedical research. *Nature*, 507(7491):181–189, 2014.

[6] Amy L Paguirigan and David J Beebe. Microfluidics meet cell biology: bridging the gap by validation and application of microscale techniques for cell biological assays. *Bioessays*, 30(9):811–821, 2008.

[7] Dan Liu, Haicong Shen, Yuqian Zhang, Danyu Shen, Mingyang Zhu, Yanling Song, Zhi Zhu, and Chaoyong Yang. A microfluidic-integrated lateral flow recombinase polymerase amplification (mi-if-rpa) assay for rapid covid-19 detection. *Lab on a Chip*, 21(10):2019–2026, 2021.

[8] Howard A Stone, Abraham D Stroock, and Armand Ajdari. Engineering flows in small devices: microfluidics toward a lab-on-a-chip. *Annu. Rev. Fluid Mech.*, 36:381–411, 2004.

[9] Vigneswaran Narayanamurthy, ZE Jeroish, KS Bhuvaneshwari, Pouriya Bayat, R Premkumar, Fahmi Samsuri, and Mashitah M Yusoff. Advances in passively driven

microfluidics and lab-on-chip devices: a comprehensive literature review and patent analysis. *RSC Advances*, 10(20):11652–11680, 2020.

[10] Chia-Yen Lee, Chin-Lung Chang, Yao-Nan Wang, and Lung-Ming Fu. Microfluidic mixing: a review. *International journal of molecular sciences*, 12(5):3263–3287, 2011.

[11] Hassan Aref, John R Blake, Marko Budišić, Silvana SS Cardoso, Julyan HE Cartwright, Herman JH Clercx, Kamal El Omari, Ulrike Feudel, Ramin Golestanian, Emmanuelle Gouillart, et al. Frontiers of chaotic advection. *Reviews of Modern Physics*, 89(2):025007, 2017.

[12] Abraham D Stroock, Stephan KW Dertinger, Armand Ajdari, Igor Mezic, Howard A Stone, and George M Whitesides. Chaotic mixer for microchannels. *Science*, 295 (5555):647–651, 2002.

[13] Emmanuel Villermaux. Mixing versus stirring. *Annual Review of Fluid Mechanics*, 51(1):245–273, 2019.

[14] Antti-Juhana Mäki, Samu Hemmilä, Juha Hirvonen, Nathaniel Narra Girish, Joose Kreutzer, Jari Hyttinen, and Pasi Kallio. Modeling and experimental characterization of pressure drop in gravity-driven microfluidic systems. *Journal of Fluids Engineering*, 137(2):021105, 2015.

[15] Martin Zimmermann, Steven Bentley, Heinz Schmid, Patrick Hunziker, and Emmanuel Delamarche. Continuous flow in open microfluidics using controlled evaporation. *Lab on a Chip*, 5(12):1355–1359, 2005.

[16] Scott Brittain, Karteri Paul, Xiao-Mei Zhao, and George Whitesides. Soft lithography and microfabrication. *Physics World*, 11(5):31, 1998.

[17] Petra S Dittrich and Andreas Manz. Lab-on-a-chip: microfluidics in drug discovery. *Nature reviews Drug discovery*, 5(3):210–218, 2006.

[18] Lorna Ewart, Eva-Maria Dehne, Kristin Fabre, Susan Gibbs, James Hickman, Ellinor Hornberg, Magnus Ingelman-Sundberg, Kyung-Jin Jang, David R Jones, Volker M Lauschke, et al. Application of microphysiological systems to enhance safety assessment in drug discovery. *Annual review of pharmacology and toxicology*, 58:65–82, 2018.

[19] Boyang Zhang, Anastasia Korolj, Benjamin Fook Lun Lai, and Milica Radisic. Advances in organ-on-a-chip engineering. *Nature Reviews Materials*, 3(8):257–278, 2018.

[20] Steven M Paul, Daniel S Mytelka, Christopher T Dunwiddie, Charles C Persinger, Bernard H Munos, Stacy R Lindborg, and Aaron L Schacht. How to improve r&d productivity: the pharmaceutical industry's grand challenge. *Nature reviews Drug discovery*, 9(3):203–214, 2010.

[21] Richard C Mohs and Nigel H Greig. Drug discovery and development: Role of basic biological research. *Alzheimer's & Dementia: Translational Research & Clinical Interventions*, 3(4):651–657, 2017.

[22] Ismail Kola and John Landis. Can the pharmaceutical industry reduce attrition rates? *Nature reviews Drug discovery*, 3(8):711–716, 2004.

[23] Nilesh Gupta, Jeffrey R Liu, Brijeshkumar Patel, Deepak E Solomon, Bhuvaneshwar Vaidya, and Vivek Gupta. Microfluidics-based 3d cell culture models: Utility in novel drug discovery and delivery research. *Bioengineering & Translational Medicine*, 1(1): 63–81, 2016.

[24] Kayla Duval, Hannah Grover, Li-Hsin Han, Yongchao Mou, Adrian F Pegoraro, Jeffery Fredberg, and Zi Chen. Modeling physiological events in 2d vs. 3d cell culture. *Physiology*, 32(4):266–277, 2017.

[25] Andreas R Baudy, Monicah A Otieno, Philip Hewitt, Jinping Gan, Adrian Roth, Douglas Keller, Radhakrishna Sura, Terry R Van Vleet, and William R Proctor. Liver microphysiological systems development guidelines for safety risk assessment in the pharmaceutical industry. *Lab on a Chip*, 20(2):215–225, 2020.

[26] TJ Maguire, E Novik, P Chao, J Barminko, Y Nahmias, ML Yarmush, and K-C Cheng. Design and application of microfluidic systems for in vitro pharmacokinetic evaluation of drug candidates. *Current drug metabolism*, 10(10):1192–1199, 2009.

[27] Lucie A Low, Christine Mummery, Brian R Berridge, Christopher P Austin, and Danilo A Tagle. Organs-on-chips: into the next decade. *Nature Reviews Drug Discovery*, 20(5):345–361, 2021.

[28] Lawrence Vernetti, Albert Gough, Nicholas Baetz, Sarah Blutt, James R Broughman, Jacquelyn A Brown, Jennifer Foulke-Abel, Nesrin Hasan, Julie In, Edward Kelly, et al. Functional coupling of human microphysiology systems: intestine, liver, kidney proximal tubule, blood-brain barrier and skeletal muscle. *Scientific reports*, 7(1):1–15, 2017.

[29] T Satoh, S Sugiura, K Shin, R Onuki-Nagasaki, S Ishida, K Kikuchi, M Kakiki, and T Kanamori. A multi-throughput multi-organ-on-a-chip system on a plate formatted

pneumatic pressure-driven medium circulation platform. *Lab on a Chip*, 18(1):115–125, 2018.

[30] Alexandra Boussommier-Calleja, Ran Li, Michelle B Chen, Siew Cheng Wong, and Roger D Kamm. Microfluidics: a new tool for modeling cancer–immune interactions. *Trends in cancer*, 2(1):6–19, 2016.

[31] Thierry Lavé, Neil Parrott, HP Grimm, A Fleury, and M Reddy. Challenges and opportunities with modelling and simulation in drug discovery and drug development. *Xenobiotica*, 37(10-11):1295–1310, 2007.

[32] Yaning Wang, Hao Zhu, Rajanikanth Madabushi, Qi Liu, Shiew-Mei Huang, and Issam Zineh. Model-informed drug development: current us regulatory practice and future considerations. *Clinical Pharmacology & Therapeutics*, 105(4):899–911, 2019.

[33] Thierry Lavé, Antonello Caruso, Neil Parrott, and Antje Walz. Translational pk/pd modeling to increase probability of success in drug discovery and early development. *Drug Discovery Today: Technologies*, 21:27–34, 2016.

[34] Tony KL Kiang, Catherine MT Sherwin, Michael G Spigarelli, and Mary HH Ensom. Fundamentals of population pharmacokinetic modelling: modelling and software. *Clinical pharmacokinetics*, 51(8):515–525, 2012.

[35] Jong Hwan Sung, Carrie Kam, and Michael L Shuler. A microfluidic device for a pharmacokinetic–pharmacodynamic (pk–pd) model on a chip. *Lab on a Chip*, 10(4): 446–455, 2010.

[36] Joseph A Leedale, Jonathan A Kyffin, Amy L Harding, Helen E Colley, Craig Murdoch, Parveen Sharma, Dominic P Williams, Steven D Webb, and Rachel N Bearon. Multiscale modelling of drug transport and metabolism in liver spheroids. *Interface focus*, 10(2):20190041, 2020.

[37] Thomas M Keenan and Albert Folch. Biomolecular gradients in cell culture systems. *Lab on a Chip*, 8(1):34–57, 2008.

[38] Glenn M Walker and David J Beebe. A passive pumping method for microfluidic devices. *Lab on a Chip*, 2(3):131–134, 2002.

[39] HM Jones and Karen Rowland-Yeo. Basic concepts in physiologically based pharmacokinetic modeling in drug discovery and development. *CPT: pharmacometrics & systems pharmacology*, 2(8):1–12, 2013.

[40] Andreas Handel, Nicole L La Gruta, and Paul G Thomas. Simulation modelling for immunologists. *Nature Reviews Immunology*, 20(3):186–195, 2020.

[41] Matthias Heil and Andrew L Hazel. Fluid-structure interaction in internal physiological flows. *Annual review of fluid mechanics*, 43(1):141–162, 2011.

[42] RD O'Dea, HM Byrne, and SL Waters. Continuum modelling of in vitro tissue engineering: a review. *Computational Modeling in Tissue Engineering*, pages 229–266, 2012.

[43] Kwang W Oh, Kangsun Lee, Byungwook Ahn, and Edward P Furlani. Design of pressure-driven microfluidic networks using electric circuit analogy. *Lab on a Chip*, 12(3):515–545, 2012.

[44] Thomas Young. Iii. an essay on the cohesion of fluids. *Philosophical transactions of the royal society of London*, (95):65–87, 1805.

[45] Robert Finn. *Equilibrium capillary surfaces*, volume 284. Springer Science & Business Media, 2012.

[46] François Dunlop, Amir H Fatollahi, Maryam Hajirahimi, and Thierry Huillet. Identities for droplets with circular footprint on tilted surfaces. *Royal Society Open Science*, 7(11):201534, 2020.

[47] Paul Concus. Static menisci in a vertical right circular cylinder. *Journal of Fluid Mechanics*, 34(3):481–495, 1968.

[48] Mark M Weislogel. Compound capillary rise. *Journal of Fluid Mechanics*, 709:622–647, 2012.

[49] Robert Finn. Capillary surface interfaces. *Notices of the AMS*, 46(7):770–781, 1999.

[50] John Norbury, GC Sander, and CF Scott. Corner solutions of the laplace–young equation. *Quarterly Journal of Mechanics and Applied Mathematics*, 58(1):55–71, 2005.

[51] Michael L Anderson, Andrew P Bassom, and Neville Fowkes. Exact solutions of the laplace–young equation. *Proceedings of the Royal Society A: Mathematical, Physical and Engineering Sciences*, 462(2076):3645–3656, 2006.

[52] AW Neumann and RJ Good. Thermodynamics of contact angles. i. heterogeneous solid surfaces. *Journal of Colloid and Interface Science*, 38(2):341–358, 1972.

[53] J Long, MN Hyder, RYM Huang, and P Chen. Thermodynamic modeling of contact angles on rough, heterogeneous surfaces. *Advances in colloid and interface science*, 118(1-3):173–190, 2005.

[54] Terence D Blake and John M Haynes. Kinetics of liquidliquid displacement. *Journal of colloid and interface science*, 30(3):421–423, 1969.

[55] OV Voinov. Hydrodynamics of wetting. *Fluid dynamics*, 11(5):714–721, 1976.

[56] Alireza Mohammad Karim. A review of physics of moving contact line dynamics models and its applications in interfacial science. *Journal of Applied Physics*, 132(8), 2022.

[57] Chun Huh and Laurence E Scriven. Hydrodynamic model of steady movement of a solid/liquid/fluid contact line. *Journal of colloid and interface science*, 35(1):85–101, 1971.

[58] LM Hocking and AD Rivers. The spreading of a drop by capillary action. *Journal of Fluid Mechanics*, 121:425–442, 1982.

[59] RG Cox. The dynamics of the spreading of liquids on a solid surface. part 1. viscous flow. *Journal of fluid mechanics*, 168:169–194, 1986.

[60] Jiandong Wu, Xun Wu, and Francis Lin. Recent developments in microfluidics-based chemotaxis studies. *Lab on a Chip*, 13(13):2484–2499, 2013.

[61] James B Bassingthwaighte, Erik Butterworth, Bartholomew Jardine, and Gary M Raymond. Compartmental modeling in the analysis of biological systems. In *Computational Toxicology: Volume I*, pages 391–438. Springer, 2012.

[62] Malcolm Rowland, Carl Peck, and Geoffrey Tucker. Physiologically-based pharmacokinetics in drug development and regulatory science. *Annual review of pharmacology and toxicology*, 51:45–73, 2011.

[63] Kenneth A Brakke. The surface evolver. *Experimental mathematics*, 1(2):141–165, 1992.

[64] InSphero AG. Akura twin microplate — insphero ag, 2023. URL `https://shop.insphero.com/pages/akura-twin`. [Online; accessed 1-October-2025].

[65] JF Joanny and Pierre-Gilles De Gennes. A model for contact angle hysteresis. *The journal of chemical physics*, 81(1):552–562, 1984.

[66] Morgan V DiLeo, John A Kellum, and William J Federspiel. A simple mathematical model of cytokine capture using a hemoadsorption device. *Annals of biomedical engineering*, 37(1):222–229, 2009.

[67] C Huh and SG Mason. The steady movement of a liquid meniscus in a capillary tube. *Journal of fluid mechanics*, 81(3):401–419, 1977.

[68] LM Hocking. Sliding and spreading of thin two-dimensional drops. *The Quarterly Journal of Mechanics and Applied Mathematics*, 34(1):37–55, 1981.

[69] Christine Poon. Measuring the density and viscosity of culture media for optimized computational fluid dynamics analysis of in vitro devices. *Journal of the Mechanical Behavior of Biomedical Materials*, 126:105024, 2022.

[70] Jaroslaw Drelich. Guidelines to measurements of reproducible contact angles using a sessile-drop technique. *Surface innovations*, 1(4):248–254, 2013.

[71] Jens Eggers and Howard A Stone. Characteristic lengths at moving contact lines for a perfectly wetting fluid: the influence of speed on the dynamic contact angle. *Journal of Fluid Mechanics*, 505:309–321, 2004.

[72] Ron Milo and Rob Phillips. *Cell biology by the numbers*. Garland Science, 2015.

[73] Christina Cruickshank Miller. The stokes-einstein law for diffusion in solution. *Proceedings of the Royal Society of London. Series A, Containing Papers of a Mathematical and Physical Character*, 106(740):724–749, 1924.

[74] MJ Santos and JA White. Theory and simulation of angular hysteresis on planar surfaces. *Langmuir*, 27(24):14868–14875, 2011.

[75] James Tegart. Three-dimensional fluid interfaces in cylindrical containers. In *27th Joint Propulsion Conference*, page 2174, 1991.

[76] Hans D Mittelmann. Symmetric capillary surface in a cube. *Mathematics and computers in simulation*, 35(2):139–152, 1993.

[77] Mark Weislogel, Steven Collicott, Dan Gotti, Charles Bunnel, Carol Kurta, and Eric Golliher. The capillary flow experiments: handheld fluids experiments for international space station. In *42nd AIAA aerospace sciences meeting and exhibit*, page 1148, 2004.

[78] NA Patankar and Y Chen. Numerical simulation of droplet shapes on rough surfaces. In *2002 International Conference on Modeling and Simulation of Microsystems-MSM 2002*, pages 116–119, 2002.

[79] Eleanor C Johnstone, Andrew L Hazel, and Oliver E Jensen. The effect of isolated ridges and grooves on static menisci in rectangular channels. *Journal of Fluid Mechanics*, 935:A32, 2022.

[80] Jan Lienemann, Andreas Greiner, and Jan G Korvink. Modeling, simulation, and optimization of electrowetting. *IEEE Transactions on Computer-Aided Design of Integrated Circuits and Systems*, 25(2):234–247, 2006.

[81] Jean Berthier, Philippe Dubois, Philippe Clementz, Patricia Claustre, Christine Peponnet, and Yves Fouillet. Actuation potentials and capillary forces in electrowetting based microsystems. *Sensors and Actuators A: physical*, 134(2):471–479, 2007.

[82] Simon Brandon, Amir Wachs, and Abraham Marmur. Simulated contact angle hysteresis of a three-dimensional drop on a chemically heterogeneous surface: a numerical example. *Journal of colloid and interface science*, 191(1):110–116, 1997.

[83] Joël De Coninck, François Dunlop, and Thierry Huillet. Contact angles of a drop pinned on an incline. *Physical Review E*, 95(5):052805, 2017.

[84] Joël De Coninck, Juan Carlos Fernández-Toledano, François Dunlop, Thierry Huillet, and Alvin Sodji. Shape of pendent droplets under a tilted surface. *Physica D: Nonlinear Phenomena*, 415:132765, 2021.

[85] Kenneth A Brakke. Surface evolver manual. *Mathematics Department, Susquehanna Univerisity, Selinsgrove, PA*, 17870(2.24):20, 1994.

[86] Taeyoon Kim and Young-Ho Cho. A pumpless cell culture chip with the constant medium perfusion-rate maintained by balanced droplet dispensing. *Lab on a Chip*, 11(10):1825–1830, 2011.

[87] Xiaoyue Zhu, Leonard Yi Chu, Bor-han Chueh, Mingwu Shen, Bhaskar Hazarika, Nandita Phadke, and Shuichi Takayama. Arrays of horizontally-oriented mini-reservoirs generate steady microfluidic flows for continuous perfusion cell culture and gradient generation. *Analyst*, 129(11):1026–1031, 2004.

[88] Jong Hwan Sung, Carrie Kam, and Michael L Shuler. A microfluidic device for a pharmacokinetic–pharmacodynamic (pk–pd) model on a chip. *Lab on a Chip*, 10(4): 446–455, 2010.

[89] Hyuna Lee, Dae Shik Kim, Sang Keun Ha, Inwook Choi, Jong Min Lee, and Jong Hwan Sung. A pumpless multi-organ-on-a-chip (moc) combined with a pharmacokinetic–pharmacodynamic (pk–pd) model. *Biotechnology and bioengineering*, 114(2):432–443, 2017.

[90] Luca Docci, Nicolò Milani, Thomas Ramp, Andrea A Romeo, Patricio Godoy, Daniela Ortiz Franyuti, Stephan Krähenbühl, Michael Gertz, Aleksandra Galetin, Neil Parrott, et al. Exploration and application of a liver-on-a-chip device in combination with modelling and simulation for quantitative drug metabolism studies. *Lab on a Chip*, 22(6):1187–1205, 2022.

[91] Mengsu Yang, Jun Yang, Cheuk-Wing Li, and Jianlong Zhao. Generation of concentration gradient by controlled flow distribution and diffusive mixing in a microfluidic chip. *Lab on a Chip*, 2(3):158–163, 2002.

[92] Ali Asgar S Bhagat, Erik TK Peterson, and Ian Papautsky. A passive planar micromixer with obstructions for mixing at low reynolds numbers. *Journal of micromechanics and microengineering*, 17(5):1017, 2007.

[93] Andreas Karoly Gombert and Jens Nielsen. Mathematical modelling of metabolism. *Current opinion in biotechnology*, 11(2):180–186, 2000.

[94] Mehdi Dehghan. Numerical solution of the three-dimensional advection–diffusion equation. *Applied Mathematics and Computation*, 150(1):5–19, 2004.

[95] Rohit Sharma and Om Prakash Yadav. The evolution of finite element approaches in reaction-diffusion modeling. *Archives of Computational Methods in Engineering*, pages 1–22, 2025.

[96] Albert Puigferrat, Miguel Masó, Ignasi de Pouplana, Guillermo Casas, and Eugenio Onate. Semi-lagrangian formulation for the advection-diffusion-absorption equation at high péclet numbers.

[97] AC Galeao, RC Almeida, SMC Malta, and AFD Loula. Finite element analysis of convection dominated reaction–diffusion problems. *Applied Numerical Mathematics*, 48(2):205–222, 2004.

[98] Debby Lanser and Jan G Verwer. Analysis of operator splitting for advection–diffusion–reaction problems from air pollution modelling. *Journal of computational and applied mathematics*, 111(1-2):201–216, 1999.

[99] David A Benson and Mark M Meerschaert. Simulation of chemical reaction via particle tracking: Diffusion-limited versus thermodynamic rate-limited regimes. *Water Resources Research*, 44(12), 2008.

[100] Dong Ding, David A Benson, Amir Paster, and Diogo Bolster. Modeling bimolecular reactions and transport in porous media via particle tracking. *Advances in Water Resources*, 53:56–65, 2013.

[101] Desmond J Higham. An algorithmic introduction to numerical simulation of stochastic differential equations. *SIAM review*, 43(3):525–546, 2001.

[102] Radek Erban, Jonathan Chapman, and Philip Maini. A practical guide to stochastic simulations of reaction-diffusion processes. *arXiv preprint arXiv:0704.1908*, 2007.

[103] Olga Shipilova et al. Particle transport method for convection-diffusion-reaction problems. 2007.

[104] Michel Speetjens, Guy Metcalfe, and Murray Rudman. Lagrangian transport and chaotic advection in three-dimensional laminar flows. *Applied Mechanics Reviews*, 73 (3):030801, 2021.

[105] MD Finn, SM Cox, and HM Byrne. Mixing measures for a two-dimensional chaotic stokes flow. *Journal of Engineering Mathematics*, 48(2):129–155, 2004.

[106] WR Dean and PE Montagnon. On the steady motion of viscous liquid in a corner. In *Mathematical Proceedings of the Cambridge Philosophical Society*, volume 45, pages 389–394. Cambridge University Press, 1949.

[107] H Keith Moffatt. Viscous and resistive eddies near a sharp corner. *Journal of Fluid Mechanics*, 18(1):1–18, 1964.

[108] Geoffrey Ingram Taylor. The dispersion of matter in turbulent flow through a pipe. *Proceedings of the Royal Society of London. Series A. Mathematical and Physical Sciences*, 223(1155):446–468, 1954.

[109] Jean-Luc Thiffeault and Matthew D Finn. Topology, braids and mixing in fluids. *Philosophical Transactions of the Royal Society A: Mathematical, Physical and Engineering Sciences*, 364(1849):3251–3266, 2006.